APPLIED COMPUTATIONAL ELECTROMAGNETICS SOCIETY JOURNAL

January 2015
Vol. 30 No. 1
ISSN 1054-4887

The ACES Journal is abstracted in INSPEC, in Engineering Index, DTIC, Science Citation Index Expanded, the Research Alert, and to Current Contents/Engineering, Computing & Technology.

The illustrations on the front cover have been obtained from the research groups at the Department of Electrical Engineering, The University of Mississippi.

EMERITUS EDITORIAL ASSISTANTS

JANUARY 2015 REVIEWERS

THE APPLIED COMPUTATIONAL ELECTROMAGNETICS SOCIETY

JOURNAL

Vol. 30 No. 1 January 2015

TABLE OF CONTENTS

Parallel Model Order Reduction for Sparse Electromagnetic/Circuit Models

Giovanni De Luca [1], Giulio Antonini [1], and Peter Benner [2]

[1] Dipartimento di Ingegneria Industriale e dell'Informazione e di Economia
Università degli Studi dell'Aquila, L'Aquila, 67100, Italy
giovanni.deluca84@gmail.com, giulio.antonini@univaq.it

[2] Computational Methods in Systems and Control Theory
Max Planck Institute for Dynamics of Complex Technical Systems, Magdeburg, Germany
benner@mpi-magdeburg.mpg.de

Abstract ─ This paper describes a parallel Model Order Reduction (MOR) technique for Linear Time Invariant (LTI) electromagnetic/circuit systems with sparse structure. The multi-point Krylov-subspace projection method is adopted as framework for the model order reduction and a parallelization strategy is proposed. More specifically, a multi-point version of the well-known PRIMA algorithm is proposed, which is parallelized with respect to the computation of the error between the original model and the reduced one. The number of moments to be matched for any expansion point is chosen adaptively as well. The numerical results show that the proposed parallelized MOR algorithm is able to preserve the accuracy of the reduced models while providing a significant compression and a satisfactory speedup with respect to the sequential one.

Index Terms ─ Model order reduction, parallel computing, sparse electromagnetic/circuit systems.

I. INTRODUCTION

The increasing demand for performance of ICs pushes operation to higher signal bandwidth and accurate modeling of previously neglected effects, such as crosstalk, reflection, delay, and coupling becomes increasingly important during circuit and system simulation [1].

When modeling complex 3D geometries, Maxwell's equations are discretized in space and reduced to time continuous-space discrete equations. Time dependence can be further removed by using approximation of time derivatives resulting in time and space discrete equations. This task can be addressed by means of numerical discretization methods like Finite Difference (FD) methods and the Finite Element Method (FEM) or integral ones as the Method of Moments (MoM) [2] or the Partial Element Equivalent Circuit (PEEC) method [3]. Independently of the approach, the direct simulation of the resulting model may be computationally expensive in time and memory storage. The generation of a compact model preserving the properties (e.g., stability, passivity and reciprocity for electrical/electronic devices) of the original physical system is an important step because it allows to use the model in a virtual prototyping environment, avoiding to resort to a physical prototype. Thus, it is possible to verify the correct functioning of the designed system at a virtual prototyping level, testing different operating conditions and undesired effects when linked to other devices. Moreover, the creation of a virtual prototype is definitely cheaper and faster than creating a physical one.

Unfortunately, depending on the mesh of the discretization, the extracted model may contain many equations and/or variables ranging from the thousands to the millions. Such complex dynamical systems need to be simplified, while preserving the accuracy of their input-output behavior, in order to perform simulations within an acceptable amount of time and limited storage capacity, but with reliable outcome [4]. In order to speed up the

Submitted On: March 9, 2014
Accepted On: September 28, 2014

simulations and to save memory space, Model Order Reduction (MOR) techniques have been developed and are efficiently used to cope with this problem [4].

Model order reduction techniques aim to quickly capture the essential features of a model while keeping minimal the number of degrees of freedom. The reduced model has to match the frequency response of the original model within a desired error tolerance, in a prescribed frequency range of interest, and at the same time, has to preserve all necessary properties such as stability and passivity. The interested reader may refer to the "MOR Wiki" web site [5] for a list of model order reduction methodologies and benchmarks.

Model reduction methods based on balanced truncation are very efficient for medium to large-scale problems [6]. It is well known, that a global error bound for the reduced model makes the model reduction process automatic. Although, model reduction methods based on Krylov subspace and moment-matching are much simpler to be implemented and also require usually less computational complexity than methods based on balanced truncation; the most difficult task is choosing suitable expansion points, and in many cases using only an expansion point at zero is not sufficient for an accurate and small reduced model. However, how to choose proper nonzero expansion points and how to decide upon the corresponding number of moments accordingly is still an open problem, despite some progress as reported in [6].

An early method called CFH (Complex Frequency Hopping) is proposed in [7]. By using a binary search algorithm, the expansion points are chosen with respect to the common poles contained in both circles of the neighboring expansion points. However, the poles of the transfer function are computed based on explicit moment-matching; i.e., the moments are computed by recursive matrix-vector multiplications, in the same way as the Asymptotic Waveform Evaluation method in [8]. Therefore, the poles computed are actually not accurate because of numerical instability; although, they would represent the actual poles if computed with precise arithmetic. Moreover, in order to compute the actual poles, higher order moments must be computed, and explicit moment computation cannot guarantee that the higher order moments are accurately computed, again because of numerical inaccuracies [6].

In this paper, we focus on the use of a multi-point version of the well-known PRIMA algorithm [9], based on implicit moment-matching (that can maintain numerical stability), which is made adaptive and parallel by exploiting the power of modern multi-core processors. In particular, in order to obtain a reduced model with, say, a minimum order of reduction with respect to the desired accuracy, we just fix the number of frequency test-points in correspondence of which we compute the error between the dynamics of the original model and of the reduced one, employing PRIMA on those points having the maximum error value in a recursive way, and increasing the order of moments to be matched for the selected points when necessary. When the number of frequency test-points is high (which should ensure a full exploration of the frequency range of interest), the computation of the error values may be time-consuming, mostly depending on the original system dimension. For this reason in this paper, such a computation is performed in parallel.

Section II provides a brief review of the PRIMA algorithm, including the theory of deflated Krylov subspaces. Section III describes the parallelization of the multi-point PRIMA algorithm, providing remarks and comments on the adopted technique as well; several numerical results are presented in Section IV using different data sets available in public repositories. Finally, the conclusions are drawn in Section V and future perspectives are pointed out.

II. THE PRIMA ALGORITHM

A. Basic formulation

Let us assume the electromagnetic/circuit system be represented in descriptor form as:

$$\Phi:\begin{cases} C\dot{x}(t) = -Gx(t) + Bu(t) \\ y(t) = Lx(t) \end{cases}, \tag{1}$$

with zero initial condition $x(0) = 0$. The matrices $C, G \in R^{n\times n}$ contain memory and memoryless elements, respectively, $x(t) \in R^n$ denotes the vector of state variables. In a circuit environment, the Modified Nodal Analysis (MNA) [10] naturally leads to a descriptor form assuming as unknowns the node potentials and the currents flowing in inductances and voltage sources of the equivalent circuit. Also, $B \in R^{n\times m}$ and $L \in R^{m\times n}$ are the input and output matrices, respectively.

The corresponding complex-valued, matrix transfer function in the Laplace domain reads:

$$H(s) = L(G + sC)^{-1} B \cdot \tag{2}$$

The PRIMA [9] algorithm provides a unitary projection matrix V (e.g., computed by the one-side Arnoldi method, where $V^H V = I$ with I being identity matrix of appropriate dimension), and then the approximation $\hat{x}(t)$ can be represented as $\hat{x}(t) = Vz(t)$. Therefore, $x(t)$ can be approximated by $x(t) \approx Vz(t)$. Here, $z(t)$ is a vector of length $k \ll n$. Once $z(t)$ is computed, the approximate solution $\hat{x}(t) = Vz(t)$ for $x(t)$ can be obtained. The vector $z(t)$ can be computed from the reduced model:

$$\tilde{\Phi}: \begin{cases} \tilde{C}\dot{z}(t) = -\tilde{G}z(t) + \tilde{B}u(t) \\ \tilde{y}(t) = \tilde{L}z(t) \end{cases} \tag{3}$$

Besides, the reduced model preserves the main properties of the original system (stability, passivity) under some assumptions on the structure of the matrices *C* and *G* [9]. The reduced MNA matrices are:

$$\begin{aligned} \tilde{C} = V^H C V, \quad \tilde{B} = V^H B, \\ \tilde{G} = V^H G V, \quad \tilde{L} = L V. \end{aligned} \tag{4}$$

The unitary projection matrix V of dimension $n \times k$ is obtained using the block-Arnoldi procedures with the modified Gram-Schmidt process, such that its *k* column-vectors span the Krylov subspace $K_l(A, R)$ induced by the *l*-block moments, as the sequel $colspan\{V\} = K_l(A,R) = span\{R, AR, ..., A^{(l-1)}\}$, where $R \equiv (sC + G)^{-1} B$, with $s \in C$ (complex set) a selected expansion point, and $A \equiv -(sC + G)^{-1} C$.

B. Deflation of the Krylov subspace

In the case of multiple input systems, i.e., with $m > 1$, we need to use a block-version of the Arnoldi algorithm to compute the moments of the transfer function with PRIMA. Equivalently, we need to solve linear systems of the form $AX = B$ with multiple right-hand side.

An important aspect of block-Krylov subspace is represented by the possible linear dependence of the basis vectors. Such dependence can arise both in the set of starting vectors and in the following blocks, during the subspace construction phase: in the first case, linearly dependent columns of the input matrix *B* should be eliminated before starting the Arnoldi procedure, so that the solution of the linear system (which is the first moment of the transfer function in this case) is of full column rank, and this is called "initial deflation"; in the second case, linearly dependent vectors are detected within the orthogonalization process of the following blocks, this is reffered to as "Arnoldi deflation" [11]. Exact linear dependence rarely occurs in practical applications, on the contrary approximate deflation, depending on a deflation tolerance tol_{defl}, is more common and may reduce the computational cost of the iterative procedure [11].

As implemented in [11], differently from the standard rank-revealing QR (RRQR) factorization, the deflation is implemented by comparing the norm of the last orthogonalized column with the initial norm of the same column: if the ratio between the former and the latter is smaller than tol_{defl}, then, such column has to be deflated. Clearly, the accuracy in the reconstruction of the deflated systems solution depends on the choice of tol_{defl}, [11]. We set $tol_{defl} = 10^{-10}$.

Remark: Purely imaginary expansion point(s) (for single-point or multi-point PRIMA) is the common choice, since it is the response along the imaginary axis which is of interest for interconnect analysis [12]. Besides, the use of complex expansion points s_i typically results in a significantly smaller state-space dimension *k* of the reduced order model, compared to the case of real expansion point(s), since s_i can be placed closer to the frequency range of interest than any real one(s) [13].

However, using complex expansion points results in complex reduced models. Then, to generate a real ROM (as the original one), one can separate the complex projection matrix *V*, resulting from a MOR method, in real and imaginary parts to generate a unique real matrix *V*, such that:

$$\tilde{V} = \left[Re(V) \;\; Im(V) \right]. \tag{5}$$

One obvious disadvantage of this approach is that the dimension of the resulting reduced-order model is doubled to 2*k*. Furthermore, in general, the projection matrix (5) is not guaranteed to have full column rank, and so before using (5) as a projection matrix, one would need to check for and possibly delete any linearly dependent columns of (5) [13]. To avoid the linear dependent columns, one can check whether tol_{defl} is satisfied at each step of the

orthogonalization.

III. PARALLEL, ADAPTIVE MULTI-POINT PRIMA

The PRIMA algorithm approximates the original system just locally, around a selected expansion point. Wide-band modeling would require a large number of moments to be matched to obtain a prescribed accuracy. Also, in some applications, too many derivatives need to be matched to obtain a sufficient accuracy in the frequency range of interest. Without resorting to higher order moments, multiple expansion points have been considered, so that a limited number of moments need to be matched on each frequency point.

There have been many efforts and contributions in this direction: Benner, et al., developed an efficient MOR scheme which chooses the expansion points and the number of moments in a fully adaptive way [6]; an adaptive algorithm to automatically identify the expansion points and set the order of the model has been proposed in [1]; among others, Lee, et al., proposed an Adaptive-Order Rational Arnoldi (AORA) method [14] to be applied to large-scale linear systems. Also, Nakhla, et al., in [1] used a binary search method to find frequency points where the ROM is computed.

However, the choice of expansion points in the rational Krylov-based MOR theory, to reach a desired approximation of the ROM with a minimum order of reduction, while keeping the simulation time as small as possible, is still an open problem.

In order to retain a small number of expansion points and a limited number of moments for each of them, trying to catch just the dominant poles of the transfer function describing the input-output behavior of the original full order model, we propose a new method, with the following motivations.

1. We assume to know the starting and ending points of the frequency range of interest and the matrices describing the LTI, SISO or MIMO system; no information is available about the original system in terms of the exact location of the dominant poles of its transfer function, or about stability properties. Since the approximation of the ROM, with the desired accuracy over the frequency range of interest is the main goal in the MOR field, one can recursively check the error between the dynamics (accounting for modules and phases) of the original model and that of the currently computed ROM for a high number of distributed frequency test-points n_{FS} (FS stands for Frequency Samples), applying PRIMA (thus, extracting the projection matrix) on those points showing the maximum error value among all the others. This way, we would avoid heuristic searching method for the expansion points. Obviously, as the number of distributed points tends to infinity, then there will be retained a sufficient number of points which make sure the accuracy is reached in all the frequency range, matching just one or very few moments on each selected point with the use of PRIMA. But this has the big drawback of the intractable simulation time, when computing the original model's transfer matrix in correspondence of each test-point, and PRIMA (both these operations involve the solution of sparse linear systems), mostly for very large size matrices.
2. To avoid the choice of an intractable, high number of frequency test-points to be checked, we select a reasonable number of linearly distributed points in the range of interest, in correspondence to which the error has to be computed. Then, the frequency sample with the maximum error value is selected as an expansion point and a satisfactory solution of the transfer function is obtained on it, executing PRIMA with matching just one moment. Since an acceptable solution can be achieved only in the retained frequency samples used as expansion points, whilst this is not the case for frequencies belonging to the interval between two consecutive test-points, we can think of increasing the number of the moments in an adaptive way: let us assume the current maximum error of the dynamics is in correspondence to the (angular) frequency point ω_i which lies between ω_{i-1} and ω_{i+1}, such that $[\omega_{i-1}\ \omega_i\ \omega_{i+1}]$ is a subinterval of the whole range and they are linearly spaced. Then, PRIMA will be computed on $s_i = j\omega_i$, with $j = \sqrt{-1}$, matching just the first moment on ω_i. In the next step, we check the error on both

the middle points $\omega_{i-1,i}$ of the left-subinterval $[\omega_{i-1}\ \omega_i]$ and $\omega_{i,i+1}$ of the right one $[\omega_i\ \omega_{i+1}]$: until the error of at least one of the mid points is greater than the desired tolerance, we increase iteratively the number of moments to be matched at ω_i. We choose to check the middle points inside each subinterval $[\omega_{i-1}\ \omega_i\ \omega_{i+1}]$, starting from the idea adopted in [6] for the adaptive choice of the moments, where the increasing of moments depends on the accuracy (error check) on points far away from the currently selected one: in our case, the current point is ω_i and the farthest points (from it) are $\omega_{i-1,i}$ (in the left-subinterval $[\omega_{i-1}\ \omega_i]$) and $\omega_{i,i+1}$ (in the right one $[\omega_i\ \omega_{i+1}]$), respectively. Nevertheless, as pointed out in [6], it is not ensured that the farthest point exhibits the maximum error value, so that the choice of a "sufficiently" high number of linearly distributed points to be checked in the range is justified: as this number increases, the distance between the currently processed frequency point ω_i and the farthest points in the left and right subintervals $\omega_{i-1,i}$ and $\omega_{i,i+1}$, respectively, decreases; thus, these mid points are "close enough" to ω_i such that there may be also a good accuracy on them matching eventually few moments on ω_i, and the error check on them as farthest points is useful in order to accurately reproduce the dynamics on subintervals between consecutive test-point, as well. In Section IV, numerical results will be provided, which qualitatively relates the selected number of linearly distributed points for the error check and the resulting order of reduction.

3. Even with a moderate number of distributed frequency points to be checked, the computational time of the original transfer function for each point may be expensive, since it requires n_{FS} solves with (s_iC+G), according to (2), and the CPU time could increase with the size of the initial model. PRIMA also needs the inverse of the same matrix, to compute the moments. To overcome this limitation, we divide the initial frequency range into a certain number of subintervals, delegating the search for expansion points and the computations of PRIMA to different available parallel processors, as described below.

Briefly, our algorithm is based on the recursive exploration of the frequency range of interest and additional expansion points are identified through the exploration step, by comparing the frequency response of the original system and the reduced one. When the size of the modeled systems exceeds few thousands, the computation of the frequency responses and that related to the moment(s) with PRIMA are typically time consuming.

As a preliminary step, we select the desired tolerance *tol* for the accuracy of the ROM's dynamics and a number of n_{FS} frequency samples, linearly distributed in the range of interest, over which the error has to be checked and PRIMA has to be applied, when necessary; successively, we divide the range in a certain number of subintervals, each of them containing an equal number of expansion points. The number of subintervals is equal to the number of available parallel processors, and we parallelize the executions on the multiple subintervals, exploiting the power of modern multi-core processors. We assign a subinterval to each processor (such that the selected processors will cover all the subintervals, the union of which forms the entire frequency range), resulting in an "embarrassingly" task parallel execution (no communication required between the operations to be computed on each processor).

However, the efficiency of a parallelized method depends on some factors. First of all, the sequential part of the algorithm could slow down the overall performance of the algorithm, dominating over the parallelized one (Amdahl's law [15]). Also, when working with very large data sets, the data transfer time and memory demands could exceed that needed for the real computation, i.e., when the workload for each parallel processor is not "high enough" to overlap the data transfer and memory accesses (to request data from the hierarchical memory and retrieve it from the CPU, where the operations are executed). Besides, another factor causing the slowdown of the parallel performance could be the data bus contention, when each processor requests data from the RAM (mainly, when the data cannot be entirely loaded into fast, private memory blocks, namely the

cache), resulting in a waste of time for the processors waiting for data, which travels in a bus eventually shared by every one of them before proceeding with the computation. We will examine these factors in the section on numerical results.

Assuming initially to work with a single processor, then there is just one interval, which is identical to the original frequency range. As starting point, we compute the frequency response for all the n_{FS} points, storing these values (for SISO systems) or matrices (for MIMO models) in memory. Afterwards, we use PRIMA on the lowest frequency point ω_0 of the range, matching just the first moment, and extracting the first projection matrix. What follows is a further check on the farthest point from ω_0, which lies in the middle of the right subinterval $[\omega_0 \quad \omega_1]$, increasing the order of the moments at ω_0 if the error in the midpoint of this subinterval is larger than the tolerance *tol*. (*Note:* when increasing the moments and the selected point is either the lowest or the highest one in the frequency range, we just consider the right subinterval or the left one, respectively.) We define the (relative) error as:

$$err = \frac{\left|H(s) - \tilde{H}(s)\right|}{\left|H(s)\right|}, \tag{6}$$

where $H(s)$ and $\tilde{H}(s)$ are the transfer functions of the original model (already available since previously computed) and of the ROM (which changes each time a new expansion is done), respectively.

It is worth noticing that the error (6) is a matrix, where the (*i, j*)-th element corresponds to the error of the dynamics of the (*i, j*)-th transfer function; in the multi-point approach followed in [1], the error was computed as a RMS error, an average among all the error values of each ports of the model; thus, in the case that all the ports but one show an error smaller than the desired tolerance, the final RMS error may be smaller, thus the tolerance too, and PRIMA would not be computed on the processed frequency point and consequently the approximation in that point or interval was considered accurate enough but it is not. Instead, we computed the error as (6), accounting for the error value for each (*i, j*)-th transfer function, discarding the processed frequency point just in case all the ports have a satisfactory accuracy. This error formulation is suitable for both SISO and MIMO systems.

The next step is the computation of the error for each distributed frequency sample: the one exhibiting the maximum value among the others is selected, and a projection matrix is extracted using that frequency sample as expansion point. Again, we do a further check on the mid points in its left and right sub-intervals, increasing the order of the moments when required. For each (iteratively) retained frequency point, the corresponding obtained projection matrix is block-column concatenated with the previous ones. The computation of the error is repeated for the remaining points in the frequency interval, and as before, other points may be retained and used as expansion points until for all the distributed points, the error is smaller than the a-priori fixed tolerance *tol*.

Instead, when using n_{proc} processors (parallel workers), thus having n_{proc} subintervals each of the with n_{FS}/n_{proc} sample points, each worker uses the same approach as before and will only care about its own subinterval, initially applying PRIMA at the lowest point of it, eventually increasing the moments to be matched, and iteratively selecting the other points exhibiting the maximum error value repeating the computation of PRIMA until the desired accuracy is satisfied. This parallel approach is based on the independence of each subinterval on the other ones, but we will see that a little drawback could arise, in terms of redundancy of some retained expansion points. The pseudo-code of the parallel and adaptive multi-point PRIMA is shown in Algorithm 1.

The algorithm receives as inputs the matrices of the original system in the general form (1) (G, C, B, L), the starting (*fStart*) and ending (*fStop*) points of the frequency range of interest, the number of points to be linearly distributed (n_{FS}), the desired tolerance *(tol)* for the accuracy of the ROM and the number of processors (n_{proc}) to run in parallel (which will be equal to the number of subintervals). The projection-matrix V_{fin} is produced as output.

Algorithm 1 Function V_{subInt}= MultiPts$(G, C, B, L, D, fStart, fStop, n_{FS}, tol, n_{proc})$

create $subInt(n_{proc}, n_{FS}/n_{proc})$, where each row is a subinterval and contains n_{FS}/n_{proc} test-points;

compute in parallel the frequency responses of the original model for all the n_{FS} test-points, according to (2), and store the data into $freqResp(n_{proc}, n_{FS}/n_{proc})$;

set $dist_{farPts}$ as the half distance between a point and its consecutive;

for j=1:n_{proc} **do**
  V_{subInt}=parSubInt$(subInt(j,:), freqResp(j,:),$
  $G, C, B, L, D, fStart, fStop, tol)$;
end for

block-column concatenate each V_{subInt} to form V_{fin};
re-orthogonalization of V_{fin};

It is worth noticing, that in order to decrease the time needed for generating higher-order moments (higher than 1), we estimate the increased-order moment (with the *higherMomPRIMA* function in Algorithm 1) only with respect to the previously computed one (selecting from the current projection matrix V_i the moment corresponding to *lastMom*).

Regarding the final projection matrix V_{fin}, it is not unique, as a basis for the rational Krylov-subspace. In fact, we start to approximate the original transfer function from the initial point $\omega_0 = \min(subInt)$, that in the case of a unique interval (sequential execution with one processor), it is the closest to the DC component, but it can be chosen differently. The choice $\omega_0 = 0$ (or $\omega_0 \approx 0$) is widely used as it often delivers good results in a large neighborhood of the low-frequency part of the spectrum, including the steady state [16]. However, numerous simulations have shown that a random selection of the initial value for each subinterval neither affects the convergence nor the overall CPU time of the algorithm, nor the accuracy of the ROM's dynamics.

Figure 1 may better clarify the search for and selection of expansion points, for both the sequential and the parallel executions, as the algorithm proceeds.

For instance, assuming we linearly distribute $n_{FS} = 7$ frequency test-points (from ω_0 to ω_6), the sequential algorithm (top) computes in step 1 the first moment with PRIMA (filled circle) on the lowest frequency point ω_0. Then, it calculates the error in the point $\omega_{0,1}$ (the midpoint in the interval $[\omega_0\ \omega_1]$), where ω_0 and ω_1 are two consecutive points, and employs PRIMA to catch higher-order moments if the error in $\omega_{0,1}$ is greater than the tolerance (in this picture we do not show the adaptivity for the computation of higher-order moments, for simplicity). In step 2, the algorithm evaluates the error values on each test-point and select that with the maximum value (empty circle, in this case in correspondence to ω_4), and in step 3 PRIMA is executed matching the first moment at ω_4, and eventually computes those with higher order. The algorithm stops when the error values on all the test-points are less than the desired tolerance. Clearly, the method will not make the expansion on all the test-points, since a global accuracy in the entire range will be obtained by matching the moments of the original transfer function at different, selected expansion points.

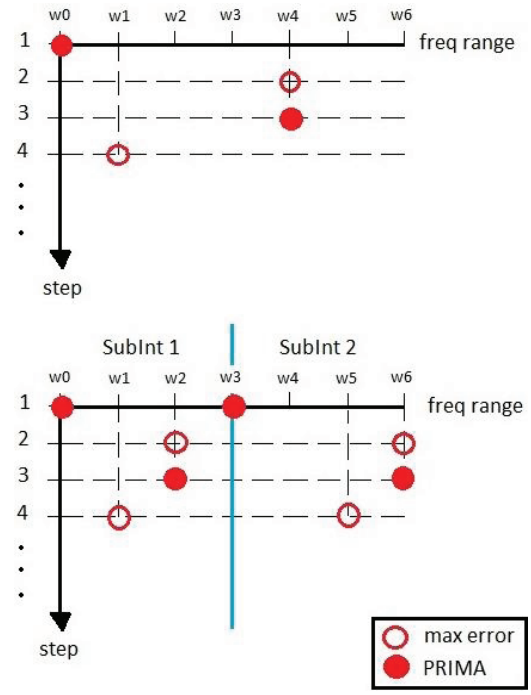

Fig. 1. Example of the sequential execution of the search method within the entire frequency range (top) and the parallel version with two processors/subintervals (bottom).

Instead, for the parallel version with two processors (bottom of Fig. 1), the method divides the frequency range into two subintervals (*SubInt1*

and *SubInt2*), and then proceeds with the same criterion of the sequential one. One can easily note, that there may be redundancies in executing PRIMA at those points that are "shared" between two consecutive subintervals (in Fig. 1 it is ω_3), but this redundancy can be eliminated with the deflation rule presented in Section II. However, other redundancies could not be deleted by the deflation, e.g., when the parallel algorithm (relying on the independence of the subintervals) retains two distinct points, which are sufficiently close in the entire range but are parts of two (distinct) consecutive subintervals. We will see that increasing the number of parallel workers (thus, the number of subintervals) could result in a slight augmentation of the final order of reduction of the ROM, but also with a better accuracy, which becomes much more satisfactory than that fixed a priori, and most important, with a gain in the CPU time execution. Nevertheless, the problem of obtaining a ROM with the desired accuracy is resolved in any case.

As a measure of the parallelization, we refer to the speedup factor:

$$SP\left(n_{proc}\right)=\frac{t_{seq}^{*}}{t_{par}\left(n_{proc}\right)}, \tag{7}$$

where t_{seq}^{*} is the execution time of the fastest sequential program solving the same problem. Moreover, as a measure of utility of the selected number of processors that work in parallel, we define the *efficiency* of the parallelization:

$$Eff\left(n_{proc}\right)=\frac{t_{seq}^{*}}{n_{proc}t_{par}\left(n_{proc}\right)}, \tag{8}$$

where n_{proc} is the number of parallel processes [17].

Another common factor used in the field of parallelization of the execution is the *strong scalability*. Fixing the problem size (i.e., the dimension *n* of any data set), a program scales linearly if the speedup factor is equal to the number of parallel processes used, n_{proc}.

Evidently, optimal (linear) scaling is attained when the speedup factor is equal or close to n_{proc} (or, stated in another way, the efficiency stays close to one) and therefore, strong scaling results can be visually inspected by plotting the speedup factor (or the efficiency) versus the number of parallel processes n_{proc}.

A. Parallelizing the computation of multiple expansion points

There are some different ways to parallelize the computation of time-expensive routines. From the hardware point of view, one can use either a local multi-core desktop or a cluster of computers, called nodes, linked in a computer network or a combination of both of them (hybrid distributed/ shared memory-based implementations). On the other hand, there are several software environments allowing high performance, parallel programming, such as the MATLAB(R) Parallel Computing Toolbox (PCT) for local desktop, and the MATLAB Distributed Computing Server for cluster workstations. Another very popular platform is the OpenMP, an API that supports multiplatform shared memory multiprocessing, which together with MPI (Message Passing Interface, a computer communications protocol for parallel computation) can be used for cluster computers (an example of the use of this latter combination was done by Ciuprina, et al., in [18], where a MOR technique for multiple expansion points is presented).

For our numerical results, we used the MATLAB Parallel Computing Toolbox. It allows to solve computationally and data-intensive problems using multi-core processors, GPUs, and computer clusters. High-level constructs-like parallel for-loops, special array types, and parallelized numerical algorithms let one parallelize MATLAB applications without CUDA(R) (Compute Unified Device Architecture, a parallel computing platform and programming model created by NVIDIA) or MPI programming. The toolbox provides a maximum of twelve parallel "workers" (MATLAB computational engines) to execute applications locally on a multi-core desktop. With slightly changing the code, one can run the same application on a computer cluster or on a grid computing service.

More in detail, we used the parallel for-loop (*parfor*), instead of the standard *for* loop, in the computation of the frequency responses of the original system (in Algorithm 1), as well as in the generation of the projection matrices for each subinterval (with the function *parSubInt* described in Algorithm 2). It runs loop iterations in parallel on

a pool of parallel workers using the parfor language construct, allowing several processors to execute individual loop iterations simultaneously. Restriction on parallel loops is that no iterations be allowed to depend on any others (in our case, each processor computes the original frequency responses at a certain number of frequency samples and works on its own subinterval, resulting in what is called an embarrassingly parallel problem, since there is no communication between each worker); besides, the body of the parfor has to be a computationally intensive routine, such that its simulation time far exceeds the one needed for the transfer of very-large data from the client to each workers, and vice versa.

Algorithm 2 Function V_{subInt}= parSubInt($subInt, freqResp, G, C, B, L, D, fStart, fStop, tol$)

$\omega_0 = \min(subInt)$;
$V_i = firstMomPRIMA(G, C, B, \omega_0, nMom = 1)$;
compute the frequency responses of the original model in $\omega_{0,1} = (\omega_0 + dist_{farPts})$ and store it;
compute the error in $\omega_{0,1}$;
while $err(\omega_{0,1}) > tol$ **do**
  $V = higherMomPRIMA(G, C, B, \omega_0, nMom + +, lastMom)$;
  $V_i = [V_i, V]$;
  compute the current ROM;
  compute the error in $\omega_{0,1}$;
end while
$V_{subInt} = V_i$;
$cycle = 1$;
while $cycle$ **do**
  for $i = 1 : size(subInt, 2)$ **do**
    compute the error for each test-points in the subinterval, using $freqResp$;
  end for
  select that frequency point ω_i exhibiting the maximum error value ($maxVal$) among the others;
  if $maxVal > tol$ **then**
    $V_i = firstMomPRIMA(G, C, B, \omega_i, nMom = 1)$;
    compute the frequency responses of the original model in $\omega_{i-1,i} = (\omega_i - dist_{farPts})$ and $\omega_{i,i+1} = (\omega_i + dist_{farPts})$ and store it;
    compute the errors in $\omega_{i-1,i}$ and $\omega_{i,i+1}$;
    while $err(\omega_{i-1,i}) > tol$ OR $err(\omega_{i,i+1}) > tol$ **do**
      $V = higherMomPRIMA(G, C, B, \omega_i, nMom + +, lastMom)$;
      $V_i = [V_i, V]$;
      re-orthogonalization of V_i;
      compute the current ROM;
      compute the errors in $\omega_{i-1,i}$ and $\omega_{i,i+1}$;
    end while
    $V_{subInt} = [V_{subInt}, V_i]$;
  else
    $cycle = 0$;
  end if
end while
re-orthogonalization of V_{subInt};
return V_{subInt};

The first step is to run a pool of n_{proc} MATLAB sessions for parallel computation, with the command *matlabpool open* n_{proc}, which connects the pool to the client. Then, to see the benefit of the parallelization, we can run the sequential algorithm, i.e., calculating the frequency responses for all the n_{FS} samples in a sequential fashion and working on the original frequency range and compare the obtained simulation time with that from the parallel version, evaluating the speedup factor with (7) and the efficiency of the parallelization with (8), as the number of available parallel processors n_{proc} increases, to analyze the scalability of the method.

IV. NUMERICAL EXPERIMENTS

The proposed algorithm is implemented in MATLAB r2012b, running on a shared-memory local desktop equipped with an Intel i7 Quad-Core Processor, CPUs operating at 3.50 GHz, with 16 GB of RAM available, on a Windows7 OS and setting the priority of the MATLAB process(es) to Real-Time, the highest one (in the Task Manager). We provide numerical results of eight sparse data sets, some coming from the Max Planck Institute of Magdeburg, others free downloadable from the SLICOT benchmarks ([19]) and from the Joost Rommes' homepage ([20]). We set a tolerance $tol = 10^{-2}$ for all the data sets, which is considered reasonable for engineering applications (it can be changed); the number of linearly distributed frequency test points was set to $n_{FS} = 96$.

Figure 2 shows magnitude, phase and error spectra of the transfer function $H_{1,4}$ of an interconnect model with $n = 980$ internal state and $m = 4$ inputs and outputs, of both the original system evaluated in 2000 frequency points (as for all the other data sets) and the reduced model of order $k = 32$, obtained with the sequential multipoint PRIMA algorithm. For this data set, the algorithm retained five expansion points (which are plotted in the module picture, translated in angular frequencies). Figure 3 shows the same dynamics of the previous model (we do not provide the phase dynamic, it is identical to that of Fig. 2), obtained from the parallel execution with two processors. As said in the previous section, one can note that the

number of retained expansion points is increased (eight in this case), resulting in a slightly bigger order of reduction $k = 44$. For this model, this has also resulted in a higher accuracy of the final ROM, as one can see in the picture of the error.

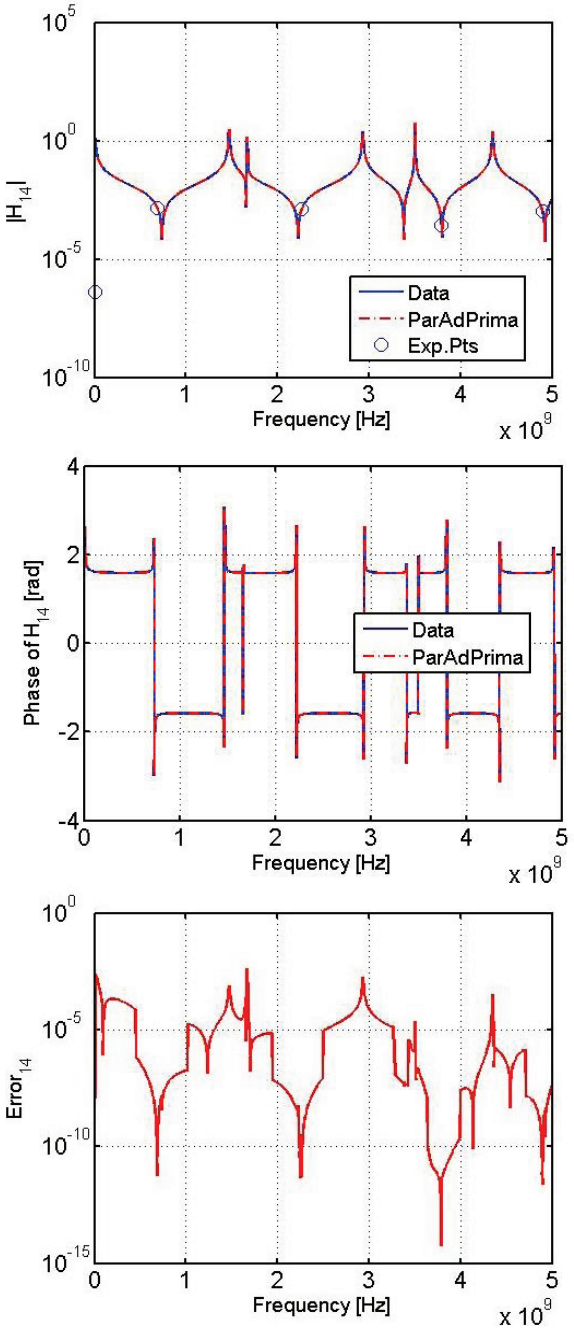

Fig. 2. Magnitude (top), error (middle) and phase (bottom) spectra of the transfer impedance of $H_{1,4}$ an interconnect model with dimension $n = 980$, running the sequential method.

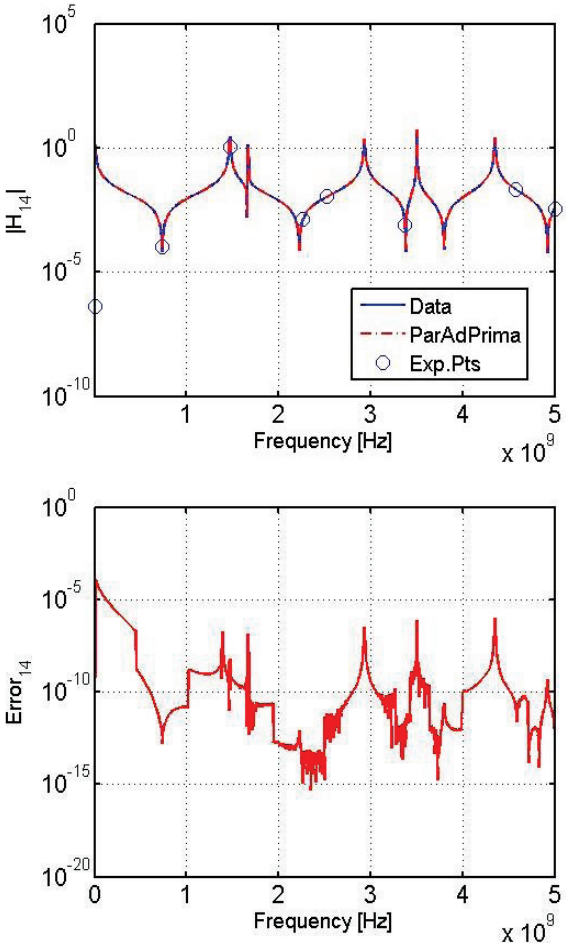

Fig. 3. Magnitude (top) and error (bottom) spectra of the transfer impedance $H_{1,4}$ of an interconnect model with dimension $n = 980$, running the parallel method with two processors.

Figure 4 plots magnitude, phase and error spectra of the transfer function $H_{4,3}$ of an interconnect model of dimension $n = 13309$ and with $m = 8$ inputs and outputs, with a ROM of dimension $k = 246$, retaining thirteen expansion points with the sequential execution. Figure 5 shows magnitude (top) and error spectra (bottom) of the same interconnection of Fig. 4, obtained with two parallel processors, resulting in an order of reduction $k = 256$ with sixteen retained expansion points. Comparing the error plots, one can note that for this interconnection, the parallel method did not result in an improvement of the accuracy, since there were few redundancies of the retained expansion points as compared to the sequential case. Indeed, in the sequential execution, the

algorithm selected points quite scattered on the frequency axis, such that with the parallel version each subinterval showed a bigger degree of independence of the other ones, compared to the model with $n = 980$.

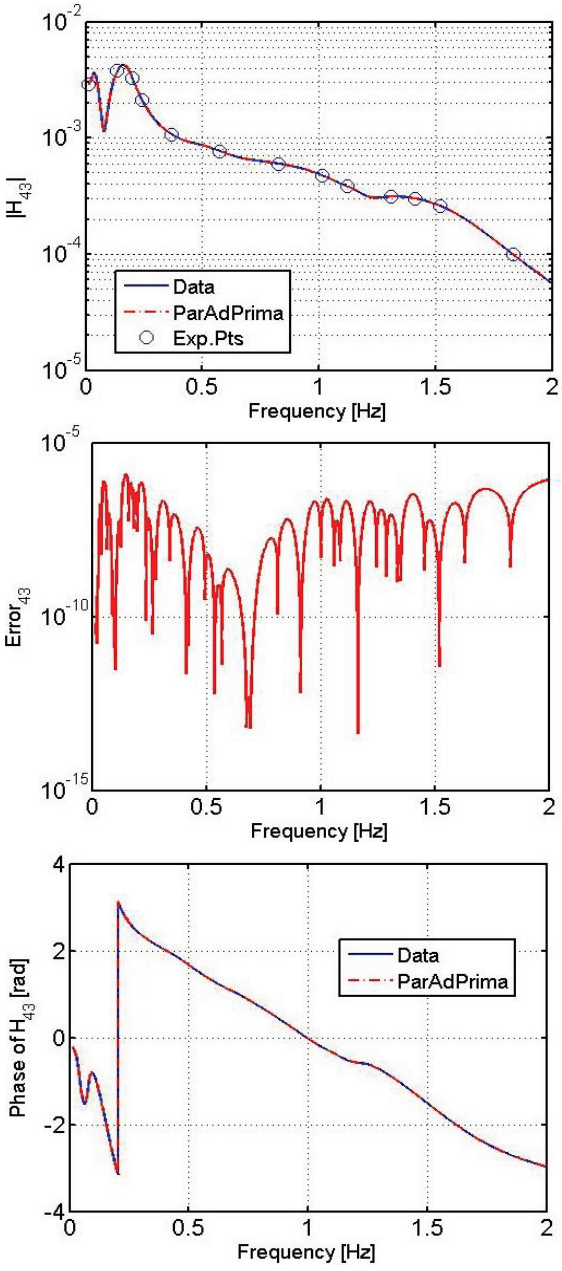

Fig. 4. Magnitude (top), error (middle) and phase (bottom) spectra of the transfer impedance $H_{4,3}$ of an interconnect model with dimension $n = 13309$, running the sequential method.

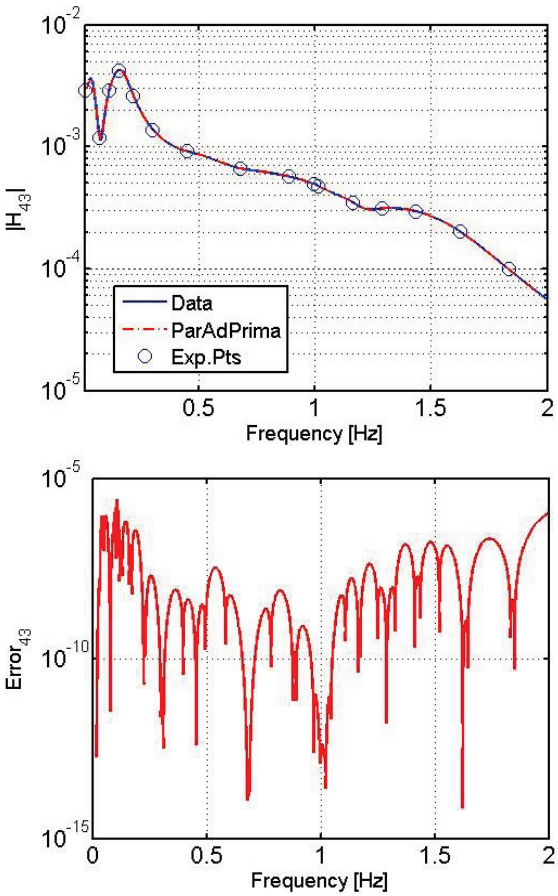

Fig. 5. Magnitude (top) and error (bottom) spectra of the transfer impedance $H_{4,3}$ of an interconnect model with dimension $n = 13309$, running the parallel method with two processors.

Finally, Table 1 provides for each data set the size n of the original model and the number of inputs/outputs m (the data set with dimension $n = 40337$ has two inputs and just one output), the simulation time results t_{seq} of the sequential version and t_{par2}, t_{par4} and t_{par8} of the parallel one with 2, 4 and 8 parallel processes, respectively, all in seconds (to analyze the strong scalability of the algorithm), Speedup (*SP*) and Efficiency (*Eff*) of the parallelization for each number of used processes; the last columns reports the order k_{seq}, k_2, k_4 and k_8 of the reduced models resulting from executing the sequential algorithm and the parallel with 2, 4 and 8 processors, respectively.

Table 1. Table of results: $tol = 0.01$, $n_{FS} = 96$, $n_{proc} = 2$, 4 and 8, respectively (all times are in seconds)

n/m	t_{seq}	t_{par2}- SP-Eff	t_{par4}- SP-Eff	t_{par8}- SP-Eff	$k_{seq,2,4,8}$
980/4	12.35	7.32- 1.69- 0.84	5.28- 2.34- 0.58	6.15- 2.01- 0.25	32-44- 66-85
6134/1	1.21	0.90- 1.34- 0.67	0.75- 1.61- 0.40	0.85- 1.43- 0.18	14-18- 23-26
4863/22	$8.00 \cdot 10^2$	$5.08 \cdot 10^2$- 1.57- 0.79	$3.78 \cdot 10^2$- 2.12- 0.53	$3.91 \cdot 10^2$- 2.05- 0.26	66-94- 149-212
9223/18	$3.48 \cdot 10^2$	$2.02 \cdot 10^2$- 1.72- 0.86	$1.45 \cdot 10^2$- 2.40- 0.60	$1.72 \cdot 10^2$- 2.02- 0.25	36-54- 68-82
13309/8	$1.48 \cdot 10^2$	$0.83 \cdot 10^2$- 1.78- 0.89	$0.44 \cdot 10^2$- 3.36- 0.84	$0.44 \cdot 10^2$- 3.36- 0.42	246- 256- 295-346
21128/4	$1.30 \cdot 10^2$	$0.53 \cdot 10^2$- 2.45- 1.23	$0.35 \cdot 10^2$- 3.71- 0.92	$0.34 \cdot 10^2$- 3.71- 0.46	204- 242- 301-371
24566/1	5.16	3.40- 1.52- 0.76	2.67- 2.31- 0.58	2.96- 1.74- 0.22	16-20- 25-29
40337/2	$2.51 \cdot 10^2$	$2.60 \cdot 10^2$- 0.96-0	$1.41 \cdot 10^2$- 1.57- 0.39	$0.79 \cdot 10^2$- 3.17- 0.40	164- 184- 218-272

A. Consideration on the parallelization

In this subsection, we describe the CPU simulation times obtained from the parallelization of the execution done on the multiple subintervals, using respectively 2, 4 and 8 cores, compared to the sequential one.

In Table 1, it can be observed that the speedup factor (and then the efficiency, too) in the case of two parallel processes is significant for almost all the data sets, but decreases as the number of involved parallel processes rises; thus, it seems the strong scalability of the algorithm is not satisfied, i.e., when increasing the number of available parallel processors, the efficiency of the parallelization being close to 1. The slowdown mostly characterized the cases with four and eight parallel processes. The cause was not the (unavoidable) sequential part of the algorithm (since each subinterval works independently of the others, the sequential part mainly characterizes the final re-orthogonalization in Algorithm 1), but an unbalanced workload issue and the way the data are made available to each parallel workers before starting the computation on them.

More in detail, using a shared-memory multi-core platform, when calling for, say, two (physical) workers core0 and core1 for the parallelization ($n_{proc} = 2$), then having two subintervals, the memory demand increases (each core needs to retrieve data to/from the hierarchical memories), then there is a data-bus contention: the data from the main memory pass through the bus and core0 (or core1) receives them, and thus starts the computation. After core0 (or core1) receives the data, the other worker can then receive the same data, and starts its processing. The waiting time for the second processors to receive the large size data can slowdown the overall parallel execution. And the higher the number of parallel workers competing for the data-bus is, the more the time is wasted in the waiting process. Mostly, during the computation of a parallel task, if the amount of arithmetic operations cannot be entirely performed in one pass (i.e., when the cache available for each core cannot accommodate all the needed data), then the memory demands can be more expensive. However, we experienced this problem mostly when analyzing dense matrices, for which the data movement was more dramatic, as the size of the original problem increases.

Regarding the simulations with eight parallel processes, efficiency-diminishing was the lack of physical computational resources, namely the cores. Indeed, we ran simulations with eight cores thanks to the HyperThreading(R) technology, which our computer is equipped with. It allows half of the cores to only exist in a virtual way (there are eight logical cores, but just four are physical); thus, there are not sufficient physical hardware resources on our computer and the memory bandwidth is insufficient to provide all required data on time.

Even though we experienced this loss of efficiency, there are remedies. To limit the data-bus contention, one can use distributed-memory local desktop, where each core has its own main memory, and thus, a private bus which links together these two components. Of course, the communication between processes is more sophisticated, but for this embarrassingly parallel problem, which does not need inter-processes exchange of data, it may be suitable.

Using such a distributed architecture, we can previously send just once the data describing the original model (1), and the related portion of frequency test-points (the subinterval). After the desired tolerance is satisfied in each subinterval,

each core needs only to send the computed projection-matrix to the client, which gathers these pieces of information and performs the last orthogonalization. One can also use clusters and network workstation, which nowadays are quite available to access to.

The last data set, instead, shows a zero value for the speedup with two processes, meaning the sequential version was at least as fast as the parallel one. This was due to an unbalanced workload issue. In Figs. 6 and 7, we can see how the retained expansion points are located along the angular frequency axis (horizontal axis). From the sequential algorithm (leftmost picture), most of the points were located on the left-half of the entire frequency range, and in those points a high number of moments were matched.

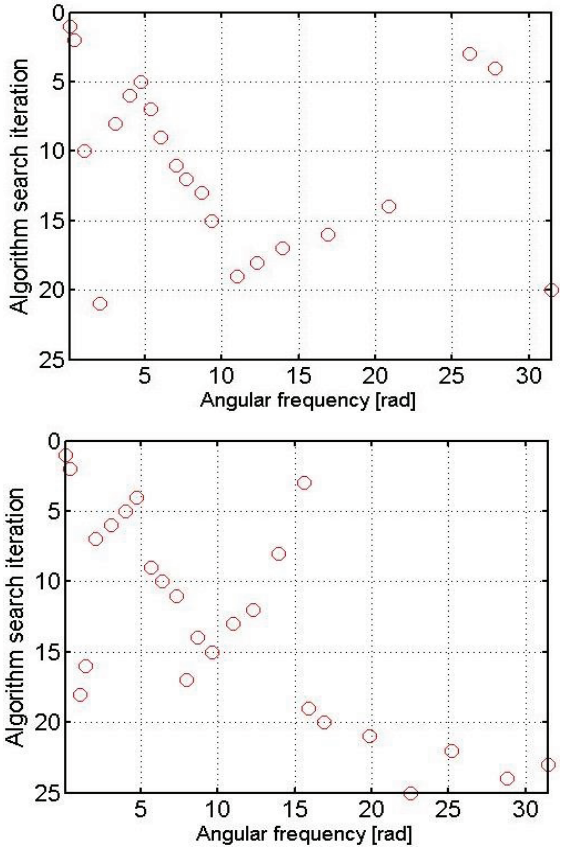

Fig. 6. Retained expansion points by the sequential algorithm (top) and by the parallel one with 2 processors (bottom), respectively, for the model with dimension $n = 40337$.

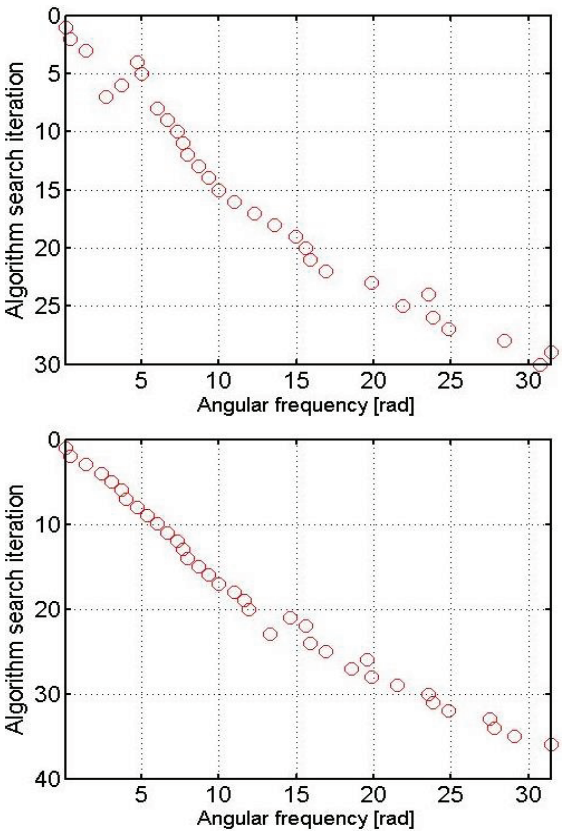

Fig. 7. Retained expansion points by the parallel algorithm with 4 processors (top) and with 8 (bottom), respectively, for the model with dimension $n = 40337$.

Then, when we divide the range into two subintervals, operating on them in parallel (second plot from left in Figs. 6 and 7), the processor responsible for the left subinterval had the biggest workload, in terms of the number of retained expansion points and that of matched moments for each point, such that the other processor, which ended before its execution, remained in the idle state until the operations on the other subinterval stopped. Thus, the slowdown was also caused by the slowest processor execution (with the biggest workload).

Indeed, the retained expansion points on the leftmost subinterval was characterized by the highest number of matched moments (computed by PRIMA), such that the processors working on the other subintervals had to wait until the slowest execution was ended, which constituted an upper

bound for the speedup. However, as the number of parallel processor increases (second picture from right and the rightmost one), it seems that the final retained points become distributed on the entire range in a more "balanced" way, as the workload of each processor, which determines a better time performance. With four parallel processes, the biggest waiting-time, characterizing the processor with the biggest workload which is also the slowest one, becomes smaller than that obtained from two processors, due to a decreasing of the workload for each core (fewer test-points to analyze), resulting in a greater speedup and efficiency factors (see the fourth last, third last and last row of Table 1), and most important in a significant reduction of the simulation time. With such a parallel method, it is difficult to statically balance the workload to each processor, since we have initially assumed we do not know how the dynamics of the interconnections evolve in the frequency domain, then where the expansions with PRIMA will be executed. Concluding, we recall that as the number of workers increases (thus, the number of independent subintervals), the redundancies, the number of retained expansion points, and thus, the final order of reduction increase, even with a greater speedup of the execution; but the obtained ROM may be a bit more expensive to be simulated by a further analysis. As previously said, there is a compromise between the CPU generation time of the ROM and its order of reduction. However, when the data set involved in the operations has a very-large size, the work-load increases, then working with parallel processes provides benefits in time performance.

Besides, when running the algorithm in the sequential mode, some operations (e.g., the backslash operator in solving a linear system of equations) exploit the implicit parallelism which the common multi-threaded computers are equipped with; instead, when calling the pool of parallel processes with MATLAB, with an explicit parallelism, each of them run in single-thread mode, giving rise to another factor which slightly limited the execution time of the parallel algorithm. But it is the case just for the factorization of large, sparse matrices with small dense sub-matrices, which takes advantage of the multi-threaded BLAS and LAPACK routines, e.g., with the multi-frontal method, originally developed by Davis [21]. This is the reason why we decided to dedicate our attention to sparse datasets, which BLAS is not optimized for. In fact, we also tested our parallel algorithm for dense models, and the time for the decomposition almost doubled in all the cases because of the single-thread mode. Again, this single-thread limitation can be avoided working with a parallel computing hardware/software environment, which supports a hybrid distributed/shared-memory architecture. Thus, very-large sparse matrices can benefit from this explicit and implicit parallelism, as well as one can use this method for full matrices too.

Another viable option is represented by Graphics Process Units (GPUs), but unfortunately MATLAB does not allow to work on it with sparse datasets. Besides, the use of a GPU seems to be not useful in this work, since it is characterized by having hundreds of dedicated processing units, which translates into hundreds of frequency subintervals. Then, as said before, this would imply more redundant, expansion points, resulting in a useless big size of the reduced model. Of course, scalability is an important requisite to be satisfied in a parallel algorithm, but it strictly depends on the application and in many cases it is difficult to achieve because of the problems one can easily meet, such as data communication and the diminishing of the workload for each processor, as the number of parallel processes increases.

It is also true that, since time performance was an equally important requisite in this work, together with the way the method searches for expansion points, we should had implemented the codes with a more suitable programming language, such as MPI or Pthread, which have more control on the parallel processes and allow different level of parallelization with distributed memories.

We would remark that, since there are no established methods to search for suitable expansion points in Krylov-based MOR in an adaptive way, the other strong point of this work was the full exploration of the frequency range, which is obviously time-consuming for very-large size datasets; thus, using a moderate number of parallel processors, one can achieve speedup with respect to a sequential search, as one can infer from Table 1, avoiding too many redundancies and a high order of reduction.

Lastly, from empirical results, we experienced that the selection of $n_{FS} = 96$ test-points, for the check of the error, was high enough to reach the desired accuracy on the whole frequency range.

Considering the sequential version of the algorithm, then with one interval, we noted a further tradeoff between the selection of the number of frequency test-points n_{FS} and the order of reduction *k* of the final ROM, keeping constant the desired accuracy *tol*.

When increasing n_{FS}, a higher number of test-points are available. It translates into a smaller distance between two consecutive points. Thus, higher-order moments may be no longer needed to be computed for a selected frequency point ω_i (exhibiting the maximum error in the current step of the algorithm), since both its neighbor $\omega_{i-1,i}$ and $\omega_{i,i+1}$ are close enough to it and their error values are likely less than *tol*, even with few moments matched when making the expansion in ω_i with PRIMA. Besides, it translates into an eventual smaller order of reduction *k*, since just the necessary moments are computed for each point, thanks to a more complete exploration of the entire frequency range of interest, without the need to recur in the computation of higher-order moments. However, we have seen that with the parallel execution, a greater accuracy (smaller error magnitudes) may be reached due to eventual redundancies, so that there may be no need to further increase n_{FS}.

On the other hand, decreasing n_{FS} below a certain threshold may not ensure that the desired accuracy will be reached in all the frequency range, since the adaptivity of the moments, computed at a frequency point ω_i, could fail in reproducing the evolution of the dynamics far away from ω_i. We experienced that for the case with $n_{FS} = 48$ selected (linearly distributed) frequency test-points, for the data set with $n = 40337$ the sequential algorithm, running on the entire interval, was not able to satisfy the accuracy in all the frequency range; i.e., for how we structured the search for the frequency points to be retained for the expansion with PRIMA, when choosing a small n_{FS}, clearly the dinstance between two consecutive test-points ω_{i-1} and ω_i increases, compared to the case $n_{FS} = 96$. Assuming ω_i error value among the others, and considering just the left subinterval $[\omega_{i-1}\ \omega_i]$, if we increase the order of moments until the error in the mid-point $\omega_{i-1,i}$ is less than the tolerance, the desired accuracy is not ensured to be reached in the whole subinterval $[\omega_{i-1,i}\ \omega_i]$ (e.g., in the case of presence of module peaks in that range), as stated in the motivation of the selection of a "relatively" high number of n_{FS}. But as said before, as we increase the processors and then the number of independent subintervals, redundancies occurred and the accuracy increased, satisfying the tolerance. From all our simulations, $n_{FS} = 96$ was always high enough to reach the desired approximation.

B. On the usefulness of multiple expansion points

In this section, we want to show that the higher the number of involved expansion points is, the higher the ensured accuracy in a wide range is. We recall that, the task of reducing a dynamical model while matching a number of moments (and/or the Markov parameters) about a point s_0 can be directly interpreted from a system theoretical point of view and employed to describe the similarity between the original and reduced models based on the following facts [16]:

- With s_0, the reduced and original model have the same DC gain, and steady state accuracy is achieved.
- Small values of s_0 result in a reduced model with a good approximation of the slow dynamics.
- Large values of s_0 (and/or matching the Markov parameters) result in a reduced model approximating the system frequency response at high frequencies.
- When matching some of the moments about different frequency points, a better approximation on a wider frequency band or on a specific frequency band of interest can be achieved.

Besides, choosing a purely imaginary expansion point leads to very good local approximation and to a very slow convergence at all frequencies away from s_0. Even though these facts give an idea on the choice of the expansion points, no specific value of s_0 can be derived based on them [16].

Here, we show that, for a test data set, it is not possible to reach the desired accuracy in all the frequency range of interest, when making the expansion on a single frequency point and increasing the order of moments to match. We

executed PRIMA on a dense data set with dimension $n = 980$ and number of inputs $m = 8$, making the expansion in the middle point ($\omega_0 = \left(\omega_{stop} + \omega_{start}\right)/2$) of the frequency range, and increasing the number of moments until the frequency errors, computed in both the starting and ending frequency points (farthest points from ω_0), are smaller than the fixed tolerance $tol = 0.01$: even matching 123 moments on the mid point, obtaining a ROM of order $k = 984$, which is greater than the initial dimension, the accuracy on the lowest frequency point was still unacceptable (whereas, with our multipoint algorithm, we satisfied the tolerance with an order of reduction $k = 576$ in the whole range. The order of reduction was relatively high since the frequency response of the model is highly resonating). Figure 8 shows a zoom of the module and error spectra of the data sets (8-1) interconnection.

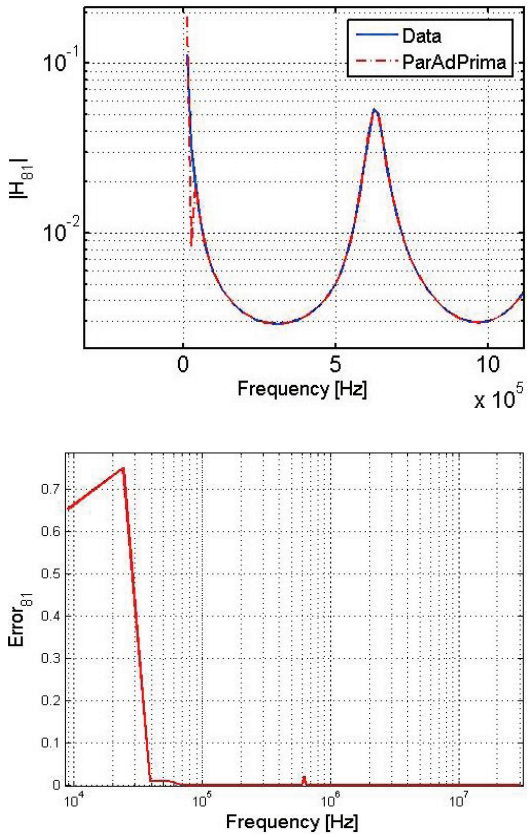

Fig. 8. Zoom of magnitude (top) and error (bottom) spectra of the transfer function $H_{8,1}$ of an interconnect model with dimension $n = 980$.

C. Accuracy evolution plots for a test data set

Lastly, in Figs. 9-22 we show how the accuracy of the ROM evolves according to each step of the algorithm, when it runs sequentially (avoiding to retain redundant expansion points), thus, only considering the entire frequency range without splitting it in subintervals, while a new expansion point (exhibiting the maximum error value) is adaptively retained and added to the previous ones and higher-order moments are eventually matched as well. This was done to provide a correlation between a, say, minimum number of retained expansion points and the location of the peaks of the module dynamics, related to the dominant poles [22] of the original system. We show the plots of the (1-1) interconnection of the SISO model with dimension $n = 6134$.

As one can see from Fig. 22, the retained expansion points ("Exp.Pts" in the legend) for this SISO model are those in proximity of most of the module peaks (e.g., resonances and anti-resonances characterizing the impedance or admittance of an RLC interconnection in the related Bode diagram), which can be related to the dominant poles of the dynamical system [22]. However, for MIMO systems this relationship is less explicit (see the module plot of Fig. 2), due to (eventual) different behaviors among all the interconnections of the transfer function, in the case an expansion point could be retained to reach a local accuracy for an interconnect, whereas it was useless for another one.

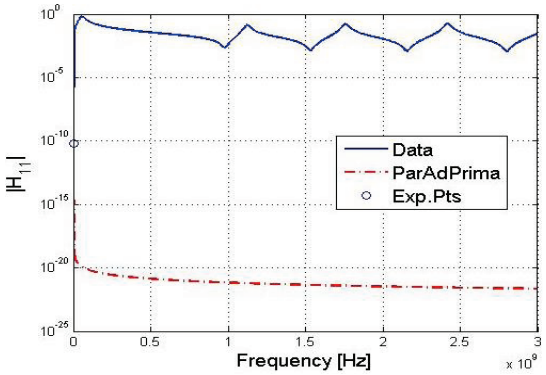

Fig. 9. Accuracy evolution as additional moments, computed in different retained expansion points (s_i), are added to the currently approximated transfer function for the model with dimension $n = 6134$: first moment matched at the expansion point $s_1 = j2\pi 10^{-2}$.

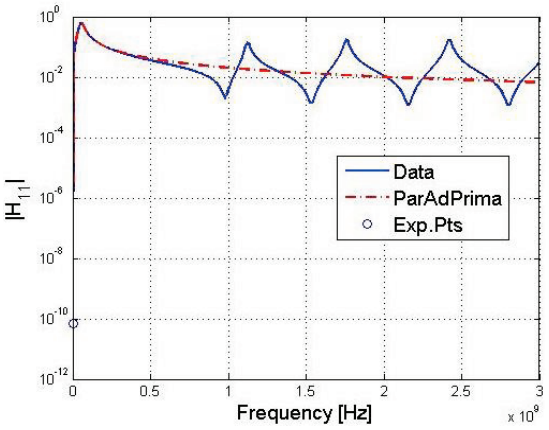

Fig. 10. Second moment matched on the expansion point $s_1 = j2\pi 10^{-2}$.

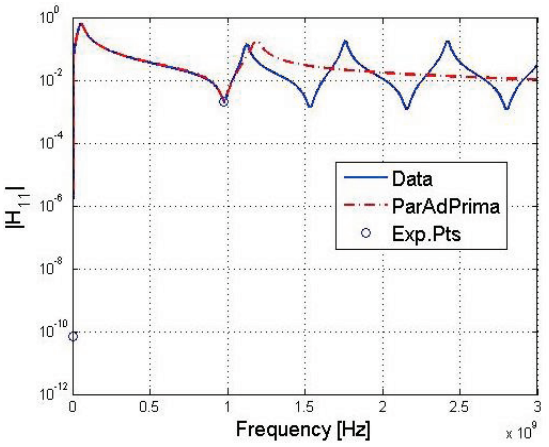

Fig. 11. First moment matched on the expansion point $s_2 = j2\pi 9.7910^{-2}$.

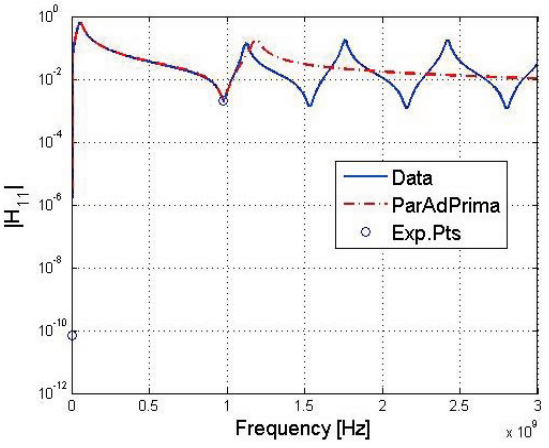

Fig. 12. Second moment matched on the expansion point $s_2 = j2\pi 9.7910^{-2}$.

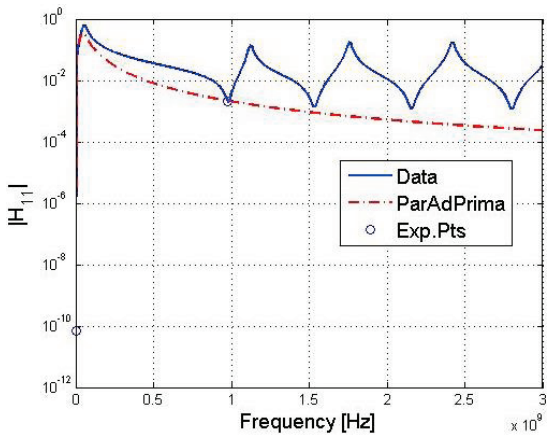

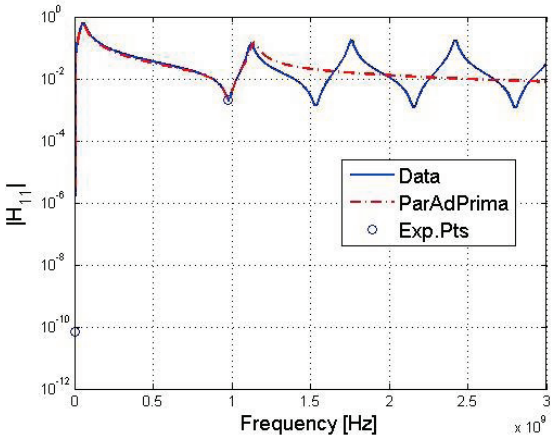

Fig. 13. Third moment matched on the expansion point $s_2 = j2\pi 9.7910^{-2}$.

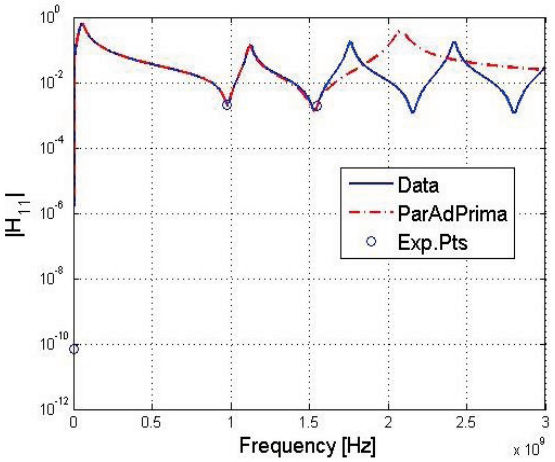

Fig. 14. First moment matched on the expansion point $s_3 = j2\pi 1.5510^{9}$.

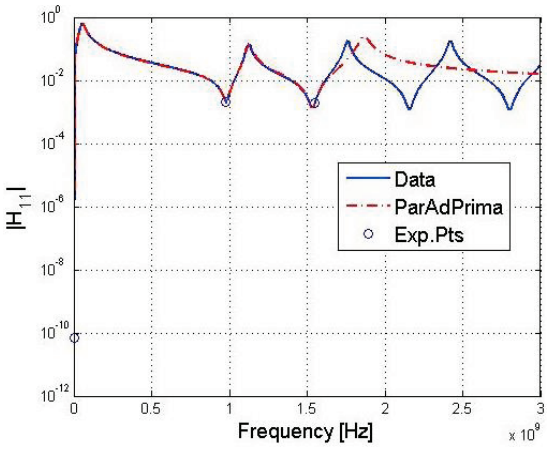

Fig. 15. Second moment matched on the expansion point $s_3 = j2\pi 1.5510^9$.

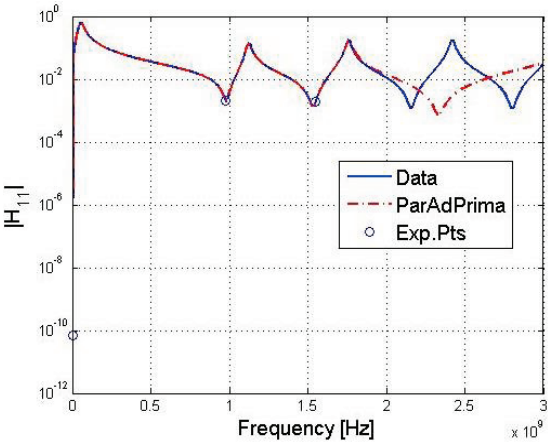

Fig. 16. Third moment matched on the expansion point $s_3 = j2\pi 1.5510^9$.

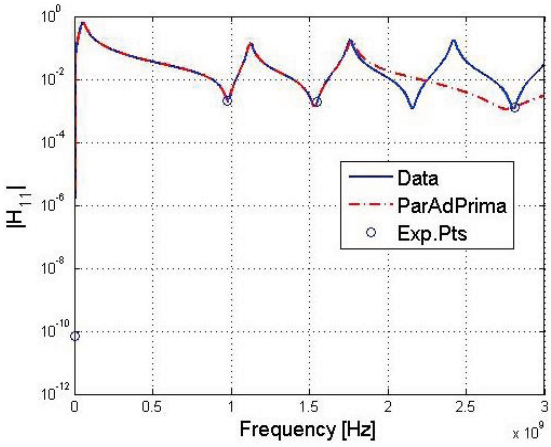

Fig. 17. First moment matched on the expansion point $s_4 = j2\pi 2.8110^9$.

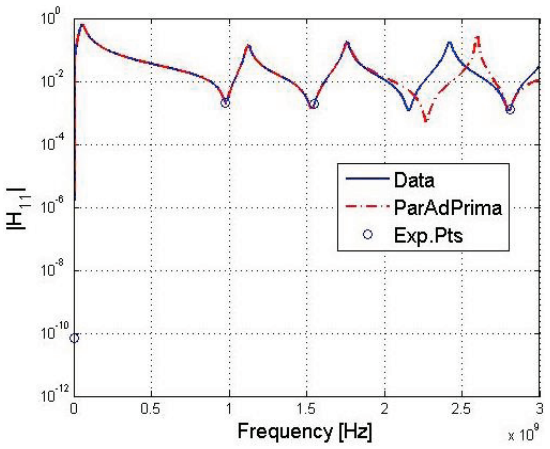

Fig. 18. Second moment matched on the expansion point $s_4 = j2\pi 2.8110^9$.

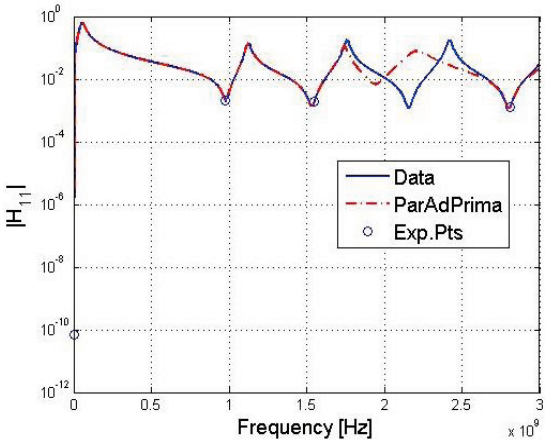

Fig. 19. Third moment matched on the expansion point $s_4 = j2\pi 2.8110^9$.

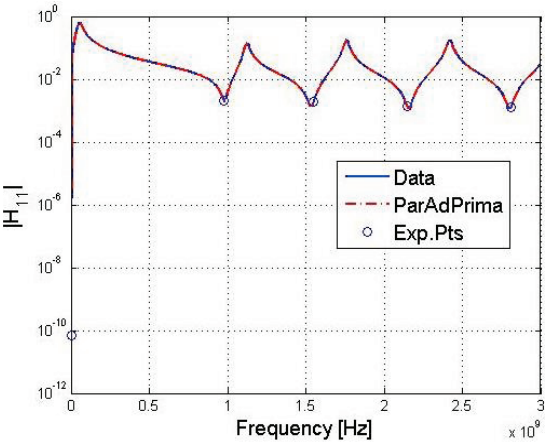

Fig. 20. First moment matched on the expansion point $s_5 = j2\pi 2.1510^9$.

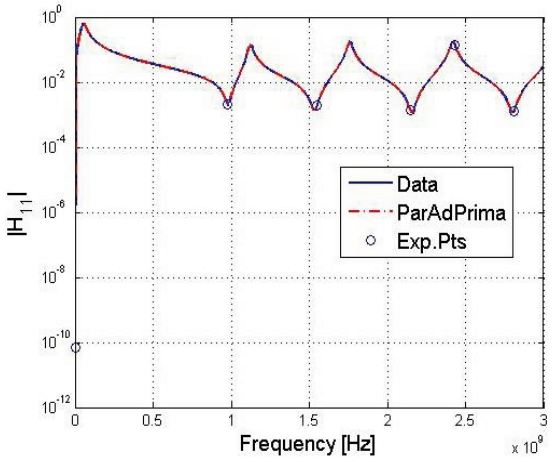

Fig. 21. First moment matched on the expansion point $s_6 = j2\pi 2.4310^9$.

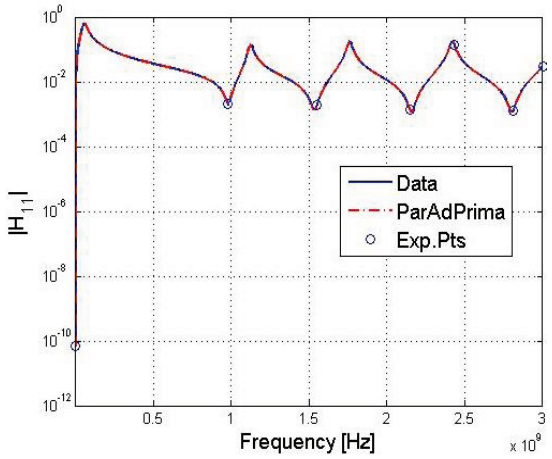

Fig. 22. First moment matched on the expansion point $s_7 = j2\pi 310^9$.

V. CONCLUSION

In this paper, a parallel adaptive multi-point model order algorithm is proposed, based on a full exploration of the frequency range of interest, trying to avoid heuristic searching methods for the expansion points, matching the most important moments of the original model transfer function in order to accurately reproduce its dynamics, without explicitly computing its dominant poles, and reducing the generation time of the ROM by exploiting the architectures of modern multi-core processors. The proposed method is able to achieve a very good approximation of the original transfer function, selecting as expansion points the frequencies in correspondence to which the error, between the response of the original model and that of the ROM, is larger than the desired tolerance, and increasing the number of moments to be matched for each point when necessary.

The numerical experiments have demonstrated that the speedup can be limited by the bus contention in the data transfer between the client and each parallel processor, in a shared-memory environment, but this issue can be handled by using distributed-memory architectures. The unbalanced loads, delegated to each processor, also may cause the performance degradation, but this can be alleviated by increasing the number of processors.

As shown, this method exhibits a slight compromise between the requirements of the ROM's generation time and its order of reduction, i.e., ROM evaluation can be obtained very quickly by slightly increasing the order of the ROM retaining redundant expansion points. However, the time performance will increase, mainly for very large size models.

In the next future, the application of the algorithm to originally-dense data sets like those obtained using integral-equation based methods (e.g., Method of Moments (MoM) or Partial Element Equivalent Circuit (PEEC) method) will be investigated. It will be presented in forthcoming reports.

ACKNOWLEDGMENT

We want to thank some persons for their tips, technical support and exchanged ideas, who contributed to this work. Especially, we are grateful to Lihong Feng, Jens Saak, Martin Köhler and Daniele Romano.

REFERENCES

[1] F. Ferranti, M. Nakhla, G. Antonini, T. Dhaene, L. Knockaert, and A. Ruehli, "Multipoint full-wave model order reduction for delayed PEEC models with large delays," *IEEE Transactions on Electromagnetic Compatibility*, 2011.

[2] R. F. Harrington, "Field computation by moment methods," *Malabar: Krieger*, 1982.

[3] A. E. Ruehli, "Equivalent circuit models for three dimensional multiconductor systems," *IEEE Transactions on Microwave Theory and Techniques*, vol. MTT-22, no. 3, pp. 216-221, March 1974.

[4] W. Schilders, "Introduction to model order reduction," *In Model Order Reduction: Theory, Research Aspects and Applications*, pp. 3-32, 2008.

[5] "The model order reduction wiki," *http://morwiki.mpi-magdeburg.mpg.de/morwiki/index.php/Main Page*, 2013.

[6] L. Feng, J. G. Korvink, and P. Benner, "A fully adaptive scheme for model order reduction based on moment-matching," *Max Planck Institute Magdeburg Preprint MPIMD/12-14*, September 2012, available from http://www.mpi-magdeburg.mpg.de/preprints/.

[7] E. Chiprout and M. Nakhla, "Analysis of interconnect networks using complex frequency hopping (CFH)," *IEEE Transactions on Computer-Aided Design of Integrated Circuits and Systems*, vol. 14, no. 2, pp. 186-200, 1995.

[8] L. Pillage and R. Rohrer, "Asymptotic waveform evaluation for timing analysis," *IEEE Transactions on Computer-Aided Design of Integrated Circuits and Systems*, vol. 9, no. 4, pp. 352-366, 1990.

[9] A. Odabasioglu, M. Celik, and L. T. Pileggi, "PRIMA: passive reduced-order interconnect macromodeling algorithm," *IEEE Transactions on Computer-Aided Design*, vol. 17, no. 8, pp. 645-654, August 1998.

[10] C. Ho, A. Ruehli, and P. Brennan, "The modified nodal approach to network analysis," *IEEE Transactions on Circuits and Systems*, vol. 22, no. 6, pp. 504-509, June 1975.

[11] G. Barbella, F. Perotti, and V. Simoncini, "Block krylov subspace methods for the computation of structural response to turbulent wind," *Computer Methods in Applied Mechanics and Engineering*, vol. 200, no. 23-24, pp. 2067-2082, 2011.

[12] M. Kamon, N. Marques, L. Silveira, and J. White, "Automatic generation of accurate circuit models of 3-D interconnect," *IEEE Transactions on Comp. Packag. Manufact. Technol. B*, vol. 21, no. 3, pp. 225-240, 1998.

[13] R. Freund, "Recent advances in structure-preserving model order reduction," *In Simulation and Verification of Electronic and Biological Systems*, P. Li, L. M. Silveira, and P. Feldmann, Eds., *Springer Netherlands*, pp. 43-70, 2011.

[14] H. J. Lee, C. C. Chu, and W. S. Feng, "An adaptive-order rational arnoldi method for model-order reductions of linear time-invariant systems," *Linear Algebra and its Applications*, vol. 415, no. 2-3, pp. 235-261, 2006.

[15] M. Creeland and W. L. Goffe, "Multi-core cpus, clusters, and grid computing: a tutorial," *Computational Economics*, vol. 32, no. 4, pp. 353-382, 2008.

[16] R. Eid, H. Panzer, and B. Lohmann, "How to choose a single expansion point in krylov-based model reduction?," *Lehrstuhl f¨ur Regelungstechnik*, TU M¨*unchen*, Tech. Rep., November 2009.

[17] D. P. Bertsekas and J. N. Tsitsiklis, "Parallel and distributed computation: numerical methods," Upper Saddle River, NJ, *USA: Prentice-Hall, Inc*., 1989.

[18] I. A. Lazar, G. Ciuprina, and D. Ioan, "Effective extraction of accurate reduced order models for hf-ics using multi-cpu architectures," *Inverse Problems in Science and Engineering*, vol. 20, no. 1, pp. 15-27, 2012.

[19] "SLICOT: benchmark examples for model order reduction," http://www.slicot.org/index.php?site=benchmodred.

[20] "Homepage of Joost Rommes," https://sites.google.com/site/rommes/software.

[21] T. A. Davis, "Algorithm 832: umfpack v4.3-an unsymmetric pattern multifrontal method," *ACM Trans. Math. Softw*., 2004.

[22] J. Rommes and N. Martins, "Efficient computation of transfer function dominant poles using subspace acceleration," *IEEE Transactions on Power Systems*, vol. 21, no. 3, pp. 1218-1226, 2006.

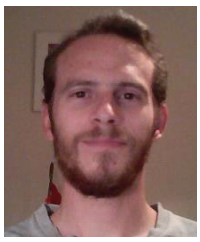

Giovanni De Luca received his M.Sc. degree in Computer Science and Control System Theory Engineering in 2012 from the Univesity of L'Aquila. He worked in the Dept. of Geniuses of Automated Production, Ecole de Technologie Superieure (ETS) in Montréal (CA), winning the scholarship for the preparation of the final thesis abroad 2010/2011. In 2013, he was a Visiting Researcher in the Max Planck Institute in Magdeburg (GE), for a period of seven months, working on Model Order Reduction techniques and parallelization theoretical aspects. Since March 2014, he is a Ph.D. candidate at the Technical University of Eindhoven (NL), with the goal of accelerating the transient simulation of complex circuits.

Giulio Antonini received his Laurea degree (summa cum laude) in Electrical Engineering in 1994 from the University of L'Aquila and the Ph.D. degree in Electrical Engineering in 1998 from the University of Rome "La Sapienza." Since 1998, he has been with the *UAq EMC Laboratory*, Dept. of Industrial Engineering and Computer Science of the University of L'Aquila, where he is currently Full Professor. His research interests focus on EMC analysis, numerical modeling and in the field of signal integrity for high-speed digital

systems. He has authored or co-authored more than 250 technical papers and 3 book chapters. Furthermore, he has given keynote lectures and chaired several special session at international conferences. He holds one European Patent.

Peter Benner is one of the Directors at the Max Planck Institute for Dynamics of Complex Technical Systems in Magdeburg and Head of the Computational Methods in System and Control group there. His research activities include numerical linear algebra, model reduction and systems approximation, parallel algorithm, linear-quadratic optimization, robust stabilization of linear and non-linear systems, and control of instationary PDEs.

A Spherical Harmonic Expansion Method for Accelerating the Interface Between the NEC-REF and NEC-BSC Codes

J. T. Quimby [1], R. Thompson [1], R. J. Marhefka [2], and J. D. Rockway [1]

[1] SPAWAR System Center Pacific
System of Systems and Platform Design Division, San Diego, CA, 92152, USA

[2] The Ohio State University
ElectroScience Laboratory, Columbus, OH, 43212, USA

Abstract ─ A spherical harmonic expansion is proposed to provide a more efficient interface between a reflector antenna simulation code and an Uniform Geometrical Theory of Diffraction (UTD) ray tracing code. The principal bottleneck is a large number of dipole sources. As a consequence, a large number of dipole sources lead to a large number of ray traces, which increases the computational times in the UTD code. We propose to use a spherical harmonic expansion of the reflector fields as an efficient interface. This method saves significant computational times in the UTD code provided that the number of dipole sources per cell is large.

Index Terms ─ Dipoles, spherical harmonics, Uniform Theory of Diffraction.

I. INTRODUCTION

The issue of co-site electromagnetic interference must be carefully handled when integrating SAT-COM reflector antennas into Navy topsides. The analysis of optimizing antenna placement within a topside environment is performed here with a hybrid analysis between The Ohio State University Reflector Antenna (NEC-REF) [1] and the Numerical Electromagnetic Code-Basic Scattering Code (NEC-BSC) [2]. NEC-REF simulates the performance of the reflector antenna. Its solution results in an equivalent current representation of the reflector antenna. These equivalent currents are modeled as dipoles in NEC-BSC. The amplitude and phase of the dipoles are computed to produce the reflector antenna fields in NEC-BSC in the forward direction. NEC-BSC then computes the field as the superposition from the total fields of each of the NEC-REF dipoles based on the topside environment. For an accurate backscattering, a metal reflector plate must be placed in the NEC-BSC computational environment. Figure 1 depicts a general scenario of interest for the SAT-COM reflector antenna with rays being shown in the topside environment.

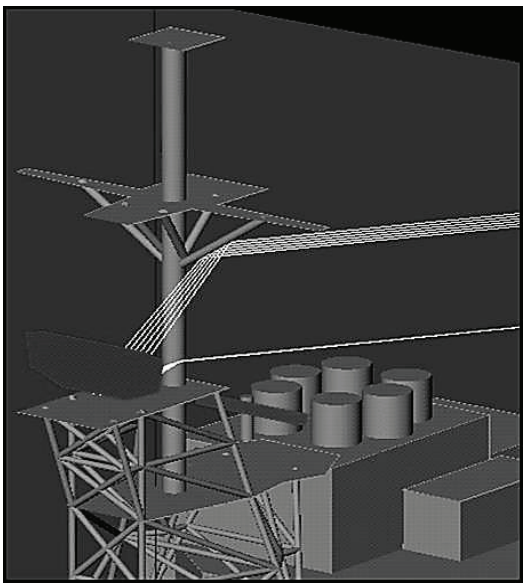

Fig. 1. Rays being depicted from an SAT-COM reflector antenna.

Due to recent antenna requirements, computational times for a NEC-REF/NEC-BSC

Submitted On: June 10, 2014
Accepted On: September 28, 2014

analysis can be on the order of several days to run a single design iteration. Typically, a designer will want to run significantly more iterations to obtain the best result. Therefore, this increase in run times can become laborious, limiting the quality of design. For example, the analysis of the SAT-COM reflector antenna onboard a ship (Fig. 1) required several different designs scenarios. When an exact replica of the SAT-COM antenna was modeled in NEC-REF, the large number of dipoles model froze the NEC-BSC code. The model required many dipole sources, which exceeded the memory allocation. The model was eventually analyzed but only after a reduced model was used in a reduced NEC-BSC computational environment (e.g., ground and only part of the superstructure and number of dipoles). The analysis still required several days.

The principal bottleneck in the current analysis is the NEC-REF equivalent current solution, which results in a large number of dipole sources. Each dipole is a ray origin in the UTD code from which multiple rays must be traced. A more efficient method must be utilized to reduce or group the number of dipoles/ray origins while still maintaining accuracy in the analysis. The more ray centers, the longer the computational times, but the proper number still needs to be maintained to provide an accurate pattern and avoid grating lobes by having the centers too far apart.

The Spherical Harmonic Interface Procedure (SHIP) [3,4] transfers spherical harmonic coefficients computed from NEC-REF dipole model to the UTD, NEC-BSC. SHIP creates a spherical harmonic expansion of the NEC-REF dipole model. By incorporating a multi-cell SHIP approach, the spherical harmonic expansion of the NEC-REF dipole model can also handle sources within the near field of the topside environment.

The paper is organized as follows. Section II discusses the overall methodology of the SHIP procedure. Details are discussed for expanding the dipole model from NEC-REF into multiple cell origins and spherical harmonic expansions. Finally, section III provides numerical results using the SHIP interface to NEC-BSC to analyze a SAT-COM antenna installed on two Navy ships. The computational times and the accuracy of the radiation patterns computed by the environmental computational code will be used to validate and show the improved efficiency for design.

II. SHIP METHODOLOGY

An efficient interface between NEC-REF and NEC-BSC is possible using the Spherical Harmonic Interface Procedure (SHIP). This method expands the free space fields generated by the reflector antenna using a spherical harmonic expansion [5,6]. The spherical harmonics coefficients are then used as an interface into the UTD code, NEC-BSC, rather than the NEC-REF dipoles model. The benefits of this procedure are the spherical harmonic expansion of the antenna fields has a single origin, which is at the cell center based upon the antenna currents. NEC-BSC utilizes these cell origins to trace the UTD rays through the environment. Figure 2 depicts the ray tracing from a single cell with the origin at the center. An optimal solution is imperative to balance the number of cells and their location with the resulting computation time to achieve sufficient accuracy.

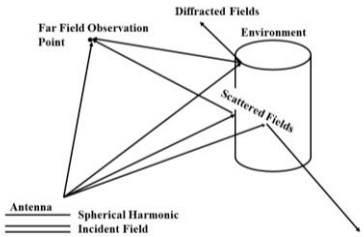

Fig. 2. UTD rays from a single cell.

SHIP decomposes the NEC-REF dipole model of the reflector antenna into a single or multiple cells. The multi-cell SHIP increases the computational time since NEC-BSC must trace rays from a number of cell origins. However, in the case of a complex environment, shadowing considerations can cause the resulting reduction in accuracy of the overall pattern, especially if grating lobes results due to large distances between origins. A greater number of ray traces will provide a higher level of accuracy when these ray origins are in the near zone of the geometry of the environment. This is especially true when the origins are placed near the

reflector plate of the SAT-COM antenna.

A. Spherical harmonic expansion

SHIP procedure begins with an initial cell of radius r_1 encompassing the entire dipole model of the SAT-COM reflector antenna. The initial cell is then segmented into smaller P cells of radius $r_P=(r_1/P^{1/3})$. The electromagnetic fields for a single cell are the sum of the spherical wave expansions of all the dipoles contained inside that cell. This expansion is stored in the spherical harmonic coefficients; thus, enabling NEC-BSC to compute the total electromagnetic fields of the dipoles from a cell. Using the spherical wave expansion, the electromagnetic fields of a given cell P is given by:

$$\begin{aligned} E_\theta^P &= -j\omega\left[A_\theta^P + \eta F_\varphi^P\right] \\ H_\varphi^P &= \frac{j\omega}{\eta}\left[A_\theta^P + \eta F_\varphi^P\right] \end{aligned}, \tag{1}$$

and

$$\begin{aligned} E_\varphi^P &= -j\omega\left[A_\varphi^P + \eta F_\theta^P\right] \\ H_\theta^P &= \frac{j\omega}{\eta}\left[A_\varphi^P - \eta F_\theta^P\right] \end{aligned}. \tag{2}$$

The magnetic vector potential in (1) and (2) are given by:

$$\begin{aligned} A^P = \frac{-j\mu}{2}\frac{e^{-jkr}}{r}\sum_{n=0}^{\infty}\sum_{m=0}^{n} & a_{nm}^P(\theta',\varphi')\mathrm{Y}_{nm}^e(\theta,\varphi) \\ & + b_{nm}^P(\theta',\varphi')\mathrm{Y}_{nm}^o(\theta,\varphi), \end{aligned} \tag{3}$$

where

$$\begin{aligned} \bar{a}_{nm} &= j^{n+1}\int_V \bar{J}_V(kr')\,j_n(kr')\,\mathrm{Y}_{nm}^e(\theta',\varphi')\,dV' \\ \bar{b}_{nm} &= j^{n+1}\int_V \bar{J}_V(kr')\,j_n(kr')\,\mathrm{Y}_{nm}^o(\theta',\varphi')\,dV' \end{aligned}, \tag{4}$$

are the even, a_{mn}, and odd, b_{mn}, spherical harmonic coefficients for the magnetic vector potential and Y^e_{nm} and Y^o_{nm} are the even and odd orthonormal spherical harmonics. The electric vector potential can be written similarly as:

$$\begin{aligned} F^P = \frac{-j\varepsilon}{2}\frac{e^{-jkr}}{r}\sum_{n=0}^{\infty}\sum_{m=0}^{n} & c_{nm}^P(\theta',\phi')\mathrm{Y}_{nm}^e(\theta,\phi) \\ & + d_{nm}^P(\theta',\phi')\mathrm{Y}_{nm}^o(\theta,\phi), \end{aligned} \tag{5}$$

with

$$\begin{aligned} \bar{c}_{nm} &= j^{n+1}\int_V \bar{M}_V(kr')\,j_n(kr')\,\mathrm{Y}_{nm}^e(\theta',\varphi')\,dV' \\ \bar{d}_{nm} &= j^{n+1}\int_V \bar{J}_V(kr')\,j_n(kr')\,\mathrm{Y}_{nm}^o(\theta',\varphi')\,dV' \end{aligned}, \tag{6}$$

as the even, c_{mn}, and odd, d_{mn}, spherical harmonic coefficients for the electric vector potential.

B. Computation of the spherical harmonic coefficients

The multi-cell and single cell SHIP uses the dipoles model of the SAT-COM reflector antennas to compute the a_{mn}, b_{mn}, c_{mn} and d_{mn} coefficients for each cell P. The current description of the dipoles in the case of the magnetic vector current distribution, $\bar{J}_v$, is:

$$\bar{J}_v = \begin{cases} \bar{u}I_o e^{iI_{ph}} & -l/2 \le l' \le -l/2 \\ 0 & l' < -l/2 \\ 0 & l' > l/2 \end{cases}, \tag{7}$$

where $\bar{u}$ is the directional unit vector for an infinitesimal dipole of length l, I_o is the amplitude of the current distribution, and I_{ph} is the phase of the current distribution. The value of $\boldsymbol{u}$ is determined from the NEC-REF code. For a dipole of constant current distribution, the even spherical harmonic coefficient becomes:

$$\bar{a}_{nm}^A = j^{n+1}\bar{u}I_o e^{iI_{ph}}\int_l j_n(kr')\mathrm{Y}_{nm}^e(\theta',\phi')dl'. \tag{8}$$

A similar analysis can be used for the electric vector current distribution.

C. Computing of environmental fields given the spherical harmonic representation

The final step in the SHIP is the use of the spherical harmonic coefficients as an input into the UTD-based such as NEC-BSC. In general, the spherical harmonic coefficients contain all phase information. This phase information includes the phase of the dipole model itself as well as the phase due to an offset from the dipole model's origin. Transferring this information to NEC-BSC should be done in such a manner that the ray origins of the spherical harmonic representation for the individual cells be properly located close to the geometric center or the center weighted by dipole model amplitudes. NEC-BSC can then translate the antenna from its origin to the desired destination.

D. Truncation of spherical harmonic expansion and computational times

The truncation of the infinite series in Equation (3) and (5) must be handled properly to obtain reasonable accuracy for the

electromagnetic fields. The truncation limit [7,8,9], N_{max}, is:

$$N_{\max,1} = kr_1 + 3\ln(\pi + kr_1), \tag{9}$$

where r_1 is the maximum dimension of the cell enclosing the cell dipoles and the cell origin. As the electrical size of the antenna increases or the antenna is offset from the cell origin, $N_{max,1}$ increases as well as the number of spherical harmonic coefficients. The number of spherical harmonics coefficients is:

$$N_{H1} = N_{\max,1}^2 \approx (kr_1)^2 \quad if\ kr > 1. \tag{10}$$

The NEC-BSC computational time is dependent upon the number of harmonics, cells, and complexity of the ray traces. For either complex geometries or large number of cells, the ray tracing computational times will dominant the computational time of the spherical harmonic wave expansion. The computational times for a single cell is [3],

$$T_1 = CN_{H1}^{\beta} = C(kr_1)^{2\beta}, \tag{11}$$

where $\beta \approx 1.4$ and C is a constant dependent on the complexity of the ray trace and hardware.

For multi-cell SHIP, the number of harmonics in each of the P cells is given as:

$$\begin{aligned} N_{HP} = N_{\max,P}^2 = (kr_p)^2 &= \left(k\frac{r_1}{P^{1/3}}\right)^2 \\ &= \frac{N_{H1}}{P^{2/3}} \quad if\ krp >> 1. \end{aligned} \tag{12}$$

Since the UTD code must trace rays from each of the P origins, the total computational time for the multi-cell SHIP is:

$$\begin{aligned} T_P = P\left(CN_{HP}^{\beta}\right) &= PC\left(\frac{N_{H1}}{P^{2\alpha}}\right)^{\beta} \\ &= P^{1-2\alpha\beta}T_1 = F_P T_1, \end{aligned} \tag{13}$$

where

$$F_P = P^{1-2\alpha\beta} = P^{1-2(1/3)(1.45)} = P^{+0.033}, \tag{14}$$

is the factor to convert the single cell to the P cell computational time.

E. Multi-level cell approach for reflector antenna

The multi-cell SHIP approach uses an edge modification technique to handle correctly the reflector plate for the SAT-COM reflector antenna. The reflector plate and feed source is incorporated into the analysis by placing them as an environmental element in NEC-BSC. NEC-BSC must compute the reflector, diffraction, and scattering of the dipoles model and SHIP due to these elements. In the case of the reflector plate with the NEC-REF dipole model, this environmental element is placed very close to the dipole sources in NEC-BSC. The large number of resulting ray traces from this model provides the higher accuracy levels; avoiding a decrease of accuracy due to shadowing. In the case of the reflector plate with the SHIP model, a multi-level SHIP procedure was developed to maintain the desired accuracy and ensures the desired increase in performance.

The multi-level SHIP procedure uses an edge modification to maintain the desired accuracy due to the reflector plate. The approach uses two different cells grouping as seen in Fig. 3. The first cell grouping uses larger cell sizes to model the NEC-REF dipoles, which are located near the center of the reflector plate. The first group of cells maintains SHIP's computational enhancement. The second cell grouping uses smaller cell size to model the NEC-REF dipole, which are located near the edge of the reflector plate. The second cell grouping produces a large number of ray traces, which increases the accuracy in the side lobe regions. The first and second cell groupings maintain the overall accuracy in the broadside region.

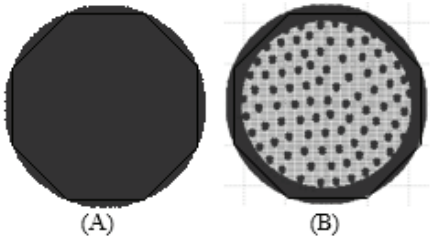

Fig. 3. (A) Infinitesimal dipole representation of a reflector dish currents, and (B) spherical harmonics representation of reflector dish currents.

III. NUMERICAL RESULTS

This section illustrates the SHIP procedure to model reflector antennas within Navy topsides. The SAT-COM reflector antenna connects the US Navy to NATO satellites. The antenna is modeled as a source feed in front of a

reflector. The NEC-REF dipole model of the SAT-COM reflector antenna is between 40,000-100,000 dipoles depending upon the desired level of accuracy. To get a realistic model of the reflector, a reflector plate must also be included near the dipoles in NEC-BSC. This reflector plate is modeled as a flat PEC plate in the NEC-BSC code. For the examples below, the SAT-COM reflector antenna will be integrated onto two examples of Navy topside environments, a generic ship and the LHA-1 amphibious assault craft. A comparison is made between the reduced computational time for the SHIP procedures versus the standard hybrid approach using NEC-REF and NEC-BSC. The UTD codes computational times will be analyzed based on a far zone pattern for all 360 angles.

The first example is the analysis of the SAT-COM reflector antenna on the generic ship. The NEC-BSC representation of the GENERIC SHIP with placement of the reflector antenna is shown in Fig. 4. The antenna is the small red plate near the front mast. In this example, the reflector PEC plate has been removed, so all NEC-REF or SHIP sources are in the far-field to NEC-BSC.

In Figs. 5 and 6, the far-field (magnitude and phase) results for SHIP accurately compares to the NEC-REF/NEC-BSC analysis approach. The results are for left-handed polarization. The SHIP analysis used 392 cells to accurately represent the same field behavior as NEC-REF using ~94,000 dipoles. The difference in computational times in NEC-BSC between SHIP and NEC-REF dipoles for the same accuracy is 15 minutes (P=392) versus 1,672 minutes (NEC-REF~94,000).

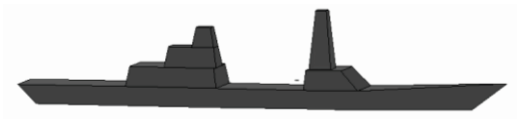

Fig. 4. NEC-BSC representation of a generic ship and location of SAT-COM reflector antenna.

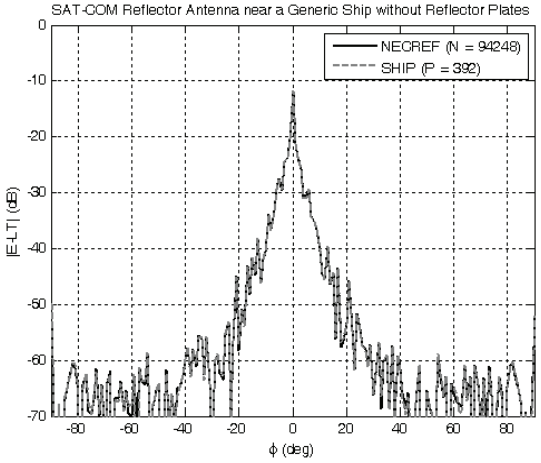

Fig. 5. |E-LT| (dB) of the SAT-COM reflector antenna near a generic ship without a reflector.

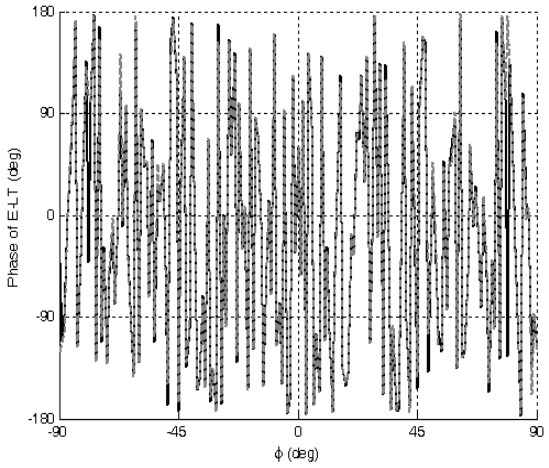

Fig. 6. Phase of E-LT (deg) of the SAT-COM reflector antenna near generic ship without reflector plates.

The second example models the SAT-COM reflector antenna near the Navy's LHA-1 amphibious assault ship. The reflector antenna of interest is shown in red in Fig. 7, surrounded by the rest of the topside environment simulated in NEC-BSC. Again, in this example, there is no reflector plate near the NEC-REF sources. All dipole sources are in the far-field to any NEC-BSC geometries.

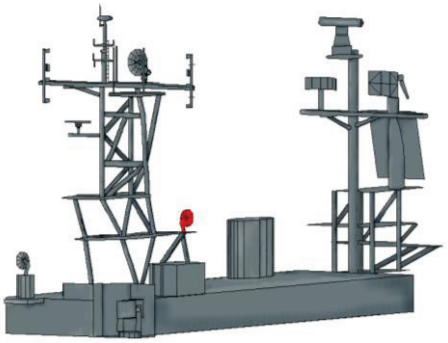

Fig. 7. NEC-BSC representation of the topside on the LHA-1 and location of the SAT-COM reflector antenna.

In Figs. 8 and 9, the far-field (magnitude and phase) has been computed using the NEC-REF/NEC-BSC analysis approach and SHIP. Again, the SHIP analysis required only 392 multiple cells to accurately represent the same field behavior as NEC-REF using ~94,248 dipoles. The difference in computational times in NEC-BSC between SHIP and NEC-REF dipoles for the similar accuracy is 2.8 hours (P=392) versus 415 hours (NEC-REF~94248).

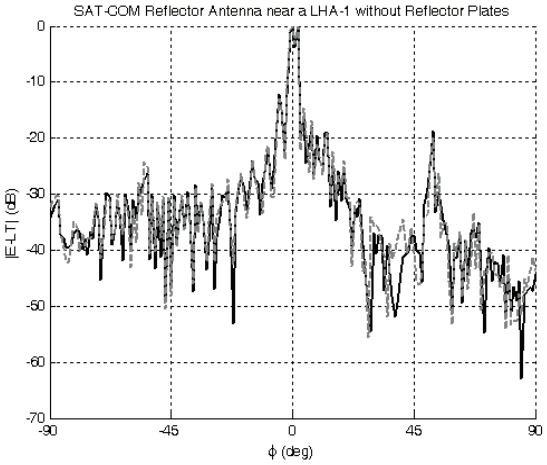

Fig. 8. |E-LT| (dB) of the SAT-COM reflector antenna near a LHA-1without reflector plates.

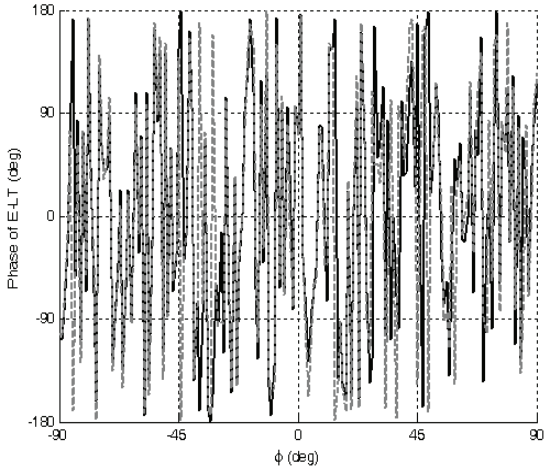

Fig. 9. Phase of E-LT (deg) of the reflector antenna near a LHA-1 without reflector plates.

In the last example, the reflector plates are used in the NEC-BSC model on a generic ship. Since the flat PEC plate is in the near field to the NEC-REF dipole model, the edge modification routine must be taken into account. This will result in a greater number of cells but with higher accuracy in the side lobes region. In Figs. 10 and 11, the far-field (magnitude and phase) results for SHIP accurately compares to the NEC-REF/NEC-BSC analysis approach, and are for left-handed polarization. The SHIP analysis used 392 dipoles to represent (~5%) the NEC-REF dipole model of ~94,000 dipoles. The multi-level SHIP analysis used 16,208 multiple cells to accurately represent (~4.2%) the same field behavior as NEC-REF model using ~94,000 dipoles. The increase in accuracy between the multi-level SHIP and SHIP is prevalent in the side lobe regions between -90º to -40º and 40º to 90º degrees. The accuracy of the multi-level SHIP is greater than SHIP in this region. At -40º to 40º degrees, SHIP and multi-level SHIP give similar accuracy with respect to NEC-REF dipole model. The difference in computational times between the SHIP and

NEC-REF dipoles model for their respective accuracy was 33 minutes (P=392), 447 minutes (*P*=16,208), versus 1,773 minutes (NEC-REF~94,000).

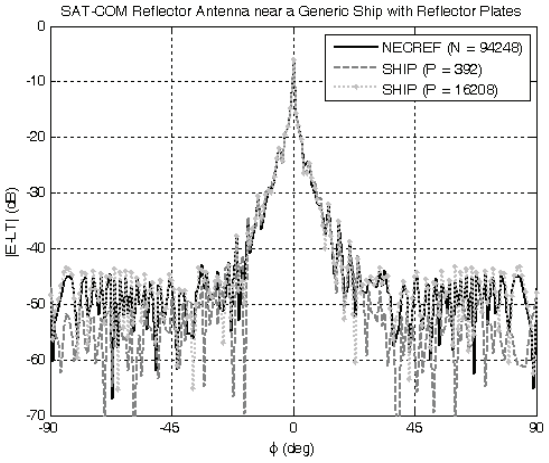

Fig. 10. |E-LT| (dB) for the SAT-COM reflector antenna (with plate) near a generic ship.

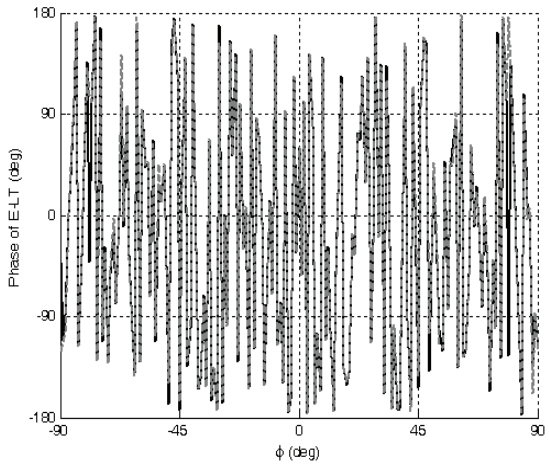

Fig. 11. Phase of E-LT (deg) for the reflector antenna with reflector plates near a generic ship.

IV. CONCLUSION

The traditional design of integrating SAT-COM reflector antenna into Navy topside environment begins with the use of a hybrid analysis between NEC-REF and the UTD code, NEC-BSC. Excessive computational times are often required by this analysis. Instead, a spherical wave expansion of the SAT-COM reflector antenna fields was used as an efficient interface between the NEC-REF and NEC-BSC. Table 1 summarized the results presented here. Computational times and number of unknowns between the hybrid analysis and the SHIP method are indicated. This method saves significant computational time in the UTD code provided that the number of dipoles per cubic wavelength is large.

Table 1: Summary of results

	NEC-REF (NF)	NEC-REF (time)	SHIP (cells)	SHIP (time)	Factor Decrease
Reflector antenna on generic ship w/o plate	94, 248	1,672 mins.	392	15 mins.	107 x
Reflector antenna on LHA-1 w/o plate	94, 248	415 hrs.	392	2.8 hrs.	166 x
Reflector antenna on generic ship w/plate	94, 248	1,773 mins.	16,208	447 mins.	3 x

REFERENCES

[1] T. H. Lee and R. C. Rudduck, "OSU reflector antenna code-version 3.0 NECREF version 3.0 user's manual," *The Ohio State University*, February 1994.

[2] R. Marhefka, "Numerical electromagnetic code-basic scattering code (NEC-BSC version 4.2) user's manual," *The Ohio State University*, June 2000.

[3] J. T. Rockway, "Electromagnetic field determination of antenna systems in complex structural environments by the spherical harmonic interface procedure," *Ph.D. dissertation, The Ohio State University*, June 2005.

[4] J. T. Rockway, E. H. Newman, and R. J. Marhefka, "The spherical harmonic interface procedure for MM and UTD codes," *Journal of Applied Computational Electromagnetics*, vol. 21, no. 2, pp. 105-110, July 2006.

[5] Y. Chen and T. Simpson, "Radiation pattern analysis of arbitrary wire antennas using spherical mode expansions with vector coefficients," *IEEE Trans. Ant. Prop*., vol. 39,

no. 12, pp. 1716-1721, December 1991.
[6] J. Stratton, "Electromagnetic theory," *McGraw-Hill Book Company*, New York 1941.
[7] W. Chew, J. Jin, E. Michielssen, and J. Song, "Fast and efficient algorithms in computational electromagnetics," *Artech House*, 2001.
[8] R. Coifman, V. Roklin, and S. Wandzura, "The fast multiple method for the wave equation: a pedestrian prescription," *IEEE Ant. And Propagat. Magazine*, vol. 35, no. 3, pp. 7-12, 1993.
[9] B. Dembart and E. Yup, "The accuracy of fast multipole method for maxwell's equation," *IEEE Computational Science & Engineering*, vol. 5, no. 3, pp. 48-56, July 1998.

Jeanne T. Quimby received her B.S.E.E degree from The University of California of San Diego in 1998 and her M.S. and Ph.D. degrees in Electrical and Computer Engineering from The Ohio State University in 2001 and 2004. Since 2006, she has been employed as a RF Engineer at SPAWAR System Center Pacific. She is the Developer of the Spherical Harmonic Interface Procedure (SHIP). Her research interests are analysis, design, fabrication and measurement of advanced antennas and the integration of these antennas on complex military platforms. She has published 5 journal papers with 3 patents.

Ronald B. Thompson received his B.S.E.E degree from San Diego State University in 1983. He is a Computer Scientist for Space and Naval Warfare Systems Center Pacific San Diego. He works with the Department of Defense High Performance Computers (DoDHPC) and Nvidia GPGPU for parallel programming. He maintains the parallel version of the Numerical Electromagnetics Code Basic Scattering Code on the DoDHPC for solving large scale models. He analyzes older serialized code to produce parallel code for the GPGPU and test the performance compare enhancements.

Ronald J. Marhefka received his B.S.E.E. degree from Ohio University, Athens, in 1969, and his M.Sc. and Ph.D. degrees in Electrical Engineering from The Ohio State University, Columbus, in 1971 and 1976, respectively. From 1969-2009, he has been with The Ohio State University ElectroScience Laboratory where he is currently a part-time Senior Research Scientist and Adjunct Professor. He retired in 2009.

John D. Rockway received his B.S. degree in Physics from The University of California at San Diego in 1995 and his Ph.D. degree in Electrical Engineering from The University of Washington in 2001. Since 2009, he has been employed as a RF Engineer at SPAWAR System Center Pacific. His research interests are electromagnetic propagation in complex environments and the analysis and design of antennas at low frequencies.

Resolution Analysis of a Polymethylmethacrylate Tapered Probe in Near-Field Terahertz Imaging

B. Zhu [1], G. He [1], J. Stiens [1,2], J. Van Erps [3], W. Ranson [1,2], C. De Tandt [1], H. Thienpont [3], and R. Vounckx [1]

[1] Department of Electronics and Informatics
Vrije Universiteit Brussel (VUB), Brussels, B-1050, Belgium
bzhu@etro.vub.ac.be, ghe@etro.vub.ac.be, jstiens@etro.vub.ac.be, wranson@etro.vub.ac.be, cdtandt@etro.vub.ac.be, rvounckx@etro.vub.ac.be

[2] SSET Department
IMEC, Kapeldreef 75, Leuven, B-3001, Belgium

[3] Department of Applied Physics and Photonics
VUB, Brussels, B-1050, Belgium
jurgen.van.erps@vub.ac.be, hthienpo@b-phot.org

Abstract ─ A Polymethylmethacrylate (PMMA) rectangular tapered probe with metal coating on the sides is analyzed as a near-field imaging probe at 100 GHz in Ansoft High Frequency Structure Simulator (HFSS). Normally, highly resistive silicon and sapphire, which are costly, are used as a near-field probe due to their low loss and high permittivity. PMMA near-field probe is usually used in Scanning Near-field Optical Microscopy (SNOM), which is made from PMMA optical fibers. We propose for the first time to use PMMA as a near-field probe in millimeter and Terahertz wave scanning near-field imaging applications. The geometrical optimization of the tapered probe is carried out on the basis of different coupling methods. The beam shape merging from the end of the tapered tip is analyzed. The operation efficiency of two-side tapered and four-side tapered probes has been compared in view of the fabrication technique. A knife edge is simulated in HFSS to define the lateral resolution. Longitudinal resolution is discussed through setting a stair step shaped sample. A high lateral resolution around the end of the probe size can be achieved and even higher longitudinal resolution. The impact of the tip-sample distance and the lateral resolution are clearly illustrated via simulations. Experiments are carried out using a two-side tapered probe provided with an aluminum coating. The resolution is defined by scanning a PMMA board which was half coated with aluminum.

Index Terms ─ Near-field, Polymethylmethacrylate tapered probe, Terahertz imaging.

I. INTRODUCTION

The history of the development of near-field optical microscopy shows that illumination techniques play an important role in the resolution improvement. An overview of sub-wavelength illumination and nano-metric shadowing [1] clearly illustrated the merits and demerits of lens-based microscopes, confocal imaging systems, and using a prism to create an evanescent field of radiation. In order to break the resolution limit, near-field scanning optical microscopy developed into aperture and aperture-less configurations. In the former, light is sent through an aperture that is much smaller than its wavelength and then the aperture or the sample are scanned relative to each other at a distance much smaller than a wavelength. The resolution of the aperture type near-field microscope always depends on the diameter of the aperture, and as such, the aperture fabrication technique is becoming the bottleneck for achieving the highest resolution. Much higher

Submitted On: October 30, 2013
Accepted On: September 28, 2014

resolutions are achieved by aperture-less type near-field imaging systems, which act as a scatterer converting the evanescent wave to propagation wave. In the millimeter and terahertz wave range, aperture type near-field imaging systems are always used in the lower frequency band. Coaxial probes, microstrip- and strip-lines, small circular and slit-like aperture in a conducting screen are the most commonly used probe-types in the microwave region [2-3]. A number of different aperture types such as a metal micro-slit probe [2-4], a metal-coated pyramidal silicon probe with a very small hole [5], and a tapered micro-strip gold line deposited on a ceramic alumina substrate [6] enabled a high resolution of the order of the dimension of the end of the probe. Even higher resolution (λ/2000) was obtained with an aperture-less probe such as a waveguide resonator coupled to a tapered metal probe [7], and the highest resolution (λ/3000) at 2.54 THz was achieved by using a single frequency source and a scattering tip [8]. Sharp metal tips acting like an antenna and strengthening the near-field signal below it, in combination with a lock-in technique applied in the near-field system, largely improve the resolution and the signal-to-noise ratio.

Although, the highest resolution was achieved by the aperture-less type solutions in near-field Terahertz wave microscopy, setting up an imaging system with a sharp metal needle which needs to keep the constant tip-sample distance, is not practicable for lowest frequency of the Terahertz waves for rough samples. Although, shear force is widely used in optical microscopy and at higher Terahertz wave frequency bands to keep the tip-sample distance constant in order to get nanometer resolution, but for micrometer resolution, it is not suitable.

In previous work [9-12], the tapered probe was designed in Teflon. Its coupling with a horn antenna through free space was combined with a tungsten needle close to the tapered probe to get a higher resolution. For a rectangular tapered probe, it is not material sensitive as we analyzed in [14]. The first use of PMMA optical fiber-made probes for SNOM has been reported in [13]. In this paper, we propose for the first time to use a rectangular tapered PMMA probe directly inserted into a standard rectangular metal waveguide to guide the Electromagnetic (EM) wave from the source onto the surface of the sample and record the reflection from it. Since PMMA is cheap, easy to process into a tapered probe and to apply the metal coating on it, we limited in this paper our resolution study to the impact of the probe's geometrical parameters. The optimization for a four-side and a two-side tapered probe is executed respectively in Section II with the emphasis on the fabrication tolerance. The resolution simulations are carried out in Section III, where we discuss the relationship between the tip-sample distance and the lateral resolution. The edge response is employed here to define the lateral resolution. The longitudinal resolution is defined by scanning a stair step shaped sample. The two-side tapered probes are fabricated and measured. Experimental results are shown in Section IV. The conclusions are drawn in Section V.

II. OPTIMIZATION OF THE FOCUSING TAPERED PROBE

A. Four-side tapered probe

There are four types of tapered probe for near-field imaging applications which can couple with standard rectangular waveguides. Figure 1 shows six probe types, we have analyzed in this paper, (a)-(d) are four-side tapered probes, according to different types of coating. These are respectively designated as FTTCN, FTTCW, FTFCN, and FTFCW, probes designed for different coupling modes. Figure 1 (e)-(f) are two-side tapered probes to discuss the influence of the fabrication technique. As illustrated in [14], two types of tapered probes were analyzed: one is a two-sided coated taper where only the narrow side of tapered parts are coated (FTTCN) [5], and the other one is a four-sided taper which has a metal coating on the full narrow sides (FTFCN) [15]. When an FTTCN type probe is inserted into a standard rectangular metal waveguide, the main mode TE10 changes to the dielectric waveguide mode and is gradually converted into a strip line mode where the electric field is confined between the two metallization pads. The FTFCN type probe directly converts the TE10 mode to a Quasi-TEM mode, which is the strip line mode. Due to the full metal coating on the narrow sides, the E-field direction is perpendicular to the narrow sides. Comparing these two kinds of probes, as illustrated by Fig. 1 (a) and (c), the FTFCN probe has a higher focusing intensity than the FTTCN probe. This narrow side coated probe can be inserted into a

standard rectangular waveguide, and when the probe is fixed just right in the end of the rectangular waveguide, the TE10 mode is still the main mode. The coating on the wide side can confine the E-field into a micro-strip line mode. Figure 2 shows a schematic picture of the tapered probe. The rectangular part has dimensions of $a \times b = 2 \times 1$ mm^2, which is convenient to couple with a standard rectangular metal waveguide WR-10 (2.54×1.27 mm^2) in the W-band (75 GHz - 110 GHz).

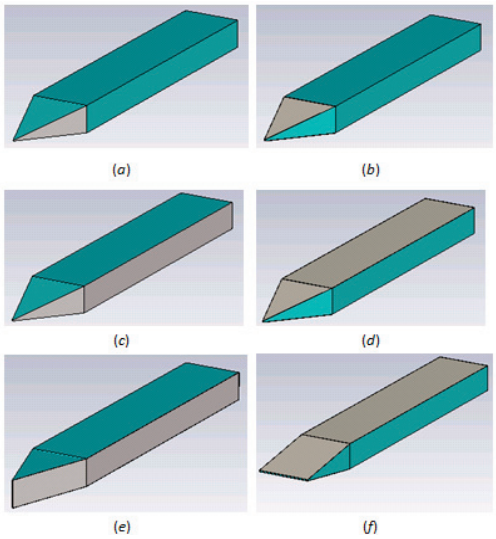

Fig. 1. Six types of tapered probes with a coating applied on different sides: (a) Four-side Tapered Two-side Coated on the Narrow tapered sides (FTTCN), (b) Four-side Tapered Two-side Coated on the Wide tapered sides (FTTCW), (c) Four-side Tapered Four-side Coated on the Narrow sides (FTFCN), (d) Four-side Tapered Four-side Coated on the Wide sides (FTFCW), (e) Two-side Tapered Four-side Coated on the Narrow sides (TTFCN), and (f) Two-side Tapered Four-side Coated on the Wide sides (TTFCW); the gray color is the metal coating, and the green color is the PMMA probe. The coating has been applied on the opposite side as well (but cannot be seen from this perspective view).

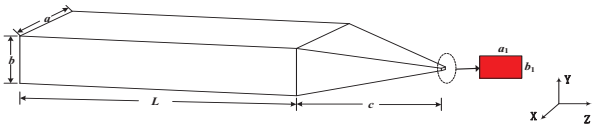

Fig. 2. A schematic picture illustrating the geometric dimensions.

The source which is used to excite the near-field probe is a TE10 mode, so the coating is applied on the wide side of the probe to confine the E-field. We choose a practical length for the rectangular part of the probe L=10 mm, and for the length of the taper we choose c=3 mm. From our optimization simulations in HFSS, this length allows focusing exactly at the end of the tip (the optimal aim is that the beam coming out from the taper can focus right at the end of the tip and the E-field intensity is the highest) when $a_1 \times b_1 = 0.02 \times 0.02$ mm^2. The permittivity of PMMA is 2.6, and its loss tangent is 0.003 at 100 GHz.

Figure 3 (a) shows the 2D E-field distribution in the vicinity of the end of the probe in the *xoz* plane, Fig. 3 (b) shows the distribution in the *yoz* plane, and Fig. 4 shows the E-field intensity along the *z* direction (x=0, y=0). It can be seen that there is good focusing at the end of the tip.

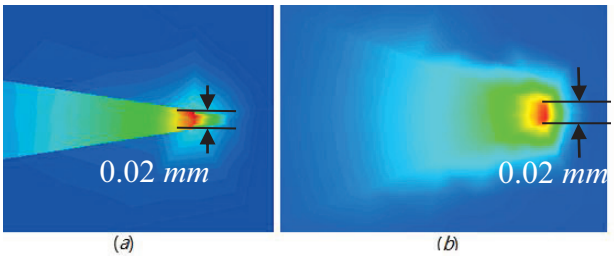

Fig. 3. 2D E-field distributions near the end of the probe for the four-side tapered probe: (a) in the *xoz* plane, and (b) in the *yoz* plane.

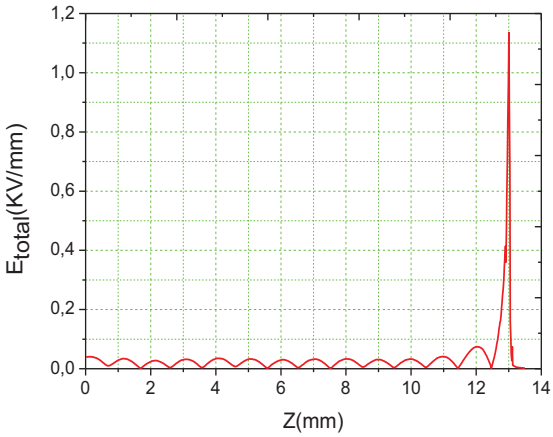

Fig. 4. E-field intensity along the *z* direction when x=0, y=0.

It can be observed from Fig. 4 that the E-field intensity quickly decays near the end of the tip.

Fitting the evanescent E-field intensity curve beyond the end of the tip with $z \geq 13$ mm using a general exponential function, $f(x)=a\exp(bx)$, in MATLAB, yields the following values for a and b respectively, a=1.741×10173 (KV/mm) which can be considered as positive infinite and b=-30.66 (KV/mm), the E-field intensity drops close to 0 in 100 μm beyond the end of the tip.

B. Two-side tapered probe

Since there are always some fabrication tolerances to take into account and a two-side tapered probe such as illustrated in Fig. 1 (e) and (f) is much easier to fabricate, we investigate the influence of a variation of parameters a_1 and b_1. First, we fix a_1=2 mm and change b_1. The metal coating is applied on the wide side since the launched mode is TE10. Fixing b_1=1 mm and changing a_1 makes no sense since the E-field is not in that direction. When b_1=0.0175 mm, the optimized beam shape is achieved.

Figure 5 shows the detailed E-field distribution near the end of the probe. In the *yoz* plane, we see that the beam size is around the dimension of the end of the probe; i.e., 0.0175 mm wide and quickly decaying. In the *xoz* plane, we observe 1 mm beam size (Full Width at Half Maximum (FWHM)). It should be noted that it is still nessesary to use a four-side taper to get smaller beam size and higher E-field intensity. Figure 6 shows the E-field intensity along the *z* direction at x=0, y=0. The maximum intensity is 0.264 KV/mm, which is only 23% of the maximum E-field intensity achieved with an optimized four-side tapered probe in Fig. 3. For the ease of fabrication, however, we opt for a two-side tapered probe for our experiments since it also shows field focusing in the end of the tip.

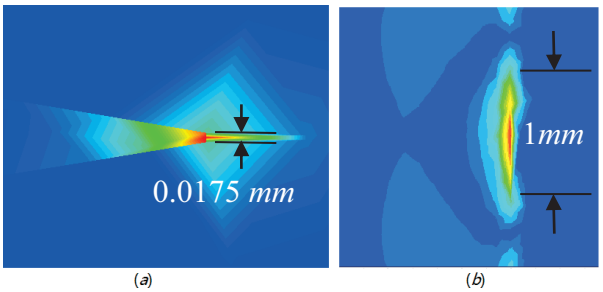

Fig. 5. 2D field distribution at the end of the probe for the wide-side tapered probe: (a) in the *xoz* plane, and (b) in the *yoz* plane.

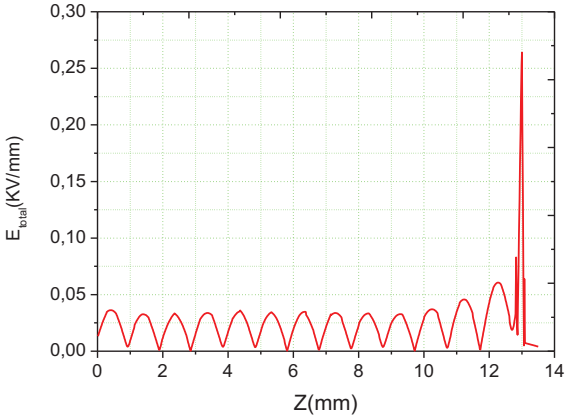

Fig. 6. E-field distribution in the end of the two-side tapered probe.

III. RESOLUTION SIMULATIONS

In Terahertz wave microscopy, the spatial resolution is always defined by the "Line Spread Function" (LSF) and the "edge response." The LSF is the response of the setup to a thin line-shape object across the light path. Similarly, the edge response is what one measures when a sharp straight discontinuity, an edge for example, is placed into the light path of the setup. Since a line is the derivative of an edge, the LSF is the derivative of the edge response in a linear system. Edge resolution is then defined as the lateral displacement with a change from 10 to 90% of the optical signal over an edge [16].

Figure 7 shows the model in HFSS, where the waveguide port source is placed at the end of the rectangular part. A sample is positioned closely to the end of the tip. The tip-sample distance is *d*, the metal plate is 0.1 mm thick and 1 mm wide. The sample is scanned from left to right. The reflection parameter S_{11} is measured. We record the data from -25 μm to +25 μm. The tapered probe used is the optimized one ($a \times b$=2×1 mm^2, L=10 mm, c=3 mm, $a_1 \times b_1$=0.02×0.02 mm^2); the beam size is around 0.02 mm (λ/150) at 100 GHz.

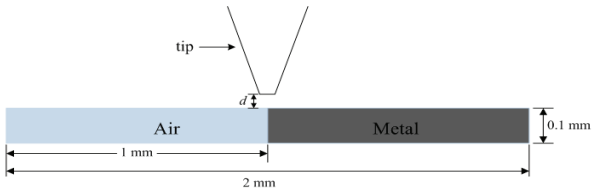

Fig. 7. Geometrical model of tip and sample.

From the simulation results shown in Fig. 8,

we can see that when the tip-sample distance is d=0 mm, one can clearly distinguish the edge from the phase, magnitude, real and imaginary part of S_{11} information. The edge is sharper in the real part information than in the imaginary one. There is around 20 μm for the 10 to 90% edge in the imaginary part information, from which we can conclude that the imgainary part cannot get a higher resolution than the size of the probe itself. Phase and magnitude information also have a 20 μm shift which exactly corresponds to the size of the tip. When the tip is scanned over the sample from left to right, the right side of the probe touches the metal edge when the probe's center point is at position -10 μm. This means that the phase information changes immediately when the probe edge touches the metal edge. The magnitude also contains the information about the beam size. When the probe goes across the edge, 20 μm beam size is shown in the process of the scanning; when the probe is located completely above the metal plate, the sharp edge effect starts. Therefore, the phase information is more sensitive than the magnitude information. The position of the phase change is right at the position where the edge is placed. The position of the magnitude change is equal to the edge position plus the beam size. In one word, the size of the beam or the dimension of the end of the probe leads to the 20 μm lag of the magnitude.

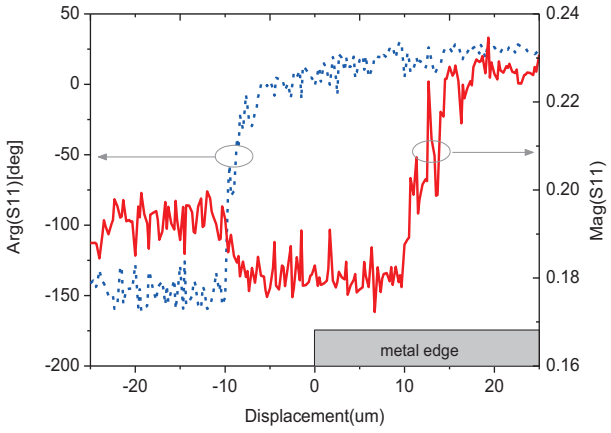

(a)

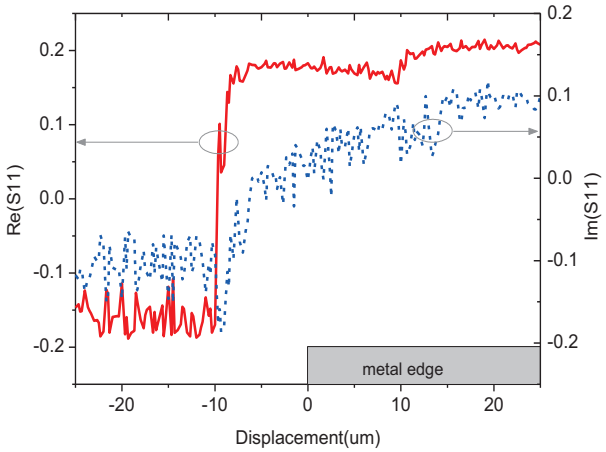

(b)

Fig. 8. Simulated reflection using a linear scanning for a tip-sample distance d=0 mm: (a) phase and magnitude, and (b) real and imaginary part of S_{11}.

Figure 9 shows the impact of the distance d for d=0, 10, 20, 100, 200, 500, 1000 nm on the phase, magnitude, real part and imaginary part of S_{11} during the linear scan of the edge. The smaller the distance, the higher the resolution is. When d is 100 nm, the edge is not sharp anymore. For d>100 nm, the edge fades away when the probe is scanned above the metal plate. Hence, in the experimental setup, one is obliged to keep the tip-sample distance d at sub-100 nm level.

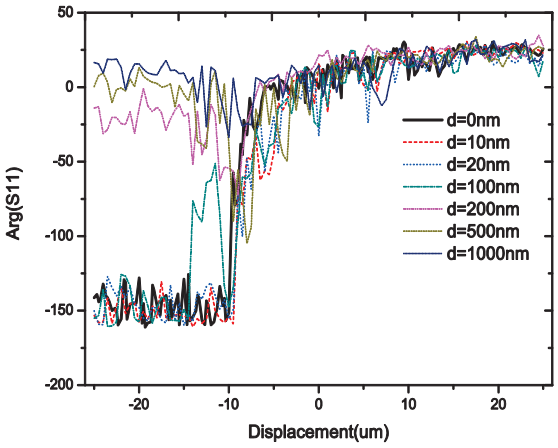

(a)

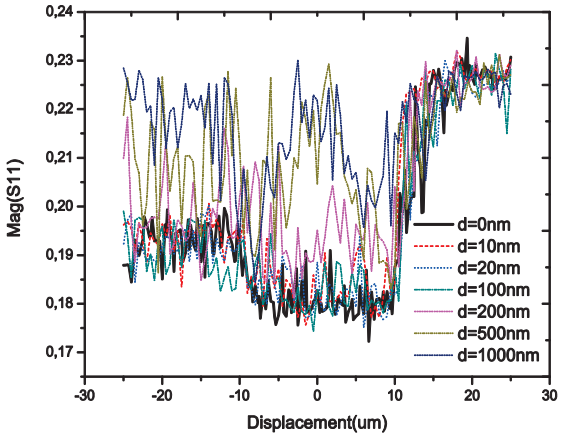

(b)

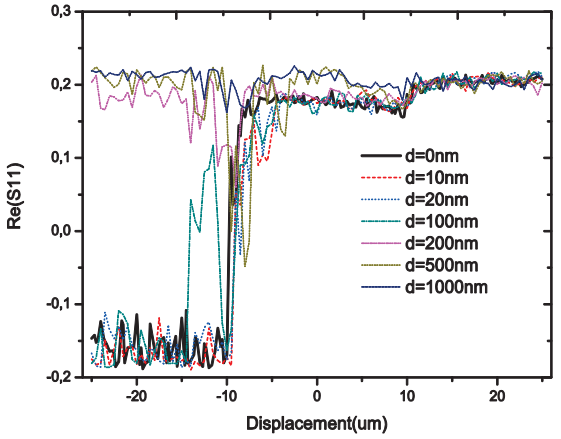

(c)

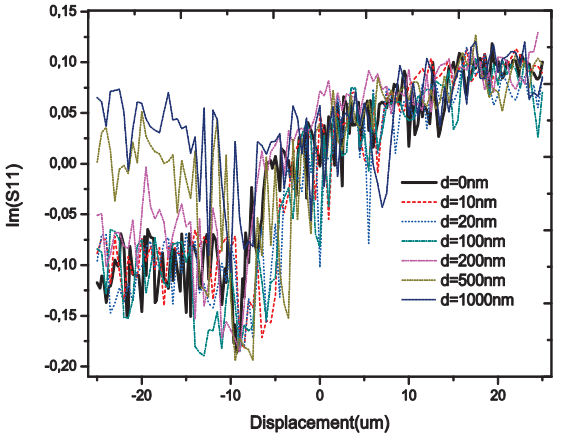

(d)

Fig. 9. Simulated reflection for a linear scanning when the tip-sample distance d=0, 10, 20, 100, 200, 500, 1000 nm: (a) phase, (b) magnitude, (c) real part, and (d) imaginary part of S_{11}.

The tip-sample distance is a key factor for the lateral resolution; the smaller the tip-sample distance, the higher the lateral resolution. The highest resolution can be extrated from the phase and magnitude and real part information of S_{11}. From those, we can get a 5 μm (λ/600) edge resolution which is 1/4 of the size of the end probe; whereas, the imaginary part cannot yield a higher resolution than 20 μm (λ/150), which is the size of the end probe when the tip-sample distance is d=0 nm. Since the phase information is most sensitive of all, phase measurements are suggested in the experiment.

In order to observe the longitudinal resolution, we make use of a stair step sample which is shown in Fig. 10. Here, the tip-sample distance is d, and step height is h. We set h as small as 500 nm (λ/6000), and d=0 nm. From the results in Fig. 11, showing the phase, magnitude, real part and imaginary part information of S_{11}, we can see the 0.5 μm step. Higher longitudinal resolution may abtained in the simulation by setting a smaller h. It costs too much computer memory to set a finer mesh and do the scanning for the resolution simulations. Therefore, λ/6000 is achievable based on the limited simulation environment.

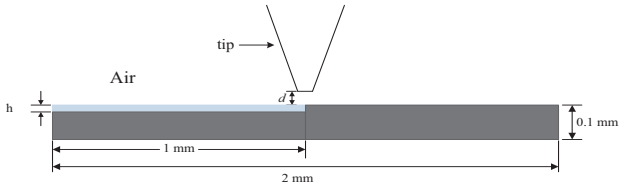

Fig. 10. Longitudinal resolution simulation model.

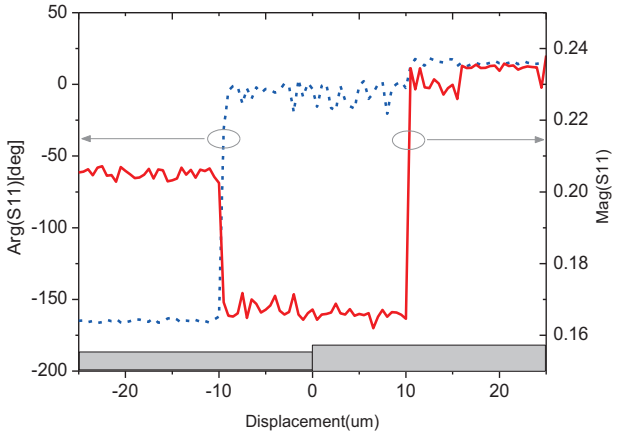

(a)

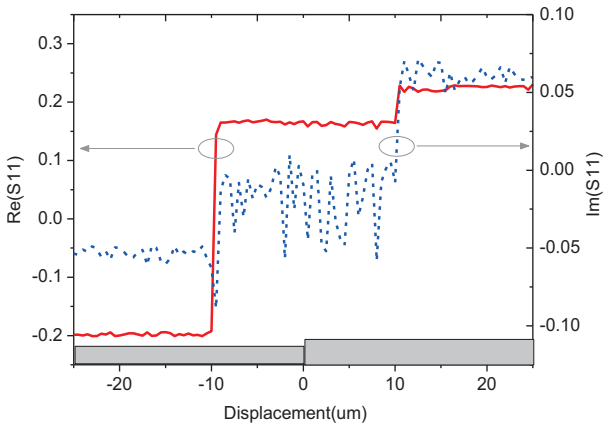

(b)

Fig. 11. Simulated reflection for the stair step sample when the step height h is equal to 0.5 μm.

IV. EXPERIMENTAL RESULTS

The two-side tapered probes were machined using a VHF CAM-100 micro-milling station. The material is PMMA of 1 mm thickness, which is sold by Notz Plastics AG under the brand name Topacryl/Hesaglas. A double-tooth carbide cutter tool with a diameter of 0.5 mm was used for the micro-machining. The resulting surface roughness of the micro-machined probe sidewalls was characterized using a non-contact optical surface profiler WYKO NT-2000 (Bruker). A root-mean-square surface roughness (Rq) of about 1 μm was measured over a surface area of 175 μm × 230 μm. An example of a measured surface profile is shown in Fig. 12 (a). This roughness is sufficiently low for this appliction at 100 GHz. TTFCN and TTFCW probes, as illustrated schematically in Fig. 1 (e) and (f), were fabricated and an evaporated aluminum coating around 600 nm thick had applied subsequently. For the evaporated aluminum coating, the uncoated parts have to be protected. Plastic tape is used to protect the sided and the end facet. Since the end facet is very small, the exact protection is quite difficult. If the tape protected area is bigger than the end facet area and covers the tapered sides, the joint line of the end facet is and the tapered sides is not sharp and there is no coating on the protected part. The end facet of the TTFCN probe is 100 μm width without aluminum coating observed with a JEOL JSM-6400 scanning electron microscope in Fig. 12 (b). The protection of the end facet of the tip during the coating application is not exact enough and there is also around 100 μm width in the sides of the probe did not cover by the metal coating. The end detail of the TTFCW probe is shown in Fig. 12 (c), the target width is 0.0175 mm and also the protection of the end facet is hard, the wide tapered sides do not have the sharp coating edge.

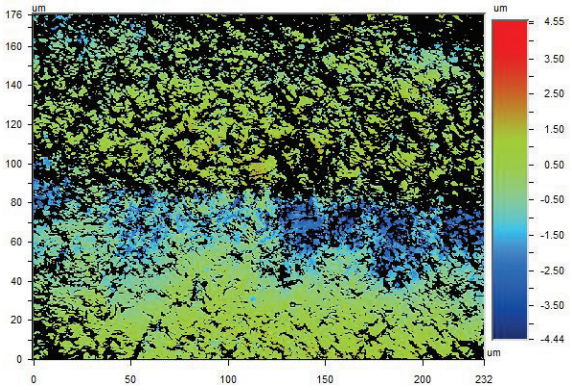

(a)

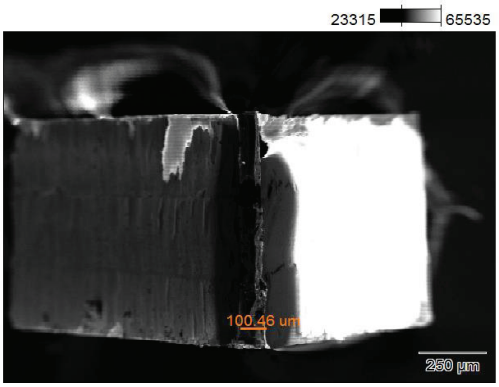

(b)

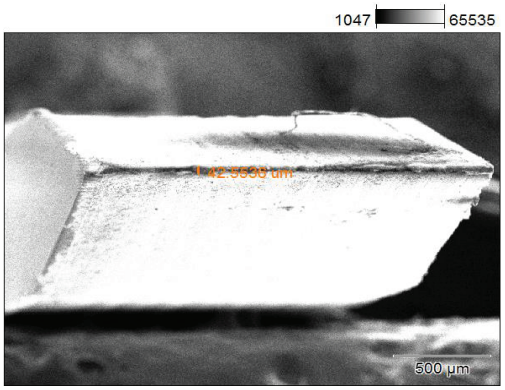

(c)

Fig. 12. (a) Measured surface profile of the micro-milled surfaces of the tapered probe, (b) image of the end of the tapered probe for TTFCN with a_1=0.098 mm, and (c) image of the end of the tapered probe for TTFCW with b_1=0.0175 mm.

The imaging setup is shown in Fig. 13, the block diagram of the imaging system and a photograph of the experimental setup, respectively. The EM wave is generated by a Backward Wave Oscillator (BWO) source sweep generator G4403E from Elmika, with a frequency range from 75 GHz to 110 GHz and accuracy around ±0.2%. Its output power can reach 15 mW over the whole band. We set it to a fixed frequency of 100 GHz in the experiments. A Directional Coupler (DC) is used after the output of the G4403E, and an FTL WDP-10 from Farran is used as reflection power detector. This detector employs finline technology and zero biased beamlead Schottky barrier diodes. The WDP-10 works from 75 to 110 GHz, and its sensitivity is typically bigger than 550 mV/mW. We used an E-Bender (EB) to change the horizontal direction to vertical direction, and a Straight Waveguide (SW) to extend the length. The PMMA Tapered Probe (TP) is coupled with the SW. The end of the probe is contacted with the sample since it is difficult to control the tip-sample distance in the nanometer range. The rectangular PMMA sample which is mounted on the *xy* stage is half coated with aluminum to make an edge effect. Two types of the coupling mode have been tested in the experimental setup. One is using the TTFCN probe which is inserted into the SW, and the other one is using the TTFCW probe which is fixed at the end of the SW. Reflection is observed through this setup.

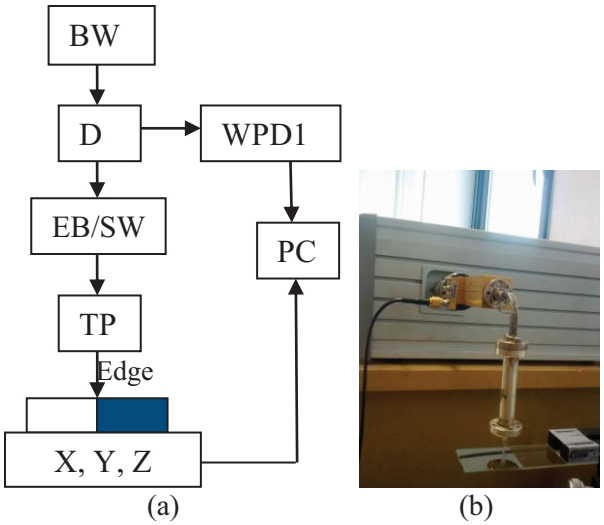

Fig. 13. (a) Block diagram of the imaging setup, and (b) photograph of the experimental.

We scan the sample from the aluminum coated part to the uncoated part. The measurement results are shown in Fig. 14, where the scanning range is 8000 μm, and each step is 100 μm, using the 10% to 90% edge function. Figure 14 (a) shows the results for the TTFCN probe and (b) depicts the results for the TTFCW probe. It is observed that the edge width is around 1.12 mm and 0.75 mm respectively. The TTFCN probe has an $a_1 \times b_1 = 0.1 \times 1$ mm^2 end facet and the measured edge width is around 1 mm, which is the wide size of the end of the taper. The TTFCW probe has an $a_1 \times b_1 = 2 \times 0.0175$ mm^2 end facet and the measured edge width is around 0.75 mm, which is bigger than the beam size (0.0175 mm) in the *yoz* plane and less than the beam size (1 mm) in the *xoz* plane. Since the simulations are carried out in the ideal conditions which are different from the experimental environment, especially for the aluminum coating of the probes which are shown in Fig. 12 (b) and (c), the uncoated area on the tapered sides exists as the protection for a small facet is quite difficult. The probe and standard waveguide connection impacts the results as well since the designed probe is smaller than the standard waveguide WR-10, two types of the coupling modes are different from the ideal simulations. The differences between the experimental results and simulation results are reasonable and understandable. Because the detector can only measure the power, the phase information is not available, and hence, the potentially most sensitive way of measuring has not yet been verified experimentally.

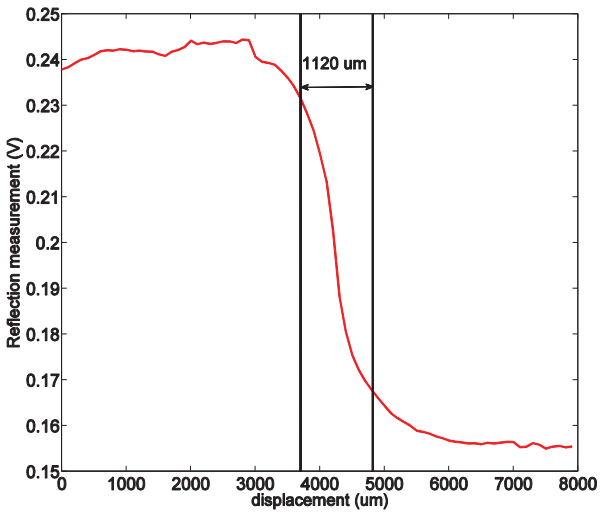

(a)

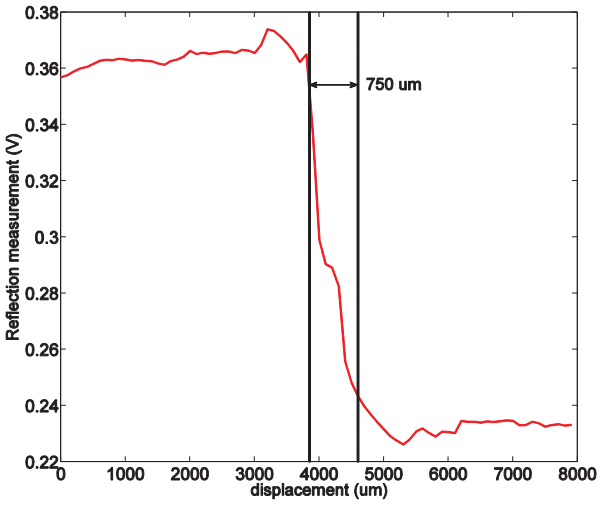

(b)

Fig. 14. Experimentally measured edge effect: (a) for the TTFCN probe, and (b) for the TTFCW probe.

V. CONCLUSION

This paper proposes for the first time the use of PMMA near-field probes to replace the costly low loss and high permittivity materials such as silicon and Sapphire, which are generally used for this purpose in millimeter and Terahertz wave imaging applications. A good field concentration in the end of the tapered probe is obtained by applying a metal coating on the PMMA probe. The coating area can be designed according to the coupling mode. When the tapered probe is totally inserted into a standard wave guide, a QTEM mode is excited in the tapered probe when its narrow side is coated. If the tapered probe is fixed in the end of a standard waveguide, a TE10 mode exists in the tapered probe if its wide side is coated. An optimization was carried out for the FTFCW and TTFCW probe. Simulations to determine the achievable lateral and longitudinal resolution have been performed for an edge (metal plate) and a stair step sample scanned with the FTFCW probe by examining the S_{11} parameters. We found that the phase information is most sensitive, and that a resolution of $\lambda/600$ laterally and at least $\lambda/6000$ longitudinally can be reached in the simulations. The TTFCN and TTFCW probes were fabricated by micro-milling and an aluminum coating was applied by evaporation. Experiments were carried out with a BWO source. The edge effect was observed and the measured results were analyzed. The resolution of 1.12 and 0.75 mm was obtained for TTFCN and TTFCW probes, respectively.

ACKNOWLEDGMENT

This work has been partially funded by FWOAL682 “Building blocks of lab-on-chip system for label-free monitoring of biomolecular interactions,” by the Industrial Research Fund of VUB, IOF242, by the Strategic Research Program of VUB, SRP-M3D2, and by the IMEC BISENS laboratory. This work is also executed in the framework of NEWFOCUS ESF Research Networking Program (RNP). J. Van Erps was supported by the FWO Vlaanderen under a post-doctoral research fellowship.

REFERENCES

[1] A. Lewis, “Near-field optics: from subwavelength illumination to nanometric shadowing,” *Nature Biotechnology*, vol. 21, no. 11, pp. 1378-1386, 2003.

[2] T. Nozokido, T. Ohbayashi, J. Bae, and K. Mizuno, “A resonant slit-type probe for millimeter-wave scanning near-field microscopy,” *IEICE Trans. Electron.*, vol. E87-C, no. 12, 2004.

[3] T. Nozokido, S. Nuimura, T. Hamano, J. Bae, and K. Mizuno, “A new object mounting structure for use in millimeter-wave scanning near-field microscopy,” *IEICE Trans. Electron.*, vol. 1, no. 6, 144-149, 2004.

[4] J. Bae, T. Okamoto, T. Fujii, and K. Mizuno, “Experimental demonstration for scanning near-field optical microscopy using a metal micro-slit probe at millimeter wavelengths,” *Applied Physics Letters*, vol. 71, no. 24, pp. 3581-3583, 1997.

[5] N. Klein, P. Lahl, and U. Poppe, “A metal-dielectric antenna for terahertz near-field imaging,” *Journal of Applied Physics*, vol. 98, no. 014910, 2005.

[6] O. Benzaim, K. Haddadi, M. M. Wang, D. Maazi, and T. Lasri, “Scanning near-field millimeter-wave microscope: application to a vector-coding technique,” *IEEE Transaction on Instrumentation and Measurement*, vol. 57, no. 11, pp. 2392-2397, 2008.

[7] M. Kim, J. Kim, H. Kim, S. Kim, J. Yang, H. Yoo, S. Kim, K. Lee, and B. Friedman, “Nondestructive high spatial resolution imaging with a 60 GHz near-field scanning millimeter-wave microscope,” *Review of Scientific Instruments*, vol. 75, no. 3, pp. 684-688, 2004.

[8] A. J. Huber, F. Keilmann, J. Wittborn, J. Aizpurua, and R. Hillenbrand, “Terahertz near-field

nanoscopy of mobile carriers in single semiconductor nanodevices," *Nano Letters*, vol. 8 no. 11 pp. 3766-3770, 2008.

[9] B. Zhu, S. Vanloocke, J. Stiens, D. De Zutter, and R. Vounckx, "A novel 3D printed focusing probe in scattering-type scanning near-field millimeter and terahertz wave microscope," *European Conference on Antennas and Propagation*, Rome, Italy, pp. 775-778, 2011.

[10] B. Zhu, J. Stiens, G. Poesen, S. Vanloocke, D. De Zutter, and R. Vounckx, "Dielectric analysis of 3D printed materials for focusing elements operating in Mm and THz wave frequency bands," *Proceedings of Symposium IEEE/LEOS Benelux Chapter*, Delft, Netherland, pp. 13-16, 2010.

[11] B. Zhu, S. Vanloocke, V. Matvejev, J. Stiens, D. De Zutter, and R. Vounckx, "Scanning near-field millimeter wave microscope combining dielectric tapered probes and metal tips," *Progress In Electromagnetics Research Symposium*, Suzhou, China, pp. 12-16, September 2011.

[12] B. Zhu, J. Stiens, V. Matvejev, and R. Vounckx, "Inexpensive and easy fabrication of multimode tapered dielectric circular probes at millimeter wave frequencis," *Progress In Electromagnetics Research*, vol. 126, pp. 237-254, 2012.

[13] H. Chibani, K. Dukenbayev, M. Mensi, S. K. Sekatskii, and G. Dietler, "Near-field scanning optical microscopy using polymethylmethacrylate optical fiber probes," *Ultramicroscopy*, vol. 110, pp. 211-215, 2010.

[14] B. Zhu, G. He, J. Stiens, and R. Vounckx, "Analysis and optimization of a focusing metal-dielectric probe for near field terahertz imaging," *EuMW2013*, Nuremberg, Germany, pp. 6~11, October 2013.

[15] M. Berta, P. Kuzel, and F. Kadlec, "Study of responsiveness of near-field terhertz imaging probes," *J. Phys. D: Appl. Phys.*, vol. 42, 2009.

[16] R. A. J. L. Adam, "Review of near-field terahertz measurement mehtods and their applications," *J. Infrared Milli. Terahz. Waves*, vol. 32, pp. 976-1019, 2011.

Bin Zhu received the B. E. degree in Electronics and Information Engineering from Harbin Engineering University, Harbin, China, in 2004, the M. S. degree in Communication and Information System from Dalian University of Technology, Dalian, China, in 2006, and the Ph.D. degree in Vrije Universiteit Brussel, Brussels, Belgium in 2014. Her research interest is focused on near-field imaging, non-destructive testing and dielectric spectroscopy.

Guoqiang He received the B. E. degree in Vacuum Electronic Technique from the University of Electronic Science and Technology of China (UESTC), Chengdu, China, in 2010, and the M. S. degree in Radio Physics from UESTC, Chengdu, China, in 2013. Currently, he is working towards the Ph. D. degree in Electrical Engineering at Vrije Universiteit Brussel (VUB), Brussels, Belgium. His current research interest is in millimeter wave and Terahertz detectors.

Johan Stiens received the Electromechanical Engineering degree with majors in Applied Physics and the Ph.D. degree (with greatest honors) from the Faculty of Engineering Sciences, Vrije Universiteit Brussel (VUB), Brussels, Belgium, in 1990 and 1996, respectively.

He is currently with VUB. His current research interests include semiconductor physics and technologies, including micromachining for microfluidics, optoelectronic devices, plasmonics, metamaterials and devices, and systems for active (near-field) imaging and sensing in the millimeter and terahertz (THz) wave domain. He is the author or coauthor of about 180 international journal and conference papers. He owns eight patents and four pending patents. He is a Reviewer of several scientific journals and has been elected as an expert for the evaluation of research grants, and national and international scientific/industrial projects. He has been a Consultant for several years for companies and research institutes. Since January 2012, he has been a "Professor." Besides his technical teaching, he is also involved in entrepreneurship courses, merging technical and business engineers. He was a Cofounder of the spin-off company Ecologic, dealing with equalizer chips.

Jürgen Van Erps was born in Etterbeek, Belgium, in 1980. He graduated as an Electrotechnical Engineer with majors in Photonics at the Vrije Universiteit Brussel (VUB) in 2003 and obtained his Ph.D. summa cum laude at the same university in 2008.

Since February 2013, he is a Part-time Professor at VUB, teaching an introductory course on Photonics and

a course on Optical Communication Systems. In 2009 and 2010, he was a Visiting Researcher at the Centre for Ultrahigh bandwidth Devices for Optical Systems (CUDOS) at the University of Sydney, Australia, under an Erasmus-Mundus Action 3 scholarship of the European Union. His research there involved high-resolution optical sampling of ultrahigh bitrate signals using dispersion-engineered highly nonlinear chalcogenide waveguides, and automatic dispersion monitoring and compensation of 1.28Tbaud links. Currently, he is continuing his research at VUB on the modeling of micro-optical systems for optical interconnects and optofluidics applications, and their fabrication by means of Deep Proton Writing, ultraprecision diamond tooling and hot embossing. He is also involved in experimental work on nonlinear optics in integrated photonic devices. He was Invited Speaker at several international conferences. He authored or co-authored 32 SCI-stated papers and more than 80 papers in international conference proceedings. He is co-inventor of 2 patents. He serves as a Reviewer for several international journals. He is a Senior Member of the SPIE, and Member of the OSA and the IEEE Photonics Society. He was also co-founder and 2006-2007 President of the SPIE Brussels Student Chapter.

Willy Ranson received the Telecommunication Engineer degree in 1975 from the University of Leuven, Belgium. He was Assistant Professor in the Department of Microwaves and Lasers at the University of Leuven until 1983, when he joined the Department of Electronics and Information Processing (ETRO) of the Vrije Universiteit Brussel (VUB).

Since 1990, he has been a Member of the Inter-university Micro-Electronics Center (IMEC) in the VUB. Ranson has participated in projects and contracted research on such diverse topics as planar antenna structures, high frequency wave-guides, chemical sensors, biological applications for breast cancer detection, optical information processing for parallel computation, CO2 laser applications, microelectronic process technology and revolutionary information and revolutionary computation theories. He is currently Senior Researcher in charge of the processing technology lab of LAMI and is a Founder Member of LIFE (Living Systems). His current research contributions are in the areas of CO2 laser modulation, millimeter imaging systems, micro machines for ultra-rapid DNA screening, fast enforcing technologies for protein engineering and Evolutionary Living Systems. Ranson is (co)author of more than 140 publications in international refereed journals and conferences.

Cathleen De Tandt graduated at the Industrial High School for Engineering of Ghent (C.T.L), in 1979, as an Industrial Engineer in Chemicals. She was teaching chemistry until 1981, and from 1982 she was working at the Vrije Universiteit Brussel-Jette together with Dr. Rogiers in the area of mucoviscidose.

In 1983, she worked as Technologist at the Vrije Universiteit Brussel in the department of Electronics and Information Processing (ETRO-LAMI). From1984 till the end of December 2008, she was a Member (Research Engineer) of the Inter University Micro Electronic Center (IMEC) with a working place on the VUB Campus. Since January 2009, she's been working as Technologist at the Vrije Universiteit Brussel in the department of Electronics and Information Processing (ETRO-LAMI).

She has participated in projects on diverse topics as: chemical gas sensors, optical information processing for parallel computation, CO2 laser applications and modulation, microelectronic process technology, field emission devices, millimeter wave monitoring, technology for half conductive Coupling, technology for Infra-Red modulators, micro-machines for ultra-rapid DNA and protein screening, fast enforcing technologies for protein engineering. She is also a co-worker for Eqcologic, a spin-off of the ETRO-LAMI-group.

Hugo Thienpont (M'99) was born in Ninove, Belgium, in 1961. He graduated with the academic degree of Electrotechnical Engineering in 1984 and received the Ph.D. degree in Applied Sciences in 1990, both from the Vrije Universiteit Brussel (VUB), Brussels, Belgium. In 1994, he became Professor at the Faculty of Applied Sciences, with teaching responsibilities in photonics. In 2000, he became Research Director of the Department of Applied Physics and Photonics at the VUB, and in 2004, he was elected Chair of the department. Currently, he is the Coordinator of several basic research and networking projects such as the European Access to Micro-Optics Expertise, Services and Technologies (ACTMOST) network. In addition to academic oriented research projects, he manages microphotonics related industrial projects with companies like Barco, Agfa-Gevaert, Tyco, and Umicore. He authored more than 220 SCI-

stated journal papers and over 400 publications in international conference proceedings. He edited 15 conference proceedings, authored 7 chapters in books, and is co-inventor of 15 patents. Thienpont was Guest Editor of several special issues on Optical Interconnects for Applied Optics and the IEEE Journal of Selected Topics in Quantum Electronics. He is the General Chair of the International Society for Optical Engineers (SPIE) Photonics Europe conferences in Strasbourg and Brussels. In 1999, he was the recipient of the International Commission for Optics Prize and the Ernst Abbe medal from Carl Zeiss. In 2003, he was awarded the title of IEEE Laser and Electrooptics Society (LEOS) Distinguished Lecturer. He was also the recipient of SPIE President's Award in 2005 for dedicated service to the European Community and the international Micro-Optics Conference Award in 2007. He was an Invited Speaker at 50 international conferences. He is a Fellow of SPIE and EOS, and a Member of the Optical Society of America, and the IEEE Photonics Society.

Roger Vounckx was born in Brussels, Belgium, on June 26, 1952. He received the Dr. Sc. degree in Physics from the Electronics Department, Vrije Universiteit Brussels (VUB), Brussels, in 1984.

From 1975 to 1980, he was a Teaching Assistant of Faculty for Sciences in the Physics Department, VUB, where he became an Associate Professor of Microelectronics in 1984 and a Full Professor in 1993. During 1978-1979, he was engaged in military service. He became the Director of the Laboratory of Micro- and Photonelectronics (LAMI) in 1987, and the Head of the Electronics and Informatics Department (ETRO) in 2008. In 1988, he started a close collaboration with the Inter-University Microelectronics Centre (IMEC), Leuven, Belgium, and in 1998, LAMI became an associated research laboratory of IMEC's. He is currently with VUB. His current research interests include semiconductor devices and systems for optical and electrical information processing and communication and millimeter-wave imaging systems. He has authored or coauthored more than 250 technical papers in international journals and conference proceedings, and holds eight international patents. He was a Reviewer for international scientific journals and is an expert for evaluation of industrial research projects for the Belgian Government. He is currently involved in research of mid-infrared optoelectronics, artificially created living systems for truly intelligent computing, and a "Strategic Basic Research" Program from the Flemish Government for millimeter-wave imaging applications. He is a Cofounder and an Executive Director of EqcoLogic NV, LAMI's first spin-off company, which designs and produces silicon chips for fast data communication. Vounckx was the Chairman and a Member of program committees for international conferences.

Efficient and Accurate Analysis of a Substrate Integrated Waveguide (SIW) Rat-Race Coupler Excited by Four U-Shape Slot-Coupled Transitions

R. Dehdasht-Heydari [1], K. Forooraghi [2], and M. Naser-Moghadasi [1]

[1] Department of Electrical Engineering, Science and Research Branch
Islamic Azad University, Tehran, Iran
dehdashtheydari@gmail.com, mn_moghaddasi@yahoo.com

[2] Department of Electrical Engineering
Tarbiat Modares University (TMU), Tehran, Iran
KEYVAN_F@modares.ac.ir

Abstract ─ In this paper, the bandwidth of one SIW rat-race (hybrid ring) coupler has been increased up to 30% by four U-shape slot-coupled transitions without disadvantages due to transmission line loss, radiation and design complexity. The SIW coupler structure has been analyzed by the mode matching method that uses the cylindrical vector expansion to minimize computational time and memory occupation. Throughout 11-15 GHz bandwidth, return loss and isolation as well as phase differences in output ports have been presented. It is observed that the numerical results are in good agreement with simulation and experimental measurement.

Index Terms ─ Boundary conditions, coaxial cables, Cylindrical Vector Waves (CVWs), Dyadic Green's Functions (DGFs), rat-race (hybrid ring) coupler, Substrate Integrated Waveguide (SIW), transition, U-shape slots.

I. INTRODUCTION

Substrate Integrated Waveguide (SIW) structures are also known as laminated waveguide or post-wall waveguide structures. They are used as a concept for the design of microwave and millimeter-wave waveguide structures and components [1]. SIWs are based on the equivalence between well-known metallic waveguide structures (usually a Rectangular Waveguide (SIRW)) and waveguide structures on a dielectric substrate using rows of metal posts (vias). Many passive components, such as filters, antennas, circulators, couplers, transitions, etc., are based on SIW or similar technologies, and they have been studied in [2-9].

Without any doubts, the transitions between excitation section and SIRW are mostly a critical element to get optimized S-parameters. Several transitions for the SIRW were presented [10-15] over the last few years, like transformers to rectangular waveguides, single layer transitions from microstrip lines to SIRWs, uniplanar CPW transitions, GCPW transitions. However, these structures have drawbacks such as not compatible with planar circuits, incompatible with low-loss SIRWs, radiation and design complexity and fabrication. Therefore, a new design of transition is necessary in order to simplify the structure and improve bandwidth.

Recently, several papers [16-22] have applied a Cylindrical Vector Wave expansion (CVW) to study the simplified 2-D case and the full 3-D case. These mode expansions allow an efficient full-wave analysis of SIW structures for metallic and dielectric posts. Nevertheless, there is a need in using efficient method of mode matching to analyze wideband SIW structures; for instance, SIW couplers.

The single-layer SIW rat race coupler basically has been proposed in [23], utilizing the transition from microstrip lines to SIW rat-race

Submitted On: October 31, 2013
Accepted On: October 4, 2014

arms. Accordingly, there was not mentioned anything about output phases (0 and 180 degrees) and the analysis of the coupler. This coupler has limited bandwidth (about 10% in X-band and 7% in Ka-band) and its dimensions should optimize to obtain further bandwidth.

In this paper, a simple SIW transition structure is designed for 8.5-16.5 GHz frequency (over 50% relative bandwidth) in Section II. The coaxial cables are accompanied with U-shape slots to excite the signal inside the SIRW. As an application, a SIW hybrid ring coupler has been modified with this new SIW transition to increase the bandwidth over than 30% and carry out a lower loss and profile coupler. The design and optimization procedure of the coupler have been presented in Section III. In Section IV, the proposed coupler has been analyzed and the vector wave functions have been used for the coupler. By imposing boundary conditions on each post and transfer the obtained equations to the matrix, the unknown coefficients have been determined and scattering parameters of the proposed rat-race coupler to be calculated. To confirm the efficiency and accuracy of the method, the coupler calculated parameters have been compared with simulated and measured results in Section V.

II. DESIGN OF U-SHAPE SLOT-COUPLED TRANSITION

The structure of U-shape slot-coupled transition is shown in Fig. 1. The structure is similar to conventional SIW, which is excited with coaxial cable directly with no need to use microstrip line transition. The sole difference is in rectangular U-shape slots above the substrate plate where the inner conductors of coaxial cables are connected to the top plate. In the first step, we simulated a two port SIW waveguide without coaxial probes for single-mode (i.e., TE10 mode) in the operating frequency range of 8.5-16.5 GHz with CST microwave studio. In the next step, it is necessary to use the transition from two coaxial probes to the SIW waveguide. We have seen in the CST package that by using a slot coupling for probe feeding to SIW transition, the input resistance increases with the thickness of SIW substrate but decreases with slot length.

This trade off can be achieved by adjusting the length and shape of the slot. Therefore, the transition bandwidth can be maximized by matching the input resistance as nearly as to the characteristic impedance of the probe feeding.

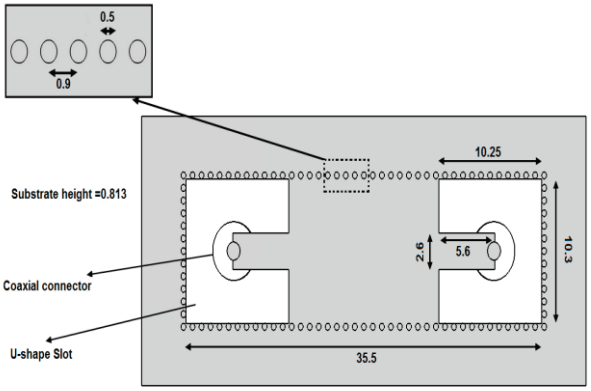

Fig. 1. The back-to-back U-shape slot-coupled transition structure (all dimensions are in millimeters).

From optimization in CST for different slot shapes along with different lengths, we realized that the best configuration to maximize the relative bandwidth of the transition can be exploited by U-shape slots rather than the other shapes (e.g., E-shape slots). Therefore, the two U-shape slots are designed to enhance the bandwidth of the SIW structure excited by coaxial cables without radiation from the slots or design complication as well as the bandwidth of the structure with waveguide ports excitation.

Entrance of the coaxial probes and the dimensions of U-shape slots are critical for the return loss performance of the SIW hybrid ring in the next section. A lot of simulations have been made to optimize the transitional performance using CST, which the optimized dimensions are demonstrated in Fig. 1. By applying these coupling slots over the top plate of SIW transition, the TEM waves from coaxial cables convert to TE10-like modes and enter into SIW structure. Thus, the performance of this proposed structure is the same as the structure when excited only with waveguide ports. This agreement is illustrated in Fig. 2. As shown in the figure, the S_{11} and S_{21} of the structure in fundamental mode when excited with coaxial cable and U-shape slot-coupled are similar to waveguide port excitation. We use this similarity in our analysis in Section IV.

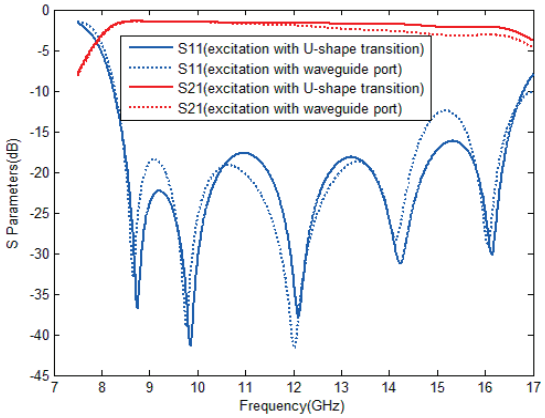

Fig. 2. S-parameters of SIW structure with waveguide port excitation and U-shape slot-coupled transition.

III. DESIGN AND OPTIMIZATION PROCEDURE OF SIW HYBRID RING (RAT-RACE) COUPLER

The optimized SIW hybrid ring (rat-race) structure has been shown in Fig. 3. The dimension of the proposed coupler has been obtained based on the following procedure:

1. In the previous section, we have designed a new SIW transition which is applied for excitation of our coupler. As shown in Fig. 3, the SIW coupler arms consist of four U-shape slots and coaxial connectors.
2. According to [23] for manufacturing considerations, the distances between the four arms should be increased one wavelength in comparison to conventional distances between the coupler arms. The spatial angles between the four ports have been shown in Fig. 3.
3. We have chosen the logical and possible ranges for inner radius (r1), $3 \le r1 \le 9$ and outer radius (r3), $10 \le r3 \le 20$ of the coupler. In addition, four matching posts have been used for improving the impedance matching of the coupler [23]. The initial radius (r2) of the matching posts is in $3.5 \le r2 \le 9.5$ range. By choosing three radiuses from above ranges, our initial coupler has been prepared for analysis. The SIW rat-race coupler analysis has been presented in detail in the next section.
4. After calculating the coupler S-parameters form analysis, we have optimized the coupler with IWO optimization algorithm [24]. The parameters under optimization are r1, r2, r3 and the matching posts diameters. In our optimization, the operating frequency band was over 8.5-16 GHz, but because of considering all goal functions, i.e., return loss, isolation, insertion loss and phase differences of the coupler; simultaneously the maximized bandwidth has been met 30% relative bandwidth, which is over 11-15 GHz for our optimized dimensions in Fig. 3. To the best of our knowledge, this relative bandwidth has not been obtained for the SIW rat-race coupler by literatures up to now, and the proposed SIW rat-race coupler is a good candidate for the wideband applications because the relative bandwidth of the coupler can be shifted in the interested band by changing and optimizing the dimensions.

Also, because of using the probe feeding instead of the microstrip line transition, our coupler is low loss and profile. The experimental measurements confirm our claim in Section V.

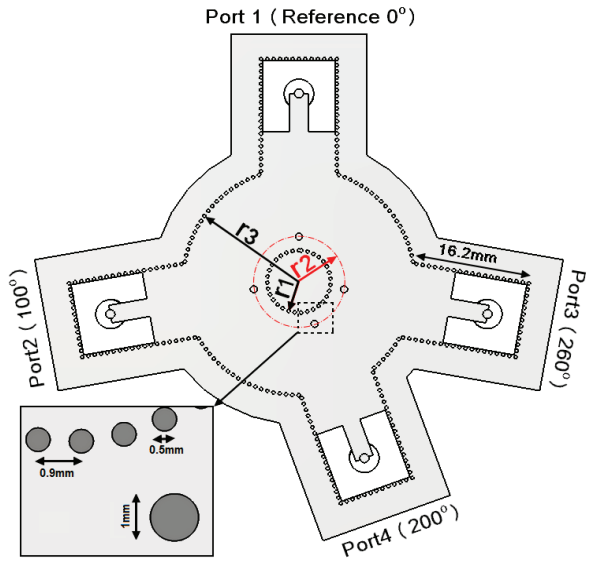

Fig. 3. The SIW hybrid ring coupler structure (r1=4.5 mm, r2=6.5 mm and r3=15.5 mm).

IV. SIW HYBRID RING (RAT-RACE) COUPLER ANALYSIS

In this section, we analyze the SIW hybrid ring (rat-race) coupler with mode matching algorithm for these reasons:

a. Our analysis minimizes memory computation and time consumption rather than the other

full wave package like CST and HFSS.

b. As mentioned in the previous section, after calculating the S-parameters of the coupler from our analysis, we can optimize the dimensions of the coupler to achieve the higher bandwidth with optimization algorithms through Matlab code, whereas the optimization of the SIW coupler takes a very long time in CST or HFSS. Furthermore, after many optimizations in CST or HFSS, the goal functions for this SIW coupler is not capable of reaching to our desired bandwidth.
c. It is worthwhile mentioning that our code can generally be handled for the SIW passive structures which require bandwidth enhancing and the analyzed and optimized algorithm have been applied for the proposed SIW coupler as a good example in our effort.

According to Section II, because the coaxial cable TEM waves are converted to TE modes through the U-shape slots, to analyze the fields in the SIW Hybrid ring (rat-race) structure, we substitute four U-shape slots and coaxial cables with rectangular waveguide port excitations (magnetic source in this paper).

Now, we can examine the incident and scattered magnetic fields from each metallic post included vias of four rectangular arms, four matching posts with radius (r2), vias of inner radius (r1) and vias of the outer radius (r3) of the SIW coupler. In general, an arbitrary total magnetic field H(r) can be expressed as:

$$H_{total}(r) = H_1 + H_2 , \tag{1}$$

where H_1 is incident wave from a magnetic source (M_s') and H_2 is scattering magnetic wave from each via. Calculating H_1, we need this equation:

$$H_1 = -j\omega\varepsilon \iiint_{V'} G_{m2} M_s' dV', \tag{2}$$

where G_{m2} is a magnetic Green's function of the second kind, which for parallel plate waveguide through using residue theorem in cylindrical coordination and [25,26], explicit form is given by:

$$\begin{aligned} &G_{m2}(r,r') = \frac{\hat{\rho}\hat{\rho}}{k^2}\delta(r-r') \\ &-\frac{1}{j4\pi}\sum_{m=0}^{N_z}\sum_{n=-N_\phi}^{N_\phi}(2-\delta_{m0})\frac{1}{k_m^2 h}\times \\ &[P_n(k_m,k_z,\rho,z)P_n'(k_m,k_z,\rho',z)+ \\ &Q_n(k_m,k_z,\rho,z)Q_n'(k_m,k_z,\rho',z)] \quad \rho \underset{<}{>} \rho', \end{aligned} \tag{3}$$

and

$$\delta_{m0} = \begin{cases} 0 & if\ m \neq 0 \\ 1 & if\ m = 0 \end{cases}.$$

In (3), we define two vector wave functions $P_n(k_m,k_z,\rho,z)$ and $Q_n(k_m,k_z,\rho,z)$ as the equivalence of magnetic fields. Calculating these functions, lets assume this harmonic scalar potential $\vartheta_n(r)$:

$$\vartheta_n(r) = \begin{cases} H_n^{(2)}(k_m\rho)e^{j(k_z z - n\phi)} & \rho > \rho' \\ J_n(k_m\rho)e^{-j(k_z z - n\phi)} & \rho \le \rho' \end{cases}, \tag{4}$$

where $H_n^{(2)}$ and J_n indicate n-order Hankel's function of the second kind and n-order Bessel's function respectively. Also, $k_m = \sqrt{k^2 - k_z^2}$, $k_z = m\pi/h$, $k = \omega\sqrt{\mu_0\varepsilon_0\varepsilon_r}$ and h is the height of substrate. In this manner, m and n are the cylindrical modes in vertical (z direction) and azimuthally (φ direction) respectively.

The relation between $P_n(k_m,k_z,\rho,z)$ and $Q_n(k_m,k_z,\rho,z)$ is as follows:

$$P_n(k_m,k_z,\rho,z) = \nabla\times(\vartheta_n(r)\hat{\rho}), \tag{5.a}$$

$$Q_n(k_m,k_z,\rho,z) = \frac{1}{k}\nabla\times P_n(k_m,k_z,\rho,z), \tag{5.b}$$

where $\hat{\rho}$ is unit normal vector on the lateral surface of each cylindrical metallic post of the hybrid ring coupler. Similarly, $P_n'(k_m,k_z,\rho',z)$ and $Q_n'(k_m,k_z,\rho',z)$ can be acquired from (5.a) and (5.b) by interchanging $\rho \le \rho'$ within (4).

We can write scattering waves for TM and TE modes as Cylindrical Vector Wave (CVW) expansions:

$$\begin{aligned} H_2(r) = &\sum_{l=1}^{P_{via}}\sum_{m=1}^{N_z}\sum_{n=0}^{N_\phi}[C_{l,m,n}^{TM}P_n(k_m,k_z,\rho,z) \\ &+D_{l,m,n}^{TE}Q_n(k_m,k_z,\rho,z)], \end{aligned} \tag{6}$$

where index l denotes to the number of the SIW coupler vias. To determine unknown coefficients ($C_{l,m,n}^{TM}$, $D_{l,m,n}^{TE}$), the boundary conditions should be imposed for the surface of each via; for metallic (PEC) vias:

$$\begin{aligned} &n\times(E_1+E_2) = 0 \\ &in\ surface\ of\ each\ PEC\ with\ radius\ a_i, \end{aligned} \tag{7}$$

where $(E_1+E_2) = (1/j\omega\varepsilon)\nabla\times(H_1+H_2)$ and a_i is each metallic via radius of the coupler as the radiuses of the four matching posts are twice of the other vias in Fig. 3.

By operating (7), the unknown coefficient vector $F_{l,m,n}^{TM/TE}=[C_{l,m,n}^{TM}, D_{l,m,n}^{TE}]$ can be expressed as:

$$\begin{bmatrix} F_{1,1,0}^{TM/TE} \\ . \\ . \\ . \\ F_{l,m,n}^{TM/TE} \end{bmatrix} = [U]^{-1}[S], \tag{8}$$

where U and S are interaction matrix between the vias and excitation vector respectively.

After determining the coefficients from (8), we use the admittance matrix of rectangular waveguide [27] which is replaced with coaxial cable and U-shape slot coupling:

$$\begin{aligned} Y_{i,j} &= j\omega\varepsilon Z_i Z_j \iint G_{m2}(r_i, r_j) h^i h^j dS_i dS_j \\ &+ Z_i \int H_2^j(r) h^i dS_i \end{aligned}, \tag{9}$$

where h^i and h^j are magnetic field modal vector and Z_i, Z_j are wave impedance for each waveguide port. If we regard cross section of the SIW coupler waveguide port in the x-direction with the equivalent width of waveguide port a_{eqv} and y-direction with the substrate height h, for TE mode, h^i or h^j in (9) is obtained as:

$$\begin{aligned} h^{TE} &= \frac{-2}{(m^2 \frac{h}{a_{eqv}} + n^2 \frac{a_{eqv}}{h})^{\frac{1}{2}}} \hat{n}^p \times \\ &[\frac{m}{a_{eqv}} \cos(\frac{m\pi}{a_{eqv}} x) \sin(\frac{n\pi}{h} y) \hat{x} \\ &+ \frac{n}{h} \sin(\frac{m\pi}{a_{eqv}} x) \cos(\frac{n\pi}{h} y) \hat{y}]. \end{aligned} \tag{10}$$

Similarly for TM mode,

$$\begin{aligned} h^{TM} &= \frac{(\varepsilon_m \varepsilon_n)^{1/2}}{(m^2 \frac{h}{a_{eqv}} + n^2 \frac{a_{eqv}}{h})^{\frac{1}{2}}} \hat{n}^p \times \\ &[\frac{n}{h} \cos(\frac{m\pi}{a_{eqv}} x) \sin(\frac{n\pi}{h} y) \hat{x} \\ &- \frac{m}{a_{eqv}} \sin(\frac{m\pi}{a_{eqv}} x) \cos(\frac{n\pi}{h} y) \hat{y}]. \end{aligned} \tag{11}$$

In (10) and (11):

$$m, n = 0, 1, 2, 3, ...,\ m = n = 0 \ \ is\ excluded,$$

and

$$\varepsilon_k = \begin{cases} 1 & if\ k = 0 \\ 2 & if\ k \neq 0 \end{cases},$$

where $\hat{n}^p$ denotes the unit normal vector to the waveguide port.

From the knowledge of the admittance matrix, the scattering matrix of the SIW coupler can simply be computed [28].

V. RESULTS AND DISCUSSION

The proposed algorithm in Section IV has been implemented in Matlab code. The TE10 mode propagation is considered for all the waveguide ports of the analyzed SIW coupler.

Attaining to 0.01 error of the coupler parameters, N_ϕ=7 and N_z=2 cylindrical modes in (3) and (6) have been selected, and the obtained results are validated with the simulation and experimental conclusions.

In our attempt, the substrate material and the thickness are Rogers R04003 with ε_r=3.55 and h=0.813 mm in the order mentioned. Figure 4 depicts a manufactured SIW rat-race coupler with the dimensions which have been acquired in Section III.

The coupler S-parameters from the analysis, CST time domain solver and measurement are shown in Figs. 5 and 6. From Fig. 5 (a), the return losses (S_{11}) and isolations (S_{41}) are less than -18 dB and -20 dB over 11-15 GHz (30% relative bandwidth) respectively. In addition, the insertion losses between the output ports, ports 2 and 3, are divided equally from -3-1.7 dB to -3 + 1 dB in Fig. 5 (b). As shown in Fig. 6, throughout 11-15 GHz, the phase differences between ports 2 and 3 for in-phase are in the range of 0°-4.7° to 0°+2.1°, when port 4 is excited and for out-of-phase are from 180°-4° to 180°+2.5°, when port 1 is excited. Obviously, very good agreement has been obtained from our method, simulation and measurement which this matter confirms accuracy of the proposed analysis.

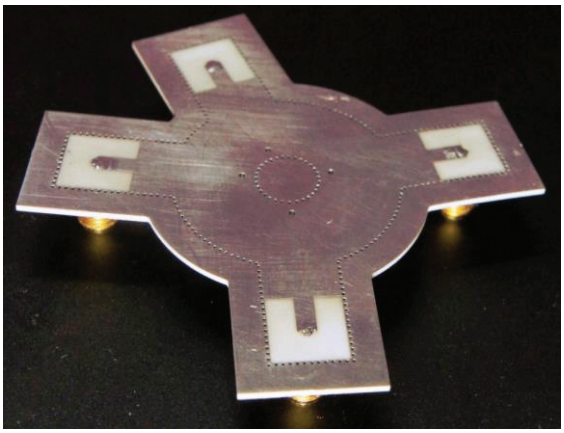

Fig. 4. The photograph of the manufactured SIW rat-race (hybrid ring) coupler.

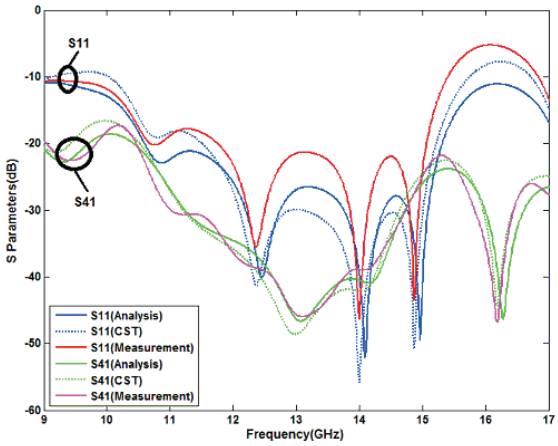

(a)

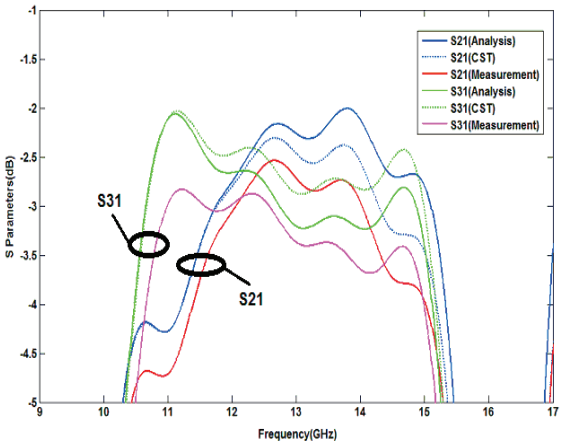

(b)

Fig. 5. Comparison of the SIW hybrid ring coupler S-parameters: (a) return loss (S_{11}) and isolation (S_{41}), and (b) insertion losses (S_{21} and S_{31}).

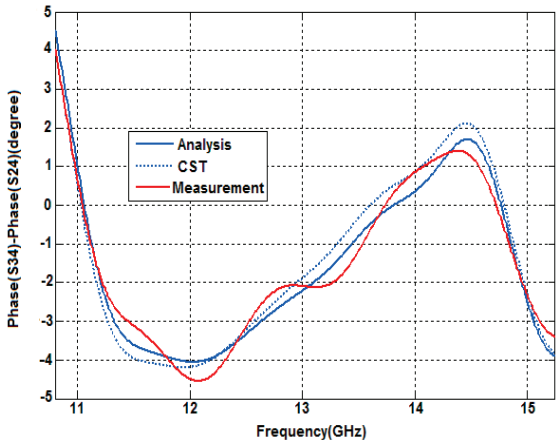

(a)

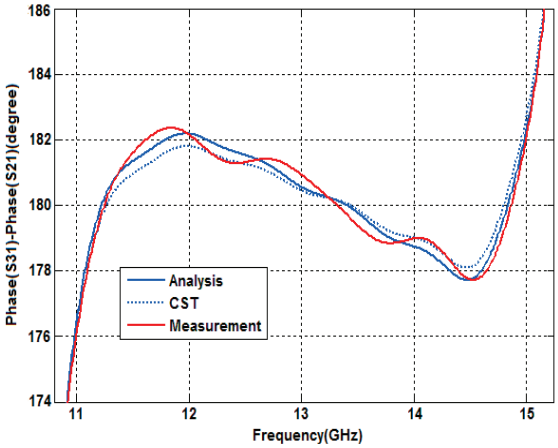

(b)

Fig. 6. The phase difference responses: (a) in-phase response, and (b) out-of-phase response.

To prove the efficiency of our analysis, the coupler has been compared with HFSS and CST frequency domain solver as well as CST time domain solver. In the case of analysis, HFSS and CST frequency domain solver, the allowed error for the S-parameters convergence of the coupler is 1% and we have used 50 frequency points for the output results. After calculating the all frequency points, the run time ratio of the analysis is related to HFSS is 1/21 and CST frequency domain solver is 1/20, while to CST time domain solver is 1/12.5 ratio. So, our method has the best efficiency and the CST time domain solver efficiency is much closer to the analysis rather than HFSS or CST frequency domain. Table 1 has reported the simulation time of the proposed coupler from the analysis, CST and HFSS.

Table 1: Simulation time on a Core i5 with 4-GB RAM (azimuthally mode numbers=7, vertically mode numbers=2)

Structure Type	Vias Number	CST CPU Time	HFSS	Analysis
		Time Domain	Frequency Domain	50 Frequency Points
SIW Hybrid ring (rat-race) coupler	324	1500s	2520s	120s

VI. CONCLUSION

This paper presents a novel SIW transition as an application for the SIW hybrid ring (rat-race) coupler under analysis. By using U-shape slot-coupled transitions, the relative bandwidth of the rat-race coupler has been increased up to 30% with low loss, low profile and high isolation in the operated frequency. This hybrid ring coupler has been analyzed with an efficient and accurate method of mode matching to calculate the scattering matrix. The output parameters of the analyzed and optimized coupler have been justified with full wave simulation and experimental results. Without losing the generality of the analysis, our method is a good candidate for the relative bandwidth improving (up to 30 percent) of the other passive SIW structures.

REFERENCES

[1] K. Wu, D. Deslandes, and Y. Cassivi, "The substrate integrated circuits-a new concept for high-frequency electronics and optoelectronics," *In Proc. 6th International Conference on Telecommunications in Modern Satellite, Cable and Broadcasting Service TELSIKS 2003*, vol. 1, pp. P-III-P-X, 2003.

[2] Z. Q. Xu, P. Wang, J. X. Liao, and Y. Shi, "Substrate integrated waveguide filter with mixed coupled modified trisections," *IET Electronic Letter*, vol. 49, pp. 482-483, March 2013.

[3] H. Min-Hua and L. Cheng-Siou, "Novel balanced bandpass filters using substrate integrated half-mode waveguide," *IEEE Microwave and Wireless Component Letters*, vol. 23, pp. 78-80, February 2013.

[4] Z. Li, M. S. Mahani, and R. Abhari, "Experiment of substrate integrated waveguide interconnect measurement for high speed data transmission application," *Microw. Opt. Technol. Lett*., vol. 54, no. 2, pp. 401-405, February 2012.

[5] F. Giuppi, A. Georgiadis, A. Collado, and M. Bozzi, "Active substrate integrated waveguide (SIW) antenna with phase-shifterless beam-scanning capabilities," *IEEE MTT-S Int. Microwave Symp. Dig*., pp. 1-3, June 2012.

[6] E. Ofli, R. Vahldieck, and S. Amari, "Novel E-plane filters and diplexers with elliptic response for millimeter-wave applications," *IEEE Trans. Microw. Theory Tech*., vol. 53, no. 3, pp. 843-851, March 2005.

[7] W. M. Abdel-Wahab and S. Safavi-Naeini, "Low loss double-layer substrate integrated waveguide-hybrid branch line coupler for mm-wave antenna arrays," *IEEE Antennas and Propagation International Society Symposium (APSURSI)*, pp. 2074-2076, 2011.

[8] K. Song, F. Zhang, F. Chen, and Y. Fan, "Wideband millimetre-wave four-way spatial power combiner based on multilayer SIW," *Journal of Electromagnetic Waves and Applications*, vol. 27, nos. 13, 1715-1719, 2013.

[9] Y. Liu, X. H. Tang, and T. Wu, "SIW-based low phase-noise millimeter-wave planar dual-port voltage-controlled oscillator," *Journal of Electromagnetic Waves and Applications*, vol. 27, nos. 8-9, 1059-1069, 2012.

[10] T. Kai, J. Hirokawa, and M. Ando, "Transformer between a thin postwall waveguide to a standard metal waveguide," *In IEEE Antennas Propagation Society Symp. Dig*., pp. 436-439, June 2002.

[11] D. Deslandes and K. Wu, "Integrated microstrip and rectangular waveguide in planar form," *IEEE Microw. Wireless Compon. Lett*., vol. 11, no. 2, pp. 68-70, February 2001.

[12] N. Jain and N. Kinayman, "A novel microstrip mode to waveguide mode transformer and its applications," *In IEEE MTT-S Int. Microwave Symp. Dig*., pp. 623-626, May 2001.

[13] Y. Huang, K. L. Wu, and M. Ehlert, "An integrated LTCC laminated waveguide-to-microstrip line T-junction," *IEEE Microw. Wireless Compon. Lett*., vol. 13, no. 8, pp. 338-339, August 2003.

[14] S. Lin, A. E. Fathy, and A. Elsherbini, "Development of a novel UWB vivaldi antenna array using SIW technology," *Progress In Electromagnetics Research, PIER 90*, 369-384, 2009.

[15] R. Kazemi, A. E. Fathy, S. Yang, and R. A. Sadeghzadeh, "Development of an ultra-wide band GCPW to SIW transition," *IEEE Radio and Wireless Symposium (RWS)*, pp. 171-174, January 2012.

[16] E. D. Caballero, H. Esteban, A. Belenguer, and V. Boria, "Efficient analysis of substrate integrated waveguide devices using hybrid mode matching between cylindrical and guided modes," *IEEE Trans. Microw. Theory Tech*., vol. 60, no. 2, pp. 232-243, February 2012.

[17] A. Belenguer, H. Esteban, E. Diaz, C. Bachiller, J. Cascon, and V. E. Boria, "Hybrid technique plus fast frequency sweep for the efficient and accurate analysis of substrate integrated waveguide devices," *IEEE Trans. Microw. Theory Tech*., vol. 59, no. 3, pp. 552-560, March 2011.

[18] E. Arnieri and G. Amendola, "Analysis of substrate integrated waveguide structures based on the parallel-plate waveguide green's function," *IEEE Trans. Microw. Theory Tech*., vol. 56, no. 7, pp. 1615-1623, July 2008.

[19] B. Wu and L. Tsang, "Full-wave modeling of

multiple vias using differential signaling and shared antipad in multilayered high speed vertical interconnects," *Progress In Electromagnetics Research, PIER 97*, 129-139, 2009.

[20] M. Casaletti, R. Sauleau, and M. Ettorre, "Efficient analysis of metallic and dielectric posts in parallel-plate waveguide structures," *IEEE Trans. Microw. Theory Tech*., vol. 60, no. 10, pp. 2979-2989, October 2012.

[21] E. Arnieri and G. Amendola, "Method of moments analysis of slotted substrate integrated waveguide arrays," *IEEE Trans. Antennas Propag*., vol. 59, no. 4, pp. 1148-1154, April 2011.

[22] H. Zairi, H. Baudrand, A. Gharsalla, and A. H. Gharb, "An efficient iterative method for analysis of a substrate integrated waveguide structures," *Microw. Opt. Technol. Lett*., vol. 52, no. 1, pp. 45-48, January 2010.

[23] W. Che, K. Deng, E. K. N. Yung, and K. Wu, "H-plane 3-dB hybrid ring of high isolation in substrate integrated rectangular waveguide (SIRW)," *Microw. Opt. Technol. Lett*., vol. 48, no. 3, pp. 502-505, March 2006.

[24] A. R. Mehrabian and C. Lucas, "A novel numerical optimization algorithm inspired from weed colonization," *Ecological Informatics*, vol. 1, 355-366, 2006.

[25] C. T. Tai, "Generalized vector and dyadic analysis: applied mathematics in field theory," series on Electromagnetic Waves, Piscataway, *IEEE Press*, 1991.

[26] C. T. Tai, "Dyadic green's function in electromagnetic theory," series on Electromagnetic Waves, Piscataway, *IEEE Press*, 1993.

[27] R. E. Collin, "Field theory of guided waves," series on Electromagnetic Waves, Piscataway, *IEEE Press*, 1993.

[28] D. M. Pozar, "Microwave engineering," 3rd edition, *John Wiley & Sons Inc*., 2005.

Ramin Dehdasht-Heydari was born in Esfahan-Iran, in 1983. He received the B.Sc. and M.Sc.degrees in Electrical Eng. in 2005 and 2008 from the Shahid Sattari and Shahed Universities, Tehran-Iran, respectively. He currently is pursuing his Ph.D. thesis with the Science & Research Branch, Islamic Azad University, Tehran-Iran. His principal fields of interest in research are UWB antennas, microwave and millimeter wave circuits, and numerical electromagnetism methods.

Keyvan Forooraghi received the M.Sc. degree in Electrical Engineering, the Licentiate of Technology degree and the Ph.D. degree in Electrical Engineering in 1991 from Chalmers University of Technology, Gothenburg, Sweden. He worked as a Researcher at Chalmers University of Technology from 1991 to 1992. In 1992, he joined the Department of Computer and Electrical Engineering, Tarbiat Modares University. Presently he is a Full Professor with the Communication Group. His research interests include electromagnetic theory and computational electromagnetic and antenna theory.

Mohammad Naser-Moghadasi was born in Saveh, Iran, in 1959. He received the B.Sc. degree in Communication Eng. in 1985 from the Leeds Metropolitan University, UK. From 1987 to 1989, he was awarded a full scholarship by the Leeds Educational Authority to pursue an M.Phil. studying in CAD of Microwave Circuits.

He received his Ph.D. in 1993, from the University of Bradford, UK. He was offered then a two years Post Doc. to pursue research on Microwave cooking of materials at the University of Nottingham, UK. In 1995, Naser-Moghadasi joined Islamic Azad University, Science & Research Branch, Iran, where he currently is an Associate Professor and Head of Postgraduate Studies.

His main areas of interest in research are Microstrip antenna, Microwave passive and active circuits, RF MEMS. He has so far published over 140 papers in different journals and conferences.

An Integral Equation-Based Approach to Analyzing Symmetrical Electromagnetic Models Through Decomposition and Recomposition of Excitation Vectors

Jianxun Su [1], Zhengrui Li [1], Yaoqing (Lamar) Yang [2], and Guizhen Lu [1]

[1] Department of Information Engineering
Communication University of China, Beijing, 100024, China
sujianxun_jlgx@163.com, lizengrui@cuc.edu.cn, luguizhen@cuc.edu.cn

[2] Department of Computer and Electronics Engineering
University of Nebraska-Lincoln, NE, 68182, USA
yyang3@unl.edu

Abstract ─ In this paper, an Integral Equation-based Simplification Method (IE-SM) is presented for the efficient analysis of the symmetrical electromagnetic model. The proposed approach stems from the decomposition and recomposition of any arbitrary excitation sources into a set of independent vectors which induce a symmetrical current distribution. Compared to the Conventional Integral Equation (CIE) method for modeling an entire structure, this simplification method not only saves computation resources and time by reducing the number of unknowns, but also maintains the computation accuracy. In addition, this method has a simple integral equation formulation, so it can be easily accelerated with fast algorithms and integrated into the existing Method of Moments (MoM) codes. Numerical examples show that the proposed method demonstrates both satisfactory accuracy and efficiency with less computational complexity.

Index Terms ─ Integral equation, recomposition, symmetry model, vector decomposition.

I. INTRODUCTION

Method of Moments (MoM)-based integral equation solvers are widely used for analyzing time-harmonic electromagnetic radiation and scattering problems. For a practical electromagnetic problem, many targets, such as tank, aircraft, missile, and some microwave & optical devices have elegant symmetric property. To take advantage of the symmetry, the numerical model can be simplified and the number of the unknowns can be greatly reduced. In [1], Lobry, et al., proposed a simplification method for rotational symmetry models with the boundary element method. In [2] and [3], Naito, et al., also made a great contribution to the simplification of symmetry model. The impedance matrix can be transformed to a bordered block diagonal matrix by using spatial eigenmodes transformation. A similar approach with discrete Fourier transform matrix has been reported [4]. However, for an electrically large problem, the matrix transformation process requires huge physical memory and longer computation time. Matrix transformation is difficult to be accelerated by fast multipole algorithms or other related algorithms. Therefore, it is not suitable for an electrically large problem. Furthermore, this transformation is too complicated to be integrated into the existing MoM code [5].

Commercial electromagnetic software such as Ansoft HFSS/Designer, Agilent ADS, EMSS FEKO, CST etc., uses electric and magnetic symmetry planes to simplify the symmetrical electromagnetic model [6]-[8]. The prerequisite of the application of magnetic or electric symmetry planes is the symmetrical distribution of the induced fields, which requires both geometry and excitation sources to be identically symmetrical. Therefore, when using magnetic or electric

Submitted On: November 26, 2013
Accepted On: October 5, 2014

symmetry planes, geometry and excitations should be symmetrical. The requirement of symmetry excitations severely limits the use of magnetic and electric symmetrical planes of commercial electromagnetic software.

In this paper, an effective simplification method for the symmetrical electromagnetic model is presented. The excitation vector is decomposed and recomposed into a set of independent vectors. For each new excitation vector, the induced current distribution is symmetrical, so that only a part of the induced current needs to be computed. This approach employs a simple integral equation in which one field triangle corresponds to multiple source triangles. Therefore, it is easy to interface with fast algorithms and integrate with the existing MoM codes. Moreover, the current continuity at the truncated boundary of the simplified model is described in detail. A new basis function is derived from the Rao-Wilton-Glisson (RWG) basis function, which is more suitable to achieve the current continuity at the truncated boundary.

II. PROBLEM FORMULATION

A. Integral-equation and basis function

Let S be the surface of a metallic object. By enforcing the boundary conditions on the Perfect Electric Conductor (PEC) surface S, the Mixed-Potential Integral Equation (MPIE) is given as [9]:

$$-\hat{n}\times\vec{E}^{inc}=\hat{n}\times\left[-j\omega\ddot{G}_A\otimes\vec{J}+\frac{1}{j\omega}(\nabla G_V)\otimes(\nabla'\vec{J})\right], \quad (1)$$

where $\vec{E}^{inc}$ is the incident electric field, $\hat{n}$ is the outside unit normal to S, $\vec{J}$ is the unknown current density on S, and $\ddot{G}_A$ and G_V are the vector and scalar potential Green's functions.

Testing equation (1) with basis function can be rewritten in a matrix form as follows;

$$[Z][I]=[V], \quad (2)$$

where [Z] is the impedance matrix. [V] is a voltage excitation vector. [I] is the unique solution to the impedance equation. Specifically, for a plane symmetry structure, impedance matrix [Z] is a multilevel block circulant matrix, where each level is a 2x2 block circulant [10].

There are two kinds of basis functions shown in Fig. 1 [11], the Rao-Wilton-Glisson (RWG) basis function and the half-RWG basis function. The half-RWG basis function is derived from the RWG:

$$f_n(\vec{r})=\begin{cases}(l_n/2A_n^+)\rho_n^+(\vec{r}), & \vec{r}\ inside\ T_n^+\\ (l_n/2A_n^-)\rho_n^-(\vec{r}), & \vec{r}\ inside\ T_n^-\\ 0, & otherwise\end{cases}, \quad (3)$$

where l_n is the length of the common edge, and $A_n^{\pm}$ is the area of triangle $T_n^{\pm}$. Vector ρ_n^- connects the observation point $\vec{r}$ to the free vertex of the minus triangle. Vector ρ_n^+ connects the free vertex of plus triangle to the observation point. The red line in Fig. 1 stands for the common edge of two adjacent triangles. Half-RWG consists only of one triangle facet.

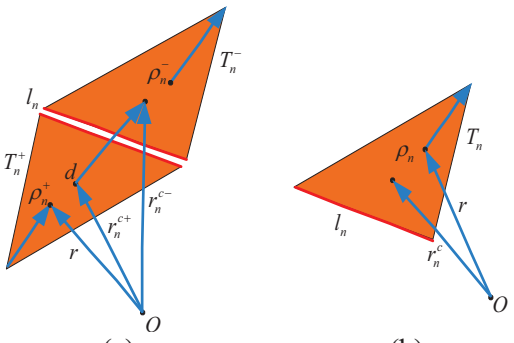

Fig. 1. Two kinds of basis function: (a) RWG basis function, and (b) half-RWG basis function.

B. Decomposition of plane wave excitation vector

In this paper, a plane wave is taken as the excitation source to introduce the presented method. Considering a scattering problem, the voltage vector is given by [12, eq. (2.8)]:

$$V_m=l_m\left(\vec{E}_m^+\vec{\rho}_m^{c+}/2+\vec{E}_m^-\vec{\rho}_m^{c-}/2\right),$$
$$\vec{E}_m^{\pm}=E^{inc}\left(\vec{r}_m^{c\pm}\right),\quad m=1,\ldots,N, \quad (4)$$

where

$$\vec{\rho}^c=\hat{x}\rho_x^c+\hat{y}\rho_y^c+\hat{z}\rho_z^c$$
$$\vec{r}^c=\hat{x}r_x^c+\hat{y}r_y^c+\hat{z}r_z^c$$

$\vec{E}^{inc}$ is the electric field of an incident electromagnetic signal; the voltage excitation vector is similar to the circuit voltage with units of Vm. The dot product in equation (4) is expanded as follows:

$$\vec{E}\vec{\rho}^c=\left(\vec{\rho}^c\vec{E}_0\right)e^{-j\vec{k}\vec{r}^c}$$
$$=(A+B+C)\left[D+E+F+G-j(H+I+J+K)\right], \quad (5)$$

where

$$A = E_{0x}\rho_x^c,\ B = E_{0y}\rho_y^c,\ C = E_{0z}\rho_z^c,$$
$$D = \cos(k_x r_x^c)\cos(k_y r_y^c)\cos(k_z r_z^c),$$
$$E = -\sin(k_x r_x^c)\sin(k_y r_y^c)\cos(k_z r_z^c),$$
$$F = -\sin(k_x r_x^c)\cos(k_y r_y^c)\sin(k_z r_z^c),$$
$$G = -\cos(k_x r_x^c)\sin(k_y r_y^c)\sin(k_z r_z^c),$$
$$H = -\sin(k_x r_x^c)\cos(k_y r_y^c)\cos(k_z r_z^c),$$
$$I = -\cos(k_x r_x^c)\sin(k_y r_y^c)\cos(k_z r_z^c),$$
$$J = -\cos(k_x r_x^c)\cos(k_y r_y^c)\sin(k_z r_z^c),$$
$$K = \sin(k_x r_x^c)\sin(k_y r_y^c)\sin(k_z r_z^c).$$

According to the linear system characteristics of a plane symmetry structure, the excitation vectors needs to be decomposed and recomposed into a set of new independent vectors. For each new vector, a MoM linear system can obtain an efficient solution.

III. CLASSIFICATION AND SIMPLIFICATION OF SYMMETRY STRUCTURES

The structure of plane symmetry can be divided into three categories as shown in Fig. 2. The number of symmetry planes of an isosceles triangle, a rectangular, and a sphere, are one, two and three respectively. The symmetry planes are orthogonal to each other.

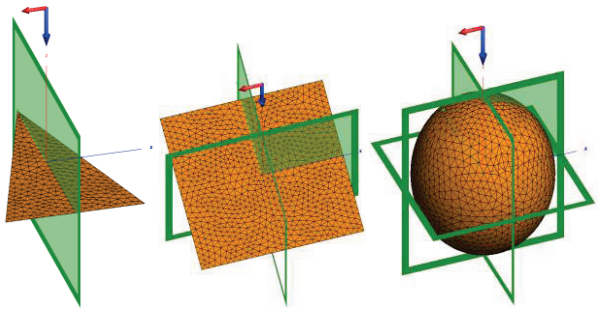

(a) (b) (c)

Fig. 2. Classification of symmetry structures: (a) single symmetry plane, (b) double symmetry planes, and (c) triple symmetry planes.

A. Single symmetry plane

An isosceles triangle patch is taken as an example of a single symmetry plane. It is symmetrical about the yoz-plane shown in Fig. 3.

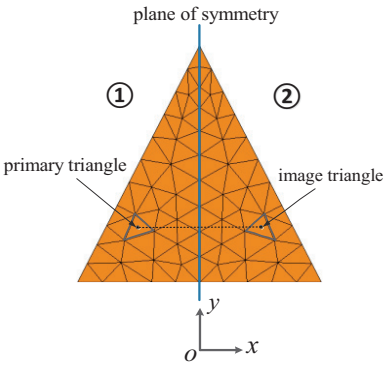

Fig. 3. Isosceles triangle patch.

The model of a single symmetry plane is divided into two subregions. The impedance matrix is a 2x2 block circulant matrix. The simultaneous equations are set up as follows:

$$\begin{bmatrix}\{Z_{11}\} & \{Z_{12}\}\\ \{Z_{12}\} & \{Z_{11}\}\end{bmatrix}\times\begin{bmatrix}\{I_1\}\\ \{I_2\}\end{bmatrix}=\begin{bmatrix}\{V_1\}\\ \{V_2\}\end{bmatrix}, \tag{6}$$

where

$$\{V_1\} = (AD - AE - AF - AG + BD - BE - BF - BG + CD - CE - CF - CG) - j(AH + AI + AJ - AK + BH + BI + BJ - BK + CH + CI + CJ - CK),$$
$$\{V_2\} = (AD + AE - AF + AG - BD - BE + BF - BG + CD + CE - CF + CG) - j(AH - AI + AJ + AK - BH + BI - BJ - BK + CH - CI + CJ + CK).$$

They can also be recomposed as follows:

$$\{V_1\} = \{\kappa_1\} + \{\kappa_2\}, \tag{7}$$
$$\{V_2\} = \{\kappa_1\} - \{\kappa_2\}, \tag{8}$$

where

$$\{\kappa_1\} = (AD - AF - BE - BG + CD - CF) - j(AH + AJ + BI - BK + CH + CJ),$$
$$\{\kappa_2\} = -(AE + AG - BD + BF + CE + CG) - j(AI - AK + BH + BJ + CI - CK).$$

Therefore, excitation vector [V] in equation (2) can be decomposed into two new independent vectors [13] as follows:

$$[V_1] = \begin{bmatrix}\{\kappa_1\}\\ \{\kappa_1\}\end{bmatrix}, \tag{9}$$

$$[V_2]=\begin{bmatrix}+\{\kappa_2\}\\-\{\kappa_2\}\end{bmatrix}. \tag{10}$$

The sign relationship of two new excitation vectors between two subregions of the geometry model is shown in Table 1.

Table 1: Sign relationship of new excitation vectors

Subregion	$[V_1]$	$[V_2]$
①	+	+
②	+	−

(1) Computing the induced current of excitation vector $[V_1]$.

Because the impedance matrix is 2x2 block circulant matrix, the sign of current expansion coefficients is the same as that of the excitation vector. We can obtain the current expansion coefficient relationship between two subregions as illustrated in Fig. 4:

$$\{I_1\}=\{I_2\}. \tag{11}$$

Because two subregions of the electromagnetic model have the same current coefficient, only one half of the current in this model needs to be solved. Consequently, the impedance matrix of the Mixed-Potential Integral Equation (MPIE) is given by:

$$\begin{aligned}Z_{mn}=\sum_{k=1}^{2}c(k)\Big\{&j\omega\left\langle f_m,\ddot{G}_A\otimes f_{nk}\right\rangle\\&+\frac{1}{j\omega}\left\langle\nabla f_m,G_V\otimes(\nabla' f_{nk})\right\rangle\Big\},\end{aligned} \tag{12}$$

where

$$c(k)=1,\ if\ k=1,2.$$

One field triangle corresponds to two source triangles as shown in Fig. 4. f_{n1} is the basis function of primary source triangle n_1; f_{n2} is the basis function of the other source triangle n_2, respectively.

The current of two parts have the relationship as follows:

$$\vec{I}_{1x}=-\vec{I}_{2x}, \tag{13}$$

$$\vec{I}_{1y}=\vec{I}_{2y}. \tag{14}$$

As shown in Fig. 4, there is no current flowing through the symmetry plane (yoz-plane). Symmetry plane is equivalent to PEC plane. Therefore, the triangle facets connecting yoz-plane are not assigned for the half-RWG basis function.

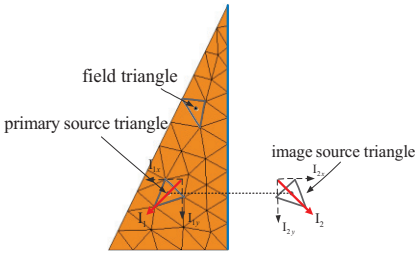

Fig. 4. The field and source triangles. Red arrows are the current direction of the two source triangles.

(2) Computing the induced current of excitation vector $[V_2]$.

We can further derive the current coefficients relationship between two subregions shown in Fig. 5:

$$\{I_1\}=-\{I_2\}. \tag{15}$$

Consequently, only one half of the model needs to be analyzed. The impedance matrix of the Mixed-Potential Integral Equation (MPIE) is given by:

$$\begin{aligned}Z_{mn}=\sum_{k=1}^{2}\Big\{&c(k)\,j\omega\left\langle f_m,\ddot{G}_A\otimes f_{nk}\right\rangle\\&+\frac{1}{j\omega}\left\langle\nabla f_m,G_V\otimes(\nabla' f_{nk})\right\rangle\Big\},\end{aligned} \tag{16}$$

where

$$c(k)=\begin{cases}1, & if\ k=1\\-1, & if\ k=2\end{cases}.$$

One field triangle corresponds to two source triangles, as shown in Fig. 5.

There is normal current flowing through the yoz-plane (blue line). The symmetry plane is equivalent to a Perfect Magnetic Conductor (PMC) plane. Therefore, to ensure current continuity at the truncated boundary, the triangle facets connecting the yoz-plane should be assigned by the half-RWG basis function.

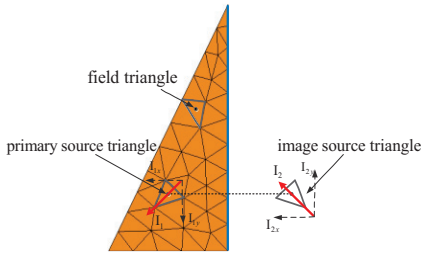

Fig. 5. The field and source triangles. Red arrows are the current direction of the two source triangles.

The assignment of half-RWG basis functions to the triangle facets connected to symmetry plane for different excitation vectors is summarized in Table 2. If there is normal current flowing through the symmetry plane, half-RWG basis functions are assigned to ensure the current continuity at the truncated edges.

Table 2: Assigned case of half-RWGs

	[V1]	[V2]
yoz-plane		H

(*H denotes half-RWG)

B. Double symmetry plane

Here, the rectangular patch is taken as an example of double symmetry planes. It is symmetrical about the xoz-plane and yoz-plane, as shown in Fig. 6.

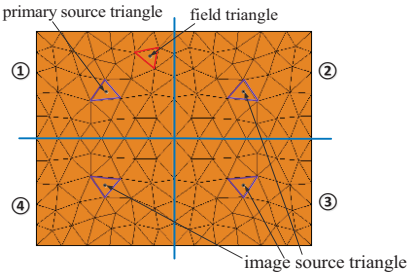

Fig. 6. Rectangular patch.

The model with double symmetry planes is divided into 4 subregions. The impedance matrix is a two-level block circulant matrix where each level is a 2x2 block circulant. The simultaneous equations are set up as follows:

$$\begin{bmatrix} \{Z_{11}\} & \{Z_{12}\} & \{Z_{13}\} & \{Z_{14}\} \\ \{Z_{12}\} & \{Z_{11}\} & \{Z_{14}\} & \{Z_{13}\} \\ \{Z_{13}\} & \{Z_{14}\} & \{Z_{11}\} & \{Z_{12}\} \\ \{Z_{14}\} & \{Z_{13}\} & \{Z_{12}\} & \{Z_{11}\} \end{bmatrix} \times \begin{bmatrix} \{I_1\} \\ \{I_2\} \\ \{I_3\} \\ \{I_4\} \end{bmatrix} = \begin{bmatrix} \{V_1\} \\ \{V_2\} \\ \{V_3\} \\ \{V_4\} \end{bmatrix}. \quad (17)$$

The excitation vector can be recomposed as follows:

$$[V] = \begin{bmatrix} \{V_1\} \\ \{V_2\} \\ \{V_3\} \\ \{V_4\} \end{bmatrix} = \begin{bmatrix} \{\kappa_1\} & +\{\kappa_2\} & +\{\kappa_3\} & +\{\kappa_4\} \\ \{\kappa_1\} & -\{\kappa_2\} & +\{\kappa_3\} & -\{\kappa_4\} \\ \{\kappa_1\} & +\{\kappa_2\} & -\{\kappa_3\} & -\{\kappa_4\} \\ \{\kappa_1\} & -\{\kappa_2\} & -\{\kappa_3\} & +\{\kappa_4\} \end{bmatrix}, \quad (18)$$

where

$$\{\kappa_1\} = (AD - BE - CF) - j(AJ - BE + CH),$$
$$\{\kappa_2\} = (-AE + BD - CG) - j(-AK + BJ + CI),$$
$$\{\kappa_3\} = (-AF - BG + CD) - j(AH + BI + CJ),$$
$$\{\kappa_4\} = (-AG - BF - CE) - j(AI + BH - CK).$$

Therefore, the excitation vector can be decomposed into 4 new independent vectors as follows:

$$[V] = [V_1] + [V_2] + [V_3] + [V_4], \quad (19)$$

where

$$[V_1] = \begin{bmatrix} +\{\kappa_1\} \\ +\{\kappa_1\} \\ +\{\kappa_1\} \\ +\{\kappa_1\} \end{bmatrix}, [V_2] = \begin{bmatrix} +\{\kappa_2\} \\ -\{\kappa_2\} \\ +\{\kappa_2\} \\ -\{\kappa_2\} \end{bmatrix}, [V_3] = \begin{bmatrix} +\{\kappa_3\} \\ +\{\kappa_3\} \\ -\{\kappa_3\} \\ -\{\kappa_3\} \end{bmatrix}, [V_4] = \begin{bmatrix} +\{\kappa_4\} \\ -\{\kappa_4\} \\ -\{\kappa_4\} \\ +\{\kappa_4\} \end{bmatrix}.$$

The sign relationship of new excitation vectors among 4 subregions of the symmetry model is shown in Table 3.

Table 3: Sign relationship of four new excitation vectors

Subregion	[V1]	[V2]	[V3]	[V4]
①	+	+	+	+
②	+	−	+	−
③	+	+	−	−
④	+	−	−	+

The assignment of half-RWG basis functions to the triangle facets connected to symmetry plane for different excitation vectors is summarized in Table 4. For example, the half-RWG basis should be assigned to the triangle facets connecting to the xoz-plane and the yoz-plane for excitation vector [V2].

Table 4: Assigned case of half-RWGs

	[V1]	[V2]	[V3]	[V4]
xoz-plane		H	H	
yoz-plane		H		H

(*H denotes half-RWG)

C. Triple symmetry plane

Here, the cuboid is taken as an example of triple symmetry planes. It is symmetrical about the xoy-plane, xoz-plane and yoz-plane, as shown in Fig. 7.

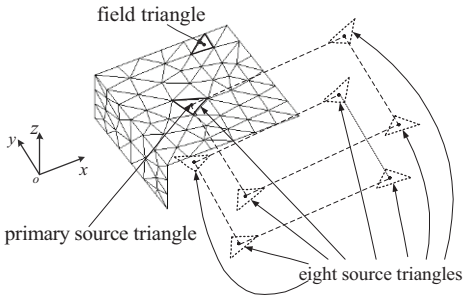

Fig. 7. Metal cuboid.

The model has three symmetry planes, so there are eight symmetrical subregions. The impedance matrix is a three-level block circulant matrix. The simultaneous equations are set up as follows:

$$\begin{bmatrix} \{Z_{11}\} & \{Z_{12}\} & \{Z_{13}\} & \{Z_{14}\} & \{Z_{15}\} & \{Z_{16}\} & \{Z_{17}\} & \{Z_{18}\} \\ \{Z_{12}\} & \{Z_{11}\} & \{Z_{14}\} & \{Z_{13}\} & \{Z_{16}\} & \{Z_{15}\} & \{Z_{18}\} & \{Z_{17}\} \\ \{Z_{13}\} & \{Z_{14}\} & \{Z_{11}\} & \{Z_{12}\} & \{Z_{17}\} & \{Z_{18}\} & \{Z_{15}\} & \{Z_{16}\} \\ \{Z_{14}\} & \{Z_{13}\} & \{Z_{12}\} & \{Z_{11}\} & \{Z_{18}\} & \{Z_{17}\} & \{Z_{16}\} & \{Z_{15}\} \\ \{Z_{15}\} & \{Z_{16}\} & \{Z_{17}\} & \{Z_{18}\} & \{Z_{11}\} & \{Z_{12}\} & \{Z_{13}\} & \{Z_{14}\} \\ \{Z_{16}\} & \{Z_{15}\} & \{Z_{18}\} & \{Z_{17}\} & \{Z_{12}\} & \{Z_{11}\} & \{Z_{14}\} & \{Z_{13}\} \\ \{Z_{17}\} & \{Z_{18}\} & \{Z_{15}\} & \{Z_{16}\} & \{Z_{13}\} & \{Z_{14}\} & \{Z_{11}\} & \{Z_{12}\} \\ \{Z_{18}\} & \{Z_{17}\} & \{Z_{16}\} & \{Z_{15}\} & \{Z_{14}\} & \{Z_{13}\} & \{Z_{12}\} & \{Z_{11}\} \end{bmatrix}. \quad (20)$$

The excitation vector can be recomposed as follows:

$$[V] = \begin{bmatrix} \{V_1\} \\ \{V_2\} \\ \vdots \\ \{V_8\} \end{bmatrix} = \begin{bmatrix} \{\kappa_1\}+\{\kappa_2\}+\{\kappa_3\}+\{\kappa_4\}+\{\kappa_5\}+\{\kappa_6\}+\{\kappa_7\}+\{\kappa_8\} \\ \{\kappa_1\}-\{\kappa_2\}+\{\kappa_3\}-\{\kappa_4\}+\{\kappa_5\}-\{\kappa_6\}+\{\kappa_7\}-\{\kappa_8\} \\ \{\kappa_1\}+\{\kappa_2\}-\{\kappa_3\}-\{\kappa_4\}+\{\kappa_5\}+\{\kappa_6\}-\{\kappa_7\}-\{\kappa_8\} \\ \{\kappa_1\}-\{\kappa_2\}-\{\kappa_3\}+\{\kappa_4\}+\{\kappa_5\}-\{\kappa_6\}-\{\kappa_7\}+\{\kappa_8\} \\ \{\kappa_1\}+\{\kappa_2\}+\{\kappa_3\}+\{\kappa_4\}-\{\kappa_5\}-\{\kappa_6\}-\{\kappa_7\}-\{\kappa_8\} \\ \{\kappa_1\}-\{\kappa_2\}+\{\kappa_3\}-\{\kappa_4\}-\{\kappa_5\}+\{\kappa_6\}-\{\kappa_7\}+\{\kappa_8\} \\ \{\kappa_1\}+\{\kappa_2\}-\{\kappa_3\}-\{\kappa_4\}-\{\kappa_5\}-\{\kappa_6\}+\{\kappa_7\}+\{\kappa_8\} \\ \{\kappa_1\}-\{\kappa_2\}-\{\kappa_3\}+\{\kappa_4\}-\{\kappa_5\}+\{\kappa_6\}+\{\kappa_7\}-\{\kappa_8\} \end{bmatrix}, \quad (21)$$

where

$$\{\kappa_1\} = (AD - BE - CF),\ \{\kappa_2\} = (-AE + BD - CG),$$
$$\{\kappa_3\} = (-AF - BG + CD),\ \{\kappa_4\} = (-AG - BF - CE),$$
$$\{\kappa_5\} = -j(AJ - BE + CH),\ \{\kappa_6\} = -j(-AK + BJ + CI),$$
$$\{\kappa_7\} = -j(AH + BI + CJ),\ \{\kappa_8\} = -j(AI + BH - CK).$$

Therefore the excitation vector in equation (2) is decomposed into eight new independent vectors as follows:

$$[V] = [V_1] + [V_2] + \cdots + [V_8]. \quad (22)$$

The sign relationship of the excitation vector among 8 subregions of the symmetry model is shown in Table 5.

Table 5: Sign relationship of eight new excitation vectors

Subregion	[V1]	[V2]	[V3]	[V4]	[V5]	[V6]	[V7]	[V8]
①	+	+	+	+	+	+	+	+
②	+	-	+	-	+	-	+	-
③	+	+	-	-	+	+	-	-
④	+	-	-	+	+	-	-	+
⑤	+	+	+	+	-	-	-	-
⑥	+	-	+	-	-	+	-	+
⑦	+	+	-	-	-	-	+	+
⑧	+	-	-	+	-	+	+	-

Table 6 shows the half-RWG basis functions, which are assigned to the triangle facets connected to the truncated edges for different excitation vectors.

Table 6: Assigned case of half-RWGs

	[V1]	[V2]	[V3]	[V4]	[V5]	[V6]	[V7]	[V8]
xoy-plane					H	H	H	H
xoz-plane		H	H			H	H	
yoz-plane		H		H		H		H

(*H denotes half-RWG)

The above analyses on three categories of plane-symmetry structure utilize a plane wave as the excitation. In practical electromagnetic applications, there are many other kinds of excitation sources, such as waveguide excitation, electric/magnetic point source, and aperture field source etc. For those excitation sources, the excitation vector of MoM linear system can also be decomposed and recomposed into a set of independent vectors with the aforementioned relationship. Therefore, the proposed approach can be used to effectively analyze symmetrical

electromagnetic models without the constraints of excitation sources.

IV. COMPUTATIONAL COMPLEXITY

Assume that the number of symmetrical subregions is *N*, the number of unknowns in each subregion is *M*, and the number of iterations to reach convergence is *k*.

The total unknown of CIE is *NM*. The complexity of matrix filling, storage and iterative solution are $o(N^2M^2)$, $o(N^2M^2)$ and $o(kN^2M^2)$, respectively.

For IE-SM, for the calculation of each impedance matrix element, one field triangle corresponds to *N* source triangles, so that *N* submatrices need to be calculated and stored. Therefore, complexity of matrix filling and storage becomes $o(NM^2)$. Actually, the matrix filling time of IE-SM would be less than $1/N$ of that of CIE. In terms of memory usage, IE-SM is $1/N$ of CIE.

In the Krylov iterative solution process, MoM linear system needs to be solved *N* times because the excitation vector is decomposed into *N* new independent vectors. Thus, complexity of the iterative solution is $o(NkM^2)$. As a result of less unknowns, IE-SM achieves more stable and rapid convergence than CIE. Actually, computation time of IE-SM is much less than $1/N$ of that of the CIE method. The comparison of the computational complexity of IE-SM and CIE is summarized in Table 7.

Table 7: Complexity statistics

	Memory	Matrix Filling Time	Iterative Solution Time
CIE	$o\left(N^2M^2\right)$	$o\left(N^2M^2\right)$	$o\left(kN^2M^2\right)$
IE-SM	$o\left(NM^2\right)$	$o\left(NM^2\right)$	$o\left(kNM^2\right)$

V. NUMERICAL SIMULATIONS

To validate the accuracy and the efficiency of the proposed approach, four numerical simulations are presented in this section. These simulations include the electromagnetic wave scatterings from a metallic sphere and a missile model, electromagnetic wave transmission through a cross-shaped quasi-optical filter, and electromagnetic wave radiation from a pyramidal horn antenna. All numerical experiments run on a HP mini workstation with quad-core 64-bit Intel i7-870 CPU and 16 GB of RAM. The resulting impedance matrices are iteratively solved using the GMRES (80) solver [14], where 80 is the restart number and the relative error tolerance is set to be 10^{-3}.

A. Metal sphere

For the first simulation, a metal sphere as shown in Fig. 8 was analyzed using the proposed simplification method. In the simulation, only one-8th of the model needs to be calculated. Our simulation results of bistatic Radar Cross-Section (RCS) agree very well with that of Mie series solution shown in Fig. 9. The normalized induced current distributions of the CIE and IE-SM method are compared in Fig. 10, and a good agreement can be observed. The one-8th model was discretized into 476 triangles, and the average side length of the triangle facets was about one-tenth of the wavelength. The matrix filling and solving time are only 3.1 and 6.8 s, respectively. The corresponding CPU time on the same PC is 26.4 and 141.8 s for modeling the whole structure with 3808 triangle facets. The number of iterations required for the norm of the relative residual to fall below 10^{-3} with IE-SM and CIE are 2 and 4, respectively.

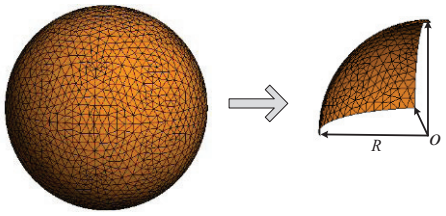

Fig. 8. The model of metal sphere with $R=1\lambda$ is simplified to one-8th model by symmetry.

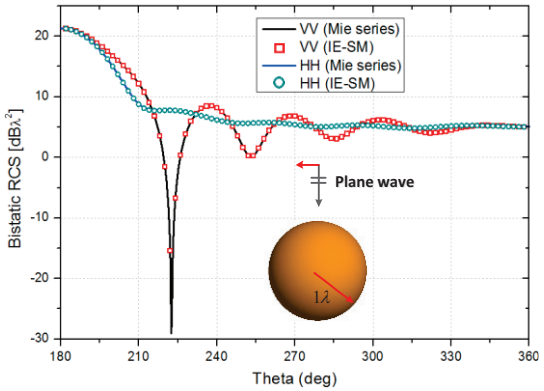

Fig. 9. The bistatic RCS of metal sphere.

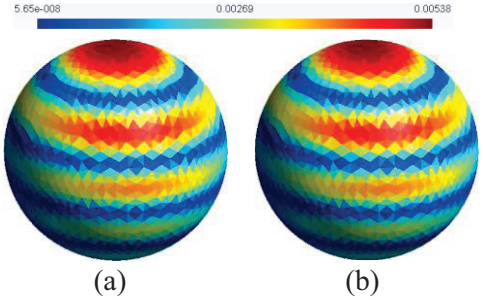

Fig. 10. Normalized current distribution of metal sphere: (a) CIE, and (b) IE-SM.

B. Missile model

Next, the bistatic RCS of a plane wave incident on a missile model is analyzed. The geometry of the problem is shown in Fig. 11. The bistatic RCS for a plane wave with vertical polarization at oblique incidence ($\theta^{inc}=45^0, \varphi^{inc}=45^0$) is plotted as a function of observation directions in Fig. 12. A very good agreement with the simulated values of modeling the entire structure is validated. Here, the one-4th model was discretized into 2600 triangular cells. The matrix filling and solving time were only 36.6 s and 175.2 s, respectively. The corresponding CPU time was 153.3 s and 2141.8 s for CIE modeling the whole structure. The number of iterations for IE-SM and CIE are 3 and 6, respectively. It is worth mentioning that the magnetic and electric symmetrical planes of commercial electromagnetic software can be used to analyze this missile structure provided the wave propagates along the axis direction of the missile with the E-field parallel to the wing.

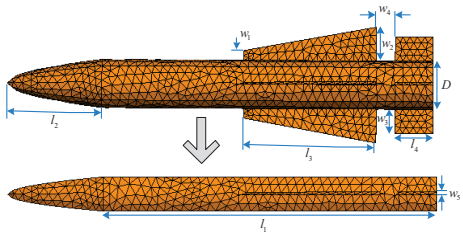

Fig. 11. The missile model is simplified to one-4th model by symmetry. Dimension are in λ: $l_1=7.0$, $l_2=2.0$, $l_3=2.8$, $l_4=0.8$, $w_1=0.2$, $w_2=0.7$, $w_3=0.5$, $w_4=0.4$, $w_5=0.04$, $D=1.0$; the depth of focus of the missile head is 1/32.

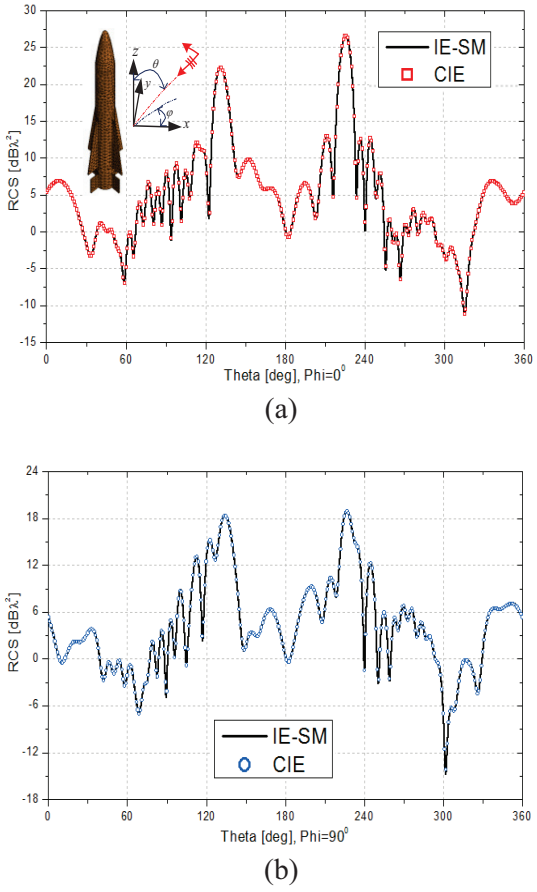

Fig. 12. The bistatic RCS of: (a) xoz-plane, and (b) yoz-plane.

C. Cross-shaped quasi-optical filter

A bandpass filter comprised of periodic cross-shaped holes with a resonance frequency of 280 GHz was analyzed as follows. The one-4th model shown in Fig. 13 is discretized into 218 triangles to ensure accurate results were obtained throughout the entire frequency band. The transmission coefficients for a plane wave with the E-field parallel to the x-axis at normal incidence (TEMx mode) are plotted as a function of frequency in Fig. 14. Black lines represent the results obtained using our proposed method, red lines represent the results using the simulation from [15], and curves with blue circles represent the measured values. A close agreement between the proposed method and the results in [15] has been achieved. The time for calculating a frequency point is 6.3 s, while it takes up to 28.4 s for computing the whole unit cell.

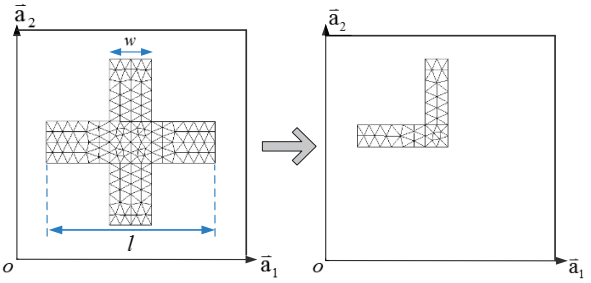

Fig. 13. The unit cell of cross-shaped aperture array is simplified to one-4th model. Dimension are in micrometers (mm): Square lattice period, $\vec{a}_1$=$\vec{a}_2$ = 810, slot length l = 570, slot width w=160.

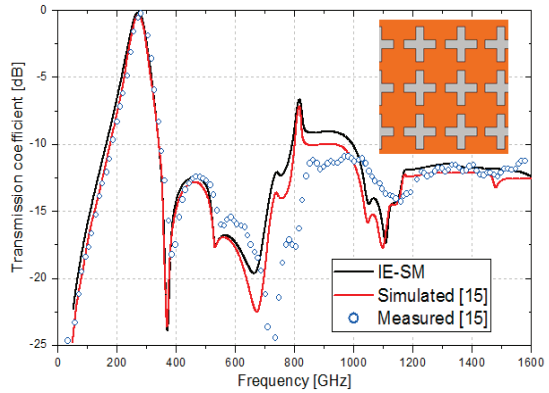

(a)

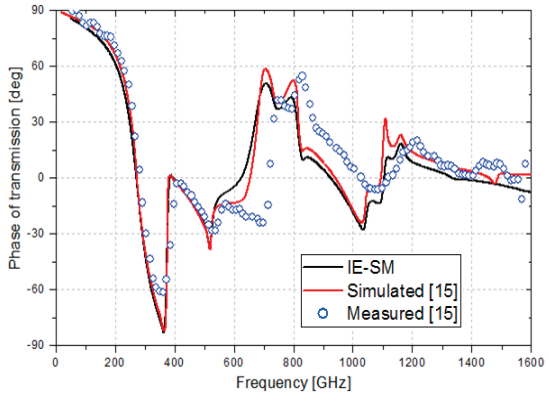

(b)

Fig. 14. (a) Magnitude, and (b) phase of the transmission coefficient.

D. Horn antenna

Finally, a pyramidal horn antenna [6] operating at the frequency 1.645 GHz was constructed and simulated. An illustration of the horn antenna is shown in Fig. 15. A waveguide mode excitation is applied to the feeding port. The desired mode (in this case a TE_{10} mode) is directly impressed to the rectangular waveguide section denoted by the red line shown in Fig. 15. The mesh size on the back face of the waveguide is one-fifteenth of the wavelength. Figure 16 shows the far field patterns of the E-plane and H-plane computed by IE-SM and the EMSS FEKO [6]. Excellent agreement is observed. Here, the one-4th model was discretized into 1300 triangular cells. The matrix filling and solving time were 9.8 and 77.5 s, respectively. If modeling the whole structure with 5200 triangle facets, the corresponding time of CIE would be 43 and 530 s. The number of iterations for IE-SM and CIE are 5 and 7, respectively.

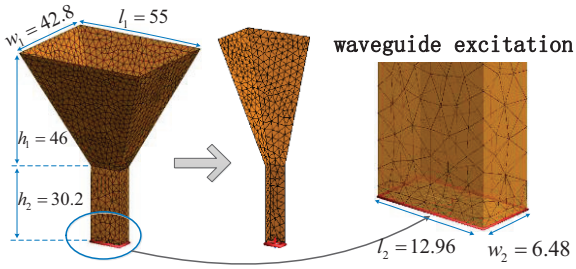

Fig. 15. The model of horn antenna is simplified to one-4th model. Dimension are in centimeters.

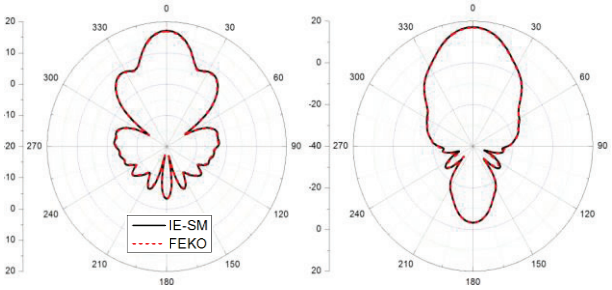

(a) (b)

Fig. 16. The far field pattern: (a) E-plane, and (b) H-plane.

VI. CONCLUSION

An integral equation-based simplification method is presented for the analysis of electromagnetic targets with plane symmetry. The proposed method does not require excitation resources to be identically symmetrical. It can make the induced current distribution symmetrical by decomposing and recomposing the excitation vector. Consequently, this method greatly reduces

the simulation time and memory usage compared with the Conventional Integral Equation (CIE) method. Numerical experiments validated the accuracy and the computational efficiency of the proposed IE-SM method.

ACKNOWLEDGMENT

This work was supported in part by the Major Program of the National Natural Science Foundation of China (NSFC) under Grant No. 61331002, in part by the NSFC under Grand No. 61201082, in part by school fund of CUC under Grand No. 3132014XNG1466, and in part by Excellent Innovation Team of CUC under Grand No. yxtd201303.

REFERENCES

[1] J. Lobry, J. Trecat, and C Broche, "Broken symmetry in the boundary element method," *IEEE Trans. Magn*., vol. 31, no. 3, May 1995.

[2] H. Tsuboi, A. Sakurai, and T. Naito, "A simplification of boundary element model with rotational symmetry in electromagnetic field analysis," *IEEE Trans. Magn*., vol. 26, no. 5, pp. 2771-2773, September 1990.

[3] H. Tsuboi, M. Tanaka, T. Misaki, M. Analoui, T. Naito, and T. Morita, "Reduction of vector unknowns using geometric symmetry in a triangular-patch moment method for electromagnetic scattering and radiation analysis," *IEEE Trans. Magn*., vol. 28, no. 2, March 1992.

[4] G. J. Burke and A. J. Poggio, "Numerical electromagnetics code (NEC)-method of moments," *Lawrence Livermore Laboratory*, January 1981.

[5] T. Naito and H. Tsuboi, "A simplification method for reflective and rotational symmetry model in electromagnetic field analysis," *IEEE Trans. Magn*., vol. 37, no. 5, September 2001.

[6] "User's manual," *FEKO Suite 6.0*, pp. 6-44, September 2010.

[7] *Ansys HFSS12 Full Book*, pp. 3.1-10, January 2010.

[8] *CST MICROWAVE STUDIO*, "*Workflow and solver Overview*," pp. 27-31, 2010.

[9] K. A. Michalski and J. R. Mosig, "Multilayered media Green's functions in integral equation formulations," *IEEE Trans. Antennas Propag*., vol. 45, pp. 508-519, March 1997.

[10] P. J. Davis, "Circulant matrices (2 edition)," *Chelsea Press*, 1994.

[11] S. M. Rao, D. R. Wilton, and A. W. Gilisson, "Electromagnetic scattering by surfaces of arbitrary shape," *IEEE Trans. Antennas Propag*., vol. AP-30, no. 3, pp. 409-518, 1982.

[12] S. N. Makarov, "Antenna and EM modeling with MATLAB," *New York: Wiley*, 2002.

[13] G. Strang, "Introduction to linear algebra," *Wellesley-Cambridge Press*, U.S., 2009.

[14] Y. Saad and M. H. Schultz, "GMRES: a generalized minimal residual algorithm for solving nonsymmetric linear systems," *SIAM J. Sci. Stat. Comput*., vol. 7, no. 3, pp. 856-869, July 1986.

[15] M. Bozzi, L. Perregrini, J. Weinzierl, and C. Winnewisser, "Efficient analysis of quasi-optical filters by a hybrid MoM/BI-RME method," *IEEE Trans. Antennas Propag*., vol. 49, no. 7, pp. 1054-1064, July 2001.

Jianxun Su received the M.S. and the Ph.D. degree in Electromagnetic Field and Microwave Technology from the Communication University of China and Beijing Institute of Technology, Beijing, China, in 2008 and 2011, respectively.

From 2011 to 2013, he was with East China Research Institute of Electronic Engineering (ECRIEE), where he engaged in phased-array research. He is currently working as Postdoctoral Fellow at Electromagnetic Laboratory, Communication University of China. His special research interests include integral equation methods for electromagnetic problems and periodic structure analysis.

Zhengrui Li received the B.S. degree in Communication and Information System from Beijing Jiaotong University, Beijing, China, in 1984; the M.S. degree in Electrical Engineering from the Communication University of China, Beijing, China, in 1987; and the Ph.D. degree in Electrical Engineering from Beijing Jiaotong University, Beijing, China, in 2009.

He is currently a Professor with the Communication University of China, Beijing, China. His research interests include the areas of computational electromagnetics, the Finite-Difference Time-Domain (FDTD) methods, electromagnetic modeling and simulation of antennas, and communication antennas. Li is a Senior Member of the Chinese Institute of Electronics.

Yaoqing (Lamar) Yang received his B.S. degree from the Beijing Jiaotong University, China, in 1983, and his M.S. degree from the Communication University of China, China, in 1986, both in Electrical Engineering. He received his Ph.D. degree in the area of Wireless Communications and Networks from the University of Texas (UT) at Austin in 2006.

He is now an Associate Professor in the Department of Computer and Electronics Engineering, University of Nebraska-Lincoln (UNL). His current research interests lie in wireless communications and networks with emphasis on radio channel characterizations, cognitive radio networks, and statistical signal processing. Yang is a Senior Member of IEEE.

Guizhen Lu was born in Beijing, China in 1957. He graduated from Peking University, Beijing, China, in 1984. From 1985 to present, he was with the Communication University of China. Now, he is a Professor in the same university. His main research interests are EMC and microwave technology.

Ultra Wideband Microwave Ten-Port Reflectometer

Amirhossein Askarian [1] and Gholamreza Moradi [2]

[1] Department of Electrical Engineering
Graduate Student of Amirkabir University of Technology, Tehran, Iran
askarian.amirhossein@aut.ac.ir

[2] Department of Electrical Engineering
Associate Professor of Amirkabir University of Technology, Tehran, Iran
ghmoradi@aut.ac.ir

Abstract ─ This paper describes and simulates the Ultra Wideband (UWB) Ten-Port Reflectometer (TPR). It is based on the concept of well-known six-port structure so that numbers of measuring ports are increased to eight in order to improve reliability and accuracy as well. This article presents UWB (2 GHz to 12 GHz) reflectometer using Rectangular Waveguide (RWG). It is proved that increasing numbers of measuring ports leads to improving accuracy and reliability of structure so that each port with corresponding port help to make wideband reflectometer as well as having reliable and robust structure. This prototype of ten-port reflectometer is simulated by Agilent ADS and using RWG that has more bandwidth, less loss and high Q-factor than other common transmission lines, say microstrip, SIW and CPW.

Index Terms ─ CPW, DUT, q-point, RWG, SIW, SPR, UWB, VNA.

I. INTRODUCTION

A six-port measurement technique (first introduced by Engen in 1977 [1]) is a simple and low cost method for measuring complex reflection coefficient in respect to conventional method using Vector Network Analyzer (VNA) [1]. Six-Port Reflectometer (SPR) is formed by a passive circuit with four scalar power detector ports for measuring the power and two ports for connecting the microwave source and Device Under Test (DUT). Very various structures for SPR proposed and analyzed in recent years, the SPRs have minimum-requirement numbers of ports for determining of complex reflection coefficient so that incapacitating of one power detector makes ambiguity in calculating of reflection coefficient. Key of solving this problem is increasing the numbers of measuring ports. In this pape,r we have increased them up to eight so that each measuring port has the back-up port. With counting two ports for signal generator and DUT mentioned structure has ten ports. In other words, simple ten-port reflectometer consisting of a structure with two ports for signal input and output and eight measuring ports with their corresponding power detectors for sampling the standing wave within the transmission line [2,3].

Figure 1 depicts the general diagram of TPR with planar structure, it consisting of two power dividers and nine 3 dB directional couplers that connected together via specified-length transmission lines. Lengths of transmission lines have been calculated in order to obtain maximum accuracy and precision for determining reflection coefficient when frequency is changed between microwave frequencies of 2 GHz and 12 GHz [1]. General equation of the TPR is presented in equation (1), which consists of six circles so that intersection of them in complex plane, obtain the unique complex reflection coefficient [1-3]:

$$p_i = k_i|\Gamma - q_i|^2 \quad i = 1,2,\dots,6, \tag{1}$$

where p_i is normalized power in each measuring port, k_i is calibration constant, Γ is complex reflection coefficient of DUT and q_i is circles center that depend on the TPR structure.

In ideal frequency-compensation TPR, when frequency is changed, characteristic (say S-

Submitted On: June 21, 2013
Accepted On: September 26, 2014

parameters) of the reflectometer must not be changed because intersection of circles should be in specified point, which only depends on the reflection coefficient of DUT. In practice, however, centers of circles q_i-points rotate in Γ plane with wide variety of frequency. As mentioned in equation (1), six equations in TPR with corresponding six q_i-points arranged symmetrically around the plane as shown in Fig. 2, in other words, phase of three q_i-points, q_1, q_2, and q_3 differ by about 120 degrees and about q_4, q_5, and q_6 as well. These two groups are arranged with 180 degrees out-of-phase in Γ plane. In other words, mentioned TPR consists of two six-port structures that coupled together by means of two 3 dB directional couplers 1 and 2 according to Fig. 2. Mentioned couplers make 180 degrees out-of-phase in each group of q_i-points.

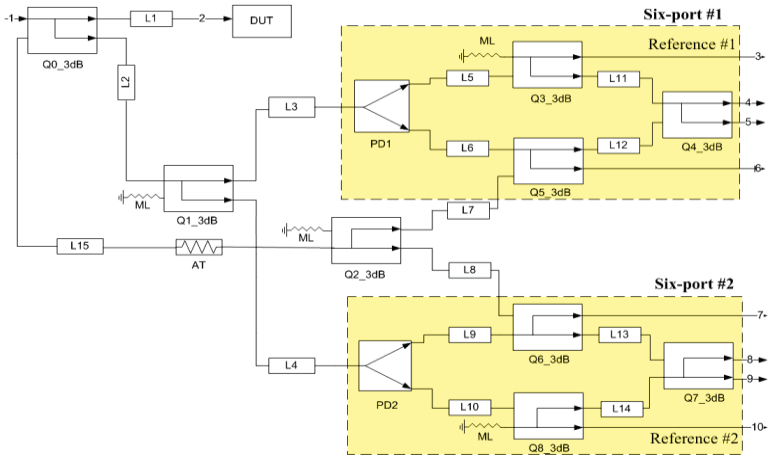

Fig. 1. General diagram of TPR.

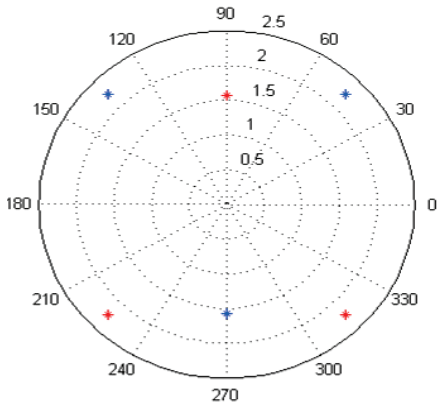

Fig. 2. Constellation of q_i-points in TPR.

II. ANALYSIS OF FREQUENCY-COMPENSATION OF TPR

In the design undertaken here, the chosen component are two power dividers , nine 3 dB directional couplers, one 3 dB attenuator and fifteen specified-length RWGs between components, with schematic shown in Fig. 1. Optimum length of transmission lines help improve accuracy. In order to analyze and determine the proper physical length of mentioned transmission lines in the TPR, assuming that all ports between components are matched or reflected wave from unmatched ports are passed up. θ_i , θ_p and θ_q are electrical length of transmission lines, power dividers and directional couplers respectively, $1/\alpha$ (where $|\alpha|>1$) is attenuation of the attenuator in linear scale and b_i ($i=3,4...10$) is detected wave in i^{th} port of TPR, a_1 is incident wave to first port (reference wave), b_2 and a_2 are incident and reflected waves from DUT respectively, so that desirable reflection coefficient is $\Gamma = a_2/b_2$. Incident wave of DUT expressed in equation (2):

$$a_1 = \sqrt{2} b_2 e^{j(\theta_1+\theta_2)}. \quad (2)$$

Incident wave to each measuring port are:

$$b_3 = -\frac{1}{4} a_1 e^{-j(3\theta_q+\theta_2+\theta_3+\theta_p+\theta_5)}, \quad (3)$$

$$b_4 = \frac{a_1}{4\sqrt{2}}\left(j e^{-j(4\theta_q+\theta_2+\theta_3+\theta_p+\theta_5+\theta_{11})} - e^{-j(4\theta_q+\theta_2+\theta_3+\theta_p+\theta_6+\theta_{12})}\right) - \frac{j a_2}{4\alpha} e^{-j(4\theta_q+\theta_1+\theta_{15}+\theta_7+\theta_{12})}, \quad (4)$$

$$b_5 = \frac{a_1}{4\sqrt{2}}\left(j e^{-j(4\theta_q+\theta_2+\theta_3+\theta_p+\theta_6+\theta_{12})} - e^{-j(4\theta_q+\theta_2+\theta_3+\theta_p+\theta_5+\theta_{11})}\right) - \frac{a_2}{4\alpha} e^{-j(4\theta_q+\theta_1+\theta_{15}+\theta_7+\theta_{12})}, \quad (5)$$

$$b_6 = -\frac{a_1}{4}e^{-j(3\theta_q+\theta_2+\theta_3+\theta_p+\theta_6)} + j\frac{a_2}{2\sqrt{2}\alpha}e^{-j(\theta_1+\theta_{15}+3\theta_q+\theta_7)}, \quad (6)$$

$$b_7 = -j\frac{a_1}{4}e^{-j(3\theta_q+\theta_2+\theta_4+\theta_p+\theta_9)} + \frac{a_2}{2\sqrt{2}\alpha}e^{-j(\theta_1+\theta_{15}+3\theta_q+\theta_8)}, \quad (7)$$

$$b_8 = \frac{-a_1}{4\sqrt{2}}\left(je^{-j(4\theta_q+\theta_2+\theta_4+\theta_p+\theta_{10}+\theta_{14})} + e^{-j(4\theta_q+\theta_2+\theta_4+\theta_p+\theta_9+\theta_{13})}\right) + \frac{ja_2}{4\sqrt{2}\alpha}e^{-j(5\theta_q+\theta_1+\theta_{15}+\theta_8+\theta_{13})}, \quad (8)$$

$$b_9 = \frac{-a_1}{4\sqrt{2}}\left(e^{-j(4\theta_q+\theta_2+\theta_4+\theta_p+\theta_9+\theta_{13})} + e^{-j(4\theta_q+\theta_2+\theta_4+\theta_p+\theta_{10}+\theta_{14})}\right) - \frac{a_2}{4\sqrt{2}\alpha}e^{-j(5\theta_q+\theta_1+\theta_{15}+\theta_8+\theta_{13})}, \quad (9)$$

$$b_{10} = -j\frac{a_1}{4}e^{-j(3\theta_q+\theta_2+\theta_4+\theta_p+\theta_{10})}. \quad (10)$$

With substituting a_1 from equation (2) into equations (3) to (10), and remember that $P_i = |b_i|^2$, detected powers to each port are:

$$\mathrm{P_3} = |\mathrm{b_3}|^2 = \frac{|\mathrm{b_2}|^2}{8}, \quad (11)$$

$$P_4 = |\mathrm{b_4}|^2 = \frac{|\mathrm{b_2}|^2}{16\alpha^2}\left|\Gamma - \alpha\left(e^{-j(-\theta_q-2\theta_1-\theta_{15}-\theta_7-\theta_{12}+\theta_2+\theta_3+\theta_p+\theta_5+\theta_{11})} + je^{-j(-\theta_q-2\theta_1-\theta_{15}-\theta_7+\theta_2+\theta_3+\theta_p+\theta_6)}\right)\right|^2, \quad (12)$$

$$P_5 = |\mathrm{b_5}|^2 = \frac{|\mathrm{b_2}|^2}{16\alpha^2}\left|\Gamma - \alpha\left(-e^{-j(-\theta_q-2\theta_1-\theta_{15}-\theta_7-\theta_{12}+\theta_2+\theta_3+\theta_p+\theta_5+\theta_{11})} + je^{-j(-\theta_q-2\theta_1-\theta_{15}-\theta_7+\theta_2+\theta_3+\theta_p+\theta_6)}\right)\right|^2, \quad (13)$$

$$P_6 = |\mathrm{b_6}|^2 = \frac{|\mathrm{b_2}|^2}{8\alpha^2}\left|\Gamma - j\alpha\left(-e^{-j(-\theta_q-2\theta_1+\theta_2+\theta_3+\theta_p+\theta_6-\theta_{15}-\theta_7)}\right)\right|^2, \quad (14)$$

$$P_7 = |\mathrm{b_7}|^2 = \frac{|\mathrm{b_2}|^2}{8\alpha^2}\left|\Gamma - j\alpha\left(e^{-j(-\theta_q-2\theta_1+\theta_2+\theta_4+\theta_p+\theta_9-\theta_{15}-\theta_8)}\right)\right|^2, \quad (15)$$

$$P_8 = |\mathrm{b_8}|^2 = \frac{|\mathrm{b_2}|^2}{32\alpha^2}\left|\Gamma - \alpha\sqrt{2}\left(-je^{-j(-2\theta_q-2\theta_1-\theta_{15}-\theta_8+\theta_2+\theta_4+\theta_p+\theta_9)} + e^{-j(-2\theta_q-2\theta_1-\theta_{15}-\theta_8-\theta_{13}+\theta_2+\theta_4+\theta_p+\theta_{10}+\theta_{14})}\right)\right|^2, \quad (16)$$

$$P_9 = |\mathrm{b_9}|^2 = \frac{|\mathrm{b_2}|^2}{32\alpha^2}\left|\Gamma - \alpha\sqrt{2}\left(-je^{-j(-2\theta_q-2\theta_1-\theta_{15}-\theta_8+\theta_2+\theta_4+\theta_p+\theta_9)} - e^{-j(-2\theta_q-2\theta_1-\theta_{15}-\theta_8-\theta_{13}+\theta_2+\theta_4+\theta_p+\theta_{10}+\theta_{14})}\right)\right|^2, \quad (17)$$

$$P_{10} = |\mathrm{b_{10}}|^2 = \frac{|\mathrm{b_2}|^2}{8}, \quad (18)$$

where $\mathrm{P_3}$ and $\mathrm{P_{10}}$ are reference ports (in this paper have been used to analyze according to reference port [1]). Whereas, in the general case, incident power to DUT is unknown parameter so it can be eliminated by normalizing equations (12) to (17) by referencing ports (equations (11) and (18)). Since ports 3 and 10 are only response to incident wave, so there are two reference ports in presented TPR. Thus, $\mathrm{P_4}$, $\mathrm{P_5}$, and $\mathrm{P_6}$ are normalized by $\mathrm{P_3}$ and $\mathrm{P_7}$, $\mathrm{P_8}$ and $\mathrm{P_9}$ are normalized by $\mathrm{P_{10}}$. The resulting six circles equations, therefore, in accordance with equation (1) are:

$$p_4 = \frac{1}{2\alpha^2}\left|\Gamma - \alpha\left(e^{-j(-\theta_q-2\theta_1-\theta_{15}-\theta_7-\theta_{12}+\theta_2+\theta_3+\theta_p+\theta_5+\theta_{11})} + je^{-j(-\theta_q-2\theta_1-\theta_{15}-\theta_7+\theta_2+\theta_3+\theta_p+\theta_6)}\right)\right|^2, \quad (19)$$

$$p_5 = \frac{1}{2\alpha^2}\left|\Gamma - \alpha\left(-e^{-j(-\theta_q-2\theta_1-\theta_{15}-\theta_7-\theta_{12}+\theta_2+\theta_3+\theta_p+\theta_5+\theta_{11})} + je^{-j(-\theta_q-2\theta_1-\theta_{15}-\theta_7+\theta_2+\theta_3+\theta_p+\theta_6)}\right)\right|^2, \quad (20)$$

$$p_6 = \frac{1}{\alpha^2}\left|\Gamma - \alpha\left(-je^{-j(-\theta_q-2\theta_1+\theta_2+\theta_3+\theta_p+\theta_6-\theta_{15}-\theta_7)}\right)\right|^2, \quad (21)$$

$$p_7 = \frac{1}{\alpha^2}\left|\Gamma - \alpha\left(je^{-j(-\theta_q-2\theta_1+\theta_2+\theta_4+\theta_p+\theta_9-\theta_{15}-\theta_8)}\right)\right|^2, \quad (22)$$

$$p_8 = \frac{1}{4\alpha^2}\left|\Gamma - \alpha\sqrt{2}\left(-je^{-j(-2\theta_q-2\theta_1-\theta_{15}-\theta_8+\theta_2+\theta_4+\theta_p+\theta_9)} + e^{-j(-2\theta_q-2\theta_1-\theta_{15}-\theta_8-\theta_{13}+\theta_2+\theta_4+\theta_p+\theta_{10}+\theta_{14})}\right)\right|^2, \quad (23)$$

$$p_9 = \frac{1}{4\alpha^2}\left|\Gamma - \alpha\sqrt{2}\left(-je^{-j(-2\theta_q-2\theta_1-\theta_{15}-\theta_8+\theta_2+\theta_4+\theta_p+\theta_9)} - e^{-j(-2\theta_q-2\theta_1-\theta_{15}-\theta_8-\theta_{13}+\theta_2+\theta_4+\theta_p+\theta_{10}+\theta_{14})}\right)\right|^2, \quad (24)$$

Solving six equations (19) to (24) obtain desirable Γ. Graphically, intersection of these six circles will be in one point in Γ plan ($|\Gamma| < 1$). Thus, far centers of circles are:

$$q_4 = \alpha\left(e^{-j(-\theta_q-2\theta_1-\theta_{15}-\theta_7-\theta_{12}+\theta_2+\theta_3+\theta_p+\theta_5+\theta_{11})} + je^{-j(-\theta_q-2\theta_1-\theta_{15}-\theta_7+\theta_2+\theta_3+\theta_p+\theta_6)}\right), \quad (25)$$

$$q_5 = \alpha\left(-e^{-j(-\theta_q-2\theta_1-\theta_{15}-\theta_7-\theta_{12}+\theta_2+\theta_3+\theta_p+\theta_5+\theta_{11})} + je^{-j(-\theta_q-2\theta_1-\theta_{15}-\theta_7+\theta_2+\theta_3+\theta_p+\theta_6)}\right), \quad (26)$$

$$q_6 = j\alpha\left(-e^{-j(-\theta_q-2\theta_1+\theta_2+\theta_3+\theta_p+\theta_6-\theta_{15}-\theta_7)}\right), \quad (27)$$

$$q_7 = j\alpha\left(e^{-j(-\theta_q-2\theta_1+\theta_2+\theta_4+\theta_p+\theta_9-\theta_{15}-\theta_8)}\right), \quad (28)$$

$$q_8 = \alpha\sqrt{2}\left(-e^{-j(-2\theta_q-2\theta_1-\theta_{15}-\theta_8+\theta_2+\theta_4+\theta_p+\theta_9)} - je^{-j(-2\theta_q-2\theta_1-\theta_{15}-\theta_8-\theta_{13}+\theta_2+\theta_4+\theta_p+\theta_{10}+\theta_{14})}\right), \quad (29)$$

$$q_9 = \alpha\sqrt{2}\left(-e^{-j(-2\theta_q-2\theta_1-\theta_{15}-\theta_8+\theta_2+\theta_4+\theta_p+\theta_9)} + je^{-j(-2\theta_q-2\theta_1-\theta_{15}-\theta_8-\theta_{13}+\theta_2+\theta_4+\theta_p+\theta_{10}+\theta_{14})}\right), \quad (30)$$

For $\theta = \beta l$ and $\beta = 2\pi/\lambda$ (TEM wave), when frequency is changed, centers of circles rotate in Γ plan; hence, additional transmission lines θ_i help to dump rotation and improve the accuracy of system where of q_i-points are in constant place by means of solving equation (31):

$$\begin{cases} -\theta_q - 2\theta_1 - \theta_{15} - \theta_7 - \theta_{12} + \theta_2 + \theta_3 + \theta_p + \theta_5 + \theta_{11} = 0 \\ -\theta_q - 2\theta_1 - \theta_{15} - \theta_7 + \theta_2 + \theta_3 + \theta_p + \theta_6 = 0 \\ -\theta_q - 2\theta_1 + \theta_2 + \theta_3 + \theta_p + \theta_6 - \theta_{15} - \theta_7 = 0 \\ -\theta_q - 2\theta_1 + \theta_2 + \theta_4 + \theta_p + \theta_9 - \theta_{15} - \theta_8 = 0 \\ -2\theta_q - 2\theta_1 - \theta_{15} - \theta_8 + \theta_2 + \theta_4 + \theta_p + \theta_9 = 0 \\ -2\theta_q - 2\theta_1 - \theta_{15} - \theta_8 - \theta_{13} + \theta_2 + \theta_4 + \theta_p + \theta_{10} + \theta_{14} = 0 \end{cases}. \quad (31)$$

So optimum lengths of transmission lines for frequency-compensate TPR are obtained. After satisfying equation (31), centers of circles that are shown in Fig. 2 are:

$$q_4 = \alpha(1+j) = \alpha\sqrt{2}e^{j\frac{\pi}{4}}, \quad (32)$$

$$q_5 = \alpha(-1+j) = \alpha\sqrt{2}e^{j\frac{3\pi}{4}}, \quad (33)$$

$$q_6 = -j\alpha = \alpha e^{-j\frac{\pi}{2}}, \quad (34)$$

$$q_7 = j\alpha = \alpha e^{j\frac{\pi}{2}}, \quad (35)$$

$$q_8 = \alpha\sqrt{2}(1-j) = 2\alpha e^{j\frac{7\pi}{4}}, \quad (36)$$

$$q_9 = \alpha\sqrt{2}(-1-j) = 2\alpha e^{j\frac{5\pi}{4}}. \quad (37)$$

Another optimization is carried out with simulation to this structure in Agilent ADS software, by means of RWG as transmission lines. In this case we have used some blocks entitled power divider (three-port block) and directional couplers (four-port block), then we have applied specific S-parameters for each block and added RWG to each port of blocks for satisfying electrical length property of them with specific electrical length according to equation (41). If the general equation of TPR is considered according to equation (38) [1]:

$$r_i^2 = |\Gamma - Q_i|^2 \quad i = 4,5,\dots,9, \quad (38)$$

where r_i and Q_i are according to equations (39) and (40) [1]:

$$\begin{cases} Q_i = \dfrac{\frac{p_i}{q_3^*} - \frac{\mu_i^2}{|q_3|^2} q_i}{\frac{p_i}{|q_3|^2} - \frac{\mu_i^2}{|q_3|^2}} & i = 4,5,6 \\ Q_i = \dfrac{\frac{p_i}{q_{10}^*} - \frac{\mu_i^2}{|q_{10}|^2} q_i}{\frac{p_i}{|q_{10}|^2} - \frac{\mu_i^2}{|q_{10}|^2}} & i = 7,8,9 \end{cases}, \quad (39)$$

$$\begin{cases} r_i^2 = \dfrac{p_i \left| -\frac{\mu_i}{q_3} + \frac{q_i \mu_i}{|q_3|^2} \right|^2}{\left| \frac{\mu_i^2}{|q_3|^2} - \frac{p_i}{|q_3|^2} \right|^2} & i = 4,5,6 \\ r_i^2 = \dfrac{p_i \left| -\frac{\mu_i}{q_{10}} + \frac{q_i \mu_i}{|q_{10}|^2} \right|^2}{\left| \frac{\mu_i^2}{|q_{10}|^2} - \frac{p_i}{|q_{10}|^2} \right|^2} & i = 7,8,9 \end{cases}, \quad (40)$$

where $p_i = P_i/P_3$, $\mu_i = h_i/h_3$ for i=4, 5, 6 and $p_i = P_i/P_{10}$, $\mu_i = h_i/h_{10}$ for i=7, 8, 9, and

$$h_i = (s_{i2}s_{21} - s_{22}s_{i1})/s_{21} \quad \text{for} \quad i = 4,5,\dots,9,$$
$$q_i = s_{i1}/(s_{22}s_{i1} - s_{i2}s_{21}) \quad \text{for} \quad i = 4,5,\dots,9.$$

Important point is that, with selection electrical length of transmission lines in center frequency according to equation (41), two groups of q_i-points (q_4, q_5, q_6 and q_7, q_8, q_9) corresponding to two six-port structures, have different behaviours consistent with frequency variations. Figure 4 shows phase change of Q_i-points in TPR structures in 2 GHz to 12 GHz frequency range with employment of equation (41):

$$\begin{aligned} &\theta_1 = \theta_p = \theta_q = 2.25°, \\ &\theta_9 = \theta_6 = \theta_3 = \theta_{15} = 3.2°, \\ &\theta_{13} = \theta_2 = \theta_{12} = \theta_{11} = \theta_{14} = 2.25°, \\ &\theta_4 = 3.6 \times \theta_3, \\ &\theta_5 = 1.2 \times \theta_q, \\ &\theta_7 = \theta_8 = 4.7°, \\ &\theta_{10} = 1.2 \times \theta_5, \\ &\text{AT=3 dB}, \\ &a_{rec} = 3000\ mils, \quad b_{rec} = 1500\ mils, \end{aligned} \quad (41)$$

where θ_i is electrical length of RWG, AT is attenuation of attenuator that changes magnitude of q_i-points (according to equation (32) to (37)), a_{rec} and b_{rec} are width and height of RWG respectively. Figure 3 shows intersections of six mentioned circles in equations (39) and (40), with transmission lines according to equation (41) for a sample DUT. As Fig. 2 shows, the magnitudes of q_i-points are about $1.5 \le |Q_i| \le 2.5$ so the approximated dynamic range required for power meters given by [2]:

$$Dynamic\ range[dB] = 20\ log_{10}\left[\frac{|Q_i|+1}{|Q_i|-1}\right]. \quad (42)$$

Dynamic range is 7.36 dB corresponding to $|Q_i|$=2.5 and 14 dB corresponding to $|Q_i|$=1.5.

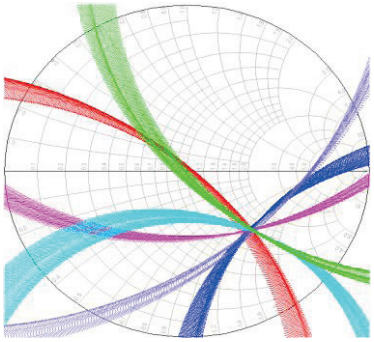

Fig. 3. Intersection of six circles in TPR for a sample DUT 0.5<-45°; thicknesses of lines indicate frequency variations of q_i-points.

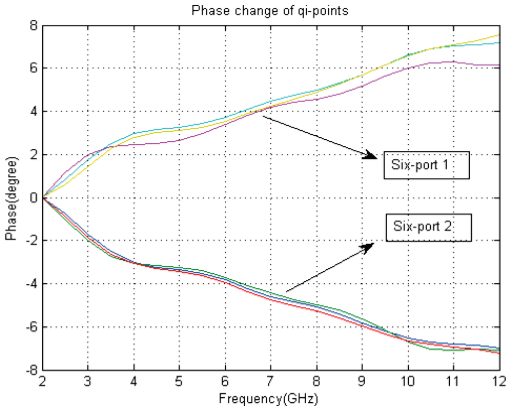

Fig. 4. Phase change of Q_i-points.

A. Improving accuracy of TPR by new qi-points

As Fig. 4 depicts, phase of Q_i-points in each group are changed in opposite direction (and changed about 8 degrees from 2 GHz to 12 GHz), in other words, three Q_i-points are rotated in clockwise and three remained Q_i-points are rotated in counter clockwise. So this property can be used for eliminating of frequency-dependent property of Q_i-points. Since each group of Q_i-points has 180 degrees out-of-phase, so with defining new three q_i'-points in accordance with equation (40):

$$\begin{aligned} q_1' &= \frac{Q_4 - Q_5}{2}, \\ q_2' &= \frac{Q_6 - Q_7}{2}, \\ q_3' &= \frac{Q_8 - Q_9}{2}, \\ q_4' &= \frac{Q_5 - Q_4}{2}, \\ q_5' &= \frac{Q_7 - Q_6}{2}, \\ q_6' &= \frac{Q_9 - Q_8}{2}. \end{aligned} \tag{43}$$

Figure 5 shows change in the phase of new centers (equation (40)), so new centers are fixing in Γ plan with wide variety frequency sweep. Table 1 shows magnitudes and phases of new q_i'-points.

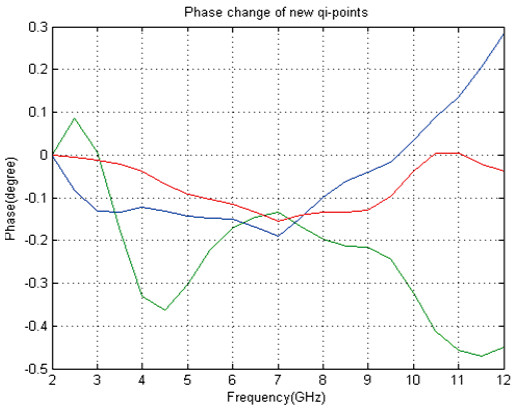

Fig. 5. Phase change of q_i'-points.

Table 1: Magnitudes and phases of q_i'-points

Frequency [GHz]	q_1'(or $-q_4'$) Mag/Phase	q_2'(or q_5') Mag/Phase	q_3'(or $-q_6'$) Mag/Phase
2	2.08/-135.246	1.415/89.926	1.980/-45.185
3	2.005/-135.113	1.413/89.939	1.979/-45.190
4	2.001/-135.122	1.413/89.965	1.985/-44.855
5	1.995/-135.103	1.411/90.017	1.996/-44.883
6	1.992/-135.095	1.410/90.042	1.997/-45.014
7	1.988/-135.057	1.409/90.082	1.997/-45.050
8	1.987/-135.146	1.408/90.059	1.996/-44.988
9	1.984/-135.205	1.408/90.056	1.995/-44.969
10	1.981/-135.280	1.408/89.964	1.992/-44.861
11	1.979/-135.382	1.404/89.923	1.992/-44.729
12	1.975/-135.531	1.403/89.966	1.996/-44.736

B. Calculating of reflection coefficient

As mentioned, in TPR intersection of six circles obtain unique point in complex plan that is reflection coefficient. Since at least three circles are needed, and of course, enough for determining one unique point in plan, six circles in calculating reflection coefficient give more assurance in TPR. On the other hand, with utilization of equation (43), calculating of reflection coefficient is carried out with more precision since new six q_i'-points are approximately frequency-independent. For evaluating operation of mentioned TPR, results of simulation for sample DUT Γ=0.5<-45°, in Agilent ADS exported to Matlab to solve equation (38) and obtain the Γ by numerical methods, calculated magnitude and phase of reflection coefficient Γ is plotted in Figs. 6 and 7 respectively. This simulation is performed by two group q_i-points that

are introduced in equations (39) and (43). The result shows that calculated phase of reflection coefficient in wide frequency range based on equation (43), is more accurate than equation (39). Figures 8 and 9 respectively, show magnitude and phase error rate for calculating reflection coefficient Γ=0.5/-45° in TPR. As shown, maximum deviation in calculating of phase and magnitude is 2.8% and 1.8% respectively when using equation (43), but the values are 7% and 1.7% with utilizing equation (39). So this kind of TPR can be very useful in applications that need to precise phase detector (that can be used in radar systems or microwave image systems, whereas, in the image processing technique, maximum information of image is concealment in the phase [5,6,8]) to work in ultra wide frequency range.

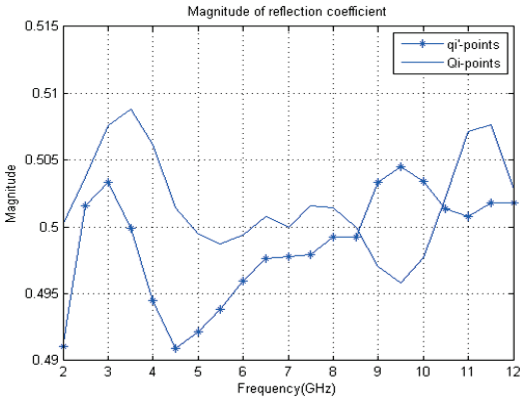

Fig. 6. Magnitude of reflection coefficient with utilizing q_i'-points (equation (43)) and Q_i-points (equation (39)) when frequency is changed between 2 GHz to 12 GHz.

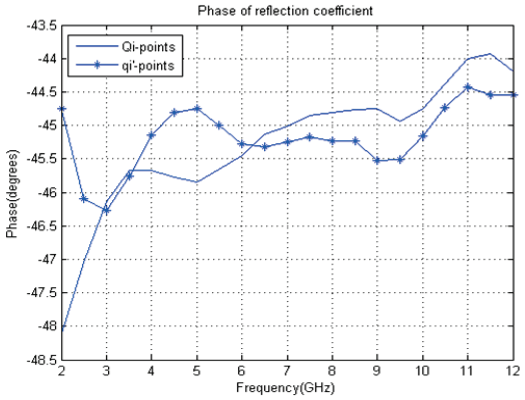

Fig. 7. Phase of reflection coefficient with utilizing q_i'-points (equation (43)) and Q_i-points (equation (39)) when frequency is changed between 2 GHz to 12 GHz.

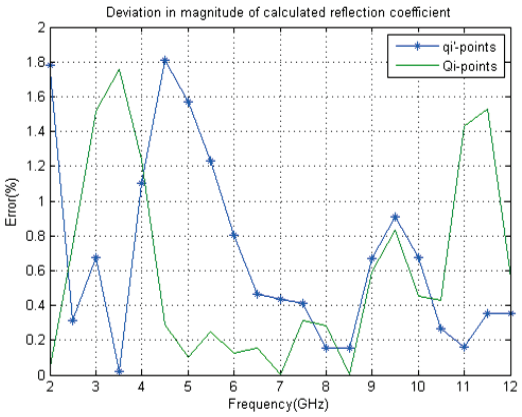

Fig. 8. Deviation in magnitude of reflection coefficient.

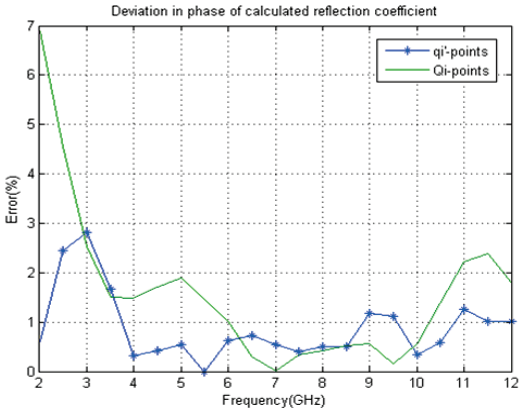

Fig. 9. Deviation in phase of reflection coefficient.

C. Optimum attenuation for attenuator

In Prototype ten-port reflectometer investigated by RWG, Ports 1 and 2 are connected to signal generator and DUT respectively. The reflected wave from DUT passes through a 3 dB attenuator in order to push away q_i-points from unit circle. By adding a 3 dB attenuator in the reflection route, Q_i-points positioned in the Γ plane push away from the center of smith chart so optimum case $1.5 < |Q_i| < 2.5$ can be chosen by equation (42) and following items. Magnitude of q_i-points should be greater than one; it should not be too near to unity because P_i (measured power) could be small for the fully reflecting terminations. Small values of P_i resulting from $|Q_i| \cong 1$ decrease the measurement accuracy. On the other hand, if $|Q_i|$ is too large, it can be seen that a small change to P_i represents a large changing Γ. Therefore, postulated that magnitude of Q_i-points should be in the range of about $\sqrt{2}$ to 2 [4].

III. CONCLUSION

In this paper a prototype of UWB ten-port reflectometer by means of RWG is designed, analyzed and simulated by Agilent ADS and Matlab softwares. Ten-port reflectometer is a proper, robust, accurate and reliable structure for calculating Γ by employing eight ports for power measuring and two ports for input and output signal. In this prototype, required dynamic range for each power detector is between 7.36 dB and 14 dB that depends on frequency change of q_i-points. Increasing number of ports up to ten is a good solution, whereas, system becomes robust and reliable as well as more accurate for important goals such as radar and microwave imaging systems [9-11]. In this paper, new method for increasing phase detection of DUT is presented according to ten-port properties. On the other hand, this structure helps to improve accuracy of system so that mentioned TPR has about 50% relative bandwidth with proper precision. One of outstanding advantage of this article, is designing and simulating by means of RWG, whereas, SIW technology is very similar to RWG in structure, propagation modes and etc. Also, SIW is a planer structure, low-cost, small size with simplicity of integration and easy to manufacture rather than RWG [7,12]. Therefore, SIW is a good candidate for RWG structure and then these results will be valid for SIW structure.

REFERENCES

[1] F. M. Ghannouchi and A. Mohammadi, "The six-port technique with microwave and wireless application," *Artech House*, September 30, 2009.

[2] V. Zhurbenka, "Advanced microwave circuits and systems," *InTech*, April 2010.

[3] J. L. Pedreno-Molina, J. Monzo-Cabrera, A. Lozano-Guerrero, and A. Toledo-Moreo, "Design and validation of a ten-port waveguide reflectometer sensor: application to efficiency measurment and optimization of microwave-heating ovens," *Sensors 2008*, 8, 7833-7849; DOI: 10.3390/s127833.

[4] J. Monzo-Cabrera, J. L. Pedreno-Molina, A. Lozano-Guerrero, and A. Toledo-Moreo, "A novel design of a robust ten-port microwave reflectometer with autonomous calibration by using neural network," *IEEE Transaction on Microwave Theory and Techniques*, vol. 56, no. 12, December 2008.

[5] M. Traii, M. Nedil, A. Gharsallah, and T. A. Denidni, "Design of a six-port junction based on single layer technology for UWB application," *In Electrical and Computer Engineering (CCECE), 2010, 23rd Canadian Conference*, pp. 1-4, Tunisia, 2010.

[6] M. E. Bialkowski, N. Seman, and W. C. Khor, "Design of a six-port reflectometer for a microwave breast cancer detection system," *AusWireless 06 Conference*, Sydney, Australia, 2006.

[7] D. Deslandes and K. Wu, "Design consideration and performance analysis of substrate integrated waveguide components," *In Proc. 32nd Eur. Microw. Conf.*, vol. 2, pp. 881-884, Milan, Italy, September 2002.

[8] Y. Zhao, J. Frigon, K. Wu, and R. Bosisio, "Numerical model of six-port and its applications," *23rd Annual Review of Progress in Applied Computational Electromagnetics (ACES)*, pp. 195-198, Verona, Italy, March 2007.

[9] Y. Xu, L. Gerardi, Y. Zhao, M. Bozzi, L. Perregrini, K. Wu, and R. Bosisio, "Review of six-port interferometer technology," *23rd Annual Review of Progress in Applied Computational Electromagnetics (ACES)*, pp. 205-209, Verona, Italy, March 2007.

[10] A. Koelpin, G. Vinci, B. Laemmle, D. Kissinger, and R. Weigel, "The six-port in modern society," *IEEE Microwave Magazine*, pp. 35-43, December 2010.

[11] M. Ivanov, J. Banys, S. Rudys, and R. Grigalaitis, "Measurments of complex dielectric constant of ferroelectrics with six-port reflectometer in 80-120 frequency range," *Ferroelectrics*, vol. 367, no. 1, pp. 229-233, 2008.

J. Monzo-Cabrera, J. L. Pedreno-Molina, A. Lozano-Guerrero, and A. Toledo-Moreo, "A novel design of a robust ten-port microwave reflectometer with autonomous calibration by using neural networks," *IEEE Trans. on Microwave Theory and Tech.*, vol. 56, no. 12, December 2008.

Modified Antipodal Vivaldi Antenna with Shaped Elliptical Corrugation for 1-18 GHz UWB Application

Muhammad Ahmad Ashraf [1,3], Khalid Jamil [2], A. R. Sebak [3,4], Mobeen Shoaib [2], Zeyad Alhekail [1], Majeed Alkanhal [1], and Saleh Alshebeili [1,3]

[1] Department of Electrical Engineering
[2] Prince Sultan Advanced Technology Research Institute
[3] KACST Technology Innovation Center in RFTONICS for the e-Society
King Saud University, Riyadh, 11421, Kingdom of Saudi Arabia
{mashraf, majeed, zeyad}@ksu.edu.sa, {mobeen.shoaib, khalid.jamil}@psatri.org.sa

[4] Electrical and Computer Engineering Department
Concordia University, Montreal, Canada
abdo@ece.concordia.ca

Abstract ─ We present two antipodal tapered slot antennas: one with elliptical strips termination and the other modified with elliptical shaped corrugations. Compared to the other, the corrugated antenna uses elliptical slots loading to improve the gain by up to 1.9 dB over operational bandwidth 0.8-18 GHz. It also improves the front to back lobe ratio. The simulated frequency and time domain results are in good agreement with measured performance of both antennas. Experimental results verify a fidelity factor greater than 0.86 for both antennas by transmitting 30ps (3-18 GHz) Ultra-Wideband (UWB) pulses.

Index Terms ─ Corrugated UWB antenna, fidelity factor, time domain, ultra-wideband.

I. INTRODUCTION

Recent years have seen a great interest in performance improvement of Tapered Slot Antenna (TSA) due to its lightweight structure, ease of fabrication, end-fire radiation and ultra-broadband characteristics [1-4]. For broadband systems, the candidate antenna performance is characterized both in frequency and time domain, in order to transmit very narrow pulses [5-7]. Printed TSAs find applications in phased/scanning array, millimeter wave, low cost radar and short-range communication systems.

Based upon their feeding mechanism, the Vivaldi tapered slot antennas are mainly classified into two different geometries: planar and antipodal [8-10]. For planar TSA, the Microstrip-to-Slotline (MSL) transition is employed as a feeding balun that limits the bandwidth over two octaves. Moreover, due to radiation losses, MSL transition causes pattern degradation at certain frequencies that reduces the antenna efficiency. To alleviate the problems caused by the MSL feeding mechanism, Langley, et al. [11] introduced an antipodal UWB feeding configuration using a balun comprising of a microstrip, a parallel stripline and a symmetric double-sided slotline.

The Antipodal Tapered Slot Antenna (ATSA) with dielectric director placed in the antenna aperture enhances the gain by focusing energy in the end-fire direction [12]. In this method, the antenna height and weight is compromised to improve the gain performance. In another method proposed in [13], the gain of ATSA is improved at the cost of increased substrate dimensions toward broadside. However, this method does not improve the gain at lower frequency range. On the other hand, corrugation configuration of ATSA mitigates the higher Side-Lobe-Levels (SLL), reduces backward radiations and increases the low frequency gain of broadband antennas without compromising the antenna dimensions [2,6,14].

The System Fidelity Factor (SFF) incorporates space, time and frequency domain characteristics

Submitted On: October 19, 2013
Accepted On: October 9, 2014

of antenna system in one value. In [7], the transmission coefficient S_{21} is used to calculate the SFF. In this technique, a calibrated Vector Network Analyzer (VNA) sweeps from 3-12 GHz to transmit a pulse with Full Width Half Maximum (FWHM) equals to 60ps.

In this paper, we present comprehensive frequency and time domain simulations and experimental measurements to investigate the frequency domain characteristics and the fidelity factor of two ATSAs system: one with elliptical shaped fins termination and the other with elliptical shaped edge corrugation (ATSA-EC). It is observed that the ATSA-EC is improving lower frequency gain of proposed UWB spectrum. The size of ATSA-EC is not increased for gain improvement. We have presented the design of ATSAs with system fidelity factor greater than 0.86 for very narrow UWB pulse with FWHM equals to 30ps, that is two times less than the pulse width of 60ps presented in [7]. In order to obtain the proposed pulse width of very short duration, VNA is used to transmit a frequency sweep signal from 3-18 GHz through the designed antenna transmit receive systems. The Inverse Fast Fourier Transform (IFFT) of the received signal (S_{21}) gave the antenna time-domain response. A novel method for analyzing the broadband antenna in time domain was demonstrated by transmitting and receiving true time domain narrow pulses through proposed antenna system, generated by wideband arbitrary waveform generator (12 GSa/s AWG) and mixed-signal oscilloscope (50 GSa/s MSO).

Furthermore, we have presented a mathematical expression for designing the exponential curve of ground plane conductor required for antipodal feed mechanism. The proposed antennas with this antipodal feed exhibit reflection coefficient of less than -14 dB for a bandwidth of 1-18 GHz. Note, that the Federal Communication Commission (FCC) unlicensed UWB band is 3.1-10.6 GHz, therefore, this antenna design leaves a big margin at both frequency ends. We also experimentally verified broadside pattern symmetry for E- and H-plane, side-lobe levels and gain performance of the two antennas.

II. ANTENNA DESIGN

The antenna elements shown in Fig. 1 are travelling wave ATSAs developed on Rogers 5880 substrate having dielectric constant, ε_r=2.2 and thickness, h=1.574 mm. The size of each antenna is 160x120 mm^2. The ATSAs contain the strip conductors on both sides of substrate. In order to have impedance matching over a bandwidth of more than 10:1, the tapered slot is designed by following the guidelines in [15]. The ATSAs are loaded with elliptical shaped strip conductors as shown in Fig. 1. The exponential taper C_g is used for the ground in order to achieve broadband microstrip to parallel plate transition. The tapered curve C_g is defined as:

$$C_g = w_y - 1 + 0.1 w_y e^{\alpha w_x}, \quad (1)$$

where α is the rate of transition for exponential curve defined as the following:

$$\alpha = \frac{1}{1.92\, w_x} \ln\left(\frac{w_y + 0.1\, w_t}{0.1\, w_t}\right), \quad (2)$$

w_x is the x-directed length of curve with w_y and w_t being the y-directed initial and final points, respectively. The variation of impedance bandwidth and radiation characteristics against different geometrical parameters of proposed ATSAs are analysed by full-wave simulation software CST Microwave Studio [16]. Table 1 presents geometry of ATSA which results 182% impedance bandwidth with required radiation performance.

In order to improve the radiation characteristics, elliptical edge corrugations are applied to ATSA as shown in Fig. 1 (b). At each edge of the antenna Unequal Half Elliptical Slots (UHES) are loaded with the period, C_s=17 mm. The largest UHES having minor axis and major axis radii R_{s1}=15 mm and R_{s2}=8 mm, respectively, is placed at the centre of elliptical fin. Whereas, the major axis radii of other UHESs are decreased linearly by the factor C_r=0.7 having the constant ellipticity ratio e_r=0.533=R_{s2}/R_{s1}.

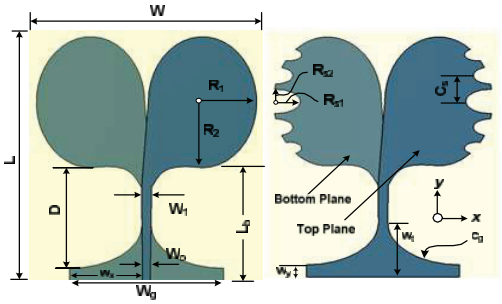

Fig. 1. Layout diagram of: (a) Antipodal Tapered Slot Antenna (ATSA) using elliptical shape loading, and (b) Antipodal Tapered Slot Antenna with elliptical shaped Edge Corrugation (ATSA-EC).

Table 1: Optimized geometrical dimensions (mm) of ATSAs

R_1	R_2	D	w_y	w_x	w_t	w_o	w_1
32.5	42.25	65	8	43.85	35	5.95	6.12

III. DISCUSSIONS AND REASONS

The photograph of fabricated ATSAs is shown in Fig. 2. The measured reflection coefficient of the corrugated fins and un-corrugated ATSAs are compared in Fig. 3. It can be seen that the performance of both antennas is comparable in terms of impedance bandwidth over a broad range of frequencies from 0.8-18 GHz. The reflection coefficient of designed ATSAs is better than 14 dB from 0.8 GHz to 18 GHz. Generally, the radiation of an ATSA is function of length, aperture width and substrate thickness. The added inductance due to edge corrugation increases the electrical length of antennas. The loading of ATSA with UHES can suppress the surface current at both back edges resulting in improved gain performance compared to un-slotted antenna gain. Similarly, the UHESs increase the effective length of the antenna resulting in more directive beams in both E- and H-planes.

Fig. 2. Photograph of fabricated ATSAs.

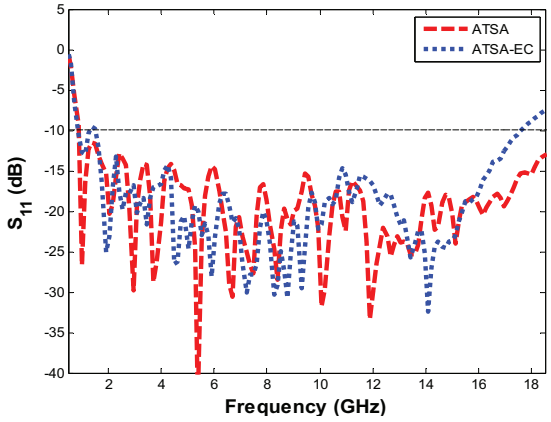

Fig. 3. Measured reflection coefficient characteristics of fabricated ATSAs.

A. Performance optimization

The performance of ATSAs against various corrugation depths is analysed by a parametric study using full wave simulations. From the parametric study the elliptical slots radii R_{s1} and R_{s2} are varied and gain performance is observed.

Figure 4 presents the simulation results of ATSAs gain performance against various corrugation depths compared to un-corrugated ATSA. The realized gain of ATSA is found between 3 dBi to 8.5 dBi over the 0.8 GHz to 6 GHz frequency band. The edge corrugation arranges the current path to be parallel with desired radiating current and opposite to the undesired surface current. The former enhances the gain, whereas, the later decreases the backward radiation. Therefore, the realized gain of ATSA-EC is improved over 0.8 GHz to 6 GHz band by varying elliptical slots radii R_{s1} and R_{s2}. Comparatively, better gain improvement is found for the ellipticity ratio $e_r=R_{s2}/R_{s2}$ less than 0.35 as depicted in Fig. 4 (a) and (b). It is worth noticing that the corrugated antenna has a stable gain performance near the lower and higher frequencies of the operating band.

Figure 5 presents the measured gain performance of fabricated prototypes from 2-18 GHz. The measured gain performances of both designs are in good agreement with simulation results, except at few frequencies with not more than ± 0.7 dB variations that may be due to fabrication tolerances regarding the top and bottom plane flair alignment and the cutting of elliptical strips for edge corrugation. Figure 5 (b) presents the results from 2 to 7 GHz to observe the

lower frequency gain improvement.

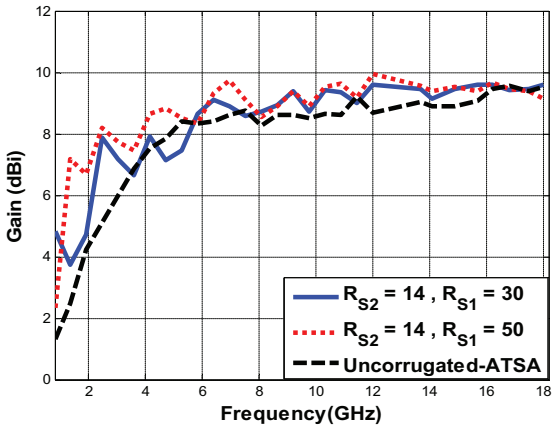

Fig. 4. Simulated gain characteristics of the ATSAs at different edge corrugation value.

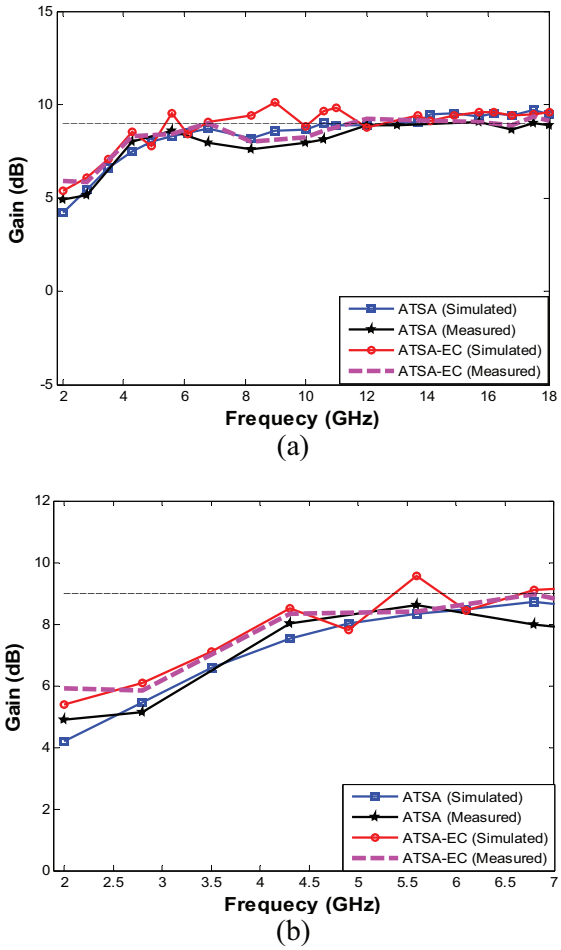

Fig. 5. Measured: (a) gain characteristics of the ATSAs, and (b) 2-7 GHZ.

B. Radiation analysis

The measured and simulated far field H-plane radiation patterns for the fabricated ATSAs prototype antennas are shown in Fig. 6 (a), (b) and (c) for frequencies 4.3, 8.2 and 16.8 GHz, respectively.

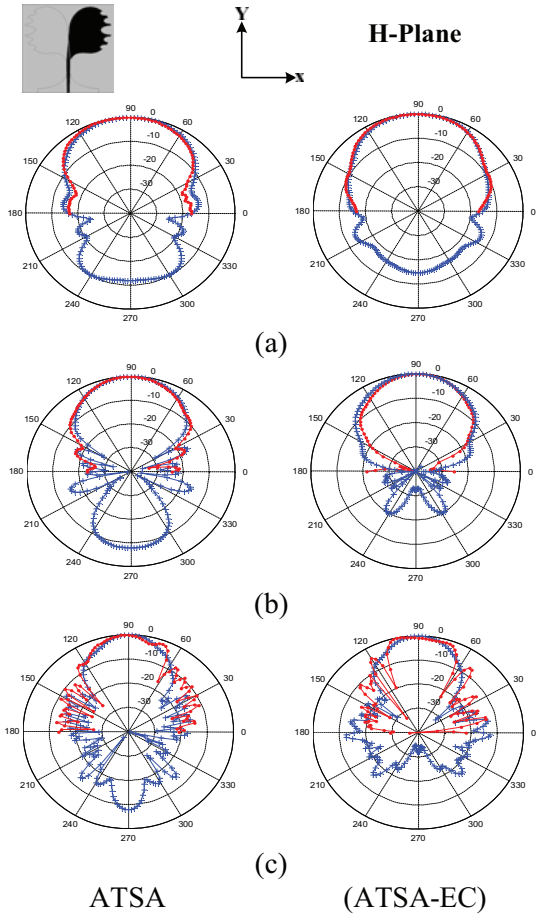

Fig. 6. H plane measured radiation patterns: (a) f=4.3 GHz, (b) f=8.2 GHz, and (c) f=16.8 GHz.

Similarly, the E-plane radiation patterns are presented in Fig. 7. The measured radiation patterns show good agreement with simulated patterns in both planes. The average 3-dB Half-Power Beam-Widths (HPBW) for the E-plane and H-plane patterns are 74° and 62°, respectively, with more than 10 dBi peak gain. The HPBW of the ATSA-EC in the H-plane is decreased to 46.9° from 56.7° at 8.2 GHz compared with ATSA. The change in E-plane beamwidth is not significant for both antennas.

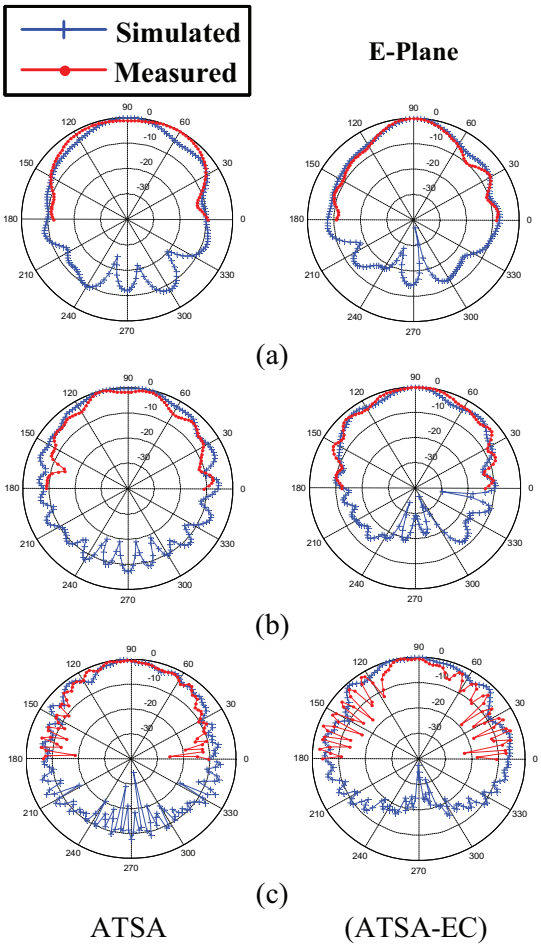

Fig. 7. E-plane measured radiation patterns: (a) f=4.3 GHz, (b) f=8.2 GHz, and (c) f=16.8 GHz.

In ATSAs currents are mainly distributed along the taper from the slot till the end of radiating element. Therefore, the maximum radiation is observed in the endfire direction. However, we have found undesired surface currents at the edges of elliptical conductors that contribute to radiating currents significantly beyond 9 GHz. An appropriate design of edge corrugation design is introduced to suppress these currents in order to reduce unwanted side lobes and back lobes resulting improvement in H-plane HPBW. Additionally, the SLL in the H-plane is significantly reduced by up to -10.2 dB from -7.2 dB for ATSA to -18.5 dB for ATSA-EC. The SLL in the E-plane is also improved by 4 dB at 8.2 GHz. The front-to-back ratio is also studied for different corrugation depths. The measured performance exhibits front-to-back ratio improvement by greater than 20 dB at certain frequencies.

C. Time domain analysis

The simulated time domain response of ATSAs when excited with passband Gaussian pulse covering the complete spectrum of operating frequency is shown in Fig. 8. The received pulses are obtained by placing an *x*-oriented *E*-field probe 10 m along the broadside direction of antenna. The FWHM of transmitted pulse is 30ps, while the received pulses preserve the Gaussian shape having maximum FWHM of 36ps related to ATSA-EC with R_{S1}=30 mm and R_{S2}=18 mm.

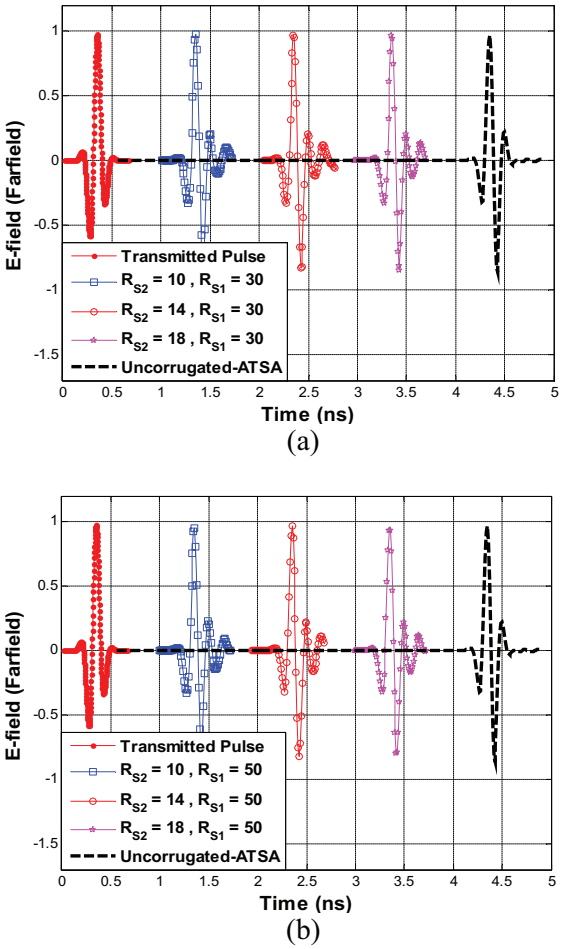

Fig. 8. Simulated transmitted and received pulses on the E-field probe for different edge corrugation parameters.

The FWHM of ATSA without corrugation and ATSA-EC with R_{S1}=50 and R_{S2}=14 is found 38ps and 39ps, respectively. The fidelity factor is calculated according to the following relation [17]:

$$Fidelity = \max_{\tau} \frac{\int_{-\infty}^{\infty} S_t(t) S_r(t-\tau) dt}{\sqrt{\int_{-\infty}^{\infty} |S_t(t)|^2 dt \, |S_r(t-\tau)|^2 dt}}, \quad (3)$$

where $S_t(t)$ and $S_r(t)$ present the transmitted and received time domain pulses, respectively. The fidelity factor for ATSA-EC at different edge corrugations is presented in Table 2.

Table 2: Calculated fidelity factor for ATSA-EC at different edge corrugation

$\frac{R_{s2}}{R_{s1}}$	10/30	14/30	18/30	10/50	14/50	18/50
Fidelity	0.89	0.88	0.87	0.91	0.92	0.9

D. Antenna system transfer function

Figure 9 presents the experimental setup for measuring the system transfer function $H(\omega)$ or S_{21} to characterize the ATSAs in time domain by IFFT. The system transfer function $H(\omega)$ is defined as the following:

$$H(\omega) = H_{TX}(\omega) H_{CH}(\omega) H_{RX}(\omega), \quad (4)$$

where $H_{TX}(w)$, $H_{CH}(w)$ and $H_{RX}(w)$ are the frequency domain transfer functions of the transmitting antenna, the channel and the receiving antenna, respectively. Two identical ATSAs are placed in front of each other at distance D=90 cm as shown in Fig. 9. The S_{21} amplitude and phase response is measured by using N5242A Vector Network Analyser (VNA) as shown in Fig. 10. In order to transmit a pulse without distortion, the S_{21} value should be constant over the desired frequency range.

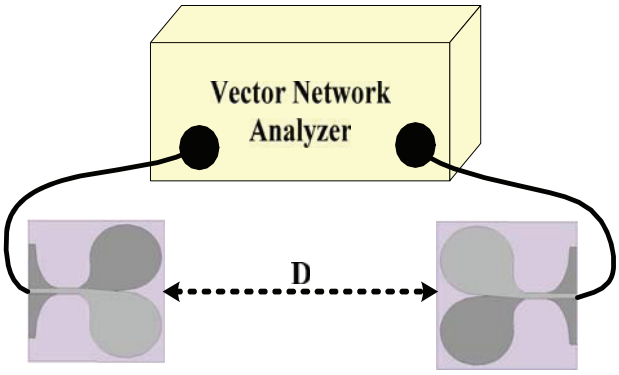

Fig. 9. Measurement Setup for time domain characteristics of ATSAs.

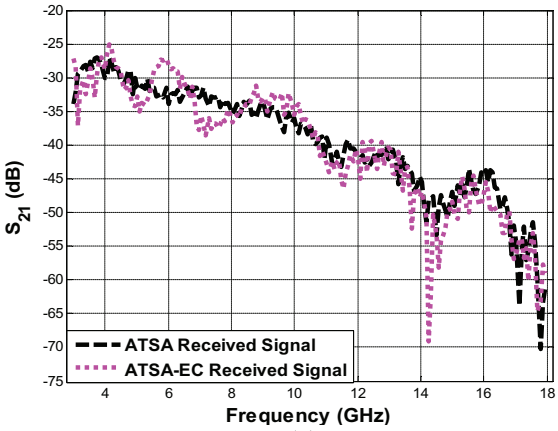

(a)

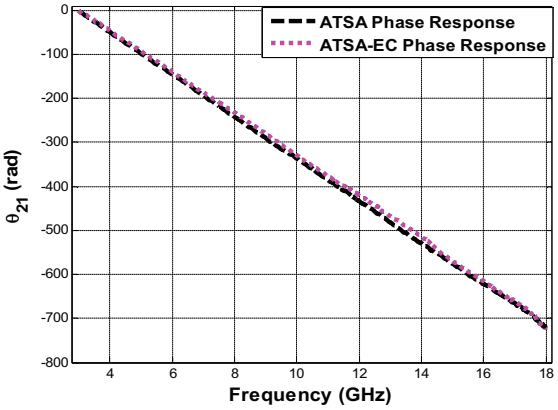

(b)

Fig. 10. Measured received: (a) signal response, and (b) phase response of ATSAs at D=90 cm.

E. Pulse distortion analysis

The magnitude (S_{21}) and phase response (θ_{21}) of antenna system is an important parameter for pulse distortion analysis. The distortion will be observed in the transmitted pulse, if the magnitude dip in S_{21} corresponds to nonlinearity in θ_{21} [7]. The magnitude response presented in Fig. 10 (a) shows linear characteristics over complete spectrum, except 14.2 GHz corresponds to lower antenna gain point. However, the phase response shown in Fig. 10 (b) is linear over the desired frequency band. The measured S_{21} parameter is then transformed into time domain by readily available analysis capability of VNA using IFFT.

In order to collect reliable data, a calibration is made from 3 GHz to 18 GHz with 800 points. The transformation from frequency to time domain is

accomplished by windowing the frequency domain data using Kaiser window with $\alpha=6$ [18]. The measured S_{21} data can be converted to time domain using the expression:

$$S_{21}(t) = sf \times IFFT\left[S_{21}(j\omega)w(n|\alpha=6)\right], \quad (5)$$

where *sf* is a scaling factor. A scaling factor of 2 is used for IFFT transformation of measured S_{21} [18]. The measured time domain response of the two antennas at D=90 cm is shown in Fig. 11. The transmitted pulse response is obtained by directly connecting both ports of the network analyser and applying IFFT to S_{21} value. The measured FWHM of transmitted pulse is 30ps. The calculated fidelity factor for ATSA and ATSA-EC is found to be 0.89 and 0.86, respectively. The FWHM of ATSA-EC is slightly greater than ATSA.

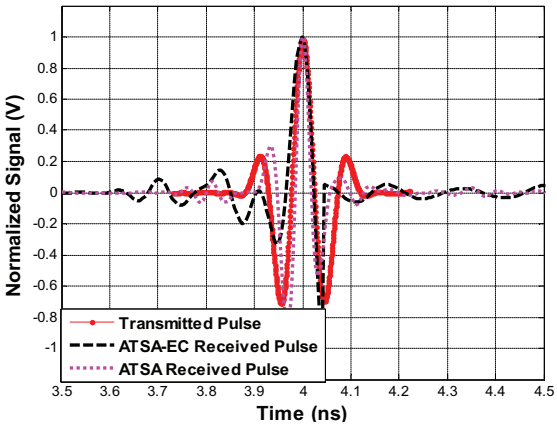

Fig. 11. Measured impulse response of the configuration shown in Fig. 9 with D=90 cm.

F. Experimental time-domain characterization

The accuracy of time domain analysis is further verified by sending true time domain pulses involving ATSA as pair of transmit and receives antennas. Figure 12 presents the experimental setup arrangement for characterization of antenna in time domain by sending UWB pulses generated by a wideband Arbitrary Waveform Generator (AWG). In this arrangement, the UWB signal is generated by M8190A 12GS/s AWG. It is then up-converted to 7 GHz using 8267D Vector Signal Generator (VSG) and transmitted via antenna. The output power of AWG is adjusted to 0 dBm. The output of VSG is divided into two paths by using 10 dB directional coupler. The Coupler's direct port (P_2) is connected to ATSA, whereas, the coupled output (P_3) is connected to four channel MSO72004 mixed signal oscilloscope. The coupled port output connected to oscilloscope is considered as reference signal, whereas, the couplers direct port output is transmitted and received by a pair of ATSA.

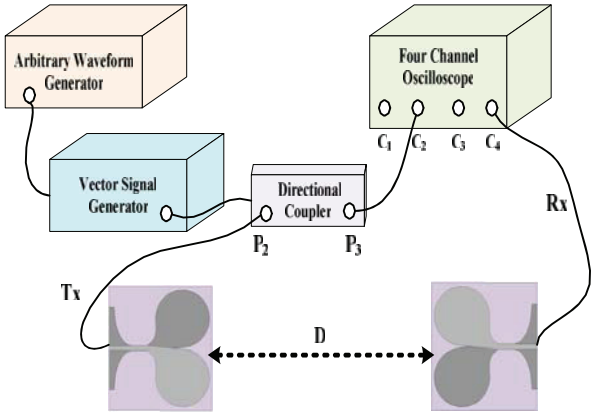

(a)

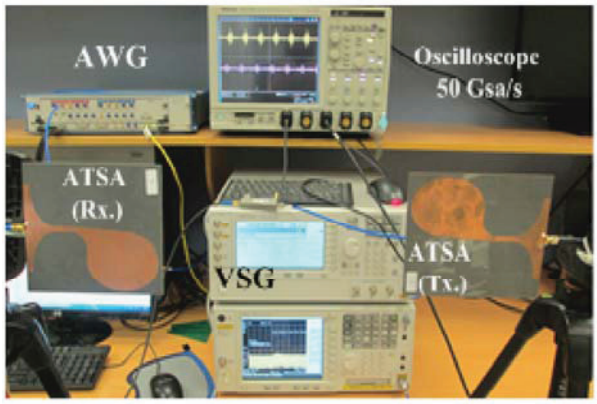

(b)

Fig. 12. Experimental setup for time domain measurement of ATSAs: (a) block diagram, and (b) photograph.

The time domain transmitted and Digitally Down Converted (DDC) received signals are shown in Fig. 13 (a). The corresponding up-converted signal with 7 GHz centre frequency is shown in Fig. 13 (b). The signal fidelity factor for transmitted signal $S_t(t)$ and received signal $S_r(t)$ is calculated by using eq. (3) and found 0.91, 0.897 at D=10 and 50 cm, respectively.

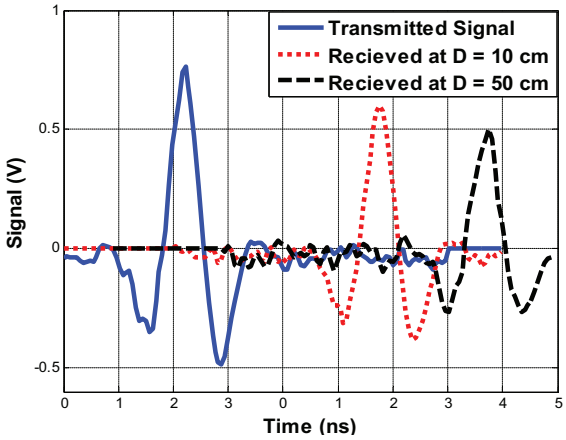

(a)

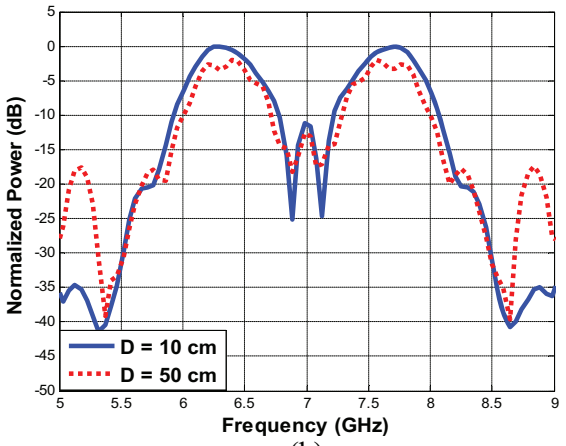

(b)

Fig. 13. Measured impulse response: (a) respected spectrum, and (b) of the configuration shown in figure at D=10cm and D=50 cm.

IV. CONCLUSION

We have presented the design of two antennas: Antipodal Tapered Slot Antenna (ATSA) and elliptical shaped Edge Corrugation (ATSA-EC). Both antennas find impedance bandwidth matched over 0.8-18 GHz corresponds to 182% fractional bandwidth. The effects of shaped elliptical corrugation on the antenna characteristics are: increase in electrical length due to added inductance which results in gain improvement at particular frequencies of proposed spectrum. Additionally, it reduces half power beamwidth and suppresses backward radiation which improves front to back ratio. The realised gain of ATSA-EC is improved up to 1.9 dB over 0.6-6 GHz band by varying the corrugation depths of elliptical shaped slots. ATSA-EC exhibits supressed back-lobe radiation up to 15 dB at higher frequencies of our proposed band. The radiation parameters and gain are optimized by the ellipticity ratio $e_r=R_{s2}/R_{s1}$ of corrugation slots. We have performed comprehensive frequency and time domain simulations and measurements to investigate impedance bandwidth, gain performance, radiation characteristics, and system transfer function and fidelity factor of antennas. For an ultra-short pulse having FWHM of 30ps, we have verified a fidelity factor greater than 0.86 for both antenna systems.

ACKNOWLEDGMENT

This research is supported by KACST Technology Innovation Center in Radio Frequency and Photonics for the e-Society.

REFERENCES

[1] L. A. Bui, A. Mitchell, K. Ghorbani, C. Tan-Huat, S. Mansoori, and E. R. Lopez, "Wide-band photonically phased array antenna using vector sum phase shifting approach," *IEEE Transactions on Antennas and Propagation*, vol. 53, no. 11, pp. 3589,3596, November 2005.

[2] L. S. Locke, J. Bornemann, and S. Claude, "Substrate integrated waveguide-fed tapered slot antenna with smooth performance characteristics over an ultra-wide bandwidth," *Applied Computational Electromagnetics Society Journal*, vol. 28, pp. 454-462, May 2013.

[3] T. Namas and M. Hasanovic, "Ultra-wideband antipodal vivaldi antenna for road surface scanner based on inverse scattering," *28th Annual Review of Progress in Applied Computational Electromagnetics (ACES)*, pp. 882-887, Monterey, CA, April 2012.

[4] S. Dai, L. Liu, and G. Fang, "A low-cost handheld integrated UWB radar for shallow underground detection," *2010 IEEE International Conference on Ultra-Wideband (ICUWB)*, vol. 2, pp. 1-4,September 2010.

[5] F. Fereidoony, S. Chamaani, and S. A. Mirtaheri, "UWB monopole antenna with stable radiation pattern and low transient distortion," *IEEE Antennas and Wireless Propagation Letters*, vol. 10, pp. 302,305, 2011.

[6] D. M. In, M. J. Lee, D. Kim, C. Y. Oh, and Y. S. Kim, "Antipodal linearly tapered slot antenna using unequal half-circular defected sides for gain improvements," *Microw. Opt. Technol. Lett.*, 54: pp. 1963-1965, May 16, 2012.

[7] G. Quintero, J. F. Zurcher, and A. K. Skriverviky, "System fidelity factor: a new method for comparing UWB antennas," *IEEE Transactions on*

Antennas and Propagation, vol. 59, no. 7, pp. 2502,2512, July 2011.

[8] Y. Che, K. Li, X. Hou, and W. Tian, "Simulation of a small sized antipodal vivaldi antenna for UWB applications," *2010 IEEE International Conference on Ultra-Wideband (ICUWB)*, vol. 1, pp. 1,3, September 20-23, 2010.

[9] K. Ebnabbasi, C. Rappaport, H. Foltz, and J. McLean, "Impulse response of vivaldi antenna using cubic-spline and exponential taper profiles for compact ground penetrating radar applications," *2010 IEEE Antennas and Propagation Society International Symposium (APSURSI)*, pp. 1,4, July 11-17, 2010.

[10] Y. J. Cheng, W. Hong, and K. Wu, "Design of a monopulse antenna using a dual V-type linearly tapered slot antenna (DVLTSA)," *IEEE Transactions on Antennas and Propagation*, vol. 56, no. 9, pp. 2903,2909, September 2008.

[11] J. D. S. Langley, P. S. Hall, and P. Newham, "Novel ultrawide-bandwidth vivaldi antenna with low cross-polarisation," *Electronics Letters*, vol. 29, no. 23, pp. 2004,2005, November 11, 1993.

[12] J. Bourqui, M. Okoniewski, and E. C. Fear, "Balanced antipodal vivaldi antenna with dielectric director for near-field microwave imaging," *IEEE Transactions on Antennas and Propagation*, vol. 58, no. 7, pp. 2318,2326, July 2010.

[13] K. Kota and L Shafai, "Gain and radiation pattern enhancement of balanced antipodal vivaldi antenna," *Electronics Letters*, vol. 47, no. 5, pp. 303,304, March 3, 2011.

[14] D. C. Chang, B. H. Zeng, and J. C. Liu, "Modified antipodal fermi antenna with piecewise-linear approximation and shaped comb corrugation for ranging applications," *IET Microwaves, Antennas & Propagation*, vol. 4, no. 3, pp. 399,407, March 2010.

[15] J. Y. Siddiqui, Y. M. M. Antar, A. P. Freundorfer, E. C. Smith, G. A. Morin, and T. Thayaparan, "Design of an ultra-wideband antipodal tapered slot antenna using elliptical strip conductors," *IEEE Antennas and Wireless Propagation Letters*, vol. 10, pp. 251-254, 2011.

[16] *CST-Computer Simulation Technology*, 2010.

[17] D. H. Kwon, "Effect of antenna gain and group delay variations on pulse-preserving capabilities of ultrawideband antennas," *IEEE Transactions on Antennas and Propagation*, vol. 54, no. 8, pp. 2208,2215, August 2006.

[18] S. Licul and W. A. Davis, "Unified frequency and time-domain antenna modeling and characterization," *IEEE Transactions on Antennas and Propagation*, vol. 53, no. 9, pp. 2882,2888, September 2005.

Muhammad Ahmad Ashraf received undergraduate education in Electrical Engineering from the University of Engineering and Technology (UET) Lahore in 2003. He received his M.S. degree in Microwave Engineering from National University of Sciences and Technology (NUST), Rawalpindi in 2009. He joined the Electrical Engineering Department, King Saud University (KSU), Riyadh where he received his Ph.D. degree in 2014. During his Ph.D. research, he was with Microwave, Antenna and Radar Systems (MARS) Laboratory at Prince Sultan Advanced Technology Research Institute (PSATRI), King Saud University. Currently he is working with the Technology Innovation Center, *RF and Photonics in the e-Society* (RFTONICS), funded by King Abdulaziz City for Science and Technology (KACST).

Abdel Sebak received the B.S. degree in Electronic and Communication Engineering from Cairo University, Egypt, in 1976, and in Applied Mathematics from Ain-Shams University, Egypt, in 1978. In 1980, he joined the Department of Electrical Engineering, University of Manitoba, Canada, where he obtained his M.Eng. and Ph.D. degrees in 1982 and 1984, respectively.

Sebak is a Professor with Concordia University. Before joining Concordia University, he was a Professor at the University of Manitoba and Cairo University. He was also with the Canadian Marconi Company, working on the design of microstrip phased array antennas.

Sebak's recent research activities cover two streams: Antenna Engineering, and Analytical and Computational Electromagnetics. Applied and sponsored projects include advanced composite materials for aerospace shielding and antenna applications, microwave sensing and imaging, ultra wideband and mm-wave antennas, microwave beamforming, and high gain mm-wave antennas.

Sebak is a Fellow of the Institute of Electrical and Electronics Engineers and Fellow of Engineering Institute of Canada. He is a Member of Concordia University Provost's Circle of Distinction for his career achievements.

Sebak is Co-Chair of IEEE ICUWB2015 and has served as Chair for the IEEE Canada Awards and Recognition Committee (2002-2004), IEEE Canada Conference Committee (2000-2002) and as the Technical Program Chair for the 2002 IEEE CCECE

Conference and the 2006 URSI-ANTEM Symposium. He has also served as a Member (2002-2004) of the IEEE RAB Awards and Recognition Committee. He is a Member of the Canadian National Committee of International Union of Radio Science (URSI) Commission B.

Mobien Shoaib received undergraduate education in Computer Engineering from National University of Sciences and Technology (NUST) in 2001. He received his M.S. degree in Telecommunication Engineering, from the Department of Electrical Engineering, Helsinki University of Technology (HUT), Espoo, Finland, in 2005. He was associated with the Department of Signal Processing and Acoustics at HUT until 2008. He is currently working in Signal and Image Processing Laboratory at Prince Sultan Advanced Technology Research Institute (PSATRI), King Saud University.

Majeed A. S. Alkanhal received the B.S. and M.S. degrees from King Saud University, Riyadh, Saudi Arabia, in 1984 and 1986, respectively, and the Ph.D. degree from Syracuse University, Syracuse, NY, in 1994, all in Electrical Engineering. He is presently a Professor and Chairman of the Electrical Engineering Department at King Saud University, Riyadh, Saudi Arabia. His research interests are in antennas and propagation, computational electromagnetics, and microwave engineering.

Saleh A Alshebeili is Professor and Chairman (2001-2005) of the Electrical Engineering Department, King Saud University. He has more than 20 years of teaching and research experience in the area of *communications* and *signal processing*. Alshebeili is Member of the Board of Directors of Prince Sultan Advanced Technologies Research Institute (PSATRI), the Vice President of PSATRI (2008-2011), the Director of Saudi-Telecom Research Chair (2008-2012), and the Director (2011-Present) of the Technology Innovation Center, *RF and Photonics in the e-Society* (RFTONICS), funded by King Abdulaziz City for Science and Technology (KACST). Alshebeili has been on the editorial board of *Journal* of *Engineering Sciences* of King Saud University (2009-2012). He has also an active involvement in the review process of a number of research journals, KACST general directorate grants programs, and national and international symposiums and conferences.

Bandwidth Enhancement of Small Square Monopole Antenna with Dual Band Notch Characteristics Using U-Shaped Slot and Butterfly Shape Parasitic Element on Backplane for UWB Applications

P. Beigi [1], J. Nourinia [2], B. Mohammadi [3], and A. Valizade [4]

[1] Department of Electrical Engineering, Science and Research Branch
Islamic Azad University, West Azerbaijan, Iran
payam.beigi@yahoo.com

[2] Department of Electrical Engineering
Urmia University, Urmia, Iran
j.nourinia@urmia.ac.ir

[3] Young Researchers and Elites Club, Sanandaj Branch
Islamic Azad University, Sanandaj, Iran
b.mohammadi@urmia.ac.ir

[4] Young Researchers and Elites Club, Qaemshahr Branch
Islamic Azad University, Qaemshahr, Iran
a.valizade@semnan.ac.ir

Abstract ─ In this study, a dual band notch microstrip antenna for UWB applications has been presented. The antenna consists of a stepped patch with U-shaped slot, two rectangular shaped slots in the ground plane and a butterfly shaped parasitic backplane element structure. By inserting two rectangular shaped slots in the ground plane, much wider impedance bandwidth can be produced. This modification significantly improves the antenna's impedance bandwidth by 155% which covers the entire UWB bandwidth range and even more. In order to generate single band notch characteristic, a butterfly shaped conductor backplane structure is utilized on the ground plane side of the substrate. In addition, by cutting a U-shaped slot on the radiating patch, a dual band notch function is achieved. The measured frequency results show an impedance bandwidth of 2.35-13 GHz for a Voltage Standing Wave Ratio (VSWR) less than 2 with two eliminated bands placed at 3.25-3.85 GHz and 4.9-6.2 GHz, which reject the Wireless Local Area Network (WLAN) band, WiMAX band, and a major part of the C-band. The measured E-plane and H-plane radiation patterns show a very good correlation with the requirements of UWB applications.

Index Terms ─ Dual band notch, monopole antenna, parasitic element, Ultra-Wideband (UWB), U-shaped slot.

I. INTRODUCTION

Nowadays, wireless communication systems are becoming increasingly popular. However, the technologies for wireless communication still need to be improved further to satisfy the demands for higher resolutions and high data rate requirements. That is why UWB communication systems covering from 3.1 to 10.6 GHz released by the FCC in 2002 are currently under development. Recently, printed monopole antennas featured with many attractive merits such as low profile, easy fabrication, wide impedance bandwidth and omnidirectional radiation patterns have drawn great attention. These features have provided a very challenging opportunity for antenna

Submitted On: March 29, 2014
Accepted On: October 5, 2014

designers. A lot of effort has been put into designing new antennas which can satisfy the requirements of modern communication systems. As a result of accelerating growth of UWB technology, there has been a vast body of literature introducing novel antennas for UWB applications and systems [1-17]. Some of the bandwidth enhancement techniques that are used to design planar antennas have been stated as below: a staircase-shaped feed technique [1-3], two L-shaped conductor backed-plane [5], different shaped slots in the ground plane to improve the antenna's impedance bandwidth [7-12], and double feed [13]. Moreover, other strategies to improve the impedance bandwidth which do not involve a modification of the geometry of the planar antenna have been investigated [14-17].

Despite all its advantages, the UWB system suffers from interference with other existing communication systems, such as WLAN (5.15-5.825 GHz), WiMAX (3.3-3.6 GHz) and C-band (3.7-4.2 GHz). Consequently, various printed microstrip antennas with single [7-9] or dual [10-17] band notch function have been recently proposed. To solve this problem, the existing techniques in extensive use can be classified into the following two categories: one method focuses on embedding various slots, such as U-shaped slot [1,10], meander-shaped slot [2], square-shaped slot [7], H-shaped slot [8] and modified co-directional Complementary Split Ring Resonator (CSRRs) slots [14]. The other effective method is loading diverse parasitic elements on the antennas [9,11-12], such as Stepped Impedance Resonators (SIRs) near the feed line [15], and angle-shaped parasitic slit [16-18]. In [13], dual band notch function is achieved by inserting a W-shaped conductor backed-plane and a modified T-shaped slot in the radiating patch.

In this paper, a dual band notch small monopole antenna has been presented. In the proposed structure in order to improve the bandwidth, two rectangular shaped slots are etched on the ground plane which creates an additional resonance, and hence, much wider impedance bandwidth can be produced. This modification significantly improves the antenna's impedance bandwidth up to 155%. Adding a butterfly shaped conductor backplane to the antenna structure leads to a single band notch function which occurs at frequencies near 5.5 GHz, and then cutting a U-shaped slot on the antenna radiating patch creates an additional band notch function at frequencies adjacent to 3.5 GHz. Good VSWR and radiation characteristics are obtained in the frequency band of interest. In the next sections, the antenna design is explained in details and simulated and measured results are presented to validate the usefulness of the proposed antenna structure for UWB applications.

II. ANTENNA DESIGN

The dual band notch small monopole antenna with U-shaped slot and butterfly shaped parasitic element fed by a 50-Ω microstrip line is shown in Fig. 1, which is printed on a FR4 substrate with thickness of 1 mm, permittivity of 4.4, and loss tangent of 0.018. The basic antenna structure consists of a triangular stub, a 50-Ω microstrip feed-line, and a rectangular truncated ground plane. The radiating stub is connected to the feed-line of width W_F and length L_F, as shown in Fig. 1. The proposed antenna is connected to a 50-Ω SMA connector for signal transmission. A single band notch function is provided by inserting a butterfly shaped conductor backplane and a dual band notch characteristic is obtained by using a U-shaped slot in the radiating patch. The planar monopole antenna with its final design parameters was constructed, and the numerical and experimental results of the input impedance and radiation characteristics are presented and discussed. The parameters of this proposed antenna are studied by changing one parameter at a time while others were kept fixed. The simulated results are obtained using Ansoft simulation software High-Frequency Structure Simulator (HFSS) [19].The final design parameters values of the presented antenna are specified in Table 1.

Table 1: The final dimensions of the designed monopole antenna

Param.	mm	Param.	mm	Param.	mm
R_1	3.3	R_2	5	R_3	2.8
W_1	18	W_2	3.85	W_3	0.5
L_G	6	L_S	2	L_u	9
W_4	2	W_S	7.5	W_u	7
W_F	1.85	L_F	8	L_1	4
W_{sub}	22	L_{sub}	22	h_{sub}	1

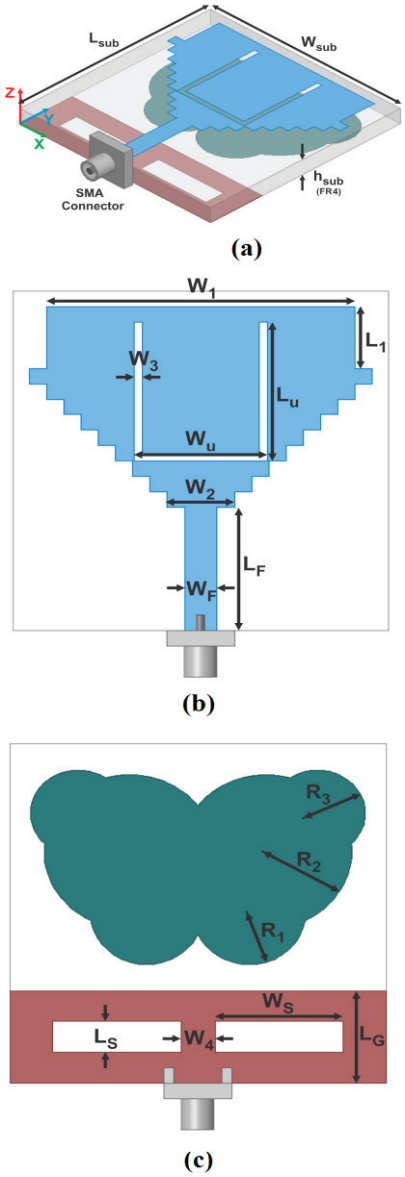

Fig. 1. Geometry of proposed microstrip-fed monopole antenna: (a) side view, (b) top view, and (c) bottom view.

Figure 2 shows the structure of various antennas which were used for simulation studies. VSWR characteristics for ordinary triangular patch antenna (Fig. 2 (a)), triangular patch antenna with stepped radiating patch (Fig. 2 (b)), and triangular staircase patch antenna with rectangular slots in the ground plane (Fig. 2 (c)) are compared in Fig. 3. As shown in Fig. 3, repeatedly embedded notches on the patch directly influence both the upper and lower band edge frequencies. The triangular patch antenna with stepped radiating patch (Fig. 2 (b)) has smooth VSWR at the frequency higher than 9 GHz, and it also shows the effect of these steps on the impedance matching. As illustrated in Fig. 3, the rectangular slots on the ground plane conductor play an important role in the broadband characteristic of the proposed antenna and also in determining the impedance matching sensitivity of this antenna [5-7]. It is found that by inserting the rectangular slots in the ground plane additional resonance (at 12.2 GHz) is excited, and hence, much wider impedance bandwidth can be produced; especially at the higher band, because of multi-resonance characteristics. The bandwidth of the antenna without the slots on the ground plane is 150%, while the antenna with the rectangular slots on the ground plane has a bandwidth of 155%. Another important parameter to be considered is the distance of W_4 between the slots as illustrated in Fig. 1. This distance should be large enough to reduce the coupling between two slots; whereas, by increasing W_4, the required exciting degree for the slots by the microstrip line is weakened. Also note, that by varying this parameter, the surface current density in the central portion of the ground plane exactly below the microstrip-fed line is adjusted. On the other side of the substrate, a conducting ground plane of width W_{Sub} and length L_G is placed. The truncated ground plane plays an important role in the broadband characteristics of this antenna, because it helps to match the patch with the feed line in a wide range of frequencies. This is because the truncation creates a capacitive load that neutralizes the inductive nature of the patch to produce nearly pure resistive input impedance [3-5].

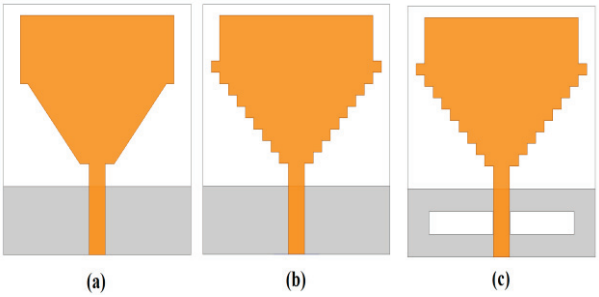

Fig. 2. (a) Ordinary triangular patch antenna, (b) triangular patch antenna with stepped radiating patch, and (c) triangular staircase patch antenna with rectangular slots in the ground plane.

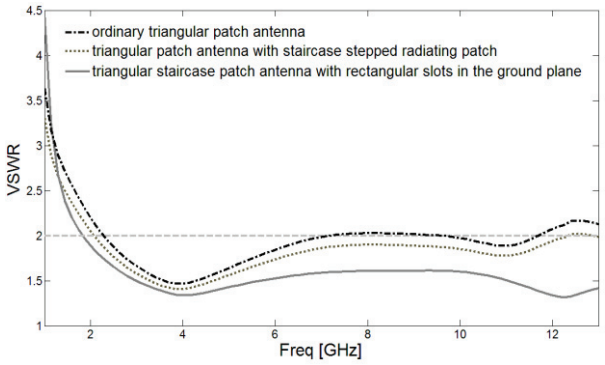

Fig. 3. Simulated VSWR characteristics for antennas shown in Fig. 2.

To understand the phenomenon behind this new exited resonance performance, the simulated current distributions on the ground plane 12 GHz for the antennas with and without slots on the ground plane are compared in Fig. 4. As it can be observed in Fig. 4, at 12 GHz the current is concentrated along the interior and exterior edges of the slots, and therefore, the antenna impedance changes at this frequency due to the resonant properties of these slots [4-6].

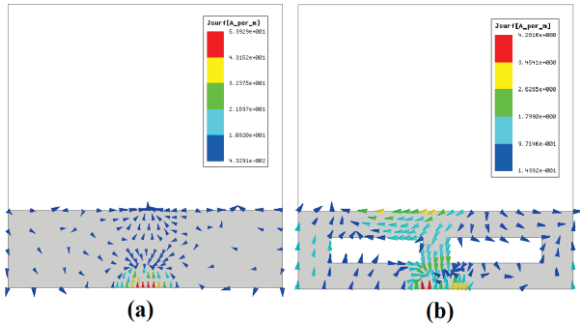

Fig. 4. Simulated surface current distribution on the ground plane for the triangular staircase patch antenna: (a) the ordinary ground plane at 12 GHz, and (b) the ground plane with rectangular slots at 12 GHz.

Figure 5 shows the structure of various antennas used for band notch function simulation studies. The VSWR characteristics for the triangular staircase patch antenna with rectangular slots in the ground plane (Fig. 5 (a)), antenna with two rectangular slots and a butterfly shaped conductor backplane on the ground plane (Fig. 5 (b)), and the proposed antenna (Fig. 5(c)) are compared in Fig. 6. As it is observed in Fig. 6, adding the conductor backplane to the antenna structure generates single band notch characteristics. Moreover, according to Fig. 5 (c) and its corresponding frequency response in Fig. 6, cutting a U-shaped slot in the radiating patch adds an additional band notch function to the performance of the antenna and consequently a dual band notch function is achieved. The implementation of the conductor backplane on the other side of the substrate of the monopole antenna acts as a dipole that can provide an additional coupling path. Moreover, this structure changes the inductance and capacitance of the input impedance, which in turn leads to change of the bandwidth. Based on electromagnetic coupling theory, the conductor backplane perturbs the resonant response and also acts as a parasitic half-wavelength resonant structure which is electrically coupled with the rectangular monopole [11-13].

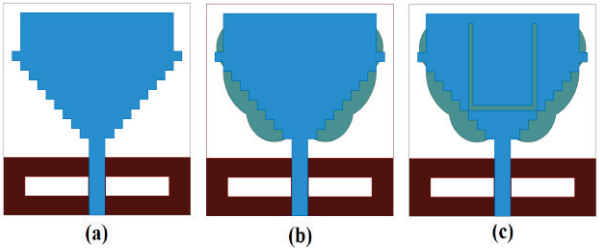

Fig. 5. (a) Triangular staircase patch antenna with rectangular slots in the ground plane, (b) antenna with two rectangular slots and a butterfly shaped conductor backed-plane in the ground plane, and (c) the proposed antenna.

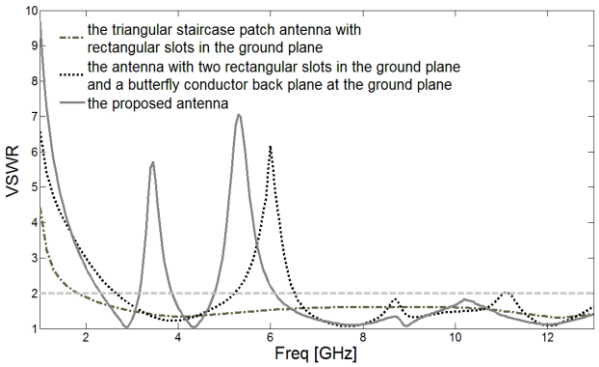

Fig. 6. Simulated VSWR characteristics for antennas shown in Fig. 5.

To understand the phenomenon behind this dual band notch performance, the simulated

current distribution for the proposed antenna at the notched center frequencies of 3.5 GHz and 5.4 GHz is presented in Figs. 7 (a) and (b), respectively. As it can be observed from Fig. 7 (a), at the lower notched center frequency (3.5 GHz), the current flows are more dominant around the U-shaped slot and they are oppositely directed between the slot edges [10]. Therefore, the antenna impedance changes at these frequencies due to the band notch properties of the proposed structure, and as a result the desired high attenuation is achieved. According to Fig. 7 (b), at the upper notched center frequency (5.4 GHz), the current flows on the parasitic element are more dominant and the surface currents are oppositely directed between this parasitic element and the radiating patch. Therefore, the resultant radiation fields cancel out, and high attenuation near the notched frequencies is produced, and as a result, the antenna does not radiate efficiently at the notched frequencies [4].

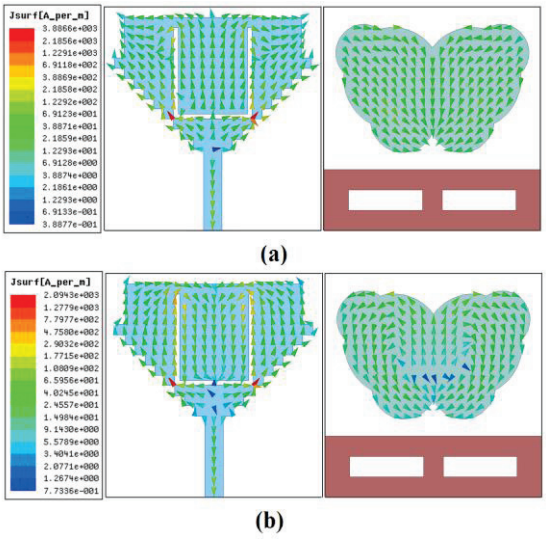

Fig. 7. Simulated surface current distributions for the proposed antenna at its notched band center frequencies: (a) at 3.5 GHz, and (b) at 5.4 GHz.

III. RESULTS AND DISCUSSIONS

The proposed antenna with final design parameters, as shown in Fig. 8, was fabricated and tested at the Northwest Antenna and Microwave Research Lboratory (NAMRL), Urmia University, Iran. Figure 9 shows the measured and simulated VSWR characteristics of the proposed antenna. The fabricated antenna covers the frequency band of 2.35-13GHz with two rejection bands at 3.25-3.85 GHz and 4.9-6.2 GHz, which reject the Wireless Local Area Network (WLAN) band, WiMAX band, and a major part of the C-band. As shown in Fig. 9, there exists a discrepancy between the measured data and the simulated results. The discrepancy is mostly due to a number of parameters, such as the fabricated antenna dimensions as well as the thickness and dielectric constant of the substrate on which the antenna is fabricated, and also the wide range of simulation frequencies. In order to confirm the accurate return loss characteristics for the designed antenna, it is recommended that the manufacturing and measurement process need to be performed carefully. Besides, SMA soldering accuracy and FR4 substrate quality need to be taken into consideration [2-5].

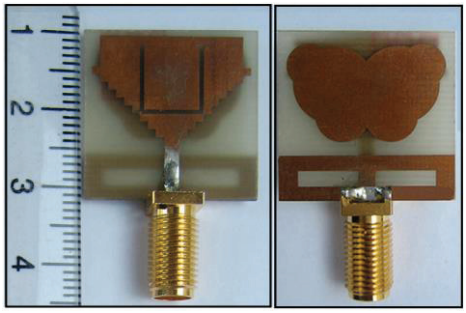

Fig. 8. Photograph of the fabricated antenna prototype with parasitic element.

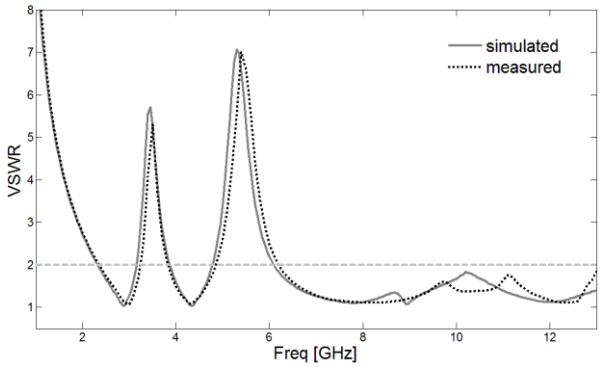

Fig. 9. Measured and simulated VSWR for the proposed antenna.

Figure 10 shows the measured radiation patterns including co-polarization and cross-polarization in the H-plane (x-z plane) and E-plane (y-z plane). The main purpose of the radiation

patterns is to demonstrate that the antenna actually radiates over a wide range of frequencies. It can be seen that the radiation patterns in x-z plane are nearly omnidirectional for the three frequencies. Moreover, the measured maximum gain for the fabricated antenna is presented in Fig. 11. As it is observed in this figure, for dual band notch performance of the antenna, the gain drops dramatically at the notched frequency bands.

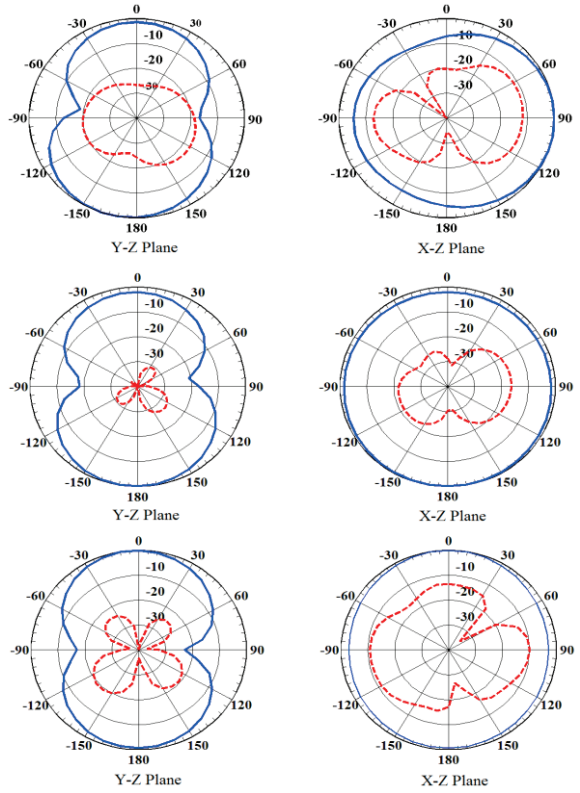

Fig. 10. Measured radiation patterns of the proposed antenna. (a) 4.4 GHz, (b) 8 GHz, and (c) 11 GHz.

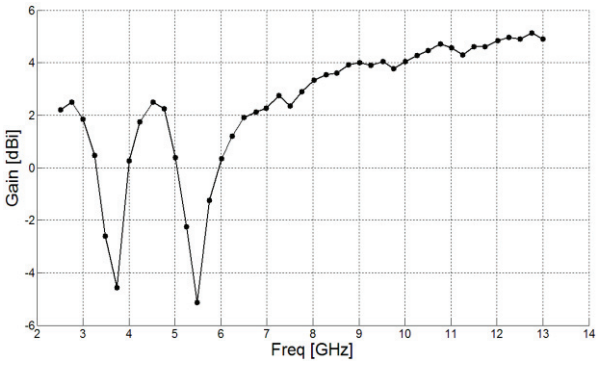

Fig. 10. Measured maximum gain.

IV. CONCLUSION

In this paper, a compact wideband planar monopole antenna with dual band notch characteristics has been proposed for various UWB applications. The fabricated antenna covers the frequency band from 2.35 to 13 GHz with two rejection bands 3.25-3.85 GHz and 4.9-6.2 GHz. In the presented structure, triangular staircase shaped radiating patch is used to improve the impedance bandwidth and also an additional resonance is excited by cutting two rectangular shaped slots on the ground plane. Moreover, by inserting a U-shaped slot on the radiating patch and a Butterfly shaped conductor backplane on the other side of the substrate, a dual band notch characteristic is generated. The designed antenna has a simple configuration and easy fabrication process. The experimental results show that the realized antenna with a very compact size, simple structure, and wide bandwidth can be a good candidate for UWB application.

ACKNOWLEDGMENT

The authors are thankful to Dynamic Microwave Electronics (DMWE) Company staff for their beneficial and professional help and support (www.dmw-electronics.com).

REFERENCES

[1] Y. J. Cho, K. H. Kim, D. H. Choi, S. S. Lee, and S. O. Park, "A miniature UWB planar monopole antenna with 5-GHz band-rejection filter and the time-domain characteristics," *IEEE Trans. Antennas Propag.*, vol. 54, no. 5, pp. 1453-1460, May 2006.

[2] A. Valizade, C. Ghobadi, J. Nourinia, N. Ojaroudi, and M. Ojaroudi, "Band notch slot antenna with enhanced bandwidth by using Ω-shaped strips protruded inside rectangular slots for UWB applications," *Applied Computational Electromagnetics Society (ACES) Journal*, vol. 27, no. 10, pp. 816-822, October 2012.

[3] A. Valizade, C. Ghobadi, J. Nourinia, and M. Ojaroudi, "A novel design of reconfigurable slot antenna with switchable band notch and multi-resonance functions for UWB applications," *IEEE Antenna and Wireless Propagation Letters*, vol. 11, pp. 1166-1169, October 2012.

[4] R. Zaker, C. Ghobadi, and J. Nourinia, "Novel modified UWB planar monopole antenna with variable frequency band notch function," *IEEE Antennas Wireless Propag. Lett.*, vol. 7, pp. 112-114, 2008.

[5] C. Liu, T. Jiang, Y. Li, and J. Zhang, "A novel UWB filter with WLAN and RFID stop-band rejection characteristic using tri-stage radial loaded stub resonators," *Applied Computational Electromagnetics Society (ACES) Journal*, vol. 27, no. 9, pp. 749-758, September 2012.

[6] N. Ojaroudi, M. Ojaroudi, N. Ghadimi, and M. Mehranpour, "UWB square monopole antenna with omni-directional radiation patterns for use in circular cylindrical microwave imaging systems," *Applied Computational Electromagnetics Society (ACES) Journal*, vol. 28, no. 2, pp. 123-129, February 2013.

[7] B. Mohammadi, J. Nourinia, C. Ghobadi, and A. Valizade, "Design and analysis of the stub and radial-stub loaded resonator band-pass filter with cross-shaped coupled feed-lines for UWB applications," *Applied Computational Electromagnetics Society (ACES) Journal*, vol. 28, no. 9, pp. 851-857, August 2013.

[8] Y. D. Dong, W. Hong, Z. Q. Kuai, and J. X. Chen, "Analysis of planar ultra wideband antennas with on-ground slot band notch structures," *IEEE Trans. Antennas Propag*., vol. 57, no. 7, pp. 1886-1893, July 2009.

[9] M. Mehranpour, H. Boudaghi, M. Ghiamy, and J. Nourinia, "A very compact monopole antenna with variable frequency band notch for ultra-wideband applications," *In 6th International Symposium on Telecommunications (IST'2012)*, pp. 7-10, 2012.

[10] B. Badamchi, J. Nourinia, C. Ghobadi, and A. Valizade, "A design of compact reconfigurable UWB slot antenna with switchable single/dual band notch functions," *IET Microw. Antennas Propag*., vol. 8, iss. 8, pp. 541-548, 2014.

[11] W. S. Lee, D. Z. Kim, K. J. Kim, and J. W. Yu, "Wideband planar monopole antennas with dual band notch characteristics," *IEEE Trans. Microw. Theory Techn*., vol. 54, no. 6, pp. 2800-2806, June 2006.

[12] A. Valizade, P. Rezaei, and A. A. Orouji, "A new design of dual-port active integrated antenna for 2.4/5.2 GHz WLAN applications," *Progress In Electromagnetics Research B*, vol. 58, pp. 83-94, January 2014.

[13] S. R. Emadian, C. Ghobadi, J. Nourinia, M. H. Mirmozafari, and J. Pourahmadazar, "Bandwidth enhancement of CPW-Fed circle-like slot antenna with dual band notch characteristic," *IEEE Antennas Wireless Propag. Lett*., vol. 11, pp. 543-546, 2012.

[14] N. Ojaroudi, M. Ojaroudi, and N. Ghadimi, "Dual band notch small monopole antenna with novel W-shaped conductor backed-plane and novel T-shaped slot for UWB applications," *IET Microw. Antennas Propag*., vol. 7, iss. 1, pp. 8-14, 2013.

[15] D. Jiang, Y. Xu, R. Xu, and W. Lin, "A compact ultra-wideband antenna with improved triple band notch characteristics," *Applied Computational Electromagnetics Society (ACES) Journal*, vol. 28, no. 2, pp. 130-136, February 2013.

[16] J. Zhang, H. Yang, and H. Liang, "Band notch split-ring resonators loaded monopole antenna for ultra-wideband applications," *Applied Computational Electromagnetics Society (ACES) Journal*, vol. 28, no. 2, pp. 137-142, February 2013.

[17] A. Subbarao and S. Raghavan, "A novel ultra-wideband planar antenna with rejection of WLAN and ITU bands," *Applied Computational Electromagnetics Society (ACES) Journal*, vol. 28, no. 9, pp. 821-828, September 2013.

[18] R. Azim, M. T. Islam, and A. T. Mobashsher, "Design of a dual band notch UWB slot antenna by means of simple parasitic slits," *IEEE Antennas Wireless Propag. Lett*., vol. 12, pp. 1412-1415, 2013.

[19] "Ansoft high frequency structure simulation (HFSS)," ver. 13, *Ansoft Corporation*, 2010.

Payam Beigi was born in 1987 in Urmia, Iran. He received his B.Sc. degree in Electrical Engineering from Azad University, Urmia Branch and his M.Sc. degree in Electrical Engineering from the Department of Electrical Engineering, Science and Research Branch, Islamic Azad University, West Azerbaijan, Iran. His research interests include monopole antenna, slot antennas, microstrip antennas, small antennas for wireless communications and reconfigurable structure.

Javad Nourinia received his B.Sc. degree in Electrical and Electronic Engineering from Shiraz University and his M.Sc. degree in Electrical and Telecommunication Engineering from Iran University of Science and Technology, and his Ph.D. degree in Electrical and Telecommunication from University of Science and Technology, Tehran Iran in 2000. From 2000, he was an Assistant Professor and now he is a Professor in the Department of Electrical Engineering of Urmia University, Urmia, Iran. His primary research interests are in antenna design, numerical methods in electromagnetic, microwave circuits.

Bahman Mohammadi received the B.S. degree in Electrical Engineering-Telecommunication from Tabriz University, Tabriz, Iran, in 2011 and M.Sc. degrees in Electrical Engineering-Microwave, Antenna and Propagation from Urmia University, Urmia, Iran, in 2013, where he is currently working as a Research Assistant in the Northwest Antenna and Microwave Research Laboratory (NAMRL) in Urmia University, Urmia, Iran. His research interests include electromagnetic computation, array antenna, reflectarray antenna and wideband passive microwave devices (filters, diplexers, couplers, crossovers, phase shifters, transitions, baluns, etc.).

Arash Valizade was born in Tehran, Iran in 1986. He received his B.Sc. in Electrical Engineering-Electronics from Azad University of Sabzevar, Iran, in 2008 and M.Sc. degrees in Electrical Engineering-Telecommunication from Urmia University, Urmia, Iran, in 2012, and he is currently a Ph.D. student at Semnan University, Semnan, Iran. His primary research interests are in numerical methods in electromagnetics, microstrip antenna design, microwave circuits, active integrated antenna and reconfigurable structures.

Analysis for Three-Dimensional Curved Objects by Runge-Kutta High Order Time-Domain Method

Min Zhu [1,3], Qunsheng Cao [1,3], Lei Zhao [2], and Yi Wang [1,3]

[1] College of Electronic and Information Engineering
Nanjing University of Aeronautics and Astronautics, Nanjing 210016, China
minzhu215@gmail.com, qunsheng@nuaa.edu.cn

[2] R&D Department
Nanjing Dodia Measure and Control Technology Co., Ltd., Nanjing, 210028, China

[3] Jiangsu Key Laboratory of Meteorological Observation and Information Processing
Nanjing University of Information Science and Technology, Nanjing, China

Abstract ― In this paper, a Conformal Runge-Kutta High Order Time Domain (C-RK-HO-FDTD) method has been presented and applied to model and analyze in curved objects. The general update equations of the method and the Effective Dielectric Constant (EDC) have been derivated. The scattering of the cylinder and ellipsoid are used to validate the proposed method, and the results are shown that the scheme provides the better accuracy than the HO-FDTD and other higher order methods.

Index Terms ― Conformal, curved, FDTD, high-order, interface, Runge-Kutta.

I. INTRODUCTION

Yee's Finite Difference Time-Domain (FDTD) formulas [1], conservative and dispersive with second-order accuracy both in time and space, has been widely used to solve various electromagnetic problems. It is known that the FDTD method has two primary drawbacks, one is the numerical dispersion is the dominate limitation to the accuracy of the FDTD method, and another is the inability to accurately model curved complex surfaces and material discontinuities by using the stair-case approach with structured grids. In the past decade, numerous efforts have been made to improve the drawbacks, including some modified high-order methods. The original high order FDTD (2, 4) method [2] has the second-order accuracy in temporal domain and the fourth-order accuracy in spatial domain, and the scheme has the better dispersion error. Kang, et al. [3], found that the high order scheme reduced the numerical dispersion and anisotropy and has improved stability. The further studied on the high-order FDTD (2, 4) [4] method had found that the accuracy improved from the application of the constitutive material parameter. But the high order FDTD method also has shortcomings to deal with the curved objects.

More attentions are focused on how to model curved PEC objects. For example, locally Conformal FDTD (CFDTD) method [5], given by Dey and Mittra, was modeled and solved to the curved metallic objects, they found the CFDTD numerical results are more accurate than that of the FDTD method. Stefan and Nicolas [7] proposed a new conformal PEC algorithm of the FDTD method, which only needed to change two field updated coefficients, it could privilege either speed or accuracy when choosing a time step reduction [6]. In reference [7], the conformal FDTD (2, 4) method had been compared with the high-order staircase and low-order conformal algorithms. Some other papers researched on curved dielectric objects using the conformal FDTD method [8-10].

However, scarcely any academic papers to use the Runge-Kutta Higher Order FDTD (RK-HO-FDTD) method with conformal techniques to

Submitted On: May 14, 2014
Accepted On: October 5, 2014

explore the scattering property of curved dielectric objects. In this paper, we mainly introduce the C-RK-HO-FDTD method and its applications of scattering problems.

II. RUNGE-KUTTA HIGH ORDER CONFORMAL FDTD METHOD

A. The RK-HO-FDTD method

For simplicity, we take E field in x-component for example, the update equation of RK$_m$-HO-FDTD (2, 2m) method can be written as [11]:

$$\frac{\partial E^x_{i+1/2,j,k}(t)}{\partial t}=\frac{1}{\varepsilon}\sum_{v=1}^{m}a(v)\left[\frac{1}{\Delta y}\left(H^z_{i+1/2,j-1/2+v,k}(\mathrm{t})-H^z_{i+1/2,j+1/2-v,k}(\mathrm{t})\right)-\frac{1}{\Delta z}\left(H^y_{i+1/2,j,k-1/2+v}(\mathrm{t})-H^y_{i+1/2,j,k+1/2-v}(\mathrm{t})\right)\right], \quad (1)$$

where coefficient m is a spatial stencil size. Parameters ε, Δt, Δx, Δy, Δz are permittivity, temporal step size and Δx=Δy=Δz, along x-, y- and z-directional spatial step sizes, respectively. The coefficients $a(v)$ [12-13] of different spatial stencil sizes are listed in Table 1.

Table 1: Coefficients for HO-FDTD method

	(2, 2)	(2, 4)	(2, 6)
$a(1)$	1.0	9/8	2250/1920
$a(2)$		-1/24	-125/1920
$a(3)$			45/1920

B. C-RK-HO-FDTD Method (derived)

In order to derive the general update equations of the CHO-FDTD (2, 2m) method, the Eq. (1) can be rewritten in another form as:

$$\begin{aligned}\varepsilon\frac{\partial E^x_{i+1/2,j,k}(t)}{\partial t}&=\frac{a(1)}{\Delta x}\left[\left(H^z_{i+1/2,j+1/2,k}(\mathrm{t})-H^z_{i+1/2,j-1/2,k}(\mathrm{t})\right)-\left(H^y_{i+1/2,j,k+1/2}(\mathrm{t})-H^y_{i+1/2,j,k-1/2}(\mathrm{t})\right)\right]\\&+\frac{3a(2)}{3\Delta x}\left[\left(H^z_{i+1/2,j+3/2,k}(\mathrm{t})-H^z_{i+1/2,j-3/2,k}(\mathrm{t})\right)-\left(H^y_{i+1/2,j,k+3/2}(\mathrm{t})-H^y_{i+1/2,j,k-3/2}(\mathrm{t})\right)\right]\\&+\cdots\\&+\frac{(2v-1)a(v)}{(2v-1)\Delta x}\left[\left(H^z_{i+1/2,j-1/2+v,k}(\mathrm{t})-H^z_{i+1/2,j+1/2-v,k}(\mathrm{t})\right)-\left(H^y_{i+1/2,j,k-1/2+v}(\mathrm{t})-H^y_{i+1/2,j,k+1/2-v}(\mathrm{t})\right)\right]. \quad (2)\end{aligned}$$

It is easy to prove the relationship of summation, $\sum_{v=1}^{m}a(v)(2v-1)=1$, so the Eq. (2) is decomposed into (2v-1) sub equations, that are:

$$a(1)\varepsilon(1)\frac{\partial E^x_{i+1/2,j,k}(t)}{\partial t}=\frac{a(1)}{\Delta x}\left(H^{z,n+1/2}_{i+1/2,j+1/2,k}-H^{z,n+1/2}_{i+1/2,j-1/2,k}-H^{y,n+1/2}_{i+1/2,j,k+1/2}+H^{y,n+1/2}_{i+1/2,j,k-1/2}\right), \quad (3)$$

$$3a(2)\varepsilon(2)\frac{\partial E^x_{i+1/2,j,k}(t)}{\partial t}=\frac{3a(2)}{3\Delta x}\left(H^{z,n+1/2}_{i+1/2,j+3/2,k}-H^{z,n+1/2}_{i+1/2,j-3/2,k}-H^{y,n+1/2}_{i+1/2,j,k+3/2}+H^{y,n+1/2}_{i+1/2,j,k-3/2}\right), \quad (4)$$

$$(2v-1)a(v)\varepsilon(2v-1)\frac{\partial E^x_{i+1/2,j,k}(t)}{\partial t}=\frac{(2v-1)a(v)}{(2v-1)\Delta x}\left(H^{z,n+1/2}_{i+1/2,j+v-1/2,k}-H^{z,n+1/2}_{i+1/2,j-v-1/2,k}-H^{y,n+1/2}_{i+1/2,j,k+v-1/2}+H^{y,n+1/2}_{i+1/2,j,k-v+1/2}\right), \quad (5)$$

where coefficient of $\varepsilon(v)$ (v=1,2,…,2v-1) is concerned permittivity of cell size Δx, $3\Delta x$,… and $(2v\text{-}1)\Delta x$, respectively. It is clear that the support interval of the FDTD method is Δx, thus, the Eqs. (4) and (5) can be treated as the support intervals $3\Delta x$ and $(2v\text{-}1)\Delta x$ of the FDTD update equation. For the sake of simplicity and generality, the C-RK$_2$-HO-FDTD (2, 6) approach is employed in this work. The multi-region decomposition of electric field E is shown in Fig. 1.

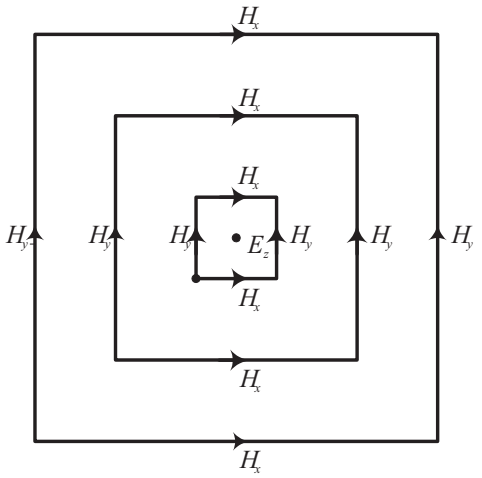

Fig. 1. E field multi-region decomposition for C-RK-HO-FDTD method.

Substituting equations (2)-(5) into the relationship of summation, the update equation of the C-RK-HO-FDTD (2, 2m) can be written as:

$$\sum_{v=1}^{m}(2v-1)a(v)\varepsilon(v)\frac{\partial E^x_{i+1/2,j,k}(t)}{\partial t}=\sum_{v=1}^{m}a(v)\frac{\Delta t}{\Delta x}\left(H^{z,n+0.5}_{i+0.5,j+v-0.5,k}-H^{z,n+0.5}_{i+0.5,j-v+0.5,k}-H^{y,n+0.5}_{i+0.5,j,k+v-0.5}+H^{y,n+0.5}_{i+0.5,j,k-v+0.5}\right). \quad (6)$$

From the equation above, the effective dielectric constant ε^{eff} can be written as:

$$\varepsilon^{eff} = \sum_{v=1}^{m} (2v-1)a(v)\varepsilon(v). \quad (7)$$

The area weighting technique is employed [14] to define $\varepsilon(v)$ as:

$$\varepsilon(v) = \frac{S_1}{S_1+S_2}\varepsilon_1 + \frac{S_2}{S_1+S_2}\varepsilon_2, \quad (8)$$

$$\varepsilon^{eff} = \sum_{v=0}^{L_s-1} \frac{a(v)}{(2v+1)S}[S_1\varepsilon_1 + ((2v+1)^2 S - S_1)\varepsilon_2], \quad (9)$$

where S, S_1 and S_2 are a regular unit area, out of the dielectric object area and dielectric object area, respectively. Figure 2 shows different distributed cases.

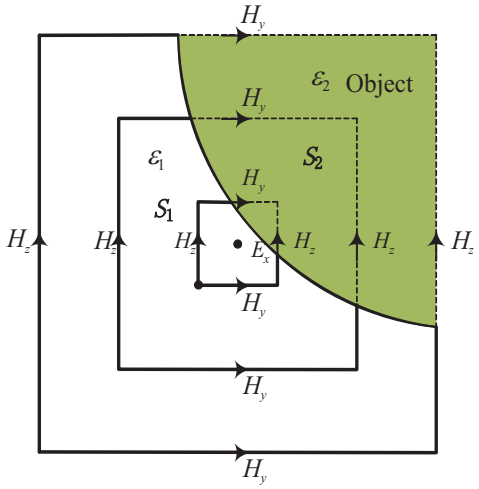

(a)

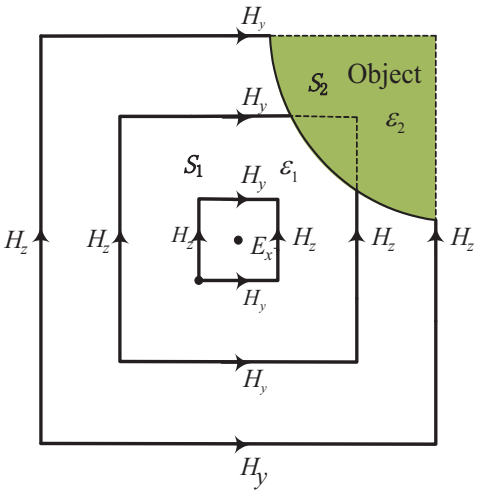

(b)

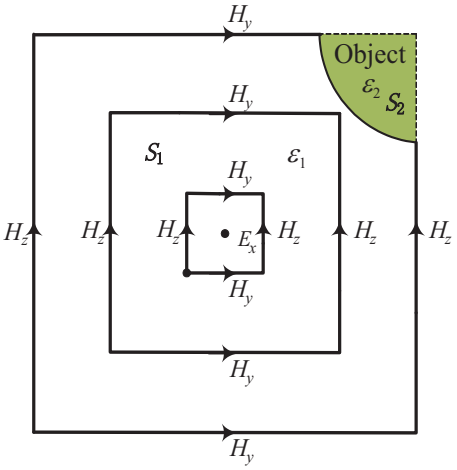

(c)

Fig. 2. Different distributed cases: (a) completely distorted, (b) partially distorted seized over two grids, and (c) partially distorted seized one cell only.

III. NUMERICAL RESULTS

In this part, the numerical simulations have provided to validate the C-RK-HO-FDTD method. The direction of propagation of the incident wave and polarization are defined in Fig. 3.

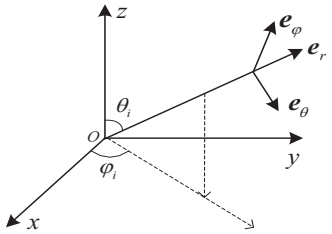

(a)

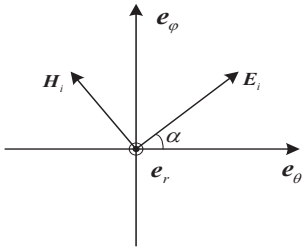

(b)

Fig. 3. Definition of direction of propagation of the incident wave and polarization (a) Definition of direction of the incident wave propagation, (b) Definition of direction of the incident wave and polarization.

A. Scattering of a dielectric cylinder

Considered to scattering of a dielectric cylinder with a radius of 0.015 m, height of 0.06 m, relative permittivity ε_r as 4, and relative permeability μ_r as 1.0. An incident sinusoidal wave of a wavelength 0.03 m propagates along the z-direction, its polarization is along the x-direction. The geometric model of the dielectric cylinder is shown in Fig. 4.

Taken 10 grids per wavelength, the number of CFL is as 0.3 for the different methods. Eight layers of Anisotropic Perfectly Matched Layer (APML) are used to truncate the computational domain.

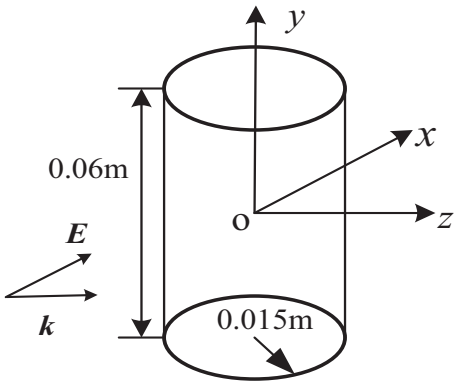

Fig. 4. Geometric model of the dielectric cylinder.

All computational simulations are based on computer of Pentium dual-core 2.8 GHz CPU and 1.87 G as memory. The total computational volume is discretized into 82×82×82 grids. The E-plane bistatic Radar Cross Sections (RCS) for different methods of the dielectric cylinder are shown in Fig. 5, which are the Method of Moment (MoM), the HO-FDTD (2, 4) and the C-RK$_2$-HO-FDTD (2, 4) methods. Compared the results with the MoM method, the C-RK$_2$-HO-FDTD (2, 4) is more consistent than the FDTD method. Figure 6 shows the results of errors are the absolute values of MoM subtracting the HO-FDTD (2, 4) and C-RK$_2$-HOFDTD (2, 4). Figure 7 is a comparison of the E-plane bistatic RCS obtained by different order conformal methods (theta is the incident angle θ in the following figures), the results show that the simulation of the CHO-FDTD (2, 6), C-RK$_2$-HO-FDTD (2, 6) and MoM, the result of C-RK$_2$-HO-FDTD (2, 6) displayed more accuracy. The errors of the CHO-FDTD (2, 6) C-RK$_2$-HO-FDTD (2, 6) are shown in Fig. 8.

In Table 2 is listed the magnitudes of the spatial discretization, temporal discretization, total computational domain, total time steps and CPU time. From the table, it is found that the CPU times of these methods are nearly the same of the non-conformal methods and conformal methods, and the accuracy of C-RK$_2$-HO-FDTD (2, 6) better agrees with that of the MoM

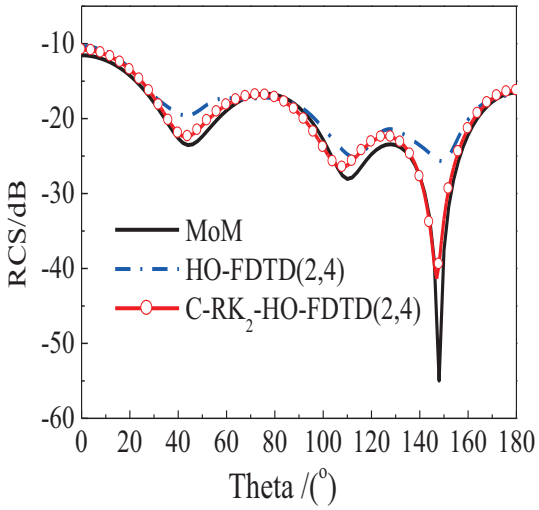

Fig. 5. RCS of E-plane bistatic in the dielectric cylinder of different methods.

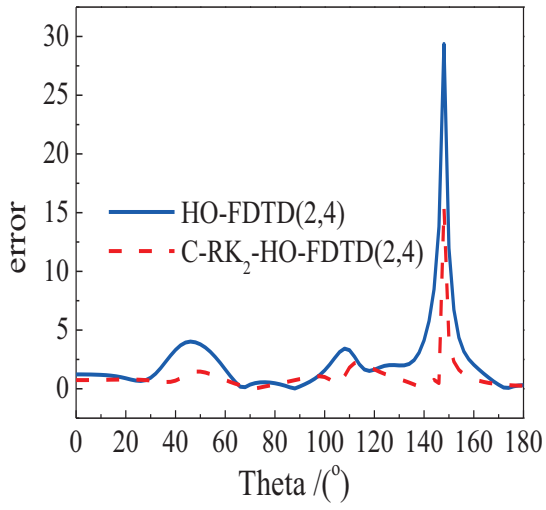

Fig. 6. Errors of the HO-FDTD (2, 4) and C-RK$_2$-HOFDTD (2, 4) methods.

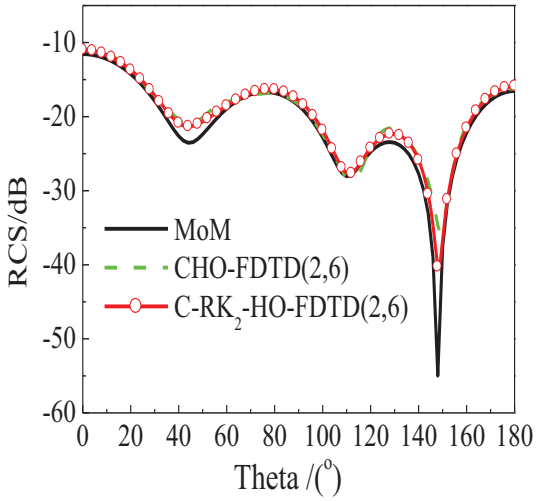

Fig. 7. RCS of *E*-plane bistatic in the dielectric cylinder of different methods

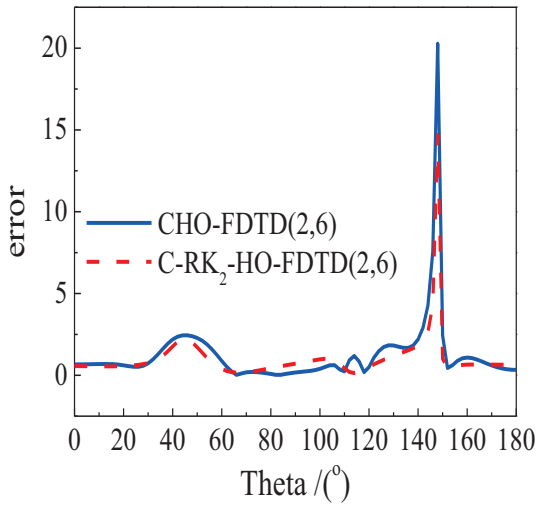

Fig. 8. Errors of the CHO-FDTD (2, 6) and C-RK$_2$-HO-FDTD (2, 6) methods.

Table2: Computational time for different methods

Methods	HO-FDTD (2, 4)	C-RK$_2$-HO-FDTD (2, 4)	HO-FDTD (2, 6)	C-RK$_2$-HO-FDTD (2, 6)
$\Delta x=\Delta y=\Delta z$ (m)	0.003	0.003	0.003	0.003
Δt (*ps*)	3.2	3.2	3.2	3.2
Cells	82×82×82	82×82×82	82×82×82	82×82×82
Total time steps	2007	2007	2007	2007
CPU time (*s*)	1416.0	3134.4	1709.2	3501.4

B. Scattering of a dielectric ellipsoid

The radius of dielectric ellipsoid are 0.6 m, 0.6 m and 0.3 m along *x*-, *y*-, *z*-direction, respectively, the relative permittivity ε_r is as 4, relative permeability μ_r is as 1, the polarization of the electric field is along *x*-direction, and the wavelength of the incident wave along the z-direction is as 0.3 m. The geometric model of the dielectric ellipsoid is shown in Fig. 11. The CFL number is chosen as 0.3.

Backward scattering bistatic RCS in the different schemes are drawn in Figs. 9 and 12. It is found that the C-RK-HO-FDTD methods are similar to the MoM method. The errors of the FDTD and MoM and C-RK$_2$-HO-FDTD (2, 6) and MoM are shown in Figs. 10 and 13. The comparisons of the CPU time in different methods are listed in Table 3.

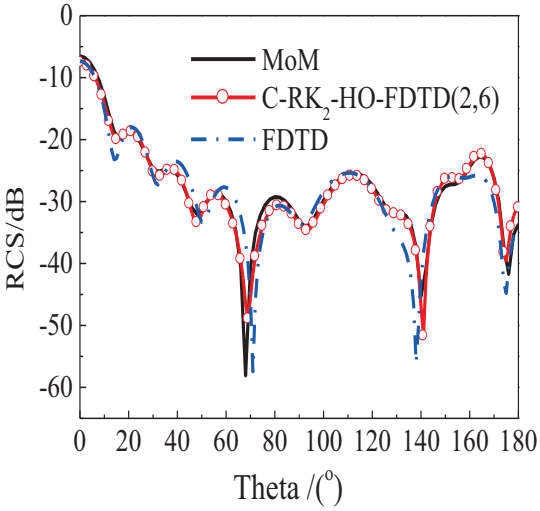

Fig. 9. RCS of *E*-plane bistatic in the dielectric ellipsoid of different methods.

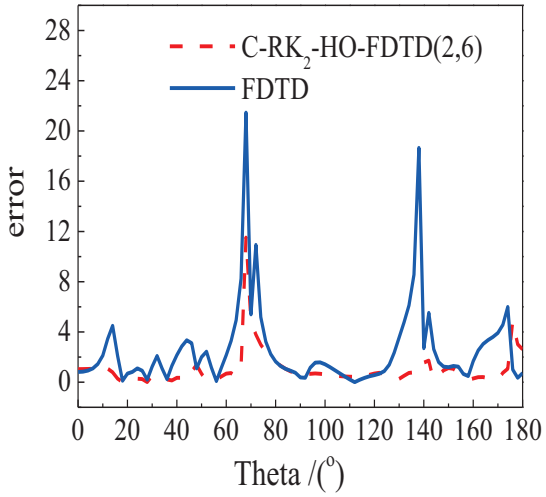

Fig. 10. Errors of the FDTD and C-RK$_2$-HO-FDTD (2, 6) methods.

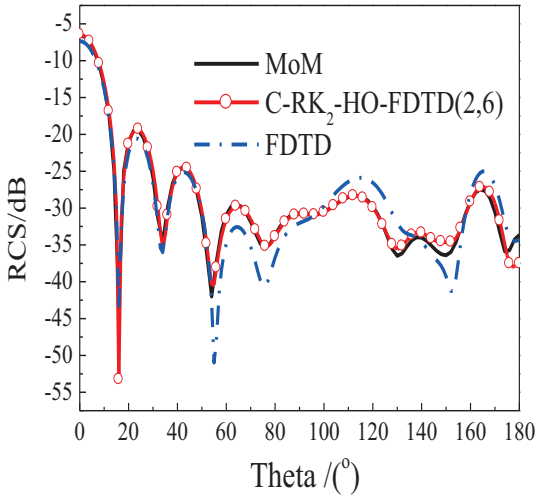

Fig. 12. RCS of *H*-plane bistatic in the dielectric ellipsoid of different methods.

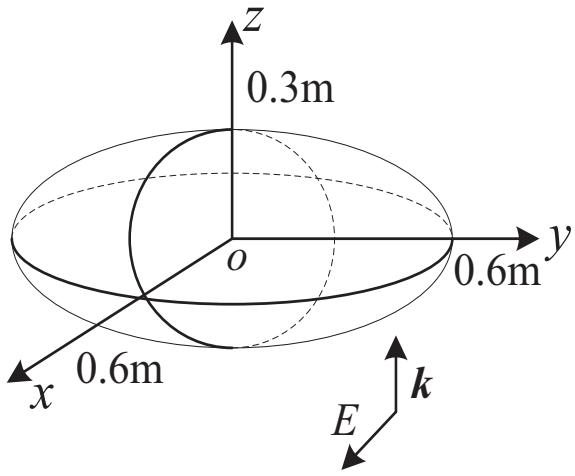

Fig. 11. Geometric model of the dielectric ellipsoid.

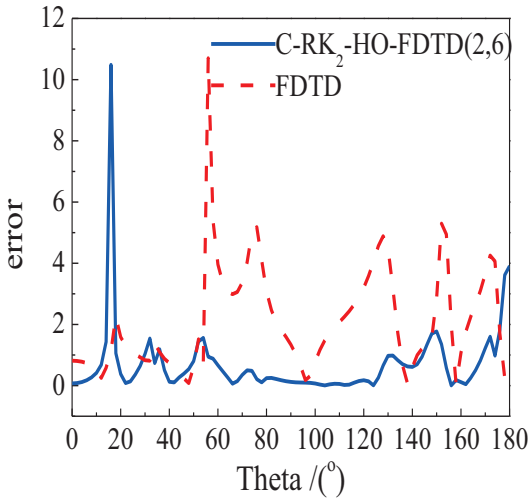

Fig. 13. Errors of the FDTD and C-RK2-HO-FDTD (2, 6) methods.

Table 3: Computational time for different methods

Methods	FDTD (2, 4)	C-RK$_2$-HO-FDTD (2, 6)	C-RK$_2$-HO-FDTD (2, 6)
$\Delta x=\Delta y=\Delta z$ (m)	0.03	0.03	0.03
Δt (*ps*)	30	30	30
Cells	118×118×92	118×118×92	118×118×92
Total time steps	2008	2008	2008
CPU time (*s*)	4026.4	7357.7	8046.5

IV. CONCLUSIONS

In this paper, we have introduced the CHO-FDTD method and its applications to the scattering of dielectric material. The multiregion decomposition technique is used to derivate the general update equations of the C-RK-HO-FDTD, and combine the conformal and EDC technique to treat the dielectric objects. The area weighting is introduced to obtain the EDC in the interface of different regions. Numerical examples of the dielectric structures for different methods have been studied. Bistatic RCSs of the dielectric

cylinder and ellipsoid are validated in the scheme. It was found that the C-RK-HO-FDTD method has more accuracy than the traditional FDTD method.

ACKNOWLEDGMENT

The work is supported by the Funding of Jiangsu Innovation Program for Graduate Education and the Fundamental Research Funds for the Central Universities under the contract cxzz12-0156. The work was also supported by the National Nature Science Foundation of China under Contract 61172024 and Open Research Program in Jiangsu Key Laboratory of Meteorological Observation and Information Processing.

REFERENCES

[1] K. S. Yee, "Numerical solution of initial boundary value problems involving maxwell's equations in isotropic media," *IEEE Trans. Antennas Propagat*., vol. AP-14, pp. 302-307, 1966.

[2] J. Fang, "Time domain finite difference computation for Maxwell's equation," Ph.D. dissertation, *Univ. of California at Berkeley*, Berkeley, CA, 1989.

[3] L. Kang, Y. W. Liu, and W. G. Lin, "A high order (2, 4) scheme for reducing dispersion in FDTD algorithm," *IEEE Trans. Electromagn. Compat*., vol. 41, no. 2, pp. 160-165, May 1995.

[4] T. T. Zygiridis and T. D. Tsiboukis, "Low-dispersion algorithms based on the higher order (2, 4) FDTD method," *IEEE Trans. Microw. Theory Tech*., vol. 52, no. 4, pp. 1321-1327, April 2004.

[5] S. Dey and R. Mittra, "A locally conformal finite-difference time-domain (FDTD) algorithm for modeling three-dimensional perfectly conducting objects," *IEEE. Microwave and Guided Wave Letters*, vol. 7, no. 9, pp. 273-275, September 1997.

[6] S. Dey and R. Mittra, "A conformal finite-difference time-domain technique for modeling cylinderical dielectric resonators," *IEEE Trans. Microw. Theory Tech*., vol. 47, no. 9, pp. 1737-1739, September 1999.

[7] B. Stefan and C. Nicolas, "A new 3-D conformal PEC FDTD scheme with user-defined geometric precision and derived stability criterion," *IEEE Trans. Antennas Propagat*., vol. 54, no. 6, pp. 1843-1849, June 2006.

[8] W. Sha and X. Wu, "A new conformal FDTD (2, 4) scheme for modeling three-dimension curved perfectly conducting objects," *IEEE Microwave Wireless Components Letter*, vol. 18, no. 3, pp. 149-151, March 2008.

[9] W. Yu and R. Mittra, "A conformal finite difference time domain technique for modeling curved dielectric surfaces," *IEEE Microwave Wireless Components Letter*, vol. 11, no. 1, pp. 25-27, January 2008.

[10] J. Wang and W. Y. Yin, "FDTD (2, 4)-compatible conformal technique for treatment of dielectric surfaces," *Electronic Letters*, vol. 45, no. 3, January 2009.

[11] M. Zhu, Q. Cao, and L. Zhao, "Study and analysis of a novel RK-HO-FDTD method," *IET Microw. Antennas Propag*., vol. 8, no. 12, pp. 951-958, September 2014.

[12] M. Zhu and Q. Cao, "Studying and analysis of the characteristic of the high-order and MRTD and RK-MRTD scheme," *Applied Computational Electromagnetics Society*, vol. 28, no. 5, pp. 380-389, May 2013.

[13] M. Zhu and Q. Cao, "Characteristic analysis of high-order FDTD method," *2012 10th International Symposium on Antennas, Propagation and EM Theory*, pp. 975-978, October 2012.

[14] J. Wang and W. Y. Yin, "Development of a novel FDTD (2, 4)-compatible conformal scheme for electromagnetic computations of complex curved PEC objects," *IEEE Trans. Antennas Propagat*., vol. 61, no. 1, pp. 299-309, January 2013.

A Novel Compact CPW-Fed Antenna with Circular Polarization Characteristics for UWB Applications

Fateme Azamian, Mohammad Naghi Azarmanesh, and Changiz Ghobadi

Department of Electrical Engineering, Urmia Branch
Islamic Azad University, Urmia, Iran
fateme.azamian@gmail.com, m.azarmanesh@urmia.ac.ir, ch.ghobadi@urmia.ac.ir

Abstract ─ A novel compact antenna with Circular Polarization (CP) characteristics is presented. The antenna structure includes an asymmetrical rectangular radiating patch from which a semi-circle shaped slot is cut. A 50 Ω Co-Planar Waveguide (CPW) feed line with two rectangular slots feeds the antenna. Two inverted L-shaped strips and also two spiral shaped slots are embedded on opposite corners of the ground plane to further enhance the antenna bandwidth and also generate the circular polarization property. The antenna is printed on a compact size FR4 substrate with the total dimensions of $20\times20\times1.6$ mm^3. The proposed antenna operates over the frequency range of 3-14.5 GHz for VSWR<2 and exhibits CP in 5.35-7.65 GHz (35%).

Index Terms ─ Circular polarization, CPW-feed line, Ultra-Wideband.

I. INTRODUCTION

The assignment of 3.1-10.6 GHz as UWB frequency range by Federal Communication Commission (FCC), can be considered an evolution in antenna design realm. As antenna is an essential component of every communication system; since then, a vast variety of antennas have been designed and published to be used in UWB frequency band [1]-[5]. One category of the antennas which has recently gained great popularity is circularly polarized antennas. By the use of CP antennas, there will be no need to consider the orientation between the transmitter and receiver. Apart from this, higher performance and better mobility and weather penetration with respect to the Linearly Polarized (LP) antennas are of the other CP antennas features [6]-[7]. Recently, a lot of CP antennas have been proposed. For instance in [8], placing of two spiral slots in the ground plane results in circular polarization generation. In [9], Chen, et al., propose a CPW-fed antenna with a widened L-type strip which exhibits CP about 17%. Three L-shaped strips are embedded on corners of the ground plane of antenna in [10] to get the desired CP operation. A simple antenna with inverted L-shaped strip is introduced in [11] that shows circular polarization characteristics in L-band. In this paper, we propose a novel structure of a CP antenna. The study antenna is printed on a cheap FR4 substrate with dimensions of $20\times20\times1.6$ mm^3 and exhibits CP in 5.35-7.65 GHz. A simple radiating patch with a semi-circle shaped slot along with a ground plane with two spiral shaped slots and also two inverted L-shaped strips on two corners, comprise the antenna's configuration. A slotted CPW feed line feeds the antenna. Small size, wide impedance and Axial Ratio (AR) bandwidth are of advantages of this antenna. The remainder of the paper is outlined as follows: The structure and design process of the antenna are discussed in Section II. The simulation results of parametric study, measured results and their comparisons are presented in Section III. Finally the conclusion of the paper is presented in Section IV.

II. ANTENNA DESIGN

The schematic of the proposed CP antenna is shown in Fig. 1 (a). The fabricated antenna is also shown in Fig. 1 (b). The proposed antenna is printed on a cheap FR4-epoxy substrate with permittivity of 4.4, loss tangent of 0.002 and

Submitted On: July 20, 2013
Accepted On: September 6, 2014

thickness of 1.6 mm. A CPW feed line with the length and width of 4.2 mm and 3.1 mm respectively, is adopted to feed the study antenna; of course two rectangular slots with dimensions of 1.2mm×0.6mm are cut from both sides of the feed line. Two inverted L-shaped strips with inner areas of 5.5×5.5 mm^2 and 3.7×3.7mm^2 on top-right and bottom-left corners of the antenna structure play the main role in CP generation. Also, two spiral shaped slots are removed from the antenna ground plane on two corners opposite to the location of L-shaped strips. To better analyze the antenna performance, four prototypes are introduced in Fig. 2 until reaching the antenna's final structure. As it is seen, Ant. I includes a simple feed line and an asymmetrical radiating patch. In Ant. II, two inverted L-shaped strips are added to the top-right and bottom-left corners of the antenna ground plane and form two square slots with the areas of 5.5×5.5 mm^2 and 3.7×3.7 mm^2 respectively. Ant. III contains two spiral shaped slots cut from the ground plane top-left and bottom-right corners (opposite of the inverted L-shaped strips' locations), and finally in Ant. IV that shows the final structure, two rectangular slots are cut from the feed line and also a semi-circle with the radius of 1.5 mm is removed from the right side of the radiating patch. The four introduced antennas have been simulated and VSWR and AR results relating to these antennas are plotted in Fig. 3 (a) and (b).

As it is seen from Fig. 3, Ant. I does not have good impedance matching and also no circular polarization is seen for this structure. In Ant. II, by the addition of two inverted L-shaped strips to the top-right and bottom-left corners, the antenna impedance matching has improved noticeably at higher frequencies. The reason is laid in the fact that by the addition of these L-shaped strips to the antenna structure, a new path is made for the current. Figure 4 shows the surface current flow through the L-shaped strips. As the current flows in the newly created path, new resonances at 8 GHz and 10.4 GHz are excited and the antenna bandwidth has improved. In this stage, still there is poor impedance matching problem in lower frequency edge and UWB spectrum is not fully covered. Ant. II generates circular polarization in 6-7.3 GHz. The problem of poor impedance matching at lower frequencies is overcome by the inclusion of the spiral shaped slots in Ant. III, but the same problem is seen at 8 GHz. By this change, the lower and higher frequency edges of AR curve are shifted toward lower and higher frequencies respectively, and a wider AR bandwidth at 5.65-7.4 GHz is obtained. Finally in Ant. IV, shows better performance at around 8 GHz. The poor impedance matching problem is completely overcome. UWB frequency range if fully covered and CP is generated in 5.6-7.4 GHz.

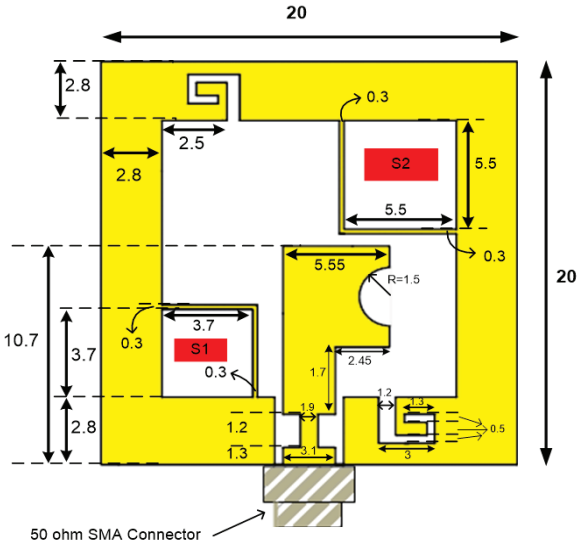

(a)

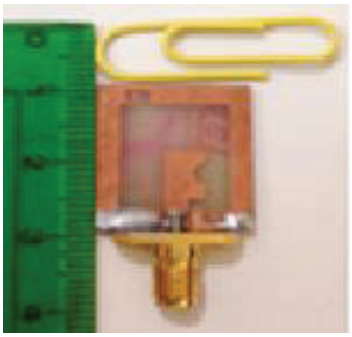

(b)

Fig. 1. (a) The schematic geometry of the proposed antenna, and (b) the fabricated antenna.

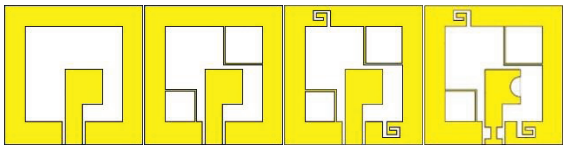

(a) (b) (c) (d)

Fig. 2. (a) Ant. I, (b) Ant. II, (c) Ant. III, and (d) Ant. IV.

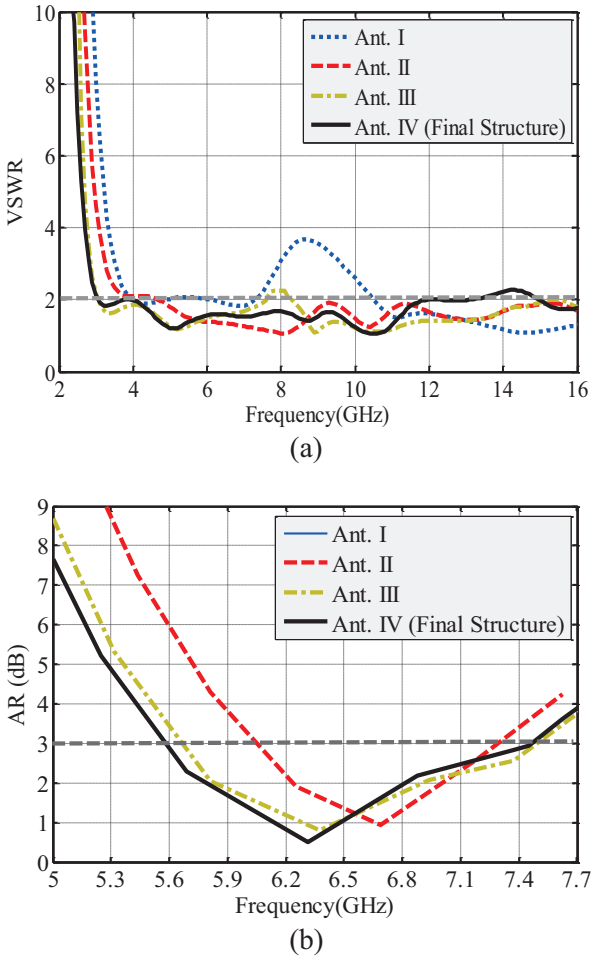

Fig. 3. (a) VSWR curves for the four mentioned antennas, and (b) AR curves for the four mentioned antennas.

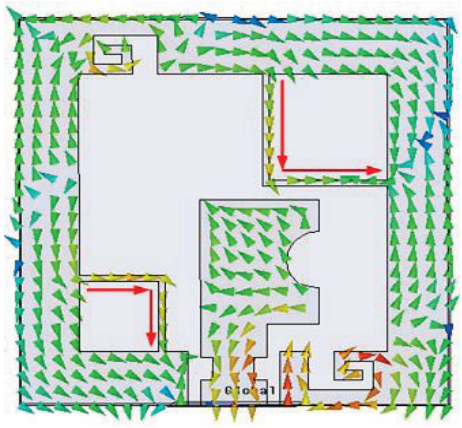

Fig. 4. Surface current distribution on the antenna at 8 GHz.

To further investigate the antenna performance, a parametric study is also carried out. Figure 5 (a) and (b) show the simulated VSWR and AR curves for three values of the semi-circle radius that is removed from the radiating patch. The semi-circle radius named as "R" is varied from 1 mm to 2 mm with a step of 0.5 mm. Simulated results clearly show that changing of R does not influence the lower frequency edge of VSWR curves but the upper frequency edge shifts toward lower frequencies, which means the bandwidth reduction. This parameter also affects AR. It is seen from Fig. 5 (b), that when R=1.5 mm, wider AR bandwidth is obtained for the antenna respect to the other two cases. The other parameter that is studied is the inner area of two square slots on two corners of the antenna named as S_1 and S_2. Figure 6 (a) and (b) show VSWR and AR curves for different values of these parameters. Three values are chosen for S_1 and S_2. As it is seen from simulated results of Fig. 6, both lower and higher frequency edges of VSWR are sensitive to the variation of S_1 and S_2. With S_1=3.2mm×3.2mm and S_2=5.2mm×5.2mm, poor impedance matching is seen in VSWR curves around 8 GHz. By increasing the areas with a step of 0.3mm×0.3mm, the VSWR value goes under 2 and leads to impedance matching enhancement at this frequency. When S_1 and S_2 are adjusted in 3.7mm×3.7mm and 5.5mm×5.5mm respectively, the widest frequency range is covered by the proposed antenna. These areas also affect the AR curve. Figure 6 (b) shows that for the first case when S_1=3.2mm×3.2mm and S_2=5.2mm×5.2mm, circular polarization is not generated and when S_1=4mm×4mm and S_2=5.8mm×5.8mm, circular polarization is seen in 6.45-7.15 GHz. The best and widest CP is seen in black color, when S_1 is 3.7mm×3.7mm and S_2 is 5.5mm×5.5mm.

Antenna CP mechanism is explained in Fig. 7, using surface current distribution at 0, 90, 180 and 270 degree phases. It is observed that the surface current distribution in 180 and 270 has equal magnitude but they are opposite in phase of 0 and 90. From the results, It is seen that the surface current rotates counter clockwise on the antenna, so the antenna shows Left-Hand Circular Polarization (LHCP) in 6.5 GHz.

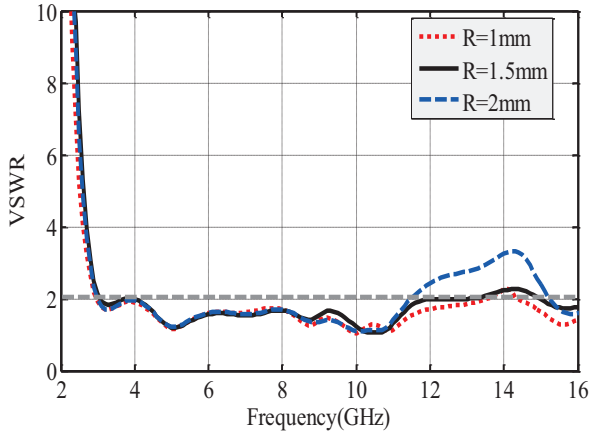

Fig. 5. (a) VSWR curves for three values of parameter "R", and (b) AR curves for three values of parameter "R."

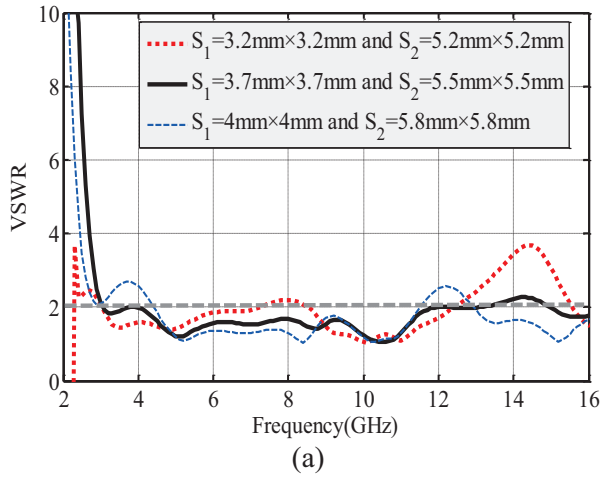

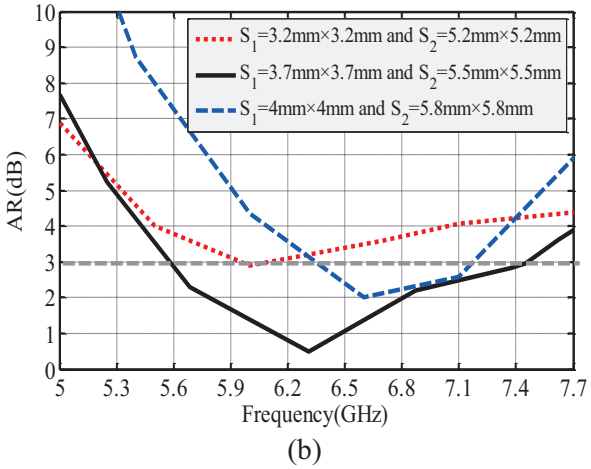

Fig. 6. (a) VSWR curves for different values of S_1 and S_2, and (b) AR curves for different values of S_1 and S_2.

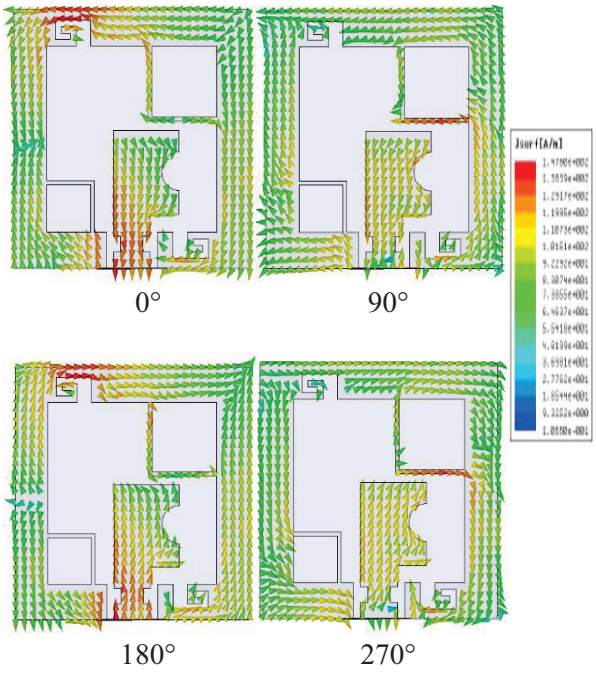

Fig. 7. Surface current distribution at 6.5 GHz.

III. RESULTS AND DISCUSSIONS

The proposed antenna with the given values in Fig. 1, has been fabricated and tested. Figure 8 (a) shows the simulated and measured VSWR curves. From the measured results, the frequency band of 3-14.5 GHz is covered by the antenna,

which is a little more than the bandwidth obtained from simulation. Also, the simulated and measured AR curves are plotted in Fig. 5 (b), 5.35-7.65 GHz is under 3 dB Axial Ratio that is in good agreement with the results from HFSS. The difference between the simulated and measured results may be due to the SMA connector that is used in measurement process and also the effect of soldering the SMA connector to antenna.

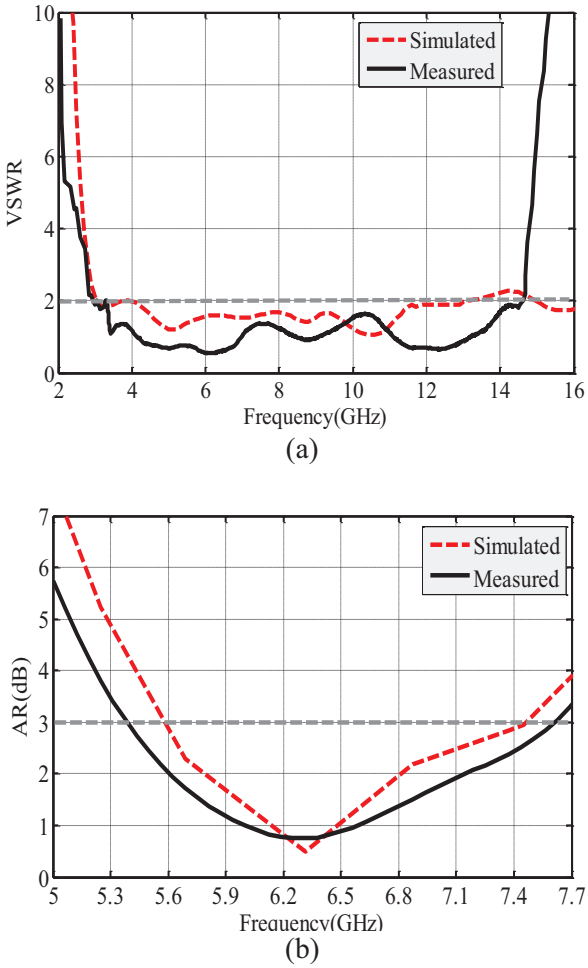

Fig. 8. (a) Simulated and measured VSWR of the proposed antenna, and (b) simulated and measured AR of the proposed antenna.

In addition to VSWR and AR, antenna gain is also measured and is plotted in Fig. 9. As it is seen, both the antenna simulated and measured gains vary in acceptable ranges.

Measured LHCP and RHCP radiation pattern of the antenna is plotted in Fig. 10 at 6.2 GHz and 7 GHz. Suitable pattern is obtained for the proposed antenna.

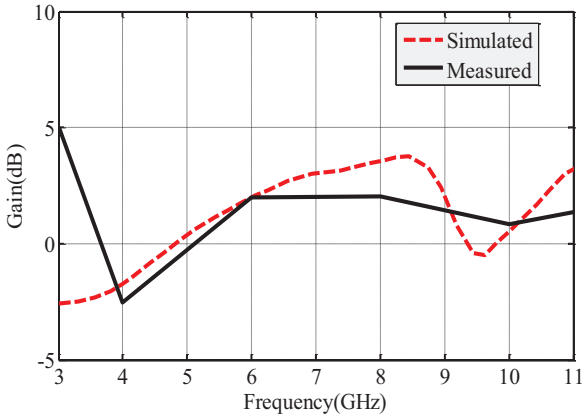

Fig. 9. Simulated and measured gain of the proposed antenna.

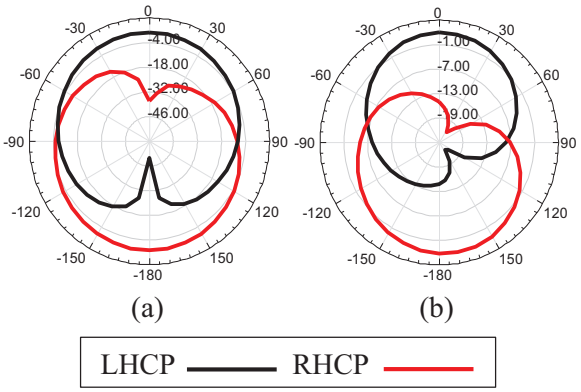

Fig. 10. Measured radiation pattern at: (a) 6.2 GHz, and (b) 7 GHz.

IV. CONCLUSION

A novel compact CPW-fed antenna with CP characteristics is introduced in this work. Antenna geometry is composed of a slotted CPW feed line, a radiating patch with a semi-circle slot, two inverted L-shaped strips and also two spiral shaped slots on the ground plane. The combination of these elements and properly adjusting their dimensions lead to impedance bandwidth extended from 3 GHz to14.5 GHz, and CP in 5.35-7.65 GHz (35%). The presented antenna is printed on FR4 substrate with the size of 20×20×1.6 mm^3. Small size, wide impedance and AR bandwidth, acceptable gain range and suitable radiation patterns are of the merits of the presented antenna, which makes it a good choice for UWB systems.

REFERENCES

[1] M. Majidzadeh and C. Ghobadi, "Compact microstrip-fed monopole antenna with modified slot ground plane for UWB applications," Applied Computational Electromagnetics Society (ACES), vol. 27, no. 10, pp. 801-807, 2012.

[2] R. Azim, M. T. Islam, and N. Misran, "Design of a planar UWB antenna with new band enhancement technique," Applied Computational Electromagnetics Society (ACES) Journal, vol. 26, no. 10, pp. 856-862, October 2011.

[3] J. Liu, S. Zhong, and K. P. Esselle, "A printed elliptical monopole antenna with modified feeding structure for bandwidth enhancement," *IEEE Trans. Antennas Propagat*., vol. 59, no. 2, pp. 667-670, February 2011.

[4] M. Ojaroudi, S. Yazdanifard, N. Ojaroudi, and M. Naser-Moghaddasi, "Small square monopole antenna with enhanced bandwidth by using inverted T-shaped slot and conductor-backed plane," *IEEE Trans. Antennas Propagat*., vol. 59, no. 2, pp. 670-674, February 2011.

[5] A. K. Gautam, S. Yadav, and B. K. Kanaujia "A CPW-fed compact UWB microstrip antenna," *IEEE Antenna and Propag. Letters*, vol. 12, pp. 151-154, 2013.

[6] K. L. Wong, F. S. Chang, and T. W. Chiou, "Low-cost broadband circularly polarized probe-fed patch antenna for WLAN base station," *In Proc. IEEE Antennas Propag. Soc. Int. Symp*., vol. 2, pp. 526-529, 2002.

[7] K. L. Lau and K. M. Luk, "A novel wideband circularly polarized patch antenna based on L-probe and slot-coupling techniques," *In Proc. IEEE Antennas Propag. Soc. Int. Symp*., vol. 3, pp. 878-881, 2003.

[8] C. Chen and E. K. N. Yung, "Dual-band dual-sense circularly-polarized CPW-fed slot antenna with two spiral slots," *IEEE Trans. on Antenna and Propag*., vol. 57, no. 6, pp. 1829-1833, 2009.

[9] Y. B. Chen, X. F. Liu, Y. C. Jiao, and F. S. Zhang, "CPW-fed broadband circularly polarized square slot antenna," *Electronics Letters*, vol. 42, no. 19, pp. 1074-1075, 2006.

[10] S. Ahdi Rezaeieh and M. Kartal, "Broadband CPW-fed circularly polarized square slot antenna with inverted L-strips for wireless applications," *Microwave and Optical Technology Letters*, vol. 54, no. 6, pp. 1399-1402, 2012.

[11] S. Fu, S. Fang, Z. Wang, and X. Li, "Broadband circularly polarized slot antenna array fed by asymmetric CPW for L-band applications," *IEEE Antenna and Propag. Letters*, vol. 8, pp. 1014-1016, 2009.

Fateme Azamian Jazi received the B.Sc. and the M.S. degrees in Communication Engineering in 2011 and 2013 respectively. Her research interests are in designing of UWB antennas and particle swarm optimization technique.

Mohammad Naghi Azarmanesh was born in Tabriz, Iran, in 1950. He received the B.S. degree in Physics from Tabriz University, Iran, in 1973, the M.S degree in Electrical Engineering from the University of Paris VI in 1976, and the Ph.D. degree in Electrical Engineering from Poly Technique De Toulouse, France. In 1979, he joined the Applied Physics Department in Urmia University, where he worked effectively in founding the Electrical Engineering Department in 1983. In 1998, he worked with three other colleagues in developing Microelectronics Research Center in Urmia University. He is currently the Head of Microelectronics Research Center. Azarmanesh is a Member of Iranian Society of Electrical Engineers and Member of IEEE, Institute of Electronics, Information and Communication Engineers (IEICE) of Japan.

Changiz Ghobadi was born on June 1, 1960 in Iran. He received the B.S. degree in Electrical and Electronic Engineering, the M.S. degree in Electrical and Telecommunication Engineering from Isfahan University of Technology, Isfahan, Iran, and the Ph.D. degree in Electrical-Telecommunication from University of Bath, Bath, UK in 1998. From 1998, he was an Assistant Professor and now is Professor in the Department of Electrical Engineering of Urmia University, Urmia, Iran. His primary research interests are in antenna, microwave, radar and adaptive filters.

Analysis of Square Coaxial Line Family

Alenka M. Milovanovic [1], Branko M. Koprivica [1],Aleksandar S. Peulic [1], and Ivan L. Milankovic [2]

[1] Faculty of Technical Sciences Cacak
University of Kragujevac, Cacak, 32000, Serbia
alenka.milovanovic@ftn.kg.ac.rs, branko.koprivica@ftn.kg.ac.rs, aleksandar.peulic@ftn.kg.ac.rs

[2] Bioengineering Research and Development Center
Prvoslava Stojanovica 6, 34000 Kragujevac, Serbia
ivan.milankovic@kg.ac.rs

Abstract ─ In this paper, the Equivalent Electrodes Method (EEM) has been proposed for the analysis of square coaxial lines family. Lines with single and two layer perfect or imperfect medium have been analyzed. The capacitance per unit length of these lines has been calculated. The results obtained by EEM have been compared with those reported in the literature, obtained by other methods, and those obtained by using software package COMSOL Multiphysics. Also, with the aim of comparison of the results, capacitance measurements based on a high resolution CDC (Capacitance to Digital Converter) have been realized. All results obtained have been found to be in very good agreement.

Index Terms ─ Capacitance per unit length, equivalent electrodes method, measurements, square coaxial line.

I. INTRODUCTION

The application of square coaxial lines is very important in transmitting RF energy, in antenna and microwave circuit design (particularly in satellite beam-forming networks in the lower microwave bands), and in equalizers, filters, branch line couplers and coaxial-to-stripline transformers. For calculating of the capacitance per unit length in the TEM mode of wave propagation in coaxial lines, quasistatic analysis can be used. The analysis of circular coaxial lines is simple and leads to exact analytical solutions. However, such a solution for square coaxial lines cannot be found. For determining of the capacitance per unit length of these lines, many numerical and analytical methods have been used. The main method in this analysis is the conformal mapping method [1], but it only gives close analytical solutions in a narrow range of geometries of square coaxial lines. Other methods which are commonly used are the numerical inversion of the Schwarz-Christoffel transformation [2], quasianalytical method of multipole theory [3], finite element method [4,5], finite-difference method [6], and other methods.

The aim of this paper is to apply the Equivalent Electrodes Method (EEM) in the analysis of square coaxial lines family. Coaxial lines, concentric and eccentric, with single layer perfect dielectric medium have been most common analyzed in the existing literature. Concerning this, the EEM has been firstly applied to the analysis of these lines. The results obtained have been compared with those found in the literature and those obtained by using the COMSOL software package (Finite Element Method). Very good agreement of the results confirms the applicability and accuracy of the EEM in solving these problems. Further, the proposed procedure and the results obtained by using EEM have been used for solving more complex problems, such as problems with two-layer perfect or imperfect medium. Additionally, an appropriate measurement system is designed and some of the obtained results are compared with measurement results.

Submitted On: April 28, 2014
Accepted On: September 8, 2014

II. THE EQUIVALENT ELECTRODES METHOD APPLICATION

EEM is a very simple method for solving non-dynamic electromagnetic fields and other potential fields of theoretical physics. The mathematical form of this method is similar to the Method of Moments (MoM) [7] and Boundary Element Method (BEM) [8,9] form, but essentially EEM has different physical basics from these methods. Furthermore, the EEM does not require any integration during the calculation procedure and the process of matrix filling differs from MoM and BEM. EEM has been successfully used in the static and quasistatic analysis of electromagnetic fields and for transmission line analysis [10-16]. Through this, EEM has been compared with other analytical and numerical methods, and very good agreement of the results obtained has been found.

In this paper, the application of the EEM will be explained on general example; i.e., on a double eccentric square coaxial line, Fig. 1 (a).

This line contains two square electrodes on the electric potentials φ_1 and φ_2. The inner electrode is shifted of the longitudinal axis of symmetry in both horizontal and vertical directions.

By applying EEM, both electrodes have been replaced with two finite systems of Equivalent Electrodes (EE), placed on the surface of the electrodes, q_i', i=1,2,…,N_1 for one side of the inner electrode, and Q_j', j=1,2,…,M_1 for one side of the outer electrode.

The total number of EE is $N_u + M_u$, where $N_u = 4N_1$ is the EE number on the inner electrode and $M_u = 4M_1$ is the EE number on the outer electrode. These equivalent electrodes have the same radius, potential and charge as the part of the real electrode they represent (in this case, thin flat strip conductor).

In our example, each thin flat strip conductor with a width Δx has been replaced with a cylindrical EE with a circular cross-section as presented in Fig. 1 (b). The equivalent radius of these EE can be calculated using conformal mapping, Joukowsky transform [10], as $a_{en} = \Delta x_1/4$ and $b_{en} = \Delta x_2/4$, where $\Delta x_1 = a/N_1$ and $\Delta x_2 = b/M_1$ for the inner and outer electrode, respectively [12].

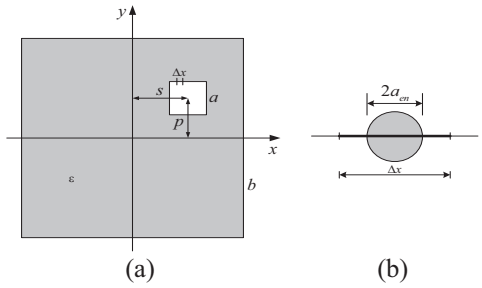

Fig. 1. (a) Double eccentric square coaxial line, and (b) thin flat strip conductor replaced with cylindrical EE.

These two systems of EE create the electric potential [12,13]:

$$\varphi = \varphi_0 + \sum_{i=1}^{N_u} q_i' G(\boldsymbol{r}, \boldsymbol{r}_n) + \sum_{j=1}^{M_u} Q_j' G(\boldsymbol{r}, \boldsymbol{r}_m), \qquad (1)$$

where

$$G(\boldsymbol{r}, \boldsymbol{r}') = -\frac{1}{2\pi\varepsilon} \ln|\boldsymbol{r} - \boldsymbol{r}'|, \qquad (2)$$

is the Green's function for the potential of uniform single line charge, $\boldsymbol{r}$ is the field point position vector, $\boldsymbol{r}'$ is the position vector of the electrical middle of the EE, ε is the electrical permittivity of dielectric medium and φ_0 is the unknown potential constant. So, the total number of unknowns which should be determined is $N_u + M_u + 1$. They can be obtained as the solution of the system of $N_u + M_u + 1$ linear equations.

By satisfying the boundary condition for the electric potential on the surface of the inner and the outer electrode, $N_u + M_u$ equations can be obtained:

$\varphi_1 = \varphi\big|_{\substack{x=x_n \\ y=y_n}}$, n=1,2,…,N_u;

$$\varphi_1 = \varphi_0 - \sum_{i=1}^{N_u} \frac{q_i'}{4\pi\varepsilon} \ln\left[|r_n^2| + a_{en}^2 \delta_{in}\right] - \\ - \sum_{j=1}^{M_u} \frac{Q_j'}{4\pi\varepsilon} \ln\left[|r_m^2|\right], \qquad (3)$$

and

$\varphi_2 = \varphi\big|_{\substack{x=x_m \\ y=y_m}}$, m=1,2,…,M_u;

$$\varphi_2 = \varphi_0 - \sum_{i=1}^{N_u} \frac{q_i'}{4\pi\varepsilon} \ln\left[|r_n^2|\right] - \\ - \sum_{j=1}^{M_u} \frac{Q_j'}{4\pi\varepsilon} \ln\left[|r_m^2| + b_{en}^2 \delta_{jm}\right], \qquad (4)$$

where

$$r_n^2 = (x - x_n)^2 + (y - y_n)^2,$$
$$r_m^2 = (x - x_m)^2 + (y - y_m)^2.$$

x_n and y_n are positions of the EE on the inner electrode, x_m and y_m are positions of the EE on the outer electrode and δ is the Kronecker symbol (equal to 1 when $i = n$ and $j = m$, otherwise is equal to 0).

Additional equation which completes the system of equations is:

$$\sum_{i=1}^{N_u} q_i' + \sum_{j=1}^{M_u} Q_j' = 0 . \quad (5)$$

After calculation of the unknown charges, the capacitance per unit length can be easily calculated as:

$$C' = \frac{1}{\varphi_1 - \varphi_2} \sum_{i=1}^{N_u} q_i' . \quad (6)$$

III. MEASUREMENT SETUP

In order to measure the unknown capacitance an appropriate system is designed, which is based on a high resolution CDC (Capacitance-to-Digital Converter) AD7746 [17]. This converter can measure up to ± 4.096 pF changing capacitance, while it can accept up to 17pF common-mode, not changing capacitance, which can be balanced by a programmable on-chip, digital-to-capacitance converter. This digital-to-capacitance converted value can be thought of as a programmable negative capacitance value which can be added to the input pin to minimize base capacitance. The AD7746 has high resolution down to 4aF, which is 21 effective numbers of bits, high linearity ±0.01%, and high accuracy ±4fF. It can communicate with a microcontroller using TWI (Two Wire Interface), I^2C (Inter-Integrated Circuit) compatible serial interface.

Besides the CDC, the system also contains a microcontroller and PC application. The main task of the microcontroller is to set the configuration of AD7746, while PC application presents the results of capacitance-to-digital conversion. The block diagram of the whole system for the capacitance measurement is presented in Fig. 2. The main part of the system from the control point of view is the microcontroller. It communicates with both the AD7746 and the PC. It sets the control registers of the AD7746 in order to enable capacitance-to-digital conversion and tells the AD7746 when to do it, after which it reads the conversion's results, processes them and sends to the PC. On the PC side, there is an application installed which communicates with microcontroller through USART (Universal Synchronous/Asynchronous Receiver/Transmitter) interface. The application receives data, processes them and presents to the end user of the system. The hardware part of the system that includes microcontroller and AD7746 and which is designed for the purpose of this experiment, is shown on the Fig. 3.

Fig. 2. Block diagram of the measurement system.

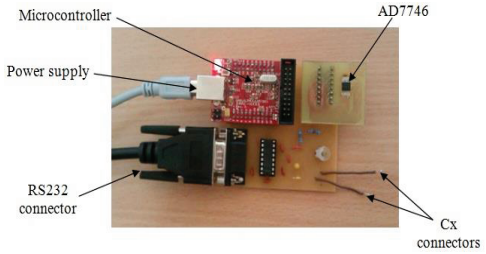

Fig. 3. Hardware part of the measurement system.

The PC application communicates with microcontroller in order to get the value of measured capacitance and to present it to the end user. It is a real time application that also graphically presents changes in measured capacitance, and which is specifically designed for the purpose of this experiment.

Two simple models of the square coaxial line have been made. Both electrodes of the first model are made of aluminum foil and dielectric between them is air. The second model represents the square coaxial line with two layer dielectric. One electrode is made of aluminum foil. For the preparation of second electrode, Printed Circuit Board (PCB) with copper on one side of the board has been used. Four identical pieces have been made using this PCB. Copper edges of these pieces have been soldered together in order to create a square electrode with a 2 mm pertinax layer around it. By placing the first electrode around the second electrode condenser with two layer dielectric medium has been created. First layer is pertinax on the inner electrode and the

second layer is the air between electrodes.

The capacitance per unit length of the condenser model can be calculated as:

$$C' = C_x / h, \quad (7)$$

where C_x is measured capacitance and h is height of the condenser model.

IV. NUMERICAL AND MEASUREMENTS RESUTS

In this section, EEM has been applied for analysis of square coaxial lines with single layer perfect medium. Then, the results obtained have been used for analysis of square coaxial lines with two layer perfect and imperfect medium. Also, some of the results which are related to the single and two layer perfect medium have been compared with results obtained by measurements.

A. Concentric square coaxial line

Firstly, the EEM has been applied to the calculation of the capacitance per unit length of the concentric square coaxial line from Fig. 1, when $p = s = 0$. The accuracy of the results obtained using EEM depends on the total number of EE. The obtained result will converge, and accuracy should be higher by increasing this number. In other words, the width of the electrode parts Δx_1 and Δx_2, which one EE represents, decreases with an increase in the total number of EE. The convergence of the capacitance per unit length, when $w = a/b = 0.5$ has been presented in Table 1.

Table 1: Convergence of the C'/ε when w=0.5

Total Number of EE	C'/ε	Total Number of EE	C'/ε
72	10.5482	4800	10.2420
120	10.4507	5400	10.2411
240	10.3585	6000	10.2404
360	10.3220	7200	10.2394
480	10.3023	8400	10.2387
600	10.2899	9600	10.2381
840	10.2751	10800	10.2377
1200	10.2635	12000	10.2373
1800	10.2542	13200	10.2370
2400	10.2494	14400	10.2368
3000	10.2465	15600	10.2366
3600	10.2445	16800	10.2364
4200	10.2430	18000	10.2363

Mathematica Wolfram software has been used to write a program code that calculates the capacitance per unit length by applying EEM. This program has been executed on a PC with Intel(R) Core(TM) i5-3210M CPU at 2.50 GHz and with 6 GB RAM memory in order to test its run time. Obtained results show that run time vary with the total number of EE, Table 2, between several second and more than 10 minutes (obtained with maximal number of EE). It can be noticed from the results presented in Table 2 that the relative difference between results obtained with 3600 or 6000 EE and the result obtained with 18000 EE is less than 0.1%. Therefore, optimal number of EE can be taken so that the run time does not last more than several minutes.

Table 2: CPU run time variation with EE number

Total Number of EE	C'/ε EEM	t [s] EEM
1200	10.2635	3
3600	10.2445	27
6000	10.2404	75
12000	10.2373	305
18000	10.2363	704
Number of Mesh Elements	C'/ε COMSOL	t [s] COMSOL
7712	10.2388	1
30848	10.2360	6
123392	10.2348	51
278316	10.2344	308

According to the results presented in Table 1 and Table 2, the total number of EE in other calculations has been set between 9600 and 15200 depending on the geometry of the line, setting the width of the electrode part Δx to be constant. In this case, since $\Delta x = \Delta x_1 = \Delta x_2$ and $w = 0.5$ then $N_u / M_u = 0.5$. Due to the symmetry in all four quadrants of the coordinate system, the total number of equations is four times smaller than the total number of EE.

Lo and Lee [18] gave the capacitance per unit length of this line with approximate expression (8):

$$\frac{C'}{\varepsilon_0} = \frac{8(0.279 + 0.721w)}{1 - w}; \quad 0.25 \le w \le 0.5. \quad (8)$$

The results for the capacitance per unit length of the square coaxial line obtained using EEM

have been presented in Table 3. In addition, a comparison of the results obtained using COMSOL, expression (8) and other methods given in the literature have been presented in this table. Good agreement between the results is evident.

According to the results for the capacitance per unit length, in the case of imperfect medium, the conductance per unit length can be determined as:

$$G' = C'\sigma/\varepsilon, \tag{9}$$

where σ is the conductivity of the imperfect medium.

Table 3: C'/ε for different w

w		0.1	0.2	0.3	0.4	0.5	0.6	0.7	0.8	0.9
EEM		2.841	4.135	5.634	7.564	10.237	14.240	20.912	34.260	74.342
COMSOL		2.844	4.141	5.642	7.573	10.249	14.255	20.932	34.283	74.340
[3]	Cockcroft	3.126	4.238	5.668	7.575	10.244	14.246	20.921	34.272	74.357
	Bowan	2.842	4.138	5.638	7.567	10.241	14.246	20.921	34.272	-
	Green	2.853	4.144	5.634	7.565	10.306	14.635	22.697	43.432	224.40
	Ivanov	2.848	4.151	5.638	7.611	10.197	14.280	-	-	-
	Costamagna	2.842	4.138	5.638	7.567	10.241	14.253	20.921	34.272	74.357
	Riblet	2.849	4.138	5.638	7.569	10.244	14.246	20.921	34.272	74.357
	Zheng	2.843	4.140	5.637	7.569	10.247	14.302	20.909	34.272	74.357
[1]		2.847	4.135	5.633	7.561	10.234	14.235	20.902	34.235	74.235
Exp. (8)		3.121	4.232	5.660	7.565	10.232	14.232	20.899	34.232	74.232

B. Single eccentric square coaxial line

The results for the capacitance per unit length of a single eccentric square coaxial line ($p \neq 0$ or $s \neq 0$, Fig. 1), when $w = 0.2$ and for different ratios s/b, have been presented in Table 4. The results have been obtained using EEM, COMSOL and measurement and they are in good agreement.

Table 4: C'/ε when $w = 0.2$ and $\varepsilon_2/\varepsilon_1 = 5.5$

	C'/ε		
s/b	EEM	COMSOL	Measured
0	4.13831	4.1407	4.14236
0.05	4.16326	4.1656	4.17268
0.10	4.24311	4.2454	4.23985
0.15	4.39528	4.3973	4.41768
0.20	4.65936	4.6610	4.66325
0.25	5.12778	5.1285	5.10983
0.30	6.06468	6.0624	6.10354
0.35	8.69264	8.6735	8.73456

The results for the capacitance per unit length for a single eccentric square coaxial line for different w and $s/b = 0.1; 0.2; 0.3$, obtained using EEM, have been presented in Table 5.

This type of line is analyzed by YuBo, et al. [2] for the $w = 0.4$ and a 40% eccentricity in the vertical direction, $0.4(b-a)/2$, and the capacitance per unit length has been calculated to be $8.19773\varepsilon_0$. By using EEM for this line, the capacitance per unit length has been calculated as $8.20778\varepsilon_0$.

Table 5: C'/ε of single eccentric coaxial line

	C'/ε		
w	$s/b = 0.1$	$s/b = 0.2$	$s/b = 0.3$
0.1	2.88931	3.06549	3.54787
0.15	3.55174	3.8285	4.65727
0.2	4.24247	4.65852	6.06283
0.25	4.99693	5.61388	8.08914
0.3	5.84673	6.76584	11.6288
0.35	6.82799	8.22542	20.9898
0.4	7.9876	10.1974	-
0.45	9.3919	13.1346	-
0.5	11.142	18.3439	-
0.55	13.4054	32.1948	-
0.6	16.4909	-	-
0.65	21.0625	-	-
0.7	28.9636	-	-
0.75	48.8447	-	-

C. Double eccentric square coaxial line

The numerical and measurement results for he capacitance per unit length of a double eccentric square coaxial line (and, Fig. 1), when $w = 0.2$ and for different ratios $k = s/b$ and p/b have been presented in Table 6.

This type of line is analyzed by YuBo, et al. [2] for the ratio $w=0.4$ and a 40% eccentricity in the diagonal direction and the capacitance per unit length has been calculated to be $8.81411\varepsilon_0$. By using EEM for this line, the capacitance per unit length has been calculated as $8.82621\varepsilon_0$.

Table 6: C'/ε when w=0.2

C'/ε–Numerical Results (EEM)							
p/b	*k* = 0.05	*k* = 0.1	*k* = 0.15	*k* = 0.2	*k* = 0.25	*k* = 0.3	*k* = 0.35
0.05	4.18801	4.26727	4.41841	4.68099	5.14744	6.08188	8.70691
0.1	4.26727	4.34469	4.49267	4.75067	5.21096	6.13762	8.75333
0.15	4.41841	4.49267	4.63519	4.88509	5.33431	6.24665	8.84473
0.2	4.68099	4.75067	4.88509	5.12273	5.55468	6.44376	9.01183
0.25	5.14744	5.21096	5.33431	5.55468	5.96116	6.81383	9.33134
0.3	6.08188	6.13762	6.24665	6.44376	6.81383	7.60981	10.0385
0.35	8.70691	8.75333	8.84473	9.01183	9.33134	10.0385	12.2968
C'/ε–Measurement Results							
p/b	*k* = 0.05	*k* = 0.1	*k* = 0.15	*k* = 0.2	*k* = 0.25	*k* = 0.3	*k* = 0.35
0.05	4.17962	4.34569	4.32568	4.70125	5.09561	6.15983	8.65214
0.1	4.34569	4.25697	4.62347	4.76589	5.24589	6.29871	8.86998
0.15	4.32568	4.62347	4.74257	4.93654	5.21458	6.36955	8.65542
0.2	4.70125	4.76589	4.93654	5.35847	5.45214	6.33224	9.11245
0.25	5.09561	5.24589	5.21458	5.45214	6.25477	7.85264	9.34569
0.3	6.15983	6.29871	6.36955	6.33224	7.85264	7.96547	9.89654
0.35	8.65214	8.86998	8.65542	9.11245	9.34569	9.89654	12.45697

The variation in the capacitance per unit length has been presented in Fig. 4.

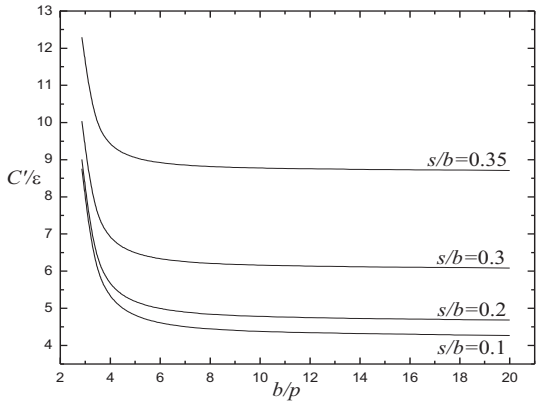

Fig. 4. Variation of C'/ε for a double eccentric square coaxial line.

D. Square coaxial lines with two layer medium

As stated in the introductory section of this paper, the results for the capacitance per unit length presented in previous sub-headings can be used for the determination of characteristic parameters of square coaxial lines with perfect or imperfect two-layer medium, Fig. 5.

For the line from Fig. 5 with two-layer perfect dielectric medium, when $\sigma_1=\sigma_2=0$, the capacitance per unit length can be determined as it is presented in [7] by using expression (10):

$$\frac{1}{C'}=\frac{2}{(\varepsilon_1+\varepsilon_2)g'_{13}}+\frac{\varepsilon_1-\varepsilon_2}{\varepsilon_1+\varepsilon_2}\left(\frac{1}{\varepsilon_2 g'_{23}}-\frac{1}{\varepsilon_1 g'_{12}}\right), \quad (10)$$

where g'_{13} is a coefficient of the proportionality of the line when $\varepsilon_1=\varepsilon_2$ and g'_{12} and g'_{23} are coefficients of the proportionality of the lines which are formed by the existing electrode and the electrode's shield coinciding with separation surface, Fig. 6 [11].

For the line in Fig. 5 with a two-layer imperfect dielectric medium, when $\sigma_1,\sigma_2\neq 0$, the admittance per unit length can be determined as presented in [7] by using the expression (11):

$$\frac{1}{\underline{Y'}}=\frac{2}{(\underline{\sigma}_1+\underline{\sigma}_2)g'_{13}}+\frac{\underline{\sigma}_1-\underline{\sigma}_2}{\underline{\sigma}_1+\underline{\sigma}_2}\left(\frac{1}{\underline{\sigma}_2 g'_{23}}-\frac{1}{\underline{\sigma}_1 g'_{12}}\right), \quad (11)$$

where $\sigma_1=\sigma_1+\mathrm{j}\omega\varepsilon_1$ and $\sigma_2=\sigma_2+\mathrm{j}\omega\varepsilon_2$. The complex effective conductivity can be calculated as:

$$\underline{\sigma}_{\mathrm{e}} = \frac{Y'}{g'_{13}} = \frac{G'_{\mathrm{e}} + \mathrm{j}\omega C'_{\mathrm{e}}}{g'_{13}} = \sigma_{\mathrm{e}} + \mathrm{j}\omega\varepsilon_{\mathrm{e}}, \qquad (12)$$

where σ_{e} and ε_{e} are the effective permittivity and effective conductivity, respectively.

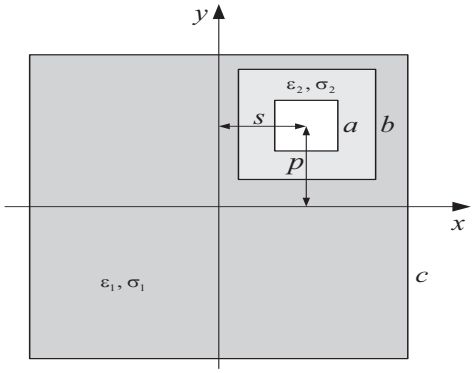

Fig. 5. Square coaxial line with two-layer medium.

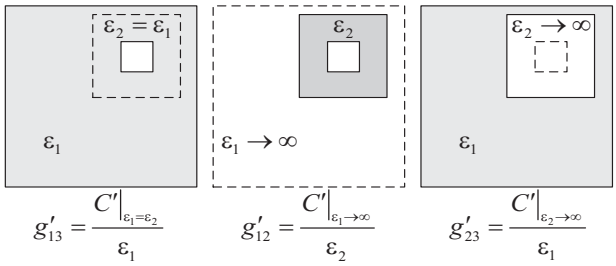

Fig. 6. Calculation of the coefficients of the proportionality.

Previously presented results for C'/ε (sub-sections A, B and C) have been used as values of coefficients of the proportionality g'_{12}, g'_{23} and g'_{13} in expressions (10), (11) and (12).

The variations in the results for the effective permittivity and effective conductivity for the line from Fig. 5 with imperfect two-layer medium obtained using EEM have been presented in Figs. 7 and 8.

The comparison of the measurement and numerical results for square coaxial line with two-layer perfect medium has been presented in Table 7.

The comparison of results for the capacitance per unit length and the complex effective conductivity for the line in Fig. 5 obtained using EEM and COMSOL, has been presented in Tables 8 and 9.

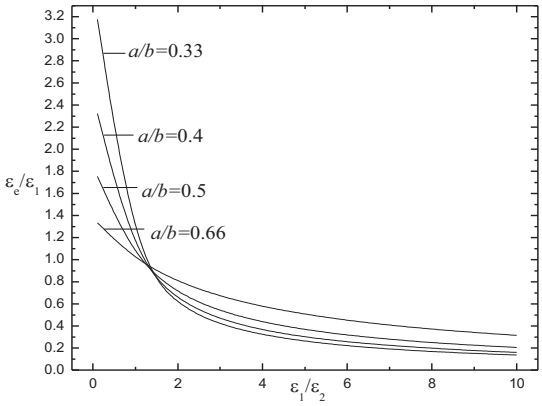

Fig. 7. Variation of $\varepsilon_{\mathrm{e}}/\varepsilon_1$ for different ratios a/b and $\varepsilon_1/\varepsilon_2$ when $s/c = p/c = 0.1$, $a/c = 0.2$, and $\sigma_1/\sigma_2 = 5$.

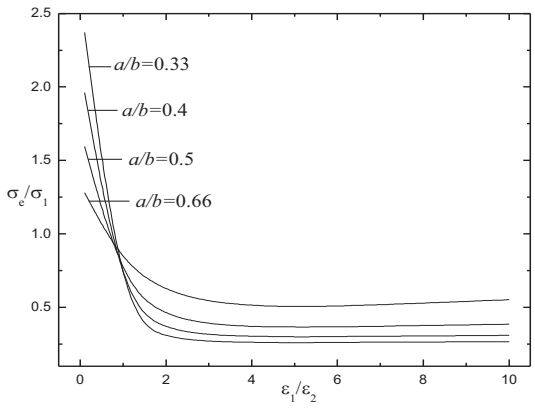

Fig. 8. Variation of $\sigma_{\mathrm{e}}/\sigma_1$ for different ratios a/b and $\varepsilon_1/\varepsilon_2$ when $s/c = p/c = 0.1$, $a/c = 0.2$, and $\sigma_1/\sigma_2 = 5$.

Table 7: C'/ε_1 when $w = 0.2$

p/c	C'/ε_1 Measured	C'/ε_1 EEM
0	6.66365	6.51268
0.05	6.73895	6.58094
0.1	6.88954	6.80707
0.15	7.49191	7.27374
0.2	8.39545	8.22093
0.25	9.67548	10.5723

Table 8: C'/ε when $a/b=0.5$, $a/c=0.2$, $\varepsilon_1/\varepsilon_2=5$ and $l=s/c$

EEM and Expression (10)						
p/*c*	*l*=0	*l*=0.05	*l*=0.1	*l*=0.15	*l*=0.2	*l*=0.25
0	1.56468	1.56791	1.57789	1.59547	1.62169	1.65379
0.05	1.56791	1.5703	1.58015	1.59751	1.62461	1.65653
0.1	1.57789	1.58015	1.58983	1.60692	1.63374	1.66520
0.15	1.59547	1.59751	1.60692	1.62365	1.65019	1.68126
0.2	1.62169	1.62461	1.63374	1.65019	1.67554	1.70726
0.25	1.65379	1.65653	1.66520	1.68126	1.70726	1.74493
COMSOL						
p/*c*	*l*=0	*l*=0.05	*l*=0.1	*l*=0.15	*l*=0.2	*l*=0.25
0	1.568526	1.571311	1.581271	1.597932	1.624109	1.660482
0.05	1.571311	1.574405	1.583967	1.600861	1.62654	1.663086
0.1	1.581271	1.583967	1.593682	1.610272	1.635559	1.671230
0.15	1.597932	1.600861	1.610272	1.626023	1.650649	1.68589
0.2	1.624109	1.62654	1.635559	1.650649	1.674832	1.708755
0.25	1.660482	1.663086	1.671230	1.685890	1.708755	1.742107

Table 9: σ_e/σ_1 when $a/b=0.5$, $a/c=0.2$, $\varepsilon_1/\varepsilon_2=5$, $\sigma_1/\sigma_2=5$, $\omega/2\pi=50$ Hz and $l=s/c$

EEM and Expression (12)						
p/*c*	*l*=0	*l*=0.05	*l*=0.1	*l*=0.15	*l*=0.2	*l*=0.25
0	0.378+j1049.75	0.376+j1045.60	0.372+j1032.41	0.363+j1007.7	0.349+j966.08	0.323+j895.88
0.05	0.376+j1045.60	0.375+j1041.53	0.370+j1028.60	0.361+j1004.33	0.347+j963.34	0.322+j893.93
0.1	0.372+j1032.41	0.370+j1028.60	0.366+j1016.46	0.358+j993.55	0.344+j954.53	0.319+j887.66
0.15	0.363+j1007.70	0.361+j1004.33	0.358+j993.55	0.350+j973.02	0.337+j937.58	0.315+j875.49
0.2	0.344+j966.08	0.347+j963.34	0.344+j954.53	0.337+j937.58	0.327+j907.75	0.307+j853.76
0.25	0.323+j895.88	0.322+j893.94	0.319+j887.66	0.315+j875.49	0.307+j853.76	0.293+j813.10
COMSOL						
p/*c*	*l*=0	*l*=0.05	*l*=0.1	*l*=0.15	*l*=0.2	*l*=0.25
0	0.380+j1055.99	0.378+j1051.55	0.373+j1038.31	0.364+j1012.99	0.349+j972.00	0.324+j902.49
0.05	0.378+j1051.55	0.376+j1047.40	0.372+j1034.21	0.363+j1009.54	0.348+j968.27	0.324+j900.45
0.1	0.373+j1038.31	0.372+j1034.21	0.367+j1021.50	0.359+j998.19	0.345+j958.89	0.321+j893.83
0.15	0.364+j1012.99	0.363+j1009.54	0.359+j998.19	0.351+j977.50	0.338+j941.61	0.317+j880.83
0.2	0.349+j972.00	0.348+j968.27	0.345+j958.89	0.338+j941.61	0.327+j910.68	0.308+j857.39
0.25	0.324+j902.49	0.324+j900.45	0.321+j893.83	0.317+j880.84	0.308+j857.390	0.293+j814.40

V. CONCLUSION

In this paper, EEM has been used for the analysis of the square coaxial lines, concentric and eccentric, with single and two-layer perfect and imperfect medium.

Application of the method is very simple, using just simple mathematical operations without numerical integrations. Short calculation time is an additional quality of the proposed method. Fast convergence of the results is evident.

All results obtained using EEM have been compared with those obtained using COMSOL and some results with those found in the literature. They have been found to be in very good agreement. By increasing the number of EE, EEM gives more accurate results compared to other methods.

Additionally, in order to confirm the numerical results, appropriate system based on the high resolution capacitance-to-digital converter is designed. Some of the results obtained have been compared to the measurement results and good agreement has been found. In the case of two-layer medium, small differences between results exist because of the simplicity of the physical model used in measurements.

The eccentricity of the lines has been analyzed in details. So, the paper contains many new results in this area which cannot be found in the existing literature.

According to this, one can conclude that EEM can be successfully used for the analysis of all types of lines with square cross section.

REFERENCES

[1] J. H. Riblet, "Expansions for the capacitance of a square in a square with a aomparison," *IEEE Transactions on Microwave Theory and Techniques*, vol. 44, no. 2, pp. 338-340, 1996.

[2] T. YuBo, Z. Bing, and W. Xin, "Numerical method for solving characteristic parameters of square coaxial line," *IEEE Antennas and Propagation Society International Symposium*, Honolulu, HI, SAD, pp. 73-76, June 9-15, 2007.

[3] Q. Zheng, W. Lin, F. Xie, and M. Li, "Multipole theory analysis of a rectangular transmission line family," *Microwave and Optical Technology Letters*, vol. 18, no. 6, pp. 382-384, 1998.

[4] S. M. Musa and M. N. O. Sadiku, "Analysis of rectangular coaxial lines," *IEEE Region 5 Technical Conference*, Fayetteville, AR, SAD, pp. 322-325, April 20-22, 2007.

[5] Ž. J. Mančić and V. V. Petrovic, "Analysis of square coaxial line with anisotropic dielectric by finite element method, *Telfor Journal*, vol. 3, no. 2, pp. 125-127, 2011.

[6] M. V. Schneider, "Computation of impedance and attenuation of TEM-line by finite difference methods," *IEEE Transactions on Microwave Theory and Techniques*, vol. 13, no. 6, pp. 793-800, 1965.

[7] R. F. Harrington, "Field computation by moment methods," *The Macmillan Company*, New York, 1969.

[8] Y. J. Liu and N. Nishimura, "The fast multipole boundary element method for potential problems: a tutorial," *Engineering Analysis with Boundary Elements*, vol. 30, no. 5, pp. 371-381, 2006.

[9] J. Singh, A. Gliere, and J. L. Achard, "A multipole expansion-based boundary element method for axisymmetric potential problem," *Engineering Analysis with Boundary Elements*, vol. 33, no. 5, 654-660, 2009.

[10] N. B. Raicevic and S. R. Aleksic, "One method for electric field determination in the vicinity of infinitely thin electrode shells," *Engineering Analysis with Boundary Elements*, vol. 34, no. 2, 97-104, 2010.

[11] A. M. Milovanovic and M. M. Bjekic, "Approximate calculation of capacitance of lines with multilayer medium," *Journal of Electrical Engineering*, vol. 62, no. 5, pp. 249-257, 2011.

[12] D. M. Velickovic, "Equivalent electrodes method," *Scientific Review*, vol. 21-22, pp. 207-248, 1996.

[13] D. M. Velickovic, "Equivalent electrodes method application in nonrotational fields theory," *Fourth International Symposium of Applied Electrostatics ПЕС 96*, Nis, Serbia, pp. 5-30, May 1996.

[14] D. M. Velickovic and A. Milovanovic, "Approximate calculation of capacitance," *Proceedings of VIII International IGTE Symposium on Numerical Field Calculation in Electrical Engineering*, Graz, Austria, pp. 339-344, September 1998.

[15] D. M. Velickovic and A. Milovanovic, "Electrostatic field of cube electrodes," *Serbian Journal of Electrical Engineering*, vol. 1, no. 2, pp. 187-198, 2004.

[16] A. Milovanovic and B. Koprivica, "Analysis of square coaxial lines by using equivalent electrodes method," *Sixteenth International Symposium on Theoretical Electrical Engineering ISTET'11*, Klagenfurt, Austria, pp. 191-197, July 2011.

[17] *Analog Devices, Inc.*, "24-bit capacitance-to-digital converter with temperature sensor, AD 7745/ AD7746," http://www.analog.com/static/imported-files/data_sheets/AD7745_7746.pdf.

[18] Y. T. Lo and S. W. Lee, "Antenna handbook," *Van Nostrand Reinhold*, New York, 1988.

Alenka M. Milovanovic was born in Cacak, Serbia in 1965. She received her M.Sc. and Ph.D. degrees in Electrical Engineering from the Faculty of Electronic Engineering of Nis in 1999 and from the Faculty of Technical Sciences in 2007, respectively. Since 1991, she has been with the Department of Electronic and Electrical Engineering of the Faculty of Technical Sciences, where she now works as Associate Professor. Her research interest includes Computational Electromagnetics and Applied Electrostatics.

Branko M. Koprivica was born in Virovitica, Croatia in 1980. He received Dipl. Ing. and M.Sc. degrees from the Technical Faculty Cacak (now Faculty of Technical Sciences) in 2006 and 2009, respectively. Since 2006, he has been engaged as Associate in the Department of Electronic and Electrical Engineering of

the Faculty of Technical Sciences. His research interest includes Computational Electromagnetics.

Aleksandar S. Peulic received his Diploma degree in Electronic Engineering and his Master of Science degree in Electrical Engineering, both from the Faculty of Electronic Engineering, University of Nis, Nis, Serbia, in 1994 and 2004, respectively. He is an Associate Professor at the Faculty of Technical Science Cacak, University of Kragujevac, Cacak, Serbia. He was a Postdoctoral Research Fellow at the University of Alabama, Huntsville, in 2008. His research interests include microcontrollers systems and wearable sensors.

Ivan l. Milankovic was born in Gornji Milanovac, Serbia in 1988. He received his Dipl. Ing. and M.Sc. degrees from the Technical Faculty Cacak (now Faculty of Technical Sciences) in 2011 and 2012, respectively. Since 2012, he has been engaged as Research Associate at the Bioengineering Research and Development Center. His research interest includes Computer Science.

Design and Analysis of an Interior Continuous Magnetic Gear Box Using Finite Element Method

Behrooz Majidi * **and Jafar Milimonfared**

Department of Electrical Engineering
Amirkabir University of Technology, Tehran 15916, Iran
* bmx@aut.ac.ir

Abstract ─ Magnetic gears offer important potential benefits compared with mechanical gears such as reduced maintenance, improved reliability, inherent overload protection, and physical isolation between the input and output shafts. This paper presents the design and analysis of a novel structure of magnet gear, which named Interior Magnetic Gear (IMG) using neodymium-iron-boron magnets for the applications in which continuous ratio of gear box is useful such as wind generators, electric vehicles and etc. The analysis is performed by Finite Element Method (FEM) to predict output torque, speed and magnetic field distribution inside the gear box. The IMG made up of an inner rotor and an outer rotor. The inner rotor is similar to the rotor of a 3 phase wound rotor induction motor and the outer rotor consists of 6 PM poles. Both the inner rotor and the outer rotor can be employed as a low/high speed rotating part. The interior arrangement of PMs result many advantage such as low torque ripple. The simulation and analytical results are in good accord.

Index Terms ─ Continuous, Finite Element Method (FEM), Interior Magnetic Gear (IMG), Permanent Magnet (PM).

I. INTRODUCTION

Mechanical gear boxes are used widely to transmit torque between separate moving parts with different speeds in various applications. For example, they are used in wind power generators to increase the rotational speed and in electric ship propulsion to decrease that. Because of the friction in mechanical gear boxes, power loss, gear noise and regular lubrication are inevitable. In the last decade magnetic gear coupling has been proposed. Magnetic gear boxes can transmit torque without any friction. They operate with the same principle as the mechanical systems where the teeth are replaced by magnet pieces. They can transform torque and speed level by interactive magnetic field between the permanent magnet pieces [1-5].

Magnetic gears offer substantial advantages compared to mechanical ones such as being maintenance free, improved reliability, minimum acoustic noise, and inherent over load protection. For example, the reduced maintenance is due to no mechanical contact and lubrication, the inherent overload protection is provided by the maximum synchronous torque, the isolation can be provided since the no mechanical contact between the inner and outer parts. At first, because of the complicated structure, low efficiency and low output torque, magnetic gear boxes in spite of some advantages have not gained much attention. In 2001, the Surface Permanent Magnet-type (SPM-type) magnetic gears has been introduced in a practical application on account of its novel design [6]. Since then, various types of magnetic gears have been proposed to develop torque density, lower torque ripple, higher ratios and efficiency [7-11]. Recent investigations focus are on implementing of continuous ratio gear boxes to be applicable for wind generators, electric vehicles and other analogous applications in which continuous ratio of gear box is essential [12-17]. Reference [18] proposes a new magnetic gear based on super conductors to achieve high torque density. In 2004-2005, in linear motors field, linear-type magnetic gears were designed [19-20]. Reference [21] proposed a new design of cycloid-type magnetic gears to achieve more torque density at high ratio. References [22-23] proposed a new type of

Submitted On: January 18, 2014
Accepted On: September 28, 2014

magnetic gear named axial-type magnetic gear. References [24-25] suggested a harmonic-type magnetic gear similar to a harmonic mechanical gear. As the coaxial magnetic gears are the most applicable type of magnetic gears, the new arrangement of PMs is applied in this type of magnetic gears. One of the most popular arrangements is Coaxial Magnetic Gear with Halbach Permanent-Magnet Arrays [26-28]. Recently, to achieve continuous ratio in gear boxes, a structure has been proposed which provides variable speed but has sophisticated structure [29].

In this paper, continuous ratio capability and simple design for manufacturing are the main goals which are analyzed by Finite Element Method (FEM) and validated by vector analytical calculation. To estimating performance of the magnetic gear, the air-gap magnetic field is computed by steady state analytical method and then compared with FEM results depicting air-gap magnetic field distribution. This adjustable continuous topology is quite suitable for many applications such as wind generators (which improves harmonic characteristics and eliminates back to back converters) and electric vehicles. This gear box can operate as a clutch and separate power from load. This advantage can make torque (speed) transmission systems very compact and simple. The operation principles of proposed magnetic gear box are presented first, and the design of this structure, which is consisted of the inner and the outer rotors is then introduced. In the next step, the proposed gear box is mathematically analyzed and its descriptive equations are derived. Finally, the validity of the obtained formulas is confirmed by simulation of proposed structure.

II. PRINCIPLE OF OPERATION

Figure 1 shows the structure of the proposed magnetic gear box. It consists of an inner rotor with three phase windings and an outer rotor which includes PMs. Each part is made up of a steel 1010, this steel has high saturation point (almost 1.8T) which is suitable for this application. In this system, the inner rotor windings produce a rotating magnetic field with desired speed and as a result of its interaction with the outer rotor permanent magnets, outer rotor rotates [30]. It is obvious that controlling the inner rotor current frequency controls the gear box ratio, which is the main idea of this paper.

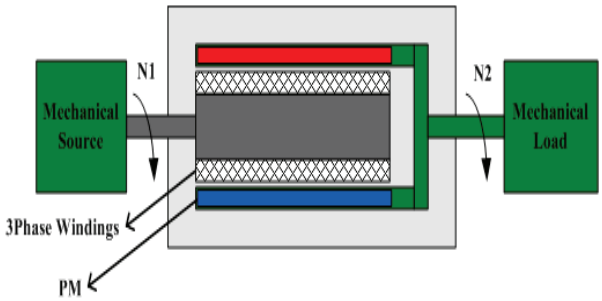

Fig. 1. Proposed topology.

It should be noted that the three-phase power is transmitted to the windings of the inner rotor through a slip ring. In other words N2=N1+Nf in which N1 is the mechanical speed of the inner rotor, Nf is the speed of the rotating magnetic field of the windings current frequency and N2 is the speed of the outer rotor.

The advantages of the purposed topology are:

1- It is possible to use this topology as a high ratio gear box which is important in gear box applications.
2- It is possible to use it as a speed regulator.
3- Possibility of controlling the output torque.
4- Inherent overload protection.
5- The proposed topology can operate as a clutch and separate the prime-mover from load.
6- Because of precision and high ratio of the proposed structure, it is possible to connect the generator output to the network (eliminating power electronic interfaces).
7- Silent working.
8- Interior arrangement reduce torque ripple.

III. DESIGN OF THE MAGNETIC GEAR PARTS

A. Windings and slots of the inner rotor

One of the important parts of the proposed structure is the inner rotor which its design has a great impact on the performance and behavior of the whole system. The cogging torque of the magnetic gear box arises from the interaction of permanent magnets and the inner rotor slotted structure without the applied driving current [31]. Since an oscillatory torque always induces vibration, acoustic noise, and possible resonance especially at high load and low speed, the slots of the inner rotor have been designed in order to minimize the cogging torque. Figure 2 shows the structure of the inner rotor.

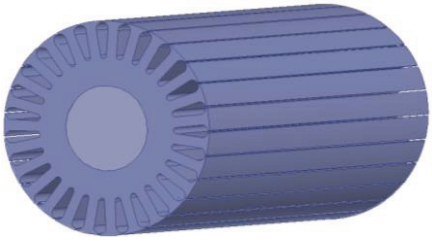

Fig. 2. 3D view of the inner rotor.

Windings type of the inner rotor is fractional slot and shorted pitch. This selection is based on evaluating of various windings performances in FEM simulation [32]. This type of the inner rotor windings improves the machine characteristics such as harmonic specifications. With proper selection of windings step, it is possible to minimize the attenuation coefficient for main frequency and maximize it for other harmonics. The inner rotor has 27 slots and its windings layout is according to Fig. 3.

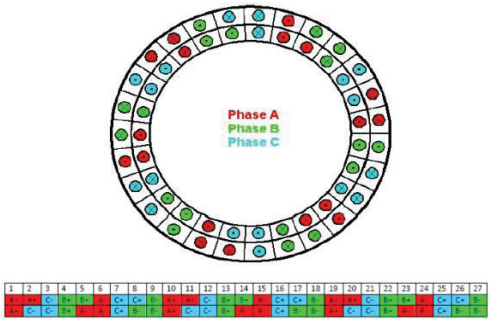

Fig. 3. Windings layout in the inner rotor.

Parameters of the inner rotor windings are presented in Table 1. In this table, q is the number of slots per pole per phase (spp), γ^{oe} is electrical pitch angle, K_d is distribution factor, K_p is shortage pitch coefficient of windings and α is the slot angle.

Table 1: Inner rotor windings parameters

Parameter	Value
q(spp)	1.5
Kd	0.985
K_p	0.998
γ^{oe}	30^{o}
α	13.33^{o}

The implemented and simulated models of the inner rotor are shown in Fig. 4.

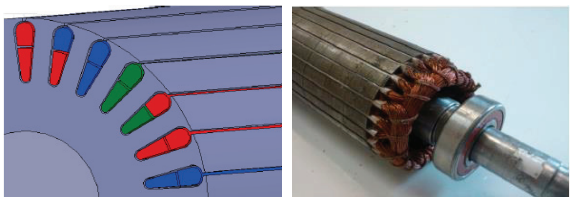

(a) (b)

Fig. 4. (a) Simulated model, and (b) implemented view of the inner rotor.

B. Outer rotor

According to the inner rotor structure, the outer rotor is designed and constructed whose model is shown in Fig. 5. More details of the outer rotor design are discussed in part 5. The permanent magnets are Neodymium rare earth type with grade of N35 (NdFe35).

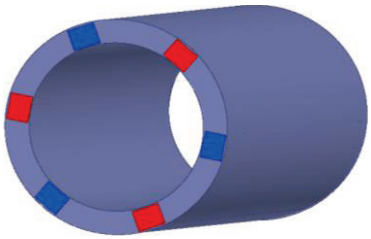

Fig. 5. Simulated model of the outer rotor.

IV. ANALYSIS OF THE INTERIOR MAGNETIC GEAR (IMG)

The aim of this section is calculation of the output torque of the IMG which is produced by interaction of two magnetic fields, one by windings current (in the inner rotor) and the other one by permanent magnets (in the outer rotor). F_{ri} is the peak value of the inner rotor windings Magneto Motive Force (MMF) and F_{ro} is the peak value of the outer rotor MMF. It is obvious that output torque is equivalent of the multiplex of these fields and sinus of the angle between them as shown in Fig. 6. For calculating output torque the following assumptions has been taken into account [33]:

- The inner and outer rotors are made of material with infinite permeability.
- Air gap length is much less than average radius; there is no difference in the inner rotor surface flux with the outer rotor surface flux.
- Only the main field component of the inner and outer rotors will be taken into account.
- Because of the mechanical consideration, the air gap length (g) can't be very small.

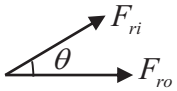

Fig. 6. Field vectors of the inner and outer rotors.

Magnitude of the resultant MMF in the air gap can be calculated as:

$$F_R = \sqrt{F_{ro}^2 + F_{ri}^2 + 2F_{ro}F_{ri}\cos\theta}. \quad (1)$$

In Eq. (1), "θ" is the angle between F_{ro} and F_{ri}.

The magnetic field intensity in the air gap H_g is:

$$H_g = \frac{F_R}{g}. \quad (2)$$

Then the average of co-energy density in the air gap is:

$$W' = \frac{1}{2}\frac{\mu_0}{g^2} \times \left(\frac{1}{2}F_R{}^2\right) = \frac{1}{4}\mu_0\left(\frac{F_R}{g}\right)^2. \quad (3)$$

Eq. (1) and Eq. (3) can be combined to calculate the total co-energy in the air gap:

$$W_t' = \frac{1}{2}\frac{\mu_0}{g^2}F_R^2\left(2\pi rlg\right) = \frac{1}{2}\frac{\mu_0\pi rl}{g}F_R^2. \quad (4)$$

Considering $\theta = \frac{P}{2}\theta_m$, the output torque can be written as:

$$\begin{aligned} T_e &= \frac{\partial W_t'}{\partial\theta_m}\left(F_{ro}, F_{ri}, \theta\right) = \frac{\partial W_t'}{\partial\theta}\left(F_{ro}, F_{ri}, \theta\right)\frac{\partial\theta}{\partial\theta_m} \\ &= \frac{P}{2}\frac{\mu_0\pi rl}{g}\frac{\partial}{\partial\theta}\left(F_{ro}^2 + F_{ri}^2 + 2F_{ro}F_{ri}\cos\theta\right) \\ &= -\frac{P}{2}\frac{\mu_0\pi rl}{g}F_{ro}F_{ri}\sin\theta. \end{aligned} \quad (5)$$

Rewriting the Eq. (5) with F_R:

$$T_e = -\frac{P}{2}\frac{\mu_0\pi rl}{g}F_{ri}F_R\sin\delta, \quad (6)$$

by substituting:

$$F_R = gH_P = g\frac{B_P}{\mu_0}, \quad (7)$$

$$\varphi = \frac{4}{P}B_P lr \rightarrow B_P = \frac{P}{4}\frac{\varphi}{lr}, \quad (8)$$

$$F_{ri} = m\frac{2\sqrt{2}}{\pi}k_w\frac{N_{ph}I}{P}, \quad (9)$$

$$\varphi = \frac{E_{ph}}{\sqrt{2}\pi f N_{ph}k_w}, \quad (10)$$

into Eq. (6), it is possible to write it in a more useful form:

$$\begin{aligned} T_e &= \frac{\pi}{8}P^2\varphi F_{ri}\sin\delta \\ &= -\frac{\pi}{8}P^2\left(\frac{E_{ph}}{\sqrt{2}\pi f N_{ph}k_w}\right)\left(m\frac{2\sqrt{2}}{\pi}k_w\frac{N_{ph}I}{P}\right)\sin\delta \\ &= \frac{P}{4\pi f}mE_{ph}I\sin\delta = \frac{1}{\omega_m}mE_{ph}I\sin\delta. \end{aligned} \quad (11)$$

In these equations φ is the air gap flux, E_{Ph} is induced voltage per phase in the inner rotor, N_{Ph} is effective turns of the inner rotor windings per phase, K_w is the inner rotor windings coefficient and I is its current. Eq. (11) can be written as in below:

$$T_e = \frac{1}{\omega_m}mE_{ph}I\sin\delta = \frac{1}{\omega_m}mE_{ph}I\cos\theta, \quad (12)$$

where $\delta = \theta + 90$ in which θ is the phase angle between E_{Ph} and I.

V. SIMULATION AND EVALUATION OF THE PROPOSED GEAR BOX

In this section, the design of the proposed magnetic gear and the associated parts are presented and discussed, and finally evaluated based on the earlier-discussed issues. Table 2 summarizes the parameters of a proposed IMG.

Table 2: Specifications of a proposed IMG

Parameter	Value	Parameter	Value
Shaft radius	15 mm	Turns per slot layer	33
PM length	9 mm	Number of PMs	6
PM width	10 mm	Current density	5 A/mm^2
Air-gap length (g)	0.8 mm	Steel grade	M19
Inner-rotor back-iron length	35.2 mm	Slot per pole per phase	1.5
Outer-rotor back-iron length	10 mm	Windings type	Fractional slot, fractional pitch
Axial length	140 mm	Number of slots	27

It is worth noting that PM specifications cannot be chosen freely, and must be selected among the

standard ones given in Table 3.

Table 3: Approximate value of PMs specification

Type	B_r (T)	H_c (kA/m)	Type	B_r (T)	H_c (kA/m)
N27	1.05	800	N40	1.27	928
N30	1.10	800	N42	1.30	928
N33	1.15	840	N45	1.35	870
N35	1.19	872	N48	1.40	840
N38	1.23	904	N50	1.42	840

The B-H characteristic of the utilized steel (M19) is depicted in Fig. 7.

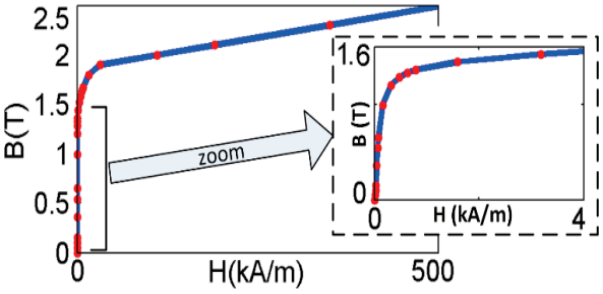

Fig. 7. B-H characteristic of the utilized steel with grade M19-29G.

Because of the mechanical considerations, the minimum air-gap length is about 0.8 mm as given in Table 2. The shaft radius also satisfies and provides us the torque transfer capability of 39 N.m. A satisfactory PM length and width are 10 mm so that the torque pulsations and back-EMF harmonics are simultaneously minimized, because of this sizing the leakage flux will be limited as well. A 2-Dimensional Time-Stepping Finite Element Method (2-D TSFEM), that its meshed regions is shown in Fig. 8, is employed to evaluate the design outcomes. It should be mentioned that the mesh size selection is critical to achieve accurate results. At first, we chose an initial mesh with relatively larger elements. Then, we made them smaller step by step until no enhancement was appeared in the accuracy of the results. So, that mesh was somewhat appropriate for the simulations since it was a trade of between the run speed and accuracy. Moreover, we paid more attention to the regions having higher flux variations; e.g., air-gap and slot areas, in which smaller elements are also adopted.

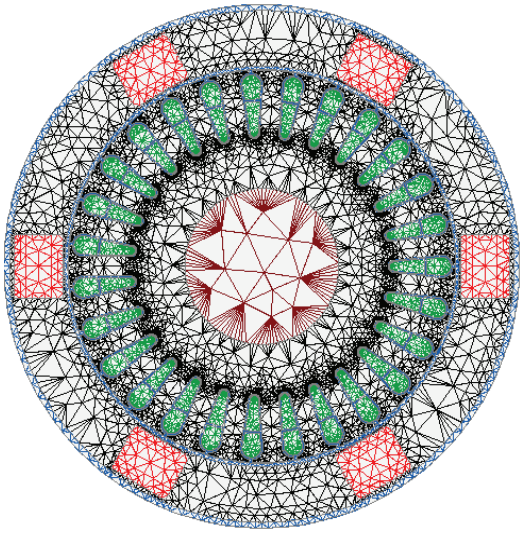

Fig. 8. Meshed regions of the FEM employed for evaluating the proposed IMG.

The proposed design also provides an appreciable demagnetization withstand capability by an appropriate field intensity ratio of $H_m/H_c=0.5$. The rotor radius is large enough to avoid saturation and the length of the outer-rotor back iron is properly designed as well. The magnetic flux density distribution within the device is shown in Fig. 9, which validates the design. This model has been used for various operating conditions to evaluate the proposed IMG behavior.

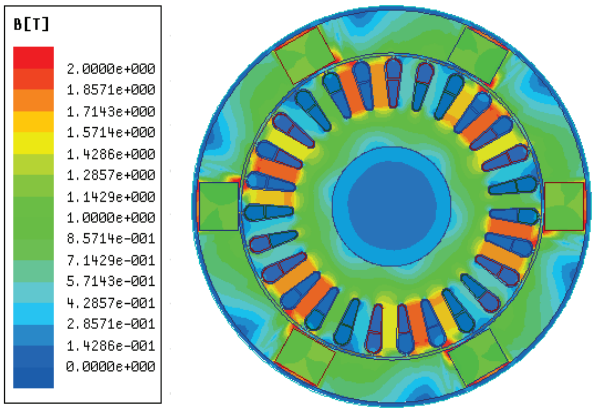

Fig. 9. Magnetic flux density distribution within the proposed IMG.

In generator mode, if the outer rotor rotates at the speed of 1000 rpm while the inner rotor is fixed, the three phase voltage induced in the windings is determined as shown in Fig. 10. It is seen that the voltage waveforms are sinusoidal that finally simplifies the drive system, all of which originates from the proper machine design; e.g., the inner-rotor windings and slots, and PMs.

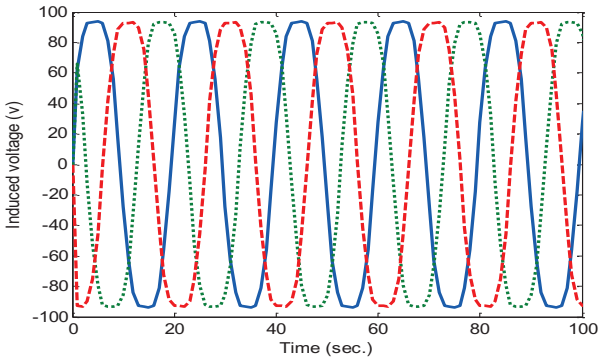

Fig. 10. Induced voltage in the inner rotor windings.

In Fig. 11, gear box torque and speed with 20 N.m loading are shown. Since the windings current frequency is 50 Hz, the rotating magnetic field is 1000 rpm, and the initial mechanical speed of the inner rotor is 500 rpm; therefore, the speed of the outer rotor is 1500 rpm, i.e., 1000+500 rpm. It is observed that the gear box has been stabilized in desired values. Since in the generator mode the back-EMF amplitude was 96 volt, while the applied voltage is on the inner rotor terminals, to compensate for the voltage drop on the windings, the applied voltage is set to V_{peak}=105 volt, i.e., a little higher. This voltage is transmitted to the windings of the inner rotor through a slip ring.

At this point, by simulating the IMG without the outer rotor permanent magnets, it is possible to plot the air gap flux density and flux linkage waveforms (Fig. 12) and evaluate Eqs. (8) and (10). Issued from the machine having the specifications given in Table 2, we achieve: $\varphi = 0.000442\ wb$, $\lambda = 0.129\ wb$ and the air gap flux density is B=0.121 T. Finally, by knowing the phase difference between voltage and current in the inner rotor windings, an output torque of 20.84 N.m is obtained. It is worth noting that the presented equations well describe the gear box behavior in steady state operation and are in good agreement with those extracted from simulations.

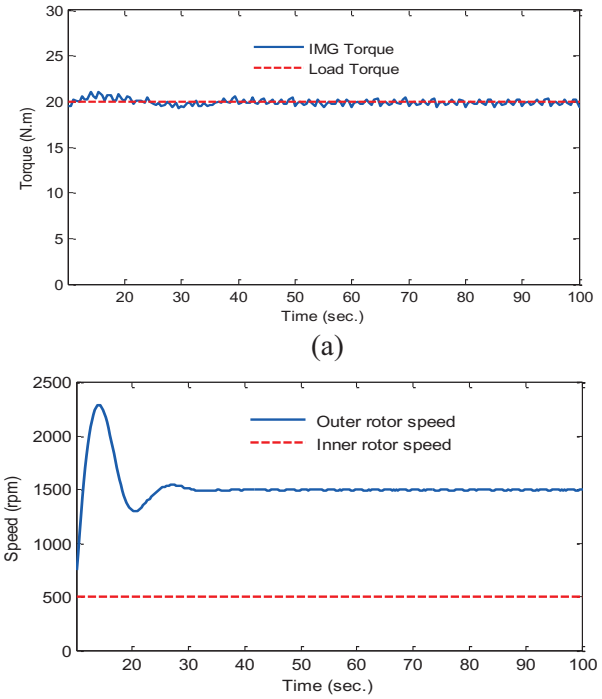

Fig. 11. (a) Output torque, and (b) speed of the IMG.

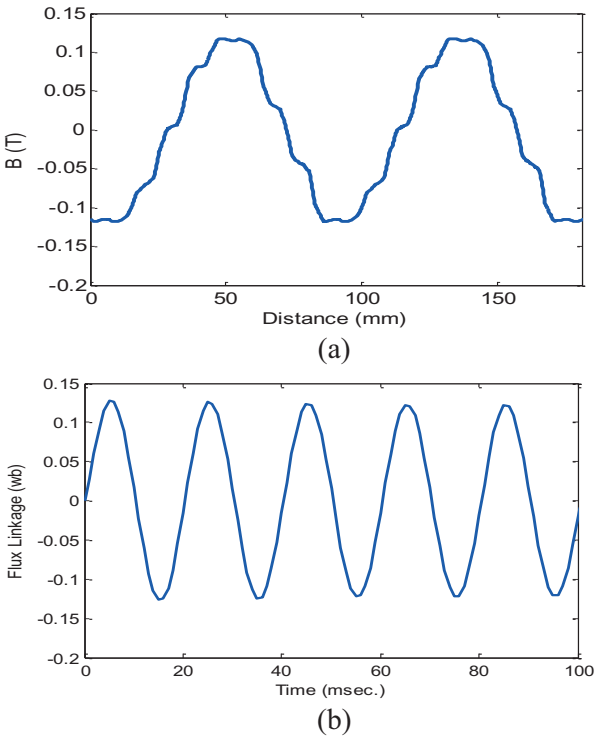

Fig. 12. (a) Flux density, and (b) flux linkage waveforms in the air gap caused by the inner rotor windings.

VI. CONCLUSION

In this paper, the analysis and simulation of a novel structure of magnet gear, which named interior magnetic gear using neodymium-iron-boron magnets is carried out in which can be employed in wind generators, electric vehicles, etc., wherein a continuous ratio of gear box is required. To this end, finite elements analyses are performed to predict the main characteristics of the device including output torque, speed and magnetic field distributions. Both the inner and the outer rotors can be exploited as a low/high speed rotating part by controlling the frequency of the inner rotor windings current. The output torque and other parameters such as B are evaluated in the steady state condition using vector analysis. Simulation results are also in good agreement with theoretical analysis.

REFERENCES

[1] K. Tsurumoto and S. Kikushi, "A new magnetic gear using permanent magnet," *IEEE Trans. Magn.*, vol. 23, no. 5, pp. 3622–3624, 1987.

[2] D.R. Huang, Y.D.Yao, S.M. Lin and S.J.Wang, "The Radial Magnetic Couplings between Magnetic Gears," *IEEE Trans. Magn.*, vol. 31, no. 6, pp. 17-21, Nov. 1995.

[3] Y.D.Yao, D.H.Huang, S.M. Lin and S.J.Wang, "Theoretical Computations of the Magnetic Coupling between Magnetic Gears," *IEEE Trans. Magn.*, vol. 32, no. 3, pp. 710-713, May 1996.

[4] A. Sarikhani , O. A. Mohammed, "Coupled electromagnetic field computation with external circuit for the evaluation the performance of electric motor designs," *ACES Journal*, vol. 26, no. 12, 2011.

[5] E. Schmidt, M. Hofer, "Application of the sliding surface method with 3D finite element analyses of a hybrid magnetic bearing," *ACES Conference, Low-Frequency Computational Electromagcs*, 2009.

[6] K. Atallah and D. Howe, "A novel high-performance magnetic gear," *IEEE Trans. Magn.*, vol. 37, no. 4, pp. 2844–2846, July. 2001.

[7] P. O. Rasmussen, T. O. Andersen, F. T. Jørgensen, and O. Nielsen, "Development of a high-performance magnetic gear," *IEEE Trans. Ind. Appl.,* vol. 41, no. 3, pp. 764–770, May/Jun. 2005.

[8] C. Huang, M. Tsai, D. G. Dorrell, and B. Lin, "Development of a magnetic planetary gearbox," *IEEE Trans. Magn.*, vol. 44, no. 3, pp. 403–412, Mar. 2008.

[9] L.L. Wang, J.X. Shen, P.C.K. Luk, W.Z. Fei, C.F. Wang and H. Hao, "Development of a Magnetic-Geared Permanent-Magnet Brushless Motor," *IEEE Trans. Magn.*, vol. 45, no. 10, pp. 4578–4581, Oct. 2009.

[10] N. Niguchi and K. Hirata, "Torque-Speed Characteristics Analysis of a Magnetic-Geared Motor Using Finite Element Method Coupled With Vector Control," *IEEE Trans. Magn.*, vol. 49, no. 5, pp. 2401–2404, 2013.

[11] P.O. Rasmussen, T.V. Frandsen, K.K. Jensen and K. Jessen, "Experimental Evaluation of a Motor-Integrated Permanent-Magnet Gear," *IEEE Trans. Ind. Appl.*, vol. 49, no. 2, pp. 850–859, 2013.

[12] L. Jian, K.T. Chau and J.Z. Jiang, "A Magnetic-Geared Outer-Rotor Permanent-Magnet Brushless Machine for Wind Power Generation*," IEEE Trans. Ind. Appl.,* vol. 45, no. 3, pp. 954–962, Nov. 2009.

[13] K.T. Chau, D. Zhang, J.Z. Jiang, Ch. Liu and Y. Zhang, "Design of a Magnetic-Geared Outer-Rotor Permanent-Magnet Brushless Motor for Electric Vehicles," *IEEE Trans. Ind. Appl.*, vol. 43, no. 6, pp. 2504–2506, Feb. 2007.

[14] M. Aubertin, A. Tounzi and Y.L. Menach, "Study of an Electromagnetic Gearbox Involving Two Permanent Magnet Synchronous Machines Using 3-D-FEM," *IEEE Trans. Ind. Appl.*, vol. 44, no. 11, pp. 81–84, Nov. 2008.

[15] Z. Haznadar, Z. Stih, S. Berberovic, G. Manenica, "The application of the finite element method in design of electric motors," *ACES Journal*, vol. 9, no. 2, 1994.

[16] O. A. Mohammed, S. Ganu, N. Abed, S. Liu, Z. Liu, "High Frequency Phase Variable Model of Electric Machines from Electromagnetic Field Computation," *ACES Journal*, vol. 22, no. 1, 2007.

[17] H. Torkaman, N. Arbab, H. Karim, E. Afjei, "Fundamental and Magnetic Force Analysis of an External Rotor Switched Reluctance Motor," *ACES Journal*, vol. 26, no. 10, 2011.

[18] M. Okano, K. Tsurumoto, Sh. Togo, N. Tamada and Sh. Fuchino, "Characteristics of the magnetic gear using a bulk high-Tc superconductor," *IEEE Trans. Appl. Supercond.,* vol. 12, no. 1, pp. 979–983, March. 2002.

[19] K. Atallah, J. Wang, and D. Howe, "A high-performance linear magnetic gear," *J. Appl. Phys.,* vol. 97, pp. 10N516-1–10N516-3, 2005.

[20] P. Zheng, B. Yu, H. Yan, Y. Sui, J. Bai, P. Wang, "Electromagnetic Analysis of a Novel Cylindrical Transverse-Flux Permanent-Magnet Linear Machine," *ACES Journal*, vol. 28, no. 9, 2013.

[20] F.T. Jorgensen, T.O. Andersen and P.O. Rasmussen, "The Cycloid Permanent Magnetic Gear," *IEEE Trans. Ind. Appl.,* vol. 44, no. 6, pp. 1659–1665, Nov. 2008.

[21] S. Mezani, K. Atallah, and D. Howe, "A high-performance axial-field magnetic gear," *J. Appl. Phys.,* vol. 99, pp. 08R303-1–08R303-3, 2006.

[22] V.M. Acharya, J.Z. Bird and M. Calvin, "A Flux Focusing Axial Magnetic Gear," *IEEE Trans. Magn.*, vol. 49, no. 7, pp. 4092–4095, 2013.

[24] J. Rens, R. Clark, S. Calverley, K. Atallah and D. Howe, "Design, analysis and realization of a novel magnetic harmonic gear," *18th International Conference on Electrical Machines (ICEM)*, pp. 1-4, 2009.

[25] J. Rens, K. Atallah, S.D. Calverley and D. Howe, "A Novel Magnetic Harmonic Gear," *IEEE Trans. Ind. Appl.,* vol. 46, no. 1, pp. 206–212, Jan./Feb. 2010.

[26] Z. Q. Zhu and D. Howe, "Halbach permanent magnet machines and applications: a review," *Inst. Electr. Eng. Proc. Electr. Power Appl.,* vol. 148, no. 4, pp. 299–308, Jul. 2001.

[27] J. Choi and J. Yoo, "Design of a Halbach magnet array based on optimization techniques," *IEEE Trans. Magn.*, vol. 44, no. 10, pp. 2361–2366, Oct. 2008.

[28] L. Jian and K.T. Chau, "A Coaxial Magnetic Gear With Halbach Permanent-Magnet Arrays," *IEEE Trans. Energy Convers.*, vol. 25, no. 2, pp. 319–328, June. 2010.

[29] L. Shah, A. Cruden and B.W. Williams, "A Variable Speed Magnetic Gear Box Using Contra-Rotating Input Shafts," *IEEE Trans. Magn.*,vol. 47, no. 2, pp. 431–438, Feb. 2011.

[30] P. Vas, "Sensorless Vector and Direct Torque Control," Oxford Press, New York, 1998.

[31] N. Niguchi and K. Hirata, "Cogging Torque Analysis of Magnetic Gear," *IEEE Trans. Ind. Electron.,* vol. 59, no. 5, pp. 2189–2197, 2012.

[32] H. Lesani, "Windings of Electric Machinery," 3nd edition," Daneshofan Press, Tehran, Iran1995.

[33] G.R. Slemon, "Electric Machines and Drives," Addison-Wesley Publication Company, 1992.

Behrooz Majidi was born in Isfahan, Iran. He received his M.Sc degree in electrical engineering from Amirkabir University of Technology (Tehran Polytechnic), Tehran, Iran. He is currently Ph.D student at Amirkabir University of Technology (AUT). His research interests include power electronics, electrical machines and variable speed drives.

Jafar milimonfared received the B.Sc. Degree in electrical engineering from Amirkabir University of Technology, and both the M.Sc. and Ph.D. degrees from Paris VI University, Paris, France in 1981 and 1984 respectively. Dr. Milimonfared joined Amirkabir University of Technology as an assistant professor in 1984 where he is now a professor of electrical engineering. From 1990 to 1993 and from 1997 to 2005, he was the deputy of Ministry of Science, Research and Technology in Iran. He is now head of Iran Mechatronics Society. His research interests include electrical machines design and analysis, power electronic and variable speed drives.

Novel Design of UWB Band-Stop Filter (BSF) Based on Koch Fractal Structures

Nasser Ojaroudi [1], Yasser Ojaroudi [2], and Sajjad Ojaroudi [2]

[1] Young Researchers and Elite Club, Ardabil Branch
Islamic Azad University, Ardabil, Iran
n.ojaroudi@yahoo.com

[2] Young Researchers and Elite Club, Germi Branch
Islamic Azad University, Germi, Iran
y.ojaroudi@iaugermi.ac.ir, s.ojaroudi.p@gmail.com

Abstract ─ In this paper, a novel design of compact microstrip Ultra-Wideband (UWB) Band-Stop Filter (BSF) for wireless applications is proposed. The proposed BSF structure is based on Koch fractal geometry where its third iteration operates over a very wide bandwidth and improves the impedance matching. The microstrip filter configuration consists of a transmission line with pairs of Koch fractal Radial Stubs Loaded Resonators (RSLRs), and a modified ground plane with triple modified Defected Ground Structures (DGSs). Operation frequencies of the filter can be easily controlled by changing the iteration of embedded fractal structure. The DGS slots evolved from Photonic Band Gap (PBG) is embedded to achieve a good impedance matching and the required filter's characteristics. The proposed BSF has a flat rejected-band characteristic around of 3.1-10.6 GHz with an insertion loss which is larger than 45 dB and a return loss less than 0.5 dB at the centre of the band-stop frequency range. An excellent agreement between measured and simulated was obtained. The proposed microstrip filter is fabricated on a *Rogers RT/Duroid* 5880 substrate with a relative dielectric constant of 2.2 and has a small size of 10×15×0.635 mm^3. The proposed filter configuration is and can be integrated into any UWB system.

Index Terms ─ Band-stop filter, DGS, Koch fractal, UWB application.

I. INTRODUCTION

In modern communications, one of the important parameters is isolation between channels in a given bandwidth. Filters with different configurations are essential components in communication systems and these are generally used as signal rejection for unwanted signals and simultaneously allow the wanted signals in required bands. In recent times, the design of filters has become an active research area as filtering is important when used in close proximity to other circuit components, like power amplifiers in the transmitter part and low noise amplifiers in receiver part, for various RF applications [1].

Conventionally the microwave filter is implemented either by all shunt stubs or by series connected high-low stepped-impedance microstrip line sections. However, generally these are not easily available in microwave band due to the high impedance microstrip line and the spurious pass-bands. To remove these disadvantages, defected ground structures for microstrip lines have been presented in recent years. They have been presented in a number of different shapes for filter applications [2-3]. The DGS applied to a microstrip line causes a resonant character of the structure transmission with a resonant frequency controllable by changing the shape and size of the slot. This technique is suitable for periodic structures, and for both band-stop and low-pass filters, e.g., [4].

Recently, the use of fractals in the design of

Submitted On: April 25, 2014
Accepted On: September 6, 2014

filters have attracted a lot of attention to achieve objectives like reduced resonant frequencies and wide bandwidth. Fractals were first defined by Benoit Mandelbrot in 1975 as a way of classifying structures whose dimensions were not whole numbers. Fractal means broken or irregular fragments that possess an inherent self-similarity in their geometrical structure. Looking at geometries whose dimensions are not limited to integers lead to the discovery of filters with compact size and improved characteristics. Till date, several fractal geometries such as Hilbert curve, Sierpinski carpet, Koch curve, etc., have been used to develop various microwave devices [5]. Subsequently, Koch fractal is applied to the conventional filter and spurious band is being suppressed successfully. Finally, the proposed filters are physically implemented and the simulated and measured results discussed.

More elaborately, in case of Koch fractal, as the number of iterations increases, stopped bandwidth of this filter increases. Also, it is observed that the imaginary part of input impedance at the resonant frequency changes from capacitive to an inductive component. This paper work deals with design and development of a microstrip band-stop filter for UWB applications. In this structure, the resonant behaviors of the RSLRs which are used here, introduces transmission zeroes to the filter response and consequently improves its band-stop performance. Also, the reason for the choice of modified DGS is that it can provide an almost constant tight coupling, which is important to generate a good frequency response. The designed filter has a small dimension of 10×15 mm^2.

II. FILTER DESIGN

The proposed microstrip filter configuration is shown in Fig. 1. This filter was designed on a *Rogers RT/Duroid* 5880 substrate with 0.635 mm in thickness and with a relative dielectric constant of 2.2. For the input/output connections 50-Ohm microstrip lines are used. The microstrip BSF was designed on both substrate sides by opening aperture in the ground metallization under the low-impedance transmission line. Replacing of the pairs of RSLRs based on Koch fractal structure, introduces transmission zeroes. Final values of the presented band-stop filter design parameters are specified in Table 1.

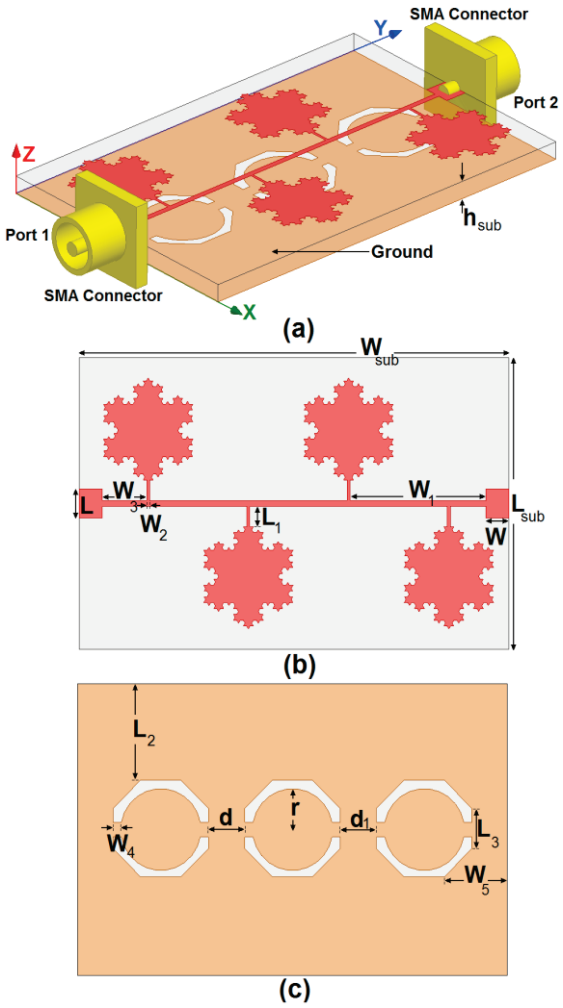

Fig.1. Geometry of proposed microstrip band-stop filter, (a) side view, (b) top layer, and (c) bottom layer

Table 1: The final dimensions of the filter

Parameter	W_{sub}	L_{sub}	h_{sub}	W
(mm)	15	10	0.635	0.8
Parameter	L_2	W_3	L_3	r
(mm)	3.4	0.4	1.35	1.4
Parameter	L	W_1	L_1	W_2
(mm)	0.9	4.75	0.7	0.1
Parameter	d	W_4	d_1	W_5
(mm)	1.25	0.3	1.25	2.2

The original curve is equilateral triangle with length of g. The triangular RSLRs with a length g are considered as the starting pattern for the proposed band stop filter as a fractal.

From this starting pattern, each of its four RSLRs is replaced by what is called the generator

structure shown in Fig. 1 (a)

All the iterations are circumscribed inside a circumference of radios $r = \sqrt{3g/3}$. On the other hand, the perimeter increases at each new iteration. The overall perimeter for iteration is given by:

$$I_K = 3g(\frac{4}{3})^K. \quad (1)$$

III. RESULTS AND DISCUSSIONS

The proposed filter with various design parameters was constructed, and the experimental results of the S-parameter characteristics are presented and discussed. The simulated results are obtained using the Ansoft simulation software High-Frequency Structure Simulator (HFSS) [6].

Investigation of the Koch fractal-shaped property, from electromagnetic simulation of a Koch fractal shape resonator it observed that the transmission zeroes becomes upper in magnitude with increase in iterations. This is due to the space-filtering property of fractal geometry. Controlling the transmission zeroes at the creating stop band, can be used to increase or decrease the stop-band generated by conventional filter.

The proposed filter with final design as shown in Fig. 2, was fabricated and tested that good S-parameters ($|S_{11}|/|S_{21}|$) are introduced to the filter response from 3.1 to 10.6 GHz.

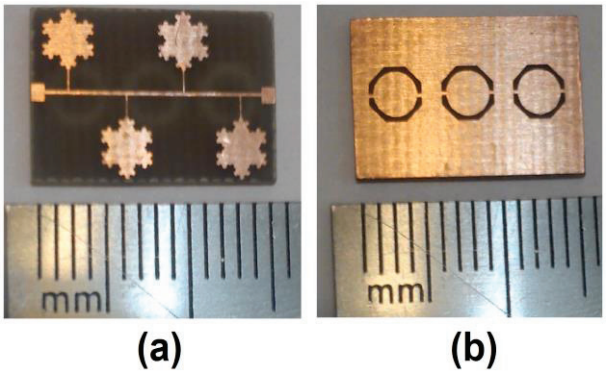

Fig. 2. Fabricated band-stop filter: (a) top view, and (b) bottom view.

Figure 3 shows the simulated and measured insertion and return loss of the filter. As shown in Fig. 3, a flat insertion and return losses are introduced to the filter response. Consequently, a very wide band-stop characteristic was achieved. The measured return and insertion losses ($|S_{11}|$ and $|S_{21}|$) are found to be better than 0.5 dB and less than 45 dB, respectively, over the entire UWB frequency range.

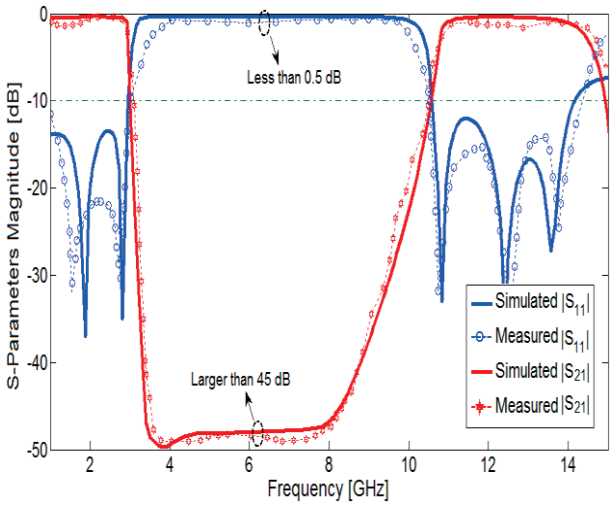

Fig. 3. Measured and simulated $|S_{11}|$ and $|S_{21}|$ characteristics for the proposed filter.

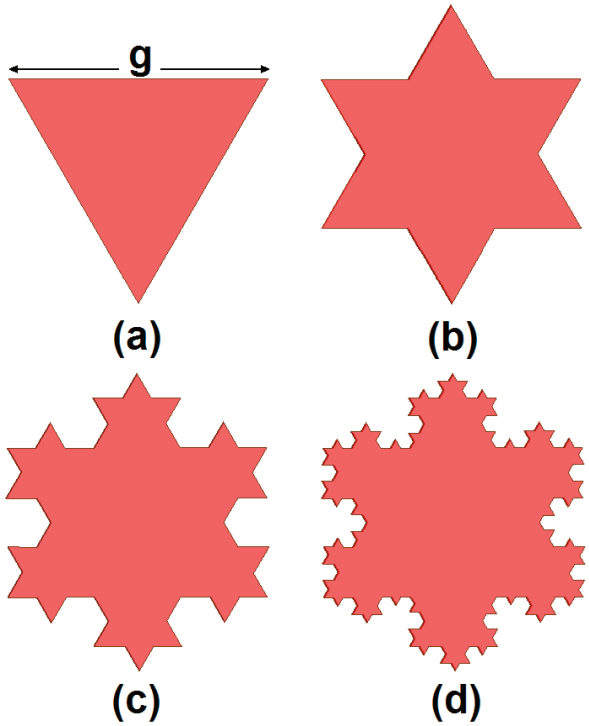

Fig. 4. Koch snowflake geometry in its different iteration stages: (a) basic geometry, (b) first iteration, (c) second iteration, and (d) third iteration.

The basic geometry of the radial stubs is an equilateral triangle of side *g*, on which repeated iterations lead to the Koch snowflake geometry as shown in Fig. 4.

The first iteration of replacing a segment with the generator is shown in Fig. 4 (a). The starting pattern is Euclidean, and therefore, the process of replacing the segment with the generator constitutes the first iteration. The generator is scaled after, such that the endpoints of the generator are exactly the same as the starting line segment. In the generation of the true fractal, the process of replacing every segment with the generator is carried out an infinite number of times. The resulting pre-fractal structure has the characteristic that the perimeter increases to infinity while maintaining the volume occupied.

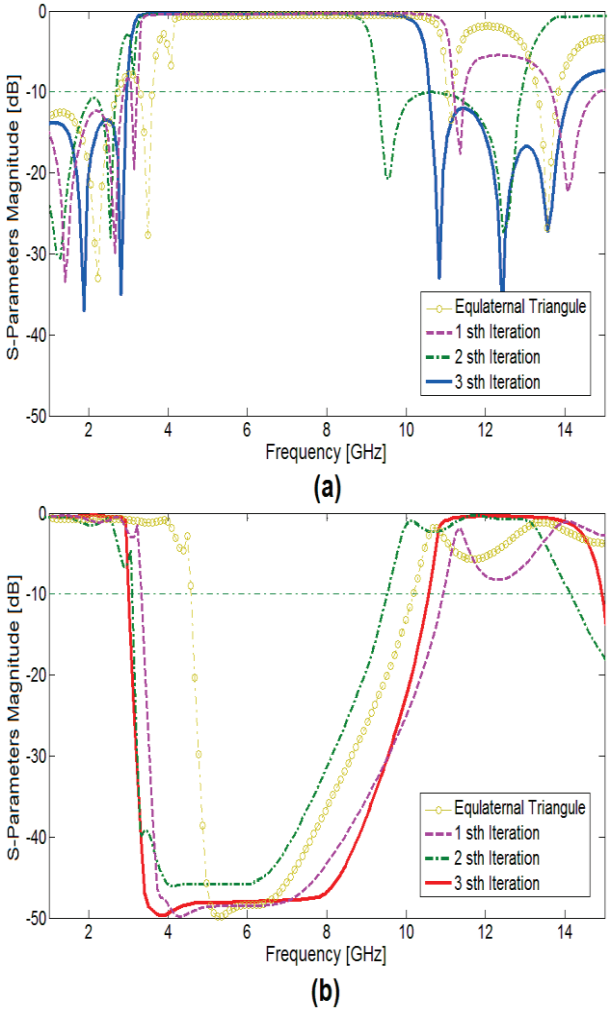

Fig. 5. Simulated S-parameters for different iterations of Koch structures: (a) $|S_{11}|$, and (b) $|S_{21}|$.

This increase in length decreases the required volume occupied for the pre-fractal band-stop filter at resonance. It has been found that:

$$P_n = (\frac{4}{3})^n \; P_{n-1}, \tag{2}$$

where P_n is the perimeter of the *n*th iteration pre-fractal structure. Theoretically, as *n* goes to infinity, the perimeter goes to infinity. The ability of the resulting structure to increase its perimeter in the successive iterations was found very promising for examining its size reduction capability as a microstrip band-stop filter. Figure 5 illustrates the simulated S-parameters of the proposed BSF, for iteration stages of the fractal geometry. It is observed that the Koch fractal geometry improves the impedance matching at the lower and upper frequencies along the bandwidth enhancement of the proposed filter. In practice, shape modification of the resulting structures is a way to increase the surface current path length compared with that of the conventional triangular resonator. As can be observed, at the third iteration the proposed band-stop filter operates very wide bandwidth from 3.1 to 10.6 GHz, which covers the UWB frequency range.

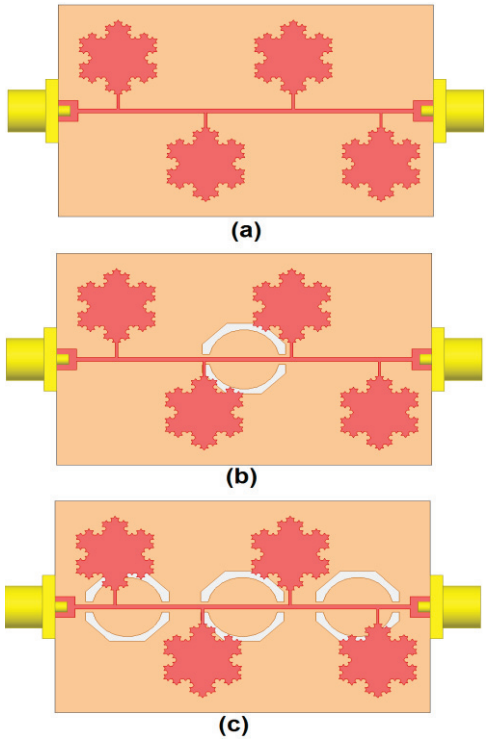

Fig. 6. (a) BSF without DGS, (b) the filter with a single DGS, and (c) the proposed filter structure.

Defected ground structure technique is now applied in the design of microstrip filters. This helps to improve the filter performance and causes a size reduction, which is considered a major benefit. This technique is currently employed to meet the increasing demand for compact structure high performance filters [4]. Various configuration of the proposed microstrip filter w/o DGSs is shown in Fig. 6.

Figure 7 shows the effects of the inserted DGS with different numbers on the return loss matching. The slots introduced at the backed ground plane layer (i.e., DGS) mainly improve the transition sharpness and widens the rejection band. This is due to the fact that the waves penetrating the structure are disturbed, causing equalization in the model phase velocity with respect to one another. This can also help in developing a more compact structure without the need to implement higher order filters with the same performance.

As illustrated, it is found that by inserting the three modified DGS of suitable dimensions in the ground plane, good impedance matching for return loss characteristics in comparison to the same filter without DGS can be achieved. As illustrated in Fig. 6 (c), the microstrip filter with slotted ground plane consisting of three modified DGS has a wider return loss bandwidth.

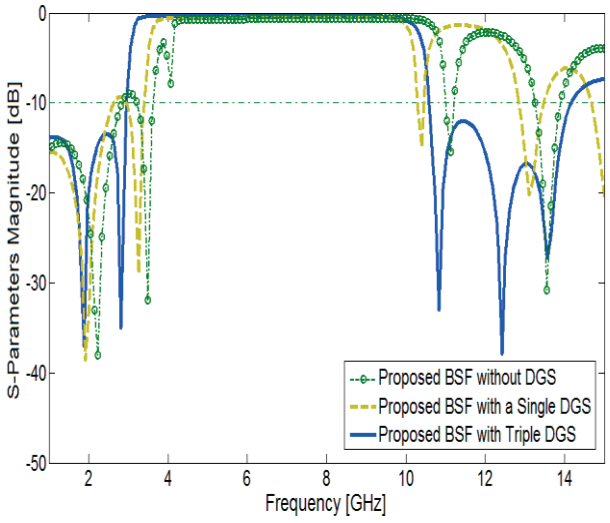

Fig. 7. Simulated $|S_{11}|$ (return loss) characteristic for the proposed BSF with and without DGSs.

Table 2 summarizes the previous designs and the proposed filter. It can be seen from Table 2, the proposed microstrip band-stop filter has a compact size with very wide bandwidth compared to the previous works. In addition, the proposed BSF has a flat rejected-band characteristic around of 3.1-10.6 GHz with an insertion loss which is larger than 45 dB and a return loss less than 0.5 dB at the centre of the band-stop frequency range.

Very good agreement is obtained between simulated and measured results. The small discrepancies can be attributed to fabrication tolerances and to the dissipative losses not taken into account in the simulation.

Table 2: Comparison of previous band-stop designs with the proposed microstrip filter

Ref.	Stop-Band (GHz)	Size (mm^2)	ε_r/h_{sub} (mm)
[7]	2.2-2.31	50×26	2.2/0.508
[8]	2.82-4.0	16×15.4	4.4/1.5
[9]	8.1-9.64	15.7×2.4	2.4/0.508
[10]	4.05-8.0	15×10	2.2/0.635
[11]	12-17.51	23×10	2.3/0.787
This work	*3.1-10.6*	*15×10*	*2.2/0.635*

IV. CONCLUSION

In this paper, a novel design of band-stop microstrip filter has been presented. The proposed filter structure is designed based on Koch fractal geometry and modified DGS. Good insertion and return losses ($|S_{11}|$ and $|S_{21}|$) are introduced to the filter response from 3.1 to 10.6 GHz, which covers the UWB frequency range. The proposed filter is promising for use in wireless technologies for UWB communications due to their compact size and excellent performance.

ACKNOWLEDGMENT

The authors are thankful to Microwave Technology (MWT) Company staff for their beneficial and professional help (www.microwave-technology.com).

REFERENCES

[1] G. L. Matthaei, L. Young, and E. M. T. Jones, "Microwave filters, impedance-matching network, and coupling structures," Norwood, MA, *Artech House*, 1980.

[2] K. L. Finch and N. G. Alexopoulos, "Shunt posts in microstrip transmission lines," *IEEE Transactions on Microwave Theory and Techniques*., vol. 38, pp. 1585-1594, 1990.

[3] N. Ojaroudi, M. Ojaroudi, and R. Habibi, "Design and implementation of very compact band-stop filter with petal-shaped stub for radar applications," *Microwave and Optical Technology Letters*, vol. 55, pp. 1130-1132, 2013.

[4] J. S. Park and J. S. Yun, "A design of the novel coupled-line bandpass filter using defected ground structure with wide stopband performance," *IEEE Transactions on Microwave Theory and Techniques*, vol. 50, no. 9, September 2002.

[5] N. Ojaroudi, H. Ojaroudi, and Y. Ojaroudi, "Very low profile ultra-wideband microstrip band-stop filter," *Microw. Opt. Technol. Lett.*, vol. 56, pp. 709-711, 2014.

[6] "Ansoft high frequency structure simulator (HFSS)," ver. 13, *Ansoft Corporation*, Pittsburgh, PA, 2010.

[7] Q. Xiang, Q. Feng, and X. Huang, "Tunable bandstop filter based on split ring resonators loaded coplanar waveguide," *Applied Computational Electromagnetics Society (ACES) Journal*, vol. 28, pp. 591-596, 2013.

[8] M. A. Abaga Abessolo, Y. Diallo, A. Jaoujal, A. E. Moussaoui, and N. Aknin, "Stop-band filter using a new metamaterial complementary split triangle resonators (CSTRs)," *Applied Computational Electromagnetics Society (ACES) Journal*, vol. 28, pp. 353-358, 2014.

[9] X. H. Wang, B. Z. Wang, H. Zhang, and K. J. Chen, "A tunable band-stop resonator based on a compact slotted ground structure," *IEEE Transactions on Microwave Theory and Techniques*, vol. 55, pp. 1912-1918, 2007.

[10] R. Habibi, C. Ghobadi, J. Nourinia, M. Ojaroudi, and N. Ojaroudi, "Very compact broad band-stop filter using periodic L-shaped stubs based on self-complementary structure for X-band application," *Electronic Letters*, vol. 48, pp. 1483-1484, 2012.

[11] M. Kazerooni1, N. P. Gandji, A. Cheldavi, and M. Kamarei, "A new microwave bandstop filter using defected microstrip structure (DMS)," *Progress In Electromagnetics Research Symposium Proceedings*, Moscow, Russia, pp. 697-700, August 18-21, 2009.

Parametric Study of Sinc Shaped Monopole Antenna for Wireless Devices

Ritesh Kumar Badhai [1] and Nisha Gupta [2]

[1] Department of Electronics and Communication Engineering
Birla Institute of Technology, Patna Campus, Patna, Bihar, 800 014, India
ritesh234@gmail.com

[2] Department of Electronics and Communication Engineering
Birla Institute of Technology, Mesra, Ranchi, Jharkhand, 835 215, India
ngupta@bitmesra.ac.in

Abstract ─ In this work, a Sinc shaped printed monopole antenna is proposed for wireless devices. The radiating element is a strip monopole configuration folded in the shape of a Sinc function where the radiating element is an extension of 50 Ω microstrip line. The proposed antenna not only represents a compact configuration but is easier to design and feed. Several configurations of truncated Sinc(*2x*) monopole geometry are taken into consideration to show the resonance behavior at single, two or more than two frequencies for multifrequency operation. The detailed parametric study has been carried out in terms of several truncated Sinc configurations, ground plane size, feed gap and Sinc strip length to achieve the desired band of operation. The design formula is also presented for the proposed monopole antenna. Finally, a prototype model is developed and the simulated results are validated experimentally for a particular configuration. It is seen that the proposed antenna occupies small area, depicts good radiation characteristics and is suitable for wireless devices operating at DCS/PCS/IMT-2000/UMTS frequencies.

Index Terms ─ Monopole antenna, multiband antenna, multifrequency antenna, patch antenna, Sinc antenna.

I. INTRODUCTION

Monopole antennas are widely used as efficient radiators in a variety of applications such as communication, navigation, mobile telephones, radio receivers, etc. It is due to its salient features in terms of light weight, planar conformal construction, low cost, ease of fabrication and integration with RF devices, etc. Recent demand of wireless devices requires a single, dual or multiband/multifrequency [1] compact monopole patch antennas.

Several techniques have been reported in the literature to realize multifrequency characteristics of printed monopole antennas such as use of bevels, slots and shorting pins [2,3], use of fractal structure [4], and mounting of slots like E-shaped slot on ground plane [5], etc. In most of the cases, by controlling the current flow on the patch and changing the resonant length, multifrequency characteristics are obtained.

Many compact printed monopole antennas have been designed for the wireless applications. Some of the monopole antenna structures among them are folded monopole antennas with shorting pins to achieve DCS, PCS, 3G and WLAN band [6], meandered patch antenna with modified ground structure for UMTS and WLAN application [7], CPW-fed strip monopole antenna with slant edge ground plane for DCS, PCS, 3G, and Bluetooth bands [8], CPW-fed dual inverted-L shaped monopole antenna for DCS, PCS and IMT 2000 [9], Y-shaped monopole antenna for PCS/WLAN application [10], dual band antenna for DCS/PCS/UMTS/WLAN/WiMAX using omega shaped structure [11], CPW-fed dual frequency monopole antenna [12], dual band CPW-fed strip-sleeve monopole antenna [13], compact dual band

Submitted On: October 14, 2013
Accepted On: October 4, 2014

antenna for DCS/2.4 GHz WLAN application [14], a compact dual band planar branched monopole antenna for DCS/2.4 GHz WLAN application [15], etc. Various interesting dual or multiband structures with large ground plane size are reported in the literature for DCS/PCS/UMTS/IMT2000 bands such as DSPSL fed and coupled line broadband antenna [16], inverted-F antenna [17] and double inverted-L branched antenna with open stub [18], etc. Most of them have a complex shape involving difficult design steps. In the present work, a simple monopole antenna is proposed where the shape of the monopole is derived from the Sinc function in order to realize a compact and simple configuration, where just by changing the Sinc geometrical parameters, the antenna may be made to operate at the desired band of operation.

The Sinc shaped microstrip configuration was first proposed by Yang, et al. [19], and then Gupta, et al. [20] also used a similar configuration to realize multi-frequency antenna. However, in both these configurations the shape of the antenna was only Sinc like and not derived from the Sinc function. In [21-23], monopole antenna configurations based on the sinusoidal geometrical function is presented for wireless sensor node applications. In proposed work, a truncated Sinc shaped printed monopole antenna geometry obtained from the Sinc($2x$) function for use as an efficient monopole radiator has been studied. The monopole geometry under consideration is a truncated Sinc giving rise to one of the compact monopole configurations. The simulation is performed for several truncated Sinc shaped monopole geometries printed on a glass epoxy substrate. Finally, a prototype is developed and the results are compared with the simulation results.

The proposed antennas in this paper are useful for several wireless applications such as DCS (1710-1880 MHz), PCS (1850-1990 MHz), IMT 2000 (1885-2070 MHz), UMTS (2120-2170 MHz), fixed mobile communication and fixed satellite communication (space to earth) (4500-4800 MHz), etc.

II. ANTENNA DESIGN

The Sinc shaped antenna of any dimension along the length or width can be visualized as one of the Sinc functions printed in the form of a strip on a substrate. The antenna dimension can be increased or decreased along the length as much needed, by taking the suitable value of the coefficient 'b' of the argument x; and along the height by taking appropriate factor 'a' of the function. Actually, the Sinc function extends up to infinity. Therefore in practice, the Sinc antenna refers to a 'truncated' Sinc function, the range of the function determining the length of the monopole strip.

The advantage of using Sinc shaped monopole antenna is in many folds. First of all, larger length can be accommodated in smaller space, thus realizing a compact structure. Secondly, the shape can be generated by a simple mathematical function. Thirdly, single, dual or multi band operation can be realized, simply by selecting a specific length of the Sinc strip. The strip width of the Sinc can be easily maintained for standard 50 Ω matching with the feed. The proposed Sinc shaped monopole antenna considers truncated Sinc($2x$) function for strip geometry and may be considered as one form of meander line. However, the proposed Sinc shaped strip monopole antennas are superior to the meandered line strip monopole antenna. Unlike the meander line strip where there is more opposition of current vectors in the parallel section of strips leading to diminishing self-inductance, in the proposed Sinc($2x$) strip configuration, the current vectors reinforce along the total strip length; thus, adding to more self-inductance as shown in Fig. 1. This is due to the fact that for proposed Sinc($2x$) geometry, least coupling is evident between the adjacent strips which in turn is more effective in realizing a compact antenna configuration. This property of the Sinc($2x$) function also facilitates the use of design formula available for simple monopole strip, conveniently for the proposed monopole strip with little modifications.

The normalized Sinc function Sinc($2x$) for the proposed antenna configurations is shown in the Fig. 2. The Sinc($2x$) configuration is considered because it shows a uniform current distribution along the strip. In higher order functions (Sinc($3x$), Sinc($4x$) etc.), the current distribution tends to become non uniform due to overlapping geometry of the radiating strip arising because of finite thickness of the strip. The simulation has been performed using a full-wave Method of Moments (MoM) software package IE3D from Zeland [24]. The geometry of the Sinc is obtained from the Sinc function using MATLAB and then imported to the

IE3D. The desired strip thickness is then set by setting the thickness of the line. The radiation characteristic of this antenna is examined with respect to several design parameters. The parametric analysis of the Sinc strip is performed both on finite and infinite substrate size, and for different set of design parameters. The strip width as equal to the 50 Ω microstrip line width and simple microstrip feeding mechanism to the monopole are selected as different set of parameters.

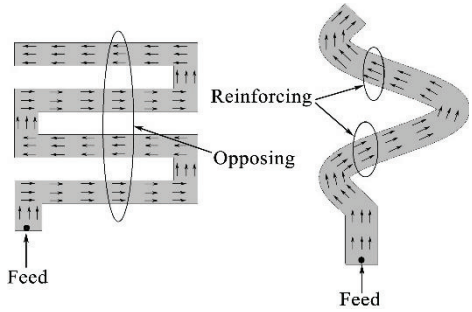

Fig. 1. Current flow in meander strip and Sinc shaped strip.

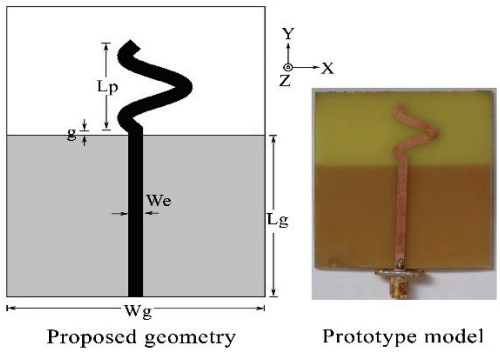

Fig. 2. Proposed Sinc shaped monopole antenna.

The Sinc shaped configuration accommodates larger electrical length in small area; therefore, the current on the strip takes a longer path compared to the unfolded strip. The Sinc strip is simply an extension of the 50 Ω transmission line which reduces the mismatch between feeding line and strip, thus shows good impedance matching behaviour. The desired band of operation can be achieved by selecting the optimized length of Sinc strip, feed gap between the ground plane and Sinc strip, ground plane size and off center position of feeding line as discussed in the next section.

The simulation is performed for Sinc(*2x*) strip configuration having two zero crossing points, considering the parameters like length of Sinc (*Lp*)=20 mm, dielectric constant (ε_r)=4.4, loss tangent (*tanδ*)=0.018, dielectric thickness (*h*)=1.57 mm, width of the 50 Ω microstrip line (*We*)=3.0 mm, feed gap (*g*)=0.3 mm and ground plane size *Wg*=52 mm, *Lg*=38 mm.

The design formula for first three resonant frequencies of proposed Sinc(*2x*) monopole antenna is given by:

$$f_n = a^{n-1}\frac{(2n-1)c}{2\sqrt{\varepsilon_r}Le}, \quad (1)$$

where *n*=1,2,3, *a*=0.82, *c*=speed of light in free space, ε_r=relative permittivity and *Le*: physical length (unfolded length) of Sinc strip=36.6 mm.

III. PARAMETRIC STUDY

A. Effect of the ground plane

The ground plane dimensions are very important parameters in the design of a monopole antenna because of the strong dependence of gain, bandwidth and antenna efficiency on ground plane size. Simulation is performed for various ground plane parameters and the effect of ground plane size on resonant frequency is shown in Figs. 3 (a) and 3 (b). As evident from the figure, the ground plane width (*Wg*) has very little impact on the first resonant frequency. However, the second resonant frequency is influenced and decreases up to 500 MHz by increasing *Wg*. The ground plane length (*Lg*) affects both the resonant frequencies with more variation for the second resonant frequency and a decrease in second resonant frequency up to 900 MHz is obtained. The results for the other antenna parameters are tabulated in Table 1. As seen, with an increase in the ground plane size, both the gain and antenna efficiency increase. The ground plane size of 52 mm (~λ_0/3) width and 38 mm (~λ_0/4) length is selected to achieve larger gain and antenna efficiency for the proposed monopole configuration.

Figure 4 shows the reflection coefficient of Sinc(*2x*) monopole antenna for the case of finite and infinite substrate size. The parameters taken into consideration are: *Wg*=0.33λ_0 (~=λ_0/3), *Lg*=0.24λ_0 (~=λ_0/4), *Lp*=0.125λ_0 (~=λ_0/8) and the physical length of the patch (*Le*)=0.23λ_0. It is observed that there is a small shift in the resonant frequencies towards the lower side with finite substrate size.

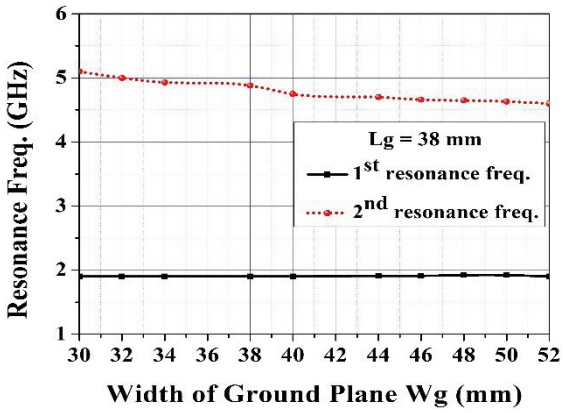

(a)

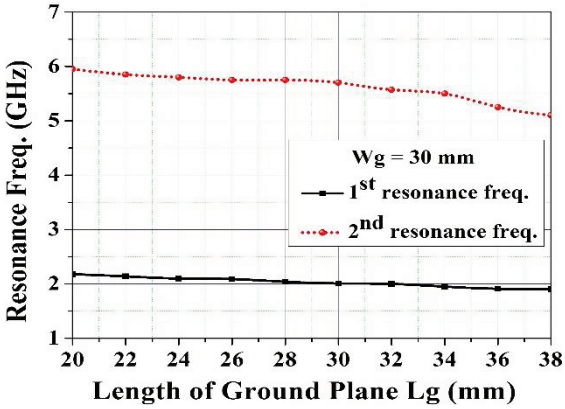

(b)

Fig. 3. Effect of ground plane dimensions on resonant frequency.

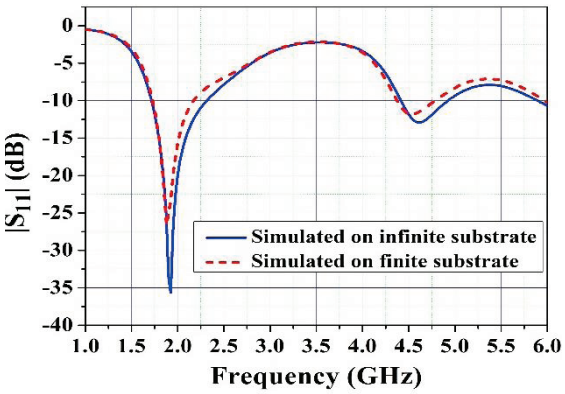

Fig. 4. Reflection coefficient ($|S_{11}|$) of Sinc($2x$) monopole antenna for infinite and finite dielectric size.

B. Effect of feed gap

Next, the effect of the feed gap on the characteristics of the antenna is examined. For the different feed gap (g) between the patch and the ground plane, it is seen that the resonance frequency is reduced with increasing feed gap for both lower and higher resonance modes; however, the impedance bandwidth deteriorates for larger values of 'g' for both the cases. On the other hand, the reflection coefficient deteriorates for larger feed gap at a lower resonant frequency, while at the second resonant frequency it improves. The effect of the feed gap between 1.0 to 10 mm is shown in Table 2. The effect of feed gap on resonant frequency and bandwidth is plotted and shown in Figs. 5 (a) and 5 (b). It is seen that for both the modes, the resonant frequencies decrease linearly with increase in feed gap, but the bandwidth reduction for both the cases is not linear. This is due to the fact that a larger feed gap offers extra inductance to the Sinc length, and deteriorates the matching.

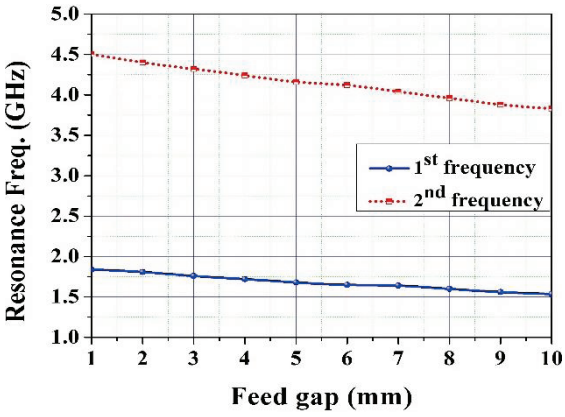

(a)

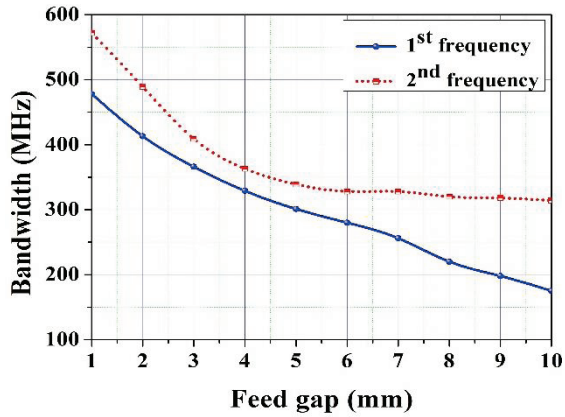

(b)

Fig. 5. Effect of feed gap on: (a) resonant frequency, and (b) bandwidth.

C. Effect of off center position

For the different off center position of microstrip feed and Sinc strip, it is seen that the first resonance frequency is constant in a range of off center position as 1 mm to 5 mm, and then in the range of 7 mm to 23 mm it reduces monotonically with an increase in off center values. The second resonance frequency is reduced between 1 mm to 7 mm and increased between 9 mm to 23 mm with increasing off center values. The effect of off center position is presented in Table 3. Here, the feed gap (g) is considered as 2 mm.

The Sinc shaped monopole antenna gives good impedance matching and impedance bandwidth between 7 mm to 13 mm for first resonance frequency, and between 11 mm to 19 mm for the second resonance frequency with increasing off center values. The optimum range for off center position of microstrip line and Sinc strip is obtained in the range of 11 mm to 13 mm.

D. Effect of Sinc strip length

The Sinc shaped monopole antenna can be made to resonate at very wide range of resonating frequencies for Sinc length variation, though the total area occupied by the Sinc does not change much. By varying the Sinc strip length (Lp) from 10 mm to 30 mm, the first resonant frequency varies from 2.98 GHz to 1.52 GHz. The Sinc strip length variation is shown in Fig. 6 and simulation results are presented in Table 4. In the range of the Sinc strip length (Lp) from 10 mm to 18 mm, the second resonant frequency f_2 disappears. Similarly, for length 28 mm and 30 mm, the third resonant frequency f_3 disappears.

Table 1: Effect of ground plane size on antenna parameters

Ground Plane Size, $Wg \times Lg$ (mm^2)	1st Resonance Frequency				2nd Resonance Frequency			
	$\|S_{11}\|$ (dB)	Bandwidth (MHz)	Gain (dBi)	Antenna Efficiency (%)	$\|S_{11}\|$ (dB)	Bandwidth (MHz)	Gain (dBi)	Antenna Efficiency (%)
30 × 24	-12.4	251	1.39	75.83	-12.9	933	1.67	48.53
30 × 26	-14.2	302	1.43	79.12	-12.7	1253	1.24	52.82
30 × 30	-19.5	369	1.43	76.00	-12.4	1317	1.24	54.32
30 × 34	-38.1	407	1.84	78.90	-10.9	1147	1.74	52.51
32 × 32	-24.1	406	1.85	77.81	-11.6	1193	1.66	54.92
34 × 34	-37.8	450	2.01	79.84	-11.2	829	1.85	56.99
38 × 38	-29.9	595	2.03	82.46	-11.2	535	2.31	51.26
44 × 38	-29.5	687	2.03	81.32	-11.8	478	2.37	59.59
48 × 38	-26.6	424	2.02	83.82	-11.6	634	2.72	63.81
52 × 38	-35.4	588	2.40	94.37	-12.9	508	3.84	81.12

Table 2: Effect of feed gap for Sinc shaped monopole antenna

Feed Gap (mm)	1st Resonance Frequency				2nd Resonance Frequency			
	f_1 (GHz)	$\|S_{11}\|$ (dB)	Bandwidth (MHz)	Gain (dBi)	f_2 (GHz)	$\|S_{11}\|$ (dB)	Bandwidth (MHz)	Gain (dBi)
1	1.84	-26.4	478	2.07	4.50	-15.2	572	3.27
2	1.80	-23.4	413	1.92	4.40	-16.7	489	3.15
3	1.76	-21.2	366	1.67	4.32	-18.2	409	2.99
4	1.72	-19.1	329	1.87	4.24	-20.2	363	3.11
5	1.68	-17.9	301	1.80	4.16	-22.6	339	3.20
6	1.65	-15.8	280	1.72	4.12	-25.1	328	3.12
7	1.64	-14.9	256	1.66	4.04	-35.8	328	3.03
8	1.60	-13.5	220	1.56	3.96	-34.4	320	2.74
9	1.56	-12.8	198	1.50	3.88	-31.5	318	1.75
10	1.53	-12.2	175	1.37	3.83	-27.5	314	0.77

Table 3: Effect of off center position of Sinc patch

Off Center Position Towards Right of Origin (mm)	1st Resonance Frequency				2nd Resonance Frequency			
	f_1 (GHz)	$\|S_{11}\|$ (dB)	Bandwidth (MHz)	Gain (dBi)	f_2 (GHz)	$\|S_{11}\|$ (dB)	Bandwidth (MHz)	Gain (dBi)
1	1.80	-23.1	414	1.89	4.40	-16.0	457	3.23
3	1.80	-26.5	463	1.93	4.36	-15.2	441	3.41
5	1.80	-26.4	445	1.72	4.35	-15.0	434	3.05
7	1.76	-34.1	476	1.88	4.34	-14.8	453	3.01
9	1.76	-27.3	507	1.78	4.36	-15.3	450	2.92
11	1.72	-24.3	530	1.59	4.40	-15.3	531	3.64
13	1.68	-18.6	517	1.29	4.49	-15.1	698	3.56
15	1.64	-19.4	416	1.63	4.52	-19.7	656	2.65
17	1.60	-17.3	366	1.51	4.68	-18.3	672	1.96
19	1.56	-16.8	325	1.34	4.76	-18.4	587	2.5
21	1.52	-15.0	277	1.36	4.78	-12.3	410	1.59
23	1.51	-14.5	249	1.42	4.75	-9.8	-	-

Table 4: Effect of Sinc strip length for Sinc(*2x*)

Sinc Strip Length, *Lp* (mm)	f_1 (GHz)	$\|S_{11}\|$ (dB)	BW (MHz)	f_2 (GHz)	$\|S_{11}\|$ (dB)	BW (MHz)	f_3 (GHz)	$\|S_{11}\|$ (dB)	BW (MHz)
10	2.98	-11.6	471	-	-	-	8.40	-11.9	1067
12	2.58	-14.6	663	-	-	-	8.25	-14.3	1540
14	2.38	-18.3	707	-	-	-	7.80	-13.4	1651
16	2.21	-22.9	703	-	-	-	7.44	-12.9	1864
18	2.05	-28.8	667	-	-	-	6.99	-13.6	1509
20	1.90	-35.4	588	4.6	-12.9	508	6.68	-13.5	1290
22	1.84	-28.8	522	4.49	-14.4	504	6.27	-11.8	1008
24	1.75	-27.3	431	4.20	-17.1	411	6.14	-10.6	527
28	1.60	-20.1	318	3.95	-23.0	330	-	-	-
30	1.52	-17.3	245	3.80	-27.9	294	-	-	-

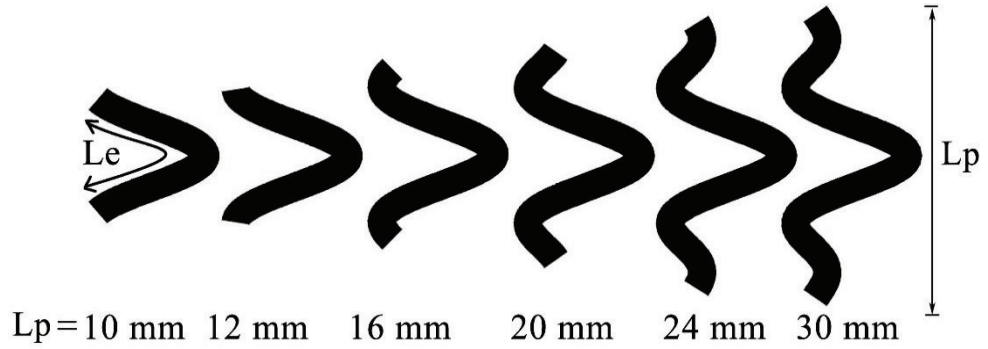

Fig. 6. Various Sinc monopole lengths for Sinc(*2x*) monopole antenna.

IV. EXPERIMENTAL RESULTS

Finally, the prototype model is developed as shown in Fig. 2, and the experimental $|S_{11}|$ characteristic of the proposed antenna is obtained using PNA series of Vector Network Analyzer. In the developed prototype model, the length of the Sinc strip (*Lp*) is considered to be 20 mm and first two resonant modes are considered. The proposed

Sinc shaped antenna operates at 1.90 GHz and 4.60 GHz with an operating bandwidth of 588 MHz (1606-2194 MHz) and 508 MHz (4346-4854 MHz) respectively. The experimental results are then compared with the simulation results as shown in Fig. 7. As seen in Fig. 7, the measured result of the reflection coefficient is better than the simulated result. This is due to the fact that coarse meshing is considered for simulation on finite dielectric material due to memory limitation. The radiation pattern of Sinc(*2x*) monopole antenna for simulation and measurement at 1.90 GHz and 4.60 GHz are shown in Figs. 8 (a) and 8 (b) respectively. A good agreement is evident between the simulated and measured results. The antenna shows a good cross-polarization characteristic at first resonant frequency compared to the second resonant frequency, which may be attributed to the asymmetric structure of the monopole configuration. The measured peak gain and radiation efficiency of the Sinc(*2x*) monopole antenna for first and second operational bands are shown in Figs. 9 (a) and 9 (b) respectively.

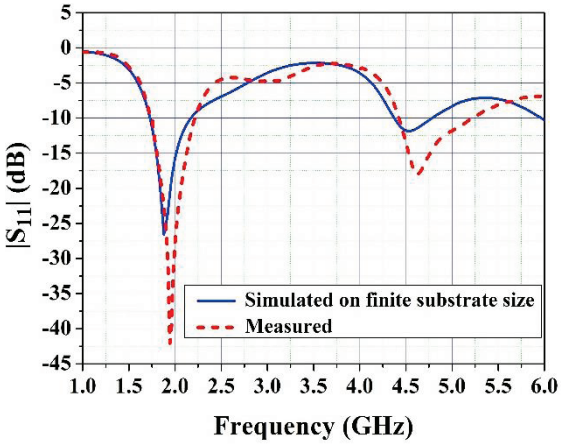

Fig. 7. Simulated and measured reflection coefficient ($|S_{11}|$) for Sinc(*2x*) monopole antenna.

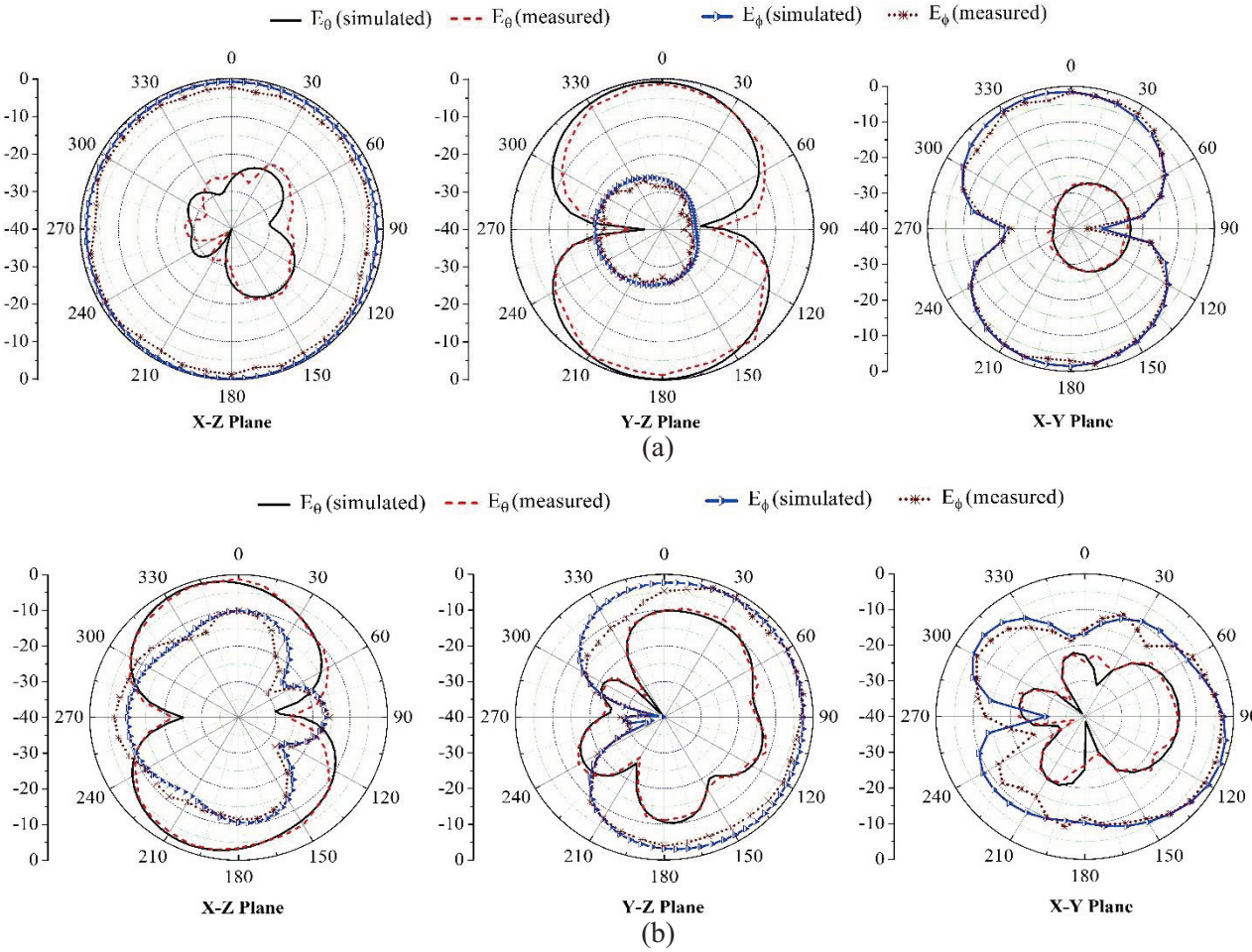

Fig. 8. 2D normalized radiation patterns for Sinc(*2x*) monopole antenna at: (a) 1.90 GHz, and (b) 4.60 GHz.

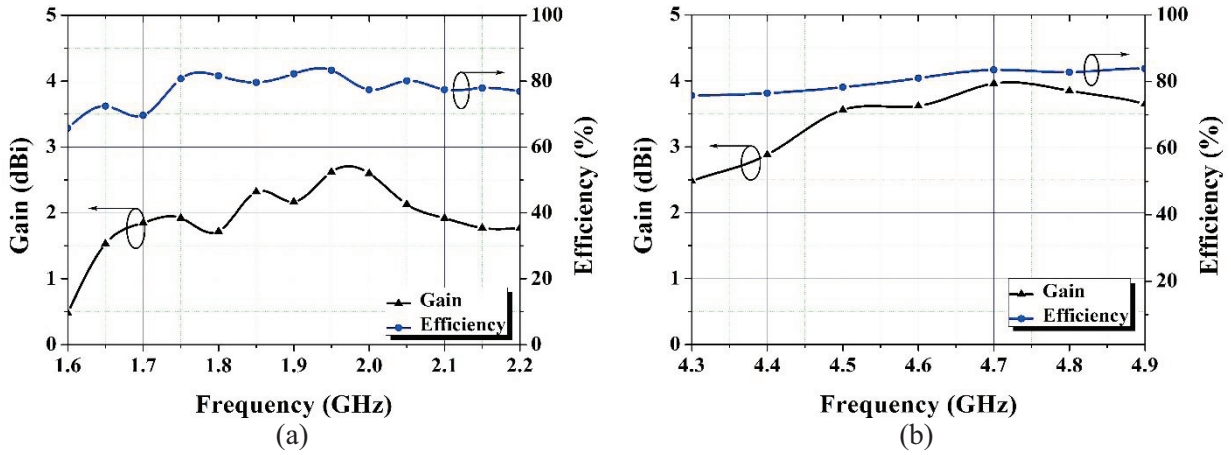

Fig. 9. Measured peak gain and radiation efficiency of Sinc shaped monopole antenna for: (a) first operating band, and (b) second operating band.

VI. CONCLUSION

A new configuration of monopole antenna is proposed for wireless communication. It has been shown that the Sinc shaped monopole antenna is a very good candidate for wireless devices, especially for non-hand held devices used in wireless communication. A detailed parametric study of the proposed antenna indicates that the desired band of operation can be obtained simply by setting the Sinc monopole design parameters without much affecting the area occupied. The antenna occupies an area of $\lambda_0/3\times3\lambda_0/7$. The antenna is found to be useful for several wireless devices operating at DCS/PCS/IMT-2000/UMTS bands.

REFERENCES

[1] H. Toshikazu, "Broadband/multiband printed antennas," *IEICE Trans. Commun*., vol. E88, no. 5, pp. 1809-1817, May 2005.

[2] M. J. Ammann and Z. N. Chen, "Wideband monopole antennas for multi-band wireless systems," *IEEE Magazine Antennas Propag*., vol. 45, no. 2, pp. 146-150, April 2003.

[3] M. Ammann and Z. Chen, "A wide-band shorted planar monopole with bevel," *IEEE Trans. Antennas Propag*., vol. 51, no. 4, pp. 901-903, April 2003.

[4] C. Mahatthanajatuphat, S. Saleekaw, P. Akkaraekthalin, and M. Krairiksh, "A rhombic patch monopole antenna with modified minkowski fractal geometry for UMTS, WLAN, and mobile WiMAX application," *Progress In Electromagnetics Research*, vol. 89, pp. 57-74, 2009.

[5] H. Abutarboush, H. Nasif, R. Nilavalan, and S. W. Cheung, "Multiband and wideband monopole antenna for GSM900 and other wireless applications," *IEEE Antennas and Wireless Propagation Letters*, vol. 11, pp. 539-542, 2012.

[6] C. Y. Huang, W. C. Hsia, and J. S. Kuo, "Compact broadband folded monopole antennas with shorting pins," *Microwave and Optical Technology Letters*, vol. 44, no. 5, pp. 1098-2760, 2005.

[7] W. C. Liu and W. R. Chen, "CPW-fed compact meandered patch antenna for dual-band operation," *Electronics Letters*, vol. 40, no. 18, pp. 1094-1095, September 2004.

[8] J. Y. Jan and T. M. Kuo, "CPW-fed wideband planar monopole antenna for operations in DCS, PCS, 3G, and Bluetooth bands," *Electronics Letters*, vol. 41, no. 18, pp. 991-993, September 2005.

[9] R. Qinjiang and T. A. Denidni, "New broadband dual-printed inverted L-shaped monopole antenna for tri-band wireless applications," *Microwave and Optical Technology Letters*, vol. 49, no. 2, pp. 1098-2760, 2007.

[10] W. C. Liu and C. F. Hsu, "Dual-band CPW-fed Y-shaped monopole antenna for PCS/WLAN application," *Electronics Letters*, vol. 41, no. 7, pp. 390-391, March 2005.

[11] M. A. Abaga Abessolo, A. El Moussaoui, and N. Aknin, "Dual-band monopole antenna with omega particles for wireless applications," *Progress In Electromagnetics Research Letters*, vol. 24, 27-34, 2011.

[12] H. D. Chen and H. T. Chen, "A CPW-fed dual-frequency monopole antenna," *IEEE Trans. Antennas Propagat*., vol. 52, no. 4, pp. 978-982, 2004.

[13] C. H. Cheng, W. J. Lv, Y. Chen, and H. B. Zhu, "A dual-band strip-sleeve monopole antenna fed byCPW," *Microwave and Optical Technology Letters*, vol. 42, no. 1, pp. 70-72, 2004.

[14] M. Joseph, R. K. Raj, M. N. Suma, and P. Mohanan, "Compact dual-band antenna for DCS/2.4 GHz WLAN applications," *Microwave and Optical Technology Letters*, vol. 48, no. 5, pp. 856-859, 2006.

[15] M. N. Suma, R. Raj, M. Joseph, P. C. Bybi, and P. Mohanan, "A compact dual band planar branched monopole antenna for DCS/2.4-GHz WLAN applications," *IEEE Microwave and Wireless Components Letters*, vol. 16, no. 5, pp. 275-277, 2006.

[16] Z. Zhanwei, L. Yuanxin, L. Zhixi, and L. Yunliang, "Biplanar monopole with DSPSL feed and coupling line for broadband mobile phone," *IEEE Antennas and Wireless Propagation Letters*, vol. 11, pp. 1326-1329, 2012.

[17] R. A. Bhatti, N. A. Nguyen, V. A. Nguyen, and S. O. Park, "Design of a compact internal antenna for multi-band personal communication handsets," *Asia-Pacific Microwave Conference, APMC 2007*, pp. 1-4, December 11-14, 2007.

[18] J. H. Chen, C. J. Ho, C. H. Wu, S. Y. Chen, and P. Hsu, "Dual-band planar monopole antenna for multiband mobile systems," *IEEE Antennas and Wireless Propagation Letters*, vol. 7, pp. 769-772, 2008.

[19] H. Y. D. Yang, J. A. Castaneda, and F. D. Flaviis, "A novel printed sinc antenna for wireless communications," *IEEE Antenna and Propag. Society Int. Symp.*, vol. 4, pp. 48-51, 2002.

[20] N. Gupta, M. Mishra, S. C. Kotha, and Y. Kiran, "Multifrequency characteristics of sinc shaped microstrip patch antenna," *Microwave and Optical Technology Letters*, vol. 49, no. 7, pp. 1673-1675, 2007.

[21] C. G. Kakoyiannis and P. Constantinou, "Radiation properties and ground-dependent response of compact printed sinusoidal antennas and arrays," *IET Microwaves, Antennas & Propagation*, vol. 4, no. 5, pp. 629-642, May 2010.

[22] C. G. Kakoyiannis, P. Gika, and P. Constantinou, "Small printed sinusoidal antennas: a simple design guide for smooth meander-line structures with augmented bandwidth," *In IEEE International Workshop on Antenna Technology, iWAT 2009*, pp. 1-4, 2009.

[23] C. G. Kakoyiannis and P. Constantinou, "Compact WSN antennas of analytic geometry based on chebyshev polynomials," *In 2012 Loughborough Antennas and Propagation Conference (LAPC)*, pp. 1-6, 2012.

[24] "IE3D user manual," *Zeland Software Inc*., USA, 2002.

Ritesh Kumar Badhai was born in India in 1984. He received the Bachelor of Engineering degree in Electronics and Communication Engineering from Rajiv Gandhi Proudyogiki Vishwavidyalaya, Bhopal, India in 2007; and the Master of Engineering degree in Electronics and Communication Engineering from Birla Institute of Technology, Mesra, Ranchi, India in 2009.

He currently is an Assistant Professor in the Department of Electronics and Communication Engineering, Birla Institute of Technology, Patna, Bihar, India and is also pursuing his Ph.D. degree.

Nisha Gupta received the Bachelor's and Master's degrees in Electronics and Telecommunication and Electrical and Electronics Engineering, both from Birla Institute of Technology, Mesra, Ranchi, India; and the Ph.D. degree from The Indian Institute of Technology, Kharagpur, India. She was a Post-doctoral Fellow at The University of Manitoba, Canada from 1997-1998 before joining the Department of Electronics and Communication Engineering, Birla Institute of Technology in 1999 as a Reader. Currently, she is a Professor in the same department. She has authored and co-authored more than 100 technical journal articles and conference papers. Her research interests are Computational Electromagnetics, Antennas for Wireless Communication, AI techniques in Wireless and Mobile Communication and EMI/EMC.

SV-Training and Kernel Change Detection Algorithm for the Abrupt Modification in EMI Data for Buried Metallic Target Localization and Identification

Yacine Matriche [1,2,3,*], Saïd Moussaoui [4], Mouloud Feliachi [3], Abdelhalim Zaoui [2], and Mehdi Abdellah [2]

[1] EST, Kolea Tipaza, Algeria

[2] Ecole Militaire Polytechnique, BP 17, B. E. Bahri, Algiers, Algeria

[3] Université de Nantes, PRES-L'UNAM, IREENA, CRTT, Bd de l'Université, BP 406, St-Nazaire Cedex 44602, France.

[4] Ecole Centrale de Nantes, IRCCYN, UMR CNRS 6597, 1 rue de la Noë, 44321 Nantes, France
*yacine.matriche@etu.univ-nantes.fr

Abstract ─ In this paper, we propose a new method to identify and to locate buried metallic object in ElectroMagnetic Induction (EMI) data based on the Kernel Change Detection (KCD) algorithm. The signature of the object in the EMI data is typically of low amplitude. Particularly, in the case where two objects are located at different depths, the amplitude of the deeper buried object is negligible compared to that of the object buried in the first centimeter of the soil. This would result in the fact that, the EMI system can neglect the signature of this object and consequently increases miss rate or False Negative Rate (FNR). The aim of the proposed method is to calculate a decision index for each EMI measurement in a so-called hypotheses space using KCD algorithm. The amplitude of these decision indexes in the case of objects at different depths are in the same range, which make their variance smaller. Indeed, this index will be compared to a threshold for judging the presence or absence of a rupture. The validation of the proposed method is performed by processing real EMI data derived from a series of measurements on real objects.

Index Terms ─ Decision index, electromagnetic induction, kernel change detection algorithm, mine detection, support vector training.

I. INTRODUCTION

Many countries around the world are affected by mines and UneXploded Ordnance (UXO). These remains threaten of the human being because their impacts still exist and can occur at any time. To fight against these threats, the researchers have developed several detection systems such as ElectroMagnetic Induction (EMI) system [1], [2] and the Ground-Penetrating Radar (GPR) [3].

The EMI system is the first prospecting system that was developed for the exploration of near basement. It is used in the geophysical survey to locate the metallic structures and objects inside the upper layer of the soil. It has been used in the field of demining during the First World War. Since then, the researchers developed it by increasing its sensitivity to find smaller amounts of metal. The first EMI system contains only a single coil [4]. Subsequently, researchers have added other coils in order to distinguish between a dummy object and a mine. The most recent EMI operates with low range frequencies (typically 1 kHz to 1 MHz) and its operating principle is quite simple. The interaction between the magnetic field and the metallic structures gives rise to eddy currents that generate a secondary field which will oppose the primary field. The use of EMI systems has become more interesting with the development of data processing

Submitted On: April 30, 2014
Accepted On: October 5, 2014

techniques based on inverse methods [1], [4].

In this context, we can mention the paper [5] in which a Normalized Surface Magnetic Source (NSMS) model is applied to UXO discrimination. A fast and accurate numerical forward model that represents an objects response using a set of equivalent magnetic dipoles distributed on a surrounding closed surface. In [6], the authors present a methodology to guarantee the convergence of the electromagnetic inverse method. It consists of using Genetic Algorithms (GA) to identify a model that will be used to estimate the electric and magnetic field radiated by the device under test. In [7], the authors propose a novel scheme for detecting the location of a metallic mine. This technique takes into account Eddy-Current Response (ECR) induced on the conducting marine mines as well as Current-Channeling Response (CCR) associated with the perturbation of currents induced in the conductive marine environment.

In [1], an Improved Particle Swarm Optimization (IPSO) and Finite Element Method (FEM) are used to inverse the EMI data. This method leads to interesting results in terms of identification and localization of buried object. However, and despite of its effectiveness, the application of the FEM method makes the exploration in the real-time almost impossible, resulting in the necessity to resort to high performance computing devices. In order to have a pre-decision in real-time about the existence of a suspicious object, we must use a faster inversion method.

In this paper, we propose a fast processing method for the EMI data based on the Kernel Change Detection (KCD) algorithm [8], [9]. It consists of detecting the ruptures due to Abrupt Change (AC) in the EMI observations (EMI measurements). The AC detection is not directly detected in the observations space, but rather in a hypotheses space using a Kernel and Support Vector (SV) training in order to obtain a data representation in this space [10], [8], [9]. Consequently, a decision index is calculated for each position of the EMI system [11]. After that, we build an image from the resulting decision index where the shape of objects is apparent.

However, even if the resulting image is not well filtered because of the roughness of the soil, the decision index of the object shall prevail and an adequate threshold will give us a clear shape of the object. Finally, the inference on the presence or the absence of the object will thus be performed with a reduced rate of false alarms.

The rest of this paper is organized as follows. In Section II, the EMI system will be presented and its basic operation will be explained. Then, in Section III, the KCD algorithm will be presented in detail, the rupture detection method using the SV estimators will be also presented in this section. Finally, in Section IV, we will adapt the KCD method to the EMI data and will detail the followed steps. The adjusting of the KCD parameters to the EMI data is also presented in this section. The effectiveness of the proposed method is tested on a real EMI data.

II. ELECTROMAGNETIC INDUCTION SYSTEM

The basic EMI system consists of a transmitter coil and two receiver coils, Fig. 1. Its operation is based on electromagnetic induction, where the transmitter coil, traversed by a variable current, generates an electromotive force across the two receiver coils disposed above and below it at the same distance [1]. In vacuum, the difference of the induced voltage (ΔV) between the two receiving coils is zero. During prospection and when the system passes over a metallic object, the transmitter coil generates an eddy current in the surface of this object. Therefore, these currents will generate an electromotive force which is only across the lower receiver coil and the balance between the two induced voltages in the receiver coils is disturbed. Thus, the ΔV quantity depends only on the field generated by the eddy current on the buried object. In this case, the ΔV gives the signature of the object since the generated field depends on its physical and geometrical characteristics [1], [4].

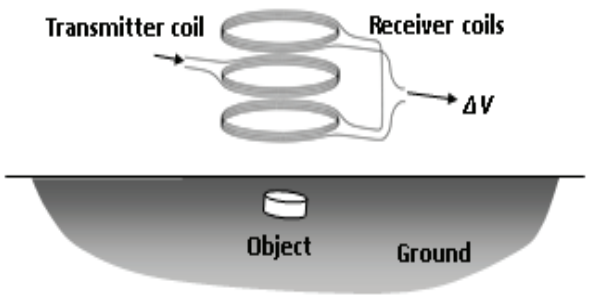

Fig. 1. Basic diagram of EMI system.

III. KERNEL CHANGE DETECTION ALGORITHM

A. General framework

AC detection in signals is a much studied problem in the signal processing literature [10] [12]. In the case of systems where the data, defined in the observation space $\mathcal{X}$ follow a known physical or statistical model according to some Probability Density Function (PDF), this task has become a simple and easy to implement. However, when the PDF is unknown, one has to use unsupervised statistical methods based on machine learning [10], [13].

In that respect, the KCD algorithm, proposed in [8], [9], finds a minimal decision region $R_x^{\mathcal{X}} \in \mathcal{X}$ where most of the data $(x_i;\, i=1,\ldots,m)$ have the same unknown PDF. The region $R_x^{\mathcal{X}}$ is defined by a representation based on a real valued decision function $f(\cdot)$, according to:

$$f(x) \geq 0, x \in R_x^{\mathcal{X}} \text{ and } f(x) < 0, x \notin R_x^{\mathcal{X}}, \quad (1)$$

with a decision function $f(\cdot)$ deduced by training a single class SVM classifier [10], [12].

B. SVM training for AC detection

Let $\boldsymbol{x} = f(x_1; x_2, \ldots, x_m) \in \mathcal{X}$ a training vector. The aim of single-class classification is the estimation of a region $R_x^X \in X$ in which the decision functions $f(\cdot) \geq 0$. In this case, we defined another space $\mathcal{F}$, where the estimate of an image of the $R_x^{\mathcal{X}}$ is possible. Let ϕ a mapping function defined over the input space $\mathcal{X}$ and taking values in hypotheses space as follows:

$$\phi : \mathcal{X} \times \mathcal{X} \rightarrow \mathcal{F} \quad (2)$$
$$< x_i, x_j > \rightarrow < \phi_i, \phi_j >.$$

Here, $\mathcal{F}$ is endowed with a dot product $< \cdot, \cdot > = k(\cdot, \cdot)$, where $k(\cdot, \cdot)$ is a normalized kernel and it fulfills the Mercer conditions where $\{\forall (x_i, x_j) \in \mathcal{X}, k(x_i, x_j) > 0 \text{ and } k(x_i, x_i) = 1\}$. In this case, all the images of the inputs $(x_i \in \mathcal{X})$ in $\mathcal{F}$ lie-on the perimeter of a circle with a unit radius and center O (O is also the center of $\mathcal{F}$), as shown in Fig. 2 (a). Therefore, the single-class SVM for the AC detection estimation consists in separating the training vectors from the hypersphere center O with a hyperplane $\mathcal{W}$ such that $\{< w,\, x >_{\mathcal{F}} - b = 0$ with $w \in \mathcal{F}$ and $b \in \mathbb{R}_+^*\}$.

However, the term $< w,\, x_i >$ can be computed using only the dot product function $k(x_i,\, x_j) = < x_i,\, x_j >$ [11]. This kernel represents a dot product in some feature space if it fulfills the Mercer conditions [8]. These conditions are satisfied for a wide range of kernels, including Gaussian radial basis functions defined as [9]:

$$k(x_i, x_j) = exp\left(-\frac{\left\| x_i - x_j \right\|_{\mathcal{X}}^2}{2\sigma^2} \right), \quad (3)$$

where σ is a parameter that controls the dispersion of the images ϕ_i of the observations x_i.

The decision function $f(\cdot)$ in equation 1 will therefore be defined as:

$$f(x_i) = < w,\, x_i >_{\mathcal{F}} - b. \quad (4)$$

Consequently, this decision function, defined in the hypotheses space $\mathcal{F}$, will allow to deduce the region $R_x^{\mathcal{X}}$ in the input $\mathcal{X}$. Thus, SVM approach for the AC detection returns to the maximization of the distance between the center O of the hypersphere and the hyperplane $\mathcal{W}$ by solving the following optimization problem:

$$min\left(\frac{1}{2}\|w\|_{\mathcal{F}}^2 + \frac{1}{vm}\sum_{i=1}^{m} \xi_i - b \right), \quad (5)$$

where $w \in \mathcal{F}, b \in \mathbb{R}_+^*$ and $\xi_i \in \mathbb{R}^m$, subject to:

$$< w,\, x_i >_{\mathcal{F}} - b \geq \xi_i \text{ and } \xi_i \geq 0, \quad (6)$$

where $\frac{1}{vm}$ is a positive parameter that tunes the possible amount of outliers and ξ_i are the so-called slack variables, added here to take-outliers [9].

In Fig. 2 (a), there are some observations which are not in above of the hyperplane $\mathcal{W}$. To take into account these observations, a smooth margin ξ_i is added in equation (5) for each observation x_i.

The minimization problem defined in equation (5) is quadratic with linear constraints. Adding the Lagrange multipliers $\alpha_i, i = 1, \ldots, m,$ brings back to the following dual minimization problem:

$$\min_{\alpha} \frac{1}{2} \boldsymbol{\alpha}^t \, \boldsymbol{K} \, \boldsymbol{\alpha}, \quad (7)$$

subject to:

$$0 \le \alpha_i \le \frac{1}{vm} \text{ and } \sum_{i=1}^{m} \alpha_i = 1, \ (\forall i = 1,\ldots,m), \quad (8)$$

which can be solved by numerical methods of quadratic programming [14], [15], where $\boldsymbol{K}$ is a matrix (whose elements are built starting from two successive subsets taken on the training vector $\boldsymbol{x} \in \mathcal{X}$) and the kernel define in equation (3).

C. Abrupt change detection method

Let $(x_1, x_2, \ldots, x_t, \ldots, x_m)$ a set of observations defined in the space $\mathcal{X}$. The goal of the method is to detect whether or not there is an AC at the observation x_t. In that respect, two subsets corresponding to the immediate past $\boldsymbol{x}_1 = (x_{t-m_1}, \ldots, x_{t-1})$ and the immediate future $\boldsymbol{x}_2 = (x_t, \ldots, x_{m_2})$ of this observation are considered (Fig. 2 (b)). Two SV estimators based on a Gaussian kernel are separately trained from these subsets. The resulting parameters w_1, b_1 and w_2, b_2 will define the two separating hyperplanes $\mathcal{W}_1$ and $\mathcal{W}_2$.

Figure 2 (c) gives a geometrical representation of the KCD method whose main principle is to assess the possible occurrence of a rupture between the two subsets by comparing the arc $(c_{(t,1)}, c_{(t,2)})$ to the sum of the two arcs $(c_{(t,1)}, p_{(t,1)})$ and $(c_{(t,2)}, p_{(t,2)})$. Indeed, it computes a dissimilarity measure according to [12]:

$$D(x_1, x_2) = \frac{(c_{(t,1)}, c_{(t,2)})}{(c_{(t,1)}, p_{(t,1)}) + (c_{(t,2)}, p_{(t,2)})}, \quad (9)$$

where:

$$(c_{(t,1)}, c_{(t,2)}) = arccos\left(\frac{\boldsymbol{\alpha}_1^t \boldsymbol{K}_{12} \boldsymbol{\alpha}_2}{\sqrt{\boldsymbol{\alpha}_1^t \boldsymbol{K}_{11} \boldsymbol{\alpha}_1} \sqrt{\boldsymbol{\alpha}_2^t \boldsymbol{K}_{22} \boldsymbol{\alpha}_2}} \right), \quad (10)$$

$$(c_{(t,j)}, c_{(t,j)})_{j=1,2} = arccos\left(\frac{b_i}{\sqrt{\boldsymbol{\alpha}_j^t \boldsymbol{K}_{jj} \boldsymbol{\alpha}_j}} \right), \quad (11)$$

where α_1 (resp. α_2) is the column vector (Lagrange multipliers) corresponding to w_1 (resp. w_2) that have been computed during training. The kernel matrix $\boldsymbol{K}_{t,uv}, (u,v) \in \{1,2\} \times \{1,2\}$ has entries at row #j and column #l given $k(x_{t,u}^j, x_{t,v}^l)$, where $x_{t,u}^j$ is the observation #j in the subset x_u [8].

Finally, a decision index $I(t) = D(x_1; x_2)$ is compared to some predefined threshold η in order to decide whether a rupture occurred at position t.

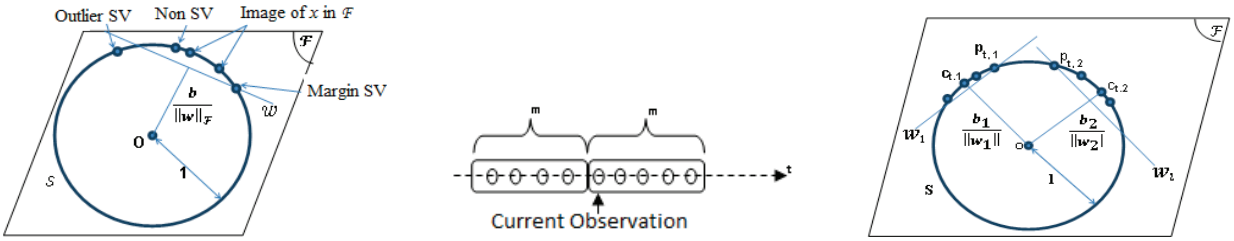

(a) (b) (c)

Fig. 2. (a) The SVM for the AC detection interpretation, (b) the scenario of the observations, and (c) geometrical representation of KCD method.

IV. APPLICATION OF THE KCD METHOD TO REAL EMI DATA

A. The aim of the proposed method

Figure 3 (a) shows the form of the induced voltage ΔV according to the EMI displacements for two real cases, where two cylindrical objects are buried at depth of 2 cm and 4,5 cm. As they are, the EMI system data does not provide much information about the object which is at the origin of this induced voltage. Particularly, in the case of the most buried object, the signature is almost invisible in the observation space. For this reason, we introduce KCD algorithm to make this information more meaningful. A decision index of

these previous EMI data is presented in Fig. 3 (b). In this case, one can see that the decision index of the most buried object is in the same magnitude of the second object.

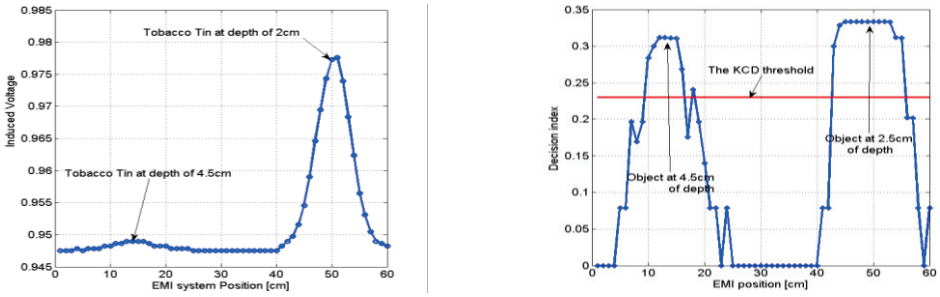

(a) (b)

Fig. 3. (a) Real EMI data (induced voltage ΔV) for two cylindrical objects buried at depth of 2 cm and 4,5 cm, and (b) decision index relative to these EMI data.

B. Overview of experimental tests performed

In this section, real cases of landmines detection are performed (a metal landmine and a plastic one), Fig. 4 (a). This testing was performed by the University of Florence-Italy in 2004, using multi-sensor system, in a bed with 3 m by 3 m in plan, with a sloping base at 60 cm to 80 cm to provide drainage, and minimize basal reflections. A multisensory system is used in the prospection. It includes the EMI system, GPR system and holographic radar system [16]. Four landmine simulants were buried at shallow depth in the test bed. These included:

- A PMA-2 simulant mine which reproduces the real PMA-2 anti-personnel plastic landmine with diameter of 6,9 cm. This landmine is buried at depth of 5 cm, Fig. 5 (a);
- Two cylindrical, metallic pipe tobacco tins with diameter of 10,5 cm. Those objects are buried at depths of 2 cm and 4,5 cm, Fig. 5 (b);
- A cylindrical plastic case with diameter of 10,5 cm. This object is buried at depth of 5,5 cm, Fig. 5 (c).

The objects were placed in the bed so as to form a square. The distance between the objects was 40 cm.

The exploration was made horizontally along parallel lines to sweep all the bed, Fig. 4 (b).

The EMI system provides a matrix of measurement points, which the number of rows is the number of the horizontal prospection lines and the number of columns is the number of the sampled measurement by line, Fig. 4 (b). In this case, all resulting responses of the EMI system give an image whose pixels are the points of measurements, and contrast of the pixel is the value of the induced voltage at these points.

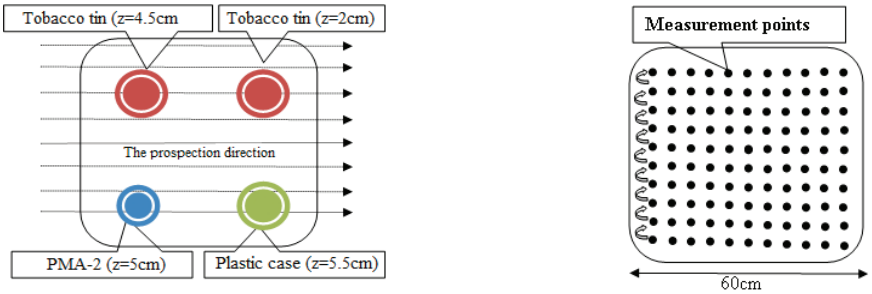

(a) (b)

Fig. 4. Schematic of buried landmine simulants: (a) objects position, and (b) prospection scenario; after a series of measurements with fixed step on the i^{th} horizontal line parallel to the X-axis, we shift for a fixed step following the Y-axis and we take again the same measurements on the $(i + 1)^{th}$ horizontal line.

C. Object detection using KCD algorithm

1) Parameters setting for EMI Data: the KCD method implementation requires several preliminary parameters settings:
   - The choice of the training subset larger m_1, m_2 : observations in a Bscan are made at a regular horizontally GPR displacement step. To ensure the rupture detection between two consecutive observations, the number of observations in the training subset multiplied by the GPR displacement step must be less than the half of the dimension of the object. Else, the KCD algorithm cannot detect a rupture since all the observations are in the same region of the observation space. Generally, we take $m_1 = m_2 = m$ where:
     $$m \times horizontal\_step \leq 0{,}5 \times object\_dimensions \quad (12)$$
   - Kernel Choice: The kernel defines implicitly the function $\phi_i : \mathcal{X} \to \mathcal{F}$. However, the elements presented below remain true for any Mercer kernel, such that satisfy the Mercer conditions defined in Section III-B [8], [9]. In the case of a Gaussian kernel, the σ sets the position of the sampled observations x_i in space $\mathcal{F}$. If $\sigma \ll \|x_i - x_j\|, (x_i, x_j) \in \mathcal{X}$, the dispersion of the observations images in $\mathcal{F}$ is important. Otherwise, all these images are close. Neither of these two cases is advantageous in the case of the rupture detection. A choice of σ approximately in the order of $\|x_i - x_j\|$ makes sense in this case [9], [11].
   - The choice of *v*: the parameter *v* determines the rate of inclusion of the abnormal observations. $v = 0$ corresponds to a hard margin algorithm. $v = 1$ corresponds to a margin released algorithm. In most cases, this parameter is taken between $0{,}2 \leq v \leq 0{,}8$.

   Generally, *v* and σ are selected in a heuristic way [11]. In our case, we used method IPSO described in [1] by taking some observations like entries for the optimization processes of these two parameters.

2) KCD algorithm for EMI Data: it is proposed to apply the KCD algorithm to detect the ruptures caused by the presence of the object using the EMI system in the previous measurements. To do this, the following steps are followed:

- Step 0: Initialization:
  – Generally the radius of the mines exceeds 3 cm. Since the horizontal step of displacement is 1 cm, we choose the size of the subsets $m_1 = m_2 = 3$.
  – The optimization process provided us the optimal $v = 0{,}5$ and $\sigma = 0{,}001$.
  – Set $t = m + 1$.
- Step 1: The Row Training:
  For each row of the resulting image, we do:
  – Initialized the subsets of training as $\boldsymbol{x}_1 = (x_{t-m}, \ldots, x_{t-1})$ and the immediate future $\boldsymbol{x}_2 = (x_t, \ldots, x_{t+m-1})$.
  – Trained independently the two subsets $\boldsymbol{x}_1$, $\boldsymbol{x}_2$ and we obtain the parameters $(w_{t,1}, b_1)$, $(w_{t,2}, b_2)$ or equivalently $(\alpha_{t,1}, b_1)$, $(\alpha_{t,2}, b_2)$.
  – Calculate the decision index $I_r(t) = D(\boldsymbol{x}_{t,1}, \boldsymbol{x}_{t,2})$ using (9-11).
- Step 2: The Increment:
  – If the maximum number of the points per row is reached, move to the next row.
  – Else increment $t \to t + 1$ and return to step 1.
- Step 3: The Columns Training:
  Once the scan of all rows is finished, we will have a decision index for each point of the image $I_r(t)$. Thereafter, we repeated the algorithm from step 1, but this time we consider the columns for the construction of the subsets. The test of step 2 is compared to the number of points per column for the passage to the next column. A decision index I_c is also calculated for each point and the global decision index for each point will be the sum of the two decision indexes.
  $$I_t = I_r + I_c. \quad (13)$$
- Step 4: On Line Rupture Detection:
  Once the total decision index is computed, the resulting image is tainted with some

residues, due to the roughness of the soil. However, the decision index magnitude of these residues is low compared to that of the objects, and to eliminate them, a thresholding is applied to the image to make it clearer, and the rupture detection is tested using:

– If $I_t(t) \geq \eta$ there is a rupture in instant t.

– If $I_t(t) < \eta$ there is no rupture in instant t.

D. The choice of rupture threshold η:

Figure 3 (a) shows the response of the EMI system for the horizontal line which passes over the two Tobacco tin objects. Note that, for the most buried object, the response is almost zero. In this case, the detection is difficult by working directly on the data in the observation space. Figure 3 (b) shows the decision index response of the EMI using the KCD algorithm applied to the EMI response of the Fig. 3 (a). Note that in this case, the response of the more buried object is more visible and which is exactly the interest of the proposed method. A threshold of $\eta = 0,23$ is acceptable in this case. Thus, for the values lower than the threshold, the background noise of the image will be considered as null. In this case, the image will be clear and the problem of noise will be solved.

E. Results and discussion

Figure 6 (a) shows the EMI response on the studied bed. It is revealed that, for the most buried object, the response is almost not visible. Indeed, the detection of this object is not evident in the observation space.

The introduction of KCD algorithm for the rupture detection based on SV-estimators becomes a necessity. Therefore, whatever the depth of the object, the algorithm KCD must detect the ruptures in the EMI response. Figure 6 (b) shows the decision index of the EMI response system without thresholding. Although, we can distinguish objects but the resulting image is tainted yet.

After a good thresholding, we have Fig. 6 (c), where all metal objects are clearly visible. We note that, the two tobacco tins are located with their precise positions and the distance between the two metal objects is 40 cm. Then, if the object is largely buried, the method provides information on the dimensions of the object even if the signature of the object is low. In this case, the diameter of the two objects is 10 cm.

The total time for processing data (3600 samples of the induced voltage corresponding to a surface scan of 60 cm × 60 cm with a step of 1 cm, Fig. 4 (b)) is $148,24s$. For the KCD treatment of one sampled induced voltage we need $41,17ms$, which makes the real-time detection possible.

Unfortunately, since the EMI system only detects the metallic objects, the other two plastic objects are not visible because of the absence of their signatures.

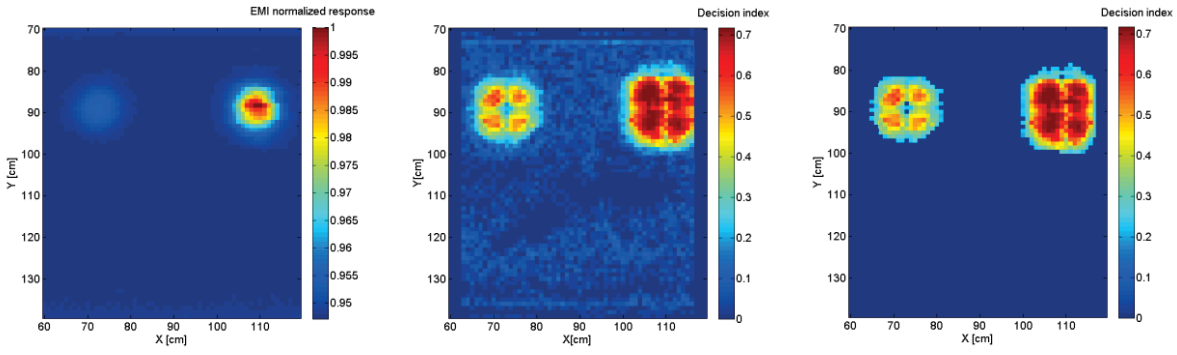

Fig. 6. (a) EMI response, (b) the total decision index without thresholding, and (c) the total decision index with thresholding.

V. CONCLUSION

The proposed method is based on the KCD algorithm and SV-training. A decision index is calculated from measurements provided in the case of an EMI inspection in a hypotheses space according to both horizontal and vertical axes. We have noticed that, for different depths of buried objects, the decision index magnitude is almost the same. Then, we set a threshold to remove more residues that are due to the roughness of the ground. An image of the soil basement is generated highlighting different objects located therein. The method was tested on real EMI data made available by the University of Florence, Italy. This test has given good results for the detection and identification of buried metallic objects.

ACKNOWLEDGMENT

The authors would like to thank Timothy D. Bechtel, Ph.D., PG Visiting Professor, Department of Earth and Environment Franklin and Marshall College, Lancaster, PA, USA for his contribution in this work and the real GPR data that provided us.

REFERENCES

[1] Y. Matriche, M. Feliachi, A. Zaoui, and M. Abdellah, "An EMI inversing problem for landmine characterization based on improved particle swarm optimization and finite element analysis," *Progress In Electromagnetics Research, B*, vol. 49, pp. 411-428, March 2013.

[2] K. Paulsen, I. Shamatava, F. Shubitidze, K. O'Neill, and K. Sun, "Fundamental mode approach to forward problem solutions in EMI scattering inferring fundamental solutions from training data," *Applied Computational Electromagnetics Society-Conference Computational Techniques*, 2004.

[3] K. P. Prokopidis and T. D. Tsiboukis, "Modeling of ground-penetrating radar for detecting buried objects in dispersive soils," *Applied Computational Electromagnetics Society*, vol. 22, no. 2, 2007.

[4] H. Huang, B. SanFilipo, A. Oren, and I. J. Won, "Coaxial coil towed EMI sensor array for uxo detection and characterization," *Journal of Applied Geophysics*., vol. 61, no. 3-4, pp. 217-226, March 2007.

[5] F. Shubitidze, J. P. Fernandez, I. Shamatava, L. R. Pasion, B. E. Barrowes, and K. O'Neill, "Application of the normalized surface magnetic source model to a blind unexploded ordnance discrimination test," *Applied Computational Electromagnetics Society*, vol. 25, no. 1, 2010.

[6] S. Saidi and J. B. S. Hadj, "Improving convergence time of the electromagnetic inverse method based on genetic algorithm using the PZMI and neural network," *Progress In Electromagnetics Research, B*, vol. 51, pp. 389-406, April 2013.

[7] M. Mahmoudi and S. Y. Tan, "Depth detection of conducting marine mines via eddy-current and current-channeling response," *Progress In Electromagnetics Research, PIER*, vol. 90, pp. 287-307, 2009.

[8] F. Desobry and M. Davy, "Support vector-based online detection of abrupt changes," *Proceedings IEEE Int. Conf. Acoust. Speech, Signal Process, (ICASSP 03)*, vol. 4, pp. 872-875, 2003.

[9] F. Desobry, M. Davy, and C. Doncarli, "An online kernel change detection algorithm," *IEEE Trans. Signal Process*, vol. 53, no. 8, pp. 2961-2974, August 2005.

[10] M. Al Sharkawy, M. Sharkas, and D. Ragab, "Breast cancer detection using support vector machine technique applied on extracted electromagnetic waves," *Applied Computational Electromagnetics Society*, vol. 27, no. 4, 2012.

[11] D. Potin, P. Vanheeghe, E. Duflos, and M. Davy, "An abrupt change detection algorithm for buried landmines localization," *IEEE Trans. Geosci. Remote Sensing*, vol. 44, no. 2, pp. 260-272, 2006.

[12] S. Caorsi, D. Anguita, E. Bermani, A. Boni, and M. Donelli, "A comparative study of NN and SVM-based electromagnetic inverse scattering approaches to on-line detection of buried objects," *Applied Computational Electromagnetics Society*, vol. 18, no. 2, 2003.

[13] V. Vapnik, "The nature of statistical learning theory," 2nd ed., *Ser. Statistics for Engineering and Information Science, Springer*, 1999.

[14] T. Coleman and Y. Li, "A reflective Newton method for minimizing a quadratic function subject to bounds on some of the variables," *SIAM Journal on Optimization*, vol. 6, no. 4, pp. 1040-1058, 1996.

[15] N. Gould and P. L. Toint, "Preprocessing for quadratic programming," *Mathematical Programming, Series B*, vol. 100, pp. 95-132, 2004.

[16] L. Capineri, S. Ivashov, T. Bechtel, A. Zhuravlev, P. Falorni, C. Windsor, G. Borgioli, I. Vasiliev, and A. Sheyko, "Comparison of GPR sensor types for landmine detection and classification," *12th International Conference on Ground Penetrating Radar*, 2008.